EBM Experimental Biology and Medicine

Volume 251 | Issue 4

Experimental Biology and Medicine

Editor-in-Chief

Nicola Conran
University of Campinas, Brazil

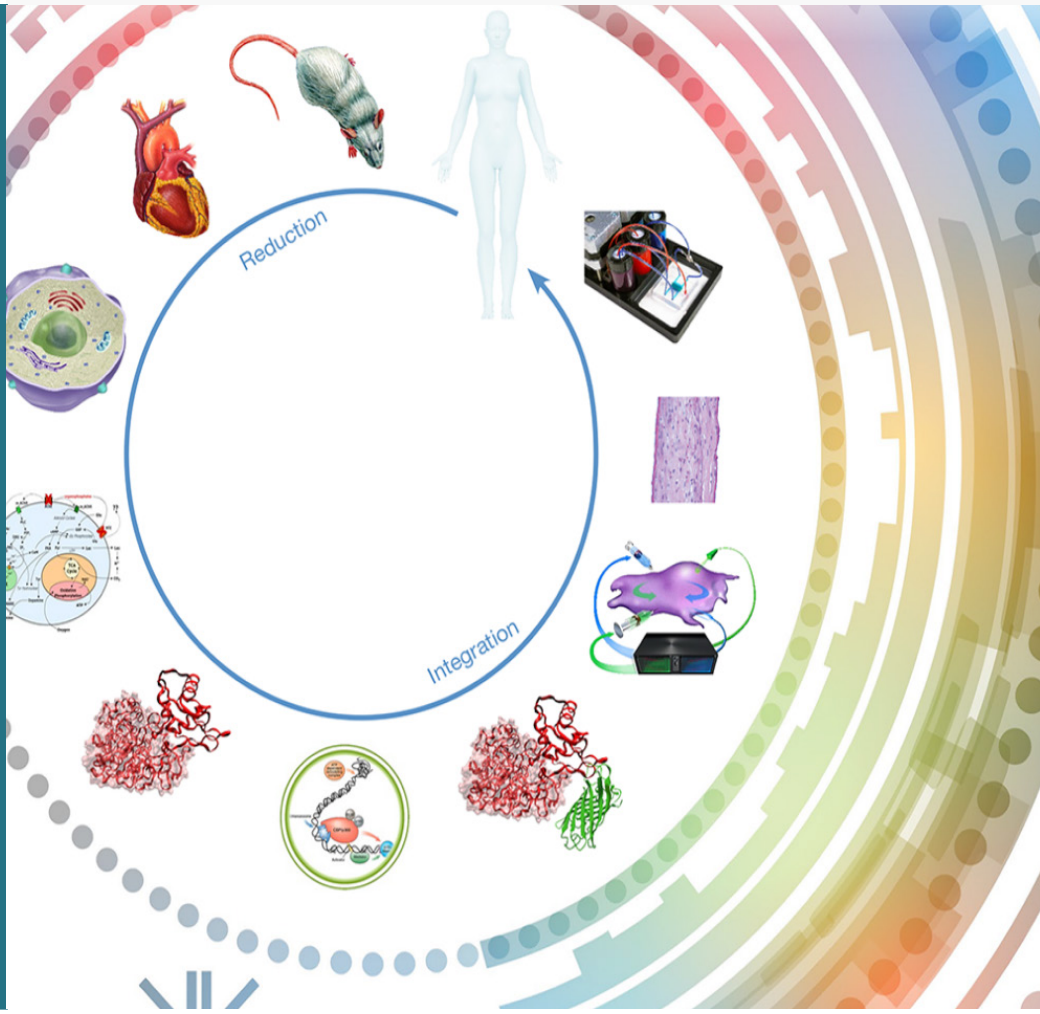

ISBN 978-2-8325-8008-0
DOI 10.3389/978-2-8325-8008-0

frontiers | Publishing Partnerships

Society for Experimental Biology and Medicine
3220 N Street NW, #179
Washington DC 20007, USA
Executive Director – ed@sebm.org

www.sebm.org

EBM Experimental Biology and Medicine

Editorial Board

ISSN 1535-3699
ISBN 978-2-8325-8008-0
DOI 10.3389/978-2-8325-8008-0

Generative AI statement
Any alternative text (Alt text) provided alongside figures in the articles in this ebook has been generated by Frontiers with the support of artificial intelligence and reasonable efforts have been made to ensure accuracy, including review by the authors wherever possible. If you identify any issues, please contact us.

EBM Experimental Biology and Medicine

2026 | Volume 251 | Issue 4 | ISSN 1535-3699

Table of contents

Physiology, Pathophysiology and Mechanisms of Disease

Structural Biology

Translational Research

EBM Experimental Biology and Medicine

TYPE Original Research
PUBLISHED 05 March 2026
DOI 10.3389/ebm.2026.10929

OPEN ACCESS

*CORRESPONDENCE
Qiang Gao,
gaoqiang_89@163.com
Jimei Chen,
jimei_1965@outlook.com

RECEIVED 09 December 2025
REVISED 03 February 2026
ACCEPTED 23 February 2026
PUBLISHED 05 March 2026

CITATION
Hu L, Zhuang W, Chen W, Yang S, Chen S, Wang X, Gao Q and Chen J (2026) Global MyoG research 2004–2024: a bibliometric analysis of trends and translational implications. *Exp. Biol. Med.* 251:10929. doi: 10.3389/ebm.2026.10929

Global MyoG research 2004–2024: a bibliometric analysis of trends and translational implications

Luoming Hu[1,2], Weizhong Zhuang[2], Weimin Chen[2,3], Song Yang[1,2], Shuo Chen[1,3], Xin Wang[3,4], Qiang Gao[2,3]* and Jimei Chen[1,2,3]*

[1]Department of Cardiac Surgery, Guangdong Provincial People's Hospital, Guangdong Academy of Medical Sciences, Southern Medical University, Guangzhou, China, [2]Guangdong Cardiovascular Institute, Guangdong Provincial People's Hospital, Guangdong Academy of Medical Sciences, Southern Medical University, Guangzhou, China, [3]Guangdong Provincial Key Laboratory of South China Structural Heart Disease, Guangzhou, China, [4]School of Medicine South China University of Technology, Guangzhou, China

Abstract

Myogenin (MyoG) is a core myogenic transcription factor that orchestrates myoblast differentiation and myofiber maturation and has been increasingly implicated in skeletal muscle degeneration and rhabdomyosarcoma, yet its global research landscape has not been systematically characterized. In this study, we performed a bibliometric analysis of MyoG-related publications from 2004 to 2024 retrieved from the Web of Science Core Collection. A total of 402 articles authored by 2,402 researchers from 1,148 institutions across 165 countries and regions were analyzed using VOSviewer, CiteSpace and R-based bibliometric tools. We quantified annual publication output, identified leading countries, institutions, authors and journals, and reconstructed collaboration, co-citation and keyword co-occurrence networks to delineate thematic evolution. The global pattern showed a multipolar structure dominated by the United States and China, with European institutions forming an additional hub and emerging countries contributing with growing but comparatively lower impact. Research hotspots exhibited a clear progression from early work on molecular mechanisms (DNA binding, MyoD family interactions, chromatin remodelling) toward regenerative biology (satellite cell regulation, muscle regeneration) and, more recently, disease-oriented studies focused on muscle atrophy, Duchenne muscular dystrophy and rhabdomyosarcoma. Landmark co-cited studies established MyoG as an indispensable regulator of skeletal muscle differentiation and highlighted its expanding relevance in pathological remodelling and therapeutic targeting. Future work is expected to concentrate on decoding MyoG-centred regulatory networks in degenerative muscle disease, integrating single-cell and spatial transcriptomics with functional genomics and multi-omics, and developing MyoG-based diagnostic and targeted therapeutic strategies. Despite the intrinsic limitations of single-database and citation-based approaches, this study

provides a panoramic overview of two decades of MyoG research and offers a structured framework to guide future basic and translational investigations in muscle biology and oncology.

KEYWORDS

bibliometric analysis, muscle atrophy, myogenin (MyoG), regenerative medicine, rhabdomyosarcoma

Impact statement

Myogenin is a key gene that controls how muscle cells develop, repair damage, and waste away in disease, yet research on this gene is scattered across many specialties. Our study is the first to draw a clear global picture of two decades of work on myogenin, covering who is doing the research, what topics they focus on, and how interests have shifted over time. We show how the field has moved from basic muscle development toward muscle wasting in aging, inherited muscle disorders, and childhood muscle cancer. By highlighting the most influential articles, the main research teams, and the major gaps in current knowledge, this work gives experimental and clinical researchers a practical roadmap for choosing important questions, building collaborations, and designing future studies that can more directly benefit patients with muscle disease.

Introduction

In 1987, Davis, R.L., H. Weintraub, and A.B. Lassar made a landmark discovery by converting mouse embryonic fibroblasts (C3H10T1/2 cells) into myoblasts through the expression of a single exogenous cDNA, which they subsequently named MyoD (myoblast determination gene 1) [1]. In 1989, myogenin (MyoG) was identified as a pivotal regulator of skeletal muscle differentiation. MyoG promotes myogenic differentiation and maturation through multiple mechanisms, including the activation of muscle-specific gene expression, modulation of the cell cycle, and synergistic interactions with MyoD and MRF4 [2]. As a key transcription factor in myogenesis, MyoG primarily governs myoblast differentiation and myofiber maturation. During embryonic development, MyoG drives the transition of muscle progenitor cells from the proliferative phase to the differentiated state by inducing cell-cycle exit and activating muscle-specific gene programs, thereby facilitating myofiber formation and muscle tissue maturation [3]. In injury-induced regeneration, MyoG activates the differentiation program of satellite cells, promoting their withdrawal from the cell cycle and subsequent fusion into newly formed myofibers, ultimately supporting muscle repair and functional recovery [4].

Although numerous studies have investigated myogenin (MyoG) in recent years, a comprehensive and systematic literature synthesis is still lacking. Bibliometrics is a quantitative approach that integrates theories and methodologies from statistics, mathematics, and related disciplines. By visualizing and analyzing scientific publications, it effectively presents large-scale literature data in structured knowledge forms, enabling researchers to rapidly identify current trends, key pathways and nodes, research hotspots, and advances within their fields. In addition, bibliometrics helps optimize the allocation of existing research resources to address ongoing scientific challenges. Therefore, this study employs bibliometric methods to systematically summarize MyoG-related publications from 2004 to 2024, further analyzing shifts in research focus, future developmental trajectories, emerging hotspots, and frontier concepts, thereby providing important guidance for future research directions and translational potential pertaining to MyoG.

Materials and methods

Data sources and search strategy

All bibliographic records were retrieved from the Web of Science Core Collection (WoSCC;[1]) via the institutional subscription of Southern Medical University. The final search was performed on 14 February 2025 and covered the period from 1 January 2004 to 31 December 2024. The topic search strategy was defined as TS = (myogenin OR MYOG) AND TS = (gene OR "transcription factor").

To obtain a clearly defined and reproducible dataset, we applied explicit inclusion criteria. Eligible records were: (1) document types indexed as "Article", "Proceedings Paper" or "Early Access"; (2) publications dated between 1 January 2004 and 31 December 2024; (3) publications written in English; and (4) studies in which myogenin (MyoG) or closely related synonyms (e.g., myogenic factor 4, myogenic regulatory factor) constituted a primary focus of the research, as reflected in the title, abstract or author keywords.

Records were excluded if they: (1) were indexed as reviews, letters, editorials, bulletins, book reviews, meeting abstracts or news items; (2) mentioned myogenin only peripherally or in a

1 https://www.webofscience.com

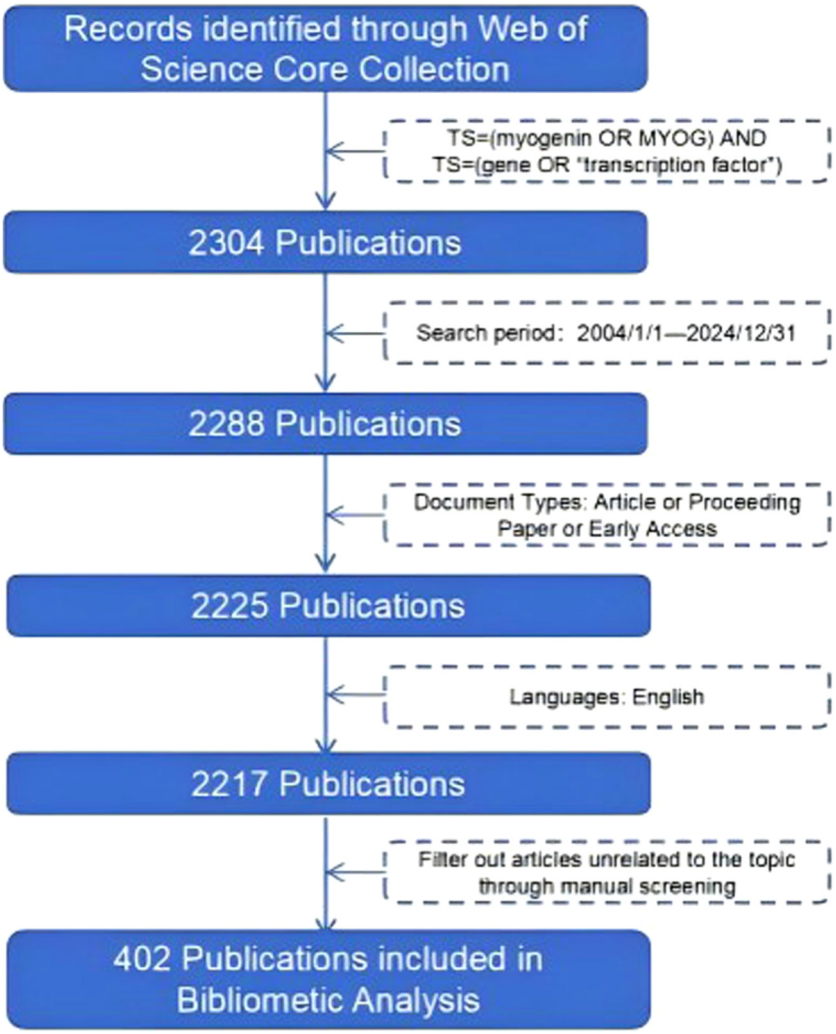

FIGURE 1
Flowchart of the literature screening process in MyoG research.

non-biological context (e.g., as part of a long gene list without specific analysis or interpretation related to myogenin); (3) were flagged as retracted in WoSCC or by journal notices; or (4) lacked essential bibliographic information (e.g., publication year or source title) required for reliable citation and network analyses.

All records retrieved from WoSCC were downloaded in plain-text format with full bibliographic and citation information and imported into EndNote (Clarivate Analytics) for reference management. Potential duplicate records arising from overlapping indexes within WoSCC were identified using EndNote's automatic duplicate detection (matching on title, first author and year) and then manually verified by checking digital object identifiers (DOIs) and journal information. Confirmed duplicates were removed, retaining a single record with the most complete metadata. Two authors independently screened the titles and abstracts of the remaining records against the inclusion and exclusion criteria, with disagreements resolved by discussion and consensus. The overall process of identification, screening, eligibility assessment and final inclusion is presented in a PRISMA-style flow diagram (Figure 1).

Keyword selection and validation

The development of the search strategy and analytical keywords followed an iterative, structured process. First, we identified core conceptual terms related to myogenin by consulting controlled vocabularies and indexing systems, including Medical Subject Headings (MeSH) in PubMed and Keywords Plus in the Web of Science Core Collection. Candidate terms (e.g., "myogenin", "MyoG", "myogenic factor 4", "myogenic regulatory factor") were initially generated from

these sources and from author keywords of seminal myogenin papers.

Second, we conducted pilot topic searches in WoSCC using different combinations of these terms and inspected the retrieved records to assess sensitivity and specificity. The final search string was refined through several iterations until additional test searches in recent years did not yield new myogenin-focused records. The approved search query was then applied consistently for the full 2004–2024 timespan.

For the keyword co-occurrence analyses, we extracted both author keywords (DE field) and Keywords Plus (ID field) from the WoSCC export files. Before analysis, two authors independently reviewed the raw keyword list to standardize terms. Standardization procedures included lowercasing, merging obvious synonyms and spelling variants (e.g., "myogenin", "MyoG", "myogenic factor 4"), unifying singular and plural forms, and removing overly generic methodological terms (e.g., "expression", "protein", "model"). Discrepancies were resolved by discussion and consensus. This keyword development and cleaning procedure was adapted from established bibliometric practices used in recent conceptual mapping studies [5, 6].

Data analysis tools

This study employed the following tools for data processing, visualization, and statistical analysis:

1. VOSviewer (version 1.6.20): Used to construct co-occurrence networks of countries/regions, institutions, journals, and gene-related terms, thereby identifying collaboration patterns and knowledge clusters.
2. CiteSpace (version 6.2.R4): Applied for systematic analyses of national contributions, institutional collaboration networks, author co-occurrence relationships, journal co-citation networks, and keyword evolution trends, revealing the spatiotemporal dynamics of MyoG research.
3. R-based toolkits:
   - Bibliometrix: Extracted bibliometric metadata and performed basic statistical analyses;
   - ComplexHeatmap and ClusterProfiler: Visualized hierarchical clustering of research themes and conducted functional enrichment analyses.
4. OriginPro (version 2024b): Utilized for geospatial mapping and advanced data visualization, with a focus on depicting the global distribution of research outputs.
5. Pajek and Scimago Graphica: Served to refine network topology and enhance the visual presentation of collaboration networks.

For all network-based analyses, parameter settings were chosen to balance analytical stability and interpretability, in line with practices in comparable bibliometric studies. In VOSviewer, co-authorship, co-citation and keyword co-occurrence maps were constructed using association-strength normalization and the default clustering algorithm. For keyword co-occurrence, we applied a minimum occurrence threshold of 5 to exclude very infrequent terms while retaining the main thematic structure of the field. For journal and reference co-citation analyses, we used a minimum citation threshold of 20 citations. In CiteSpace, we adopted one-year time slices, cosine similarity as the link strength measure and the default clustering parameters. These parameter choices are consistent with those reported in recent bibliometric analyses of biomedical topics, ensuring comparability and robustness of the identified clusters.

Results

Basic quantitative information

This study integrated the contributions of 2,402 researchers from 165 countries and regions worldwide, ultimately including 402 academic publications. These studies were produced through collaborations among 1,148 research institutions and published across 220 scientific journals. In total, the research network accumulated 12,562 citations, reflecting a broad pattern of scientific collaboration spanning multiple regions and institutions.

Annual publications trend

This study tracked the annual publication output of MyoG-related literature from 2004 to 2024. As shown in Figure 2A, the number of publications rose from 13 in 2004 to a peak of 25 in 2006. Although a decline followed, the annual output soon stabilized at approximately 20 publications, indicating rapid progress in MyoG research during the 2004–2006 period. Another notable peak appeared between 2011 and 2014, with an average of 23 publications per year. A subsequent rise occurred in 2022, reaching 25 publications. Overall, despite fluctuations with intermittent peaks and troughs, the annual number of publications in the MyoG field has remained relatively stable over the past two decades, demonstrating sustained and consistent research activity.

Based on the analysis of data from 2004 to 2024 (Figure 2A), the United States, as a traditional scientific powerhouse, has maintained a leading position, publishing 36 related articles during the four-year period from 2006 to 2009. China's research output has shown continuous growth since 2010 and reached its peak in 2022 with 12 publications, gradually emerging as a central contributor within the global research network. Japan and South Korea exhibited relatively stable research productivity,

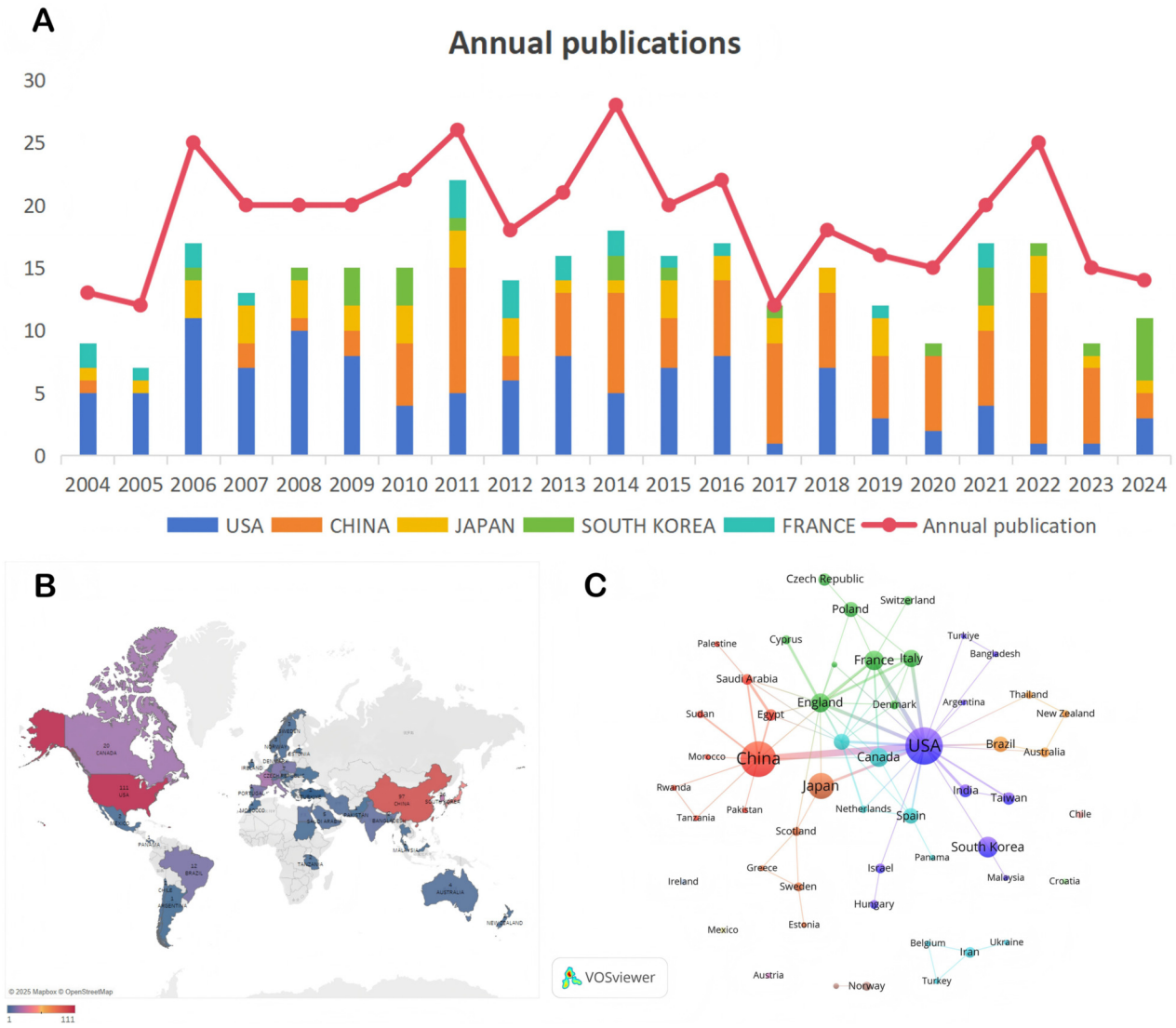

FIGURE 2
Visualizations of publication trends and international collaboration in MyoG research. **(A)** Annual publication trends in the MyoG field from 2004 to 2024, accompanied by a bar chart of the top five contributing countries, highlighting overall research activity and leading contributors. **(B)** Geographic distribution of total publications by country, illustrating global research output in the MyoG domain. **(C)** International collaboration network, depicting research partnerships and contributions among countries, with emphasis on collaborative linkages and scientific influence.

averaging 1–3 publications per year. These findings indicate that research in the MyoG field remains relatively concentrated, while emerging scientific communities are steadily expanding their presence.

Analysis of countries/regions and institution

The global landscape of MyoG research exhibits a pronounced geographic clustering effect (Figure 2B). North America (United States: 111 publications) and East Asia (China: 97 publications) form two major centers of knowledge innovation, together accounting for 51.7% of total global output. Europe constitutes a third cluster through multi-country collaborations (Germany/France/United Kingdom/Spain: 66 publications), whereas South America (Brazil: 12 publications) and Oceania (Australia: 4 publications) occupy follower positions in the research ecosystem. This "core–periphery" distribution pattern reflects a strong association between knowledge production and national economic development as well as research investment

intensity, while also highlighting the systemic challenges faced by developing countries as they attempt to catch up in frontier scientific domains.

Quality assessment based on citation metrics reveals even deeper disparities (Supplementary Material 1 Country ranking by citation counts for myogenin (MyoG) publications). The United States maintains academic leadership with a total of 4,977 citations and an average of 57.2 citations per publication, indicating substantial research depth. Notably, several medium-output countries—including the United Kingdom (53.4 citations per publication), Canada (53.1), and Italy (49.3)—maximize academic efficiency through focused research topics and extensive international collaboration. Although China, Japan, and South Korea collectively contribute 32.9% of global publications, their average citation counts (China: 13.2; Japan: 19.2; South Korea: 20.5) remain significantly lower than those of major Western countries. This "quantity–quality mismatch" underscores structural bottlenecks within East Asian research systems, particularly regarding original breakthroughs and the establishment of international academic influence. Overall, the data reflect a divergence between two innovation pathways: scale-driven expansion versus quality-oriented development.

Figure 2C presents a visualized analysis of international research collaborations, revealing a distinct "dual-core" structure dominated by China and the United States. These two countries serve as central hubs in the global collaboration network. European countries demonstrate strong regional synergy, with the United Kingdom, Germany, and France forming a cohesive regional collaboration cluster through intensive scientific interactions. Notably, developed countries such as Japan and Canada remain key nodes within the network, maintaining stable channels of knowledge exchange with major scientific powers. Meanwhile, emerging countries such as India and Brazil are gradually integrating into the international collaboration system, although their partnerships remain largely aligned with networks led by North America and Europe.

Academic Subject analysis

Author analysis

By systematically examining the author collaboration network and the temporal publication patterns of prolific researchers in the MyoG field, it is possible to accurately identify the distribution of research hotspots during specific periods. Such analysis enables researchers to comprehensively understand the dynamic evolution and developmental trajectory of research themes while effectively distinguishing core contributors and their academic influence across different stages of the field's progression.

Figures 3A,B clearly present the top ten authors in terms of publication output from 2004 to 2024, along with their corresponding research timelines. Notably, Klein William H, Meadows Eric, and Fkybb Jesse M form a closely collaborating research team that has collectively published six high-quality papers in this field. As indicated by the color intensity of the timeline nodes, the team achieved a major breakthrough in 2010 with their milestone study published in Cell, which for the first time elucidated the central regulatory role of myogenin in neurogenic muscle atrophy. Their study demonstrated that denervation-induced injury upregulates myogenin expression, which in turn directly activates the transcription of the E3 ubiquitin ligase–encoding genes MuRF1 and atrogin-1, thereby driving muscle protein degradation and the atrophic process. This groundbreaking discovery not only revealed the dual biological function of myogenin—serving as a key developmental regulator during embryonic myogenesis and functioning as a molecular switch for neurogenic atrophy in adulthood—but also established a cascade signaling axis linking epigenetic regulation (HDAC4/5), transcriptional control (MyoG), and protein degradation (MuRF1/atrogin-1). This pathway provided an entirely new paradigm for understanding the pathological mechanisms underlying neuromuscular interaction [7]. The article has accumulated a total of 357 citations, underscoring its substantial impact on the field.

Figure 3C presents the overall structure of research collaborations in the MyoG field through a visualized network. In this network, node size is positively correlated with the total citation count of each researcher, providing an intuitive measure of individual academic influence. The analysis reveals a pronounced clustering pattern, indicating that scholarly activity within this field is largely organized into distinct academic groups.

Institutional analysis

The analysis of institutional publication output, combined with the visualization of inter-institutional collaboration networks, provides insights into the distribution of major research forces and collaborative patterns within the MyoG field. Such analyses offer valuable references for identifying core research institutions and their partnership structures.

According to the rankings in Supplementary Material 2 Top 10 Institutions by Publication Volume and Citation VolumeSichuan Agricultural University leads the field with ten publications. However, its total citation count is only 134, which is markedly lower than that of the Massachusetts Institute of Technology (MIT) and the Whitehead Institute for Biomedical Research—each of which has published only two papers but achieved a high citation count of 786. This discrepancy highlights a nonlinear relationship between academic influence and publication volume in MyoG research.

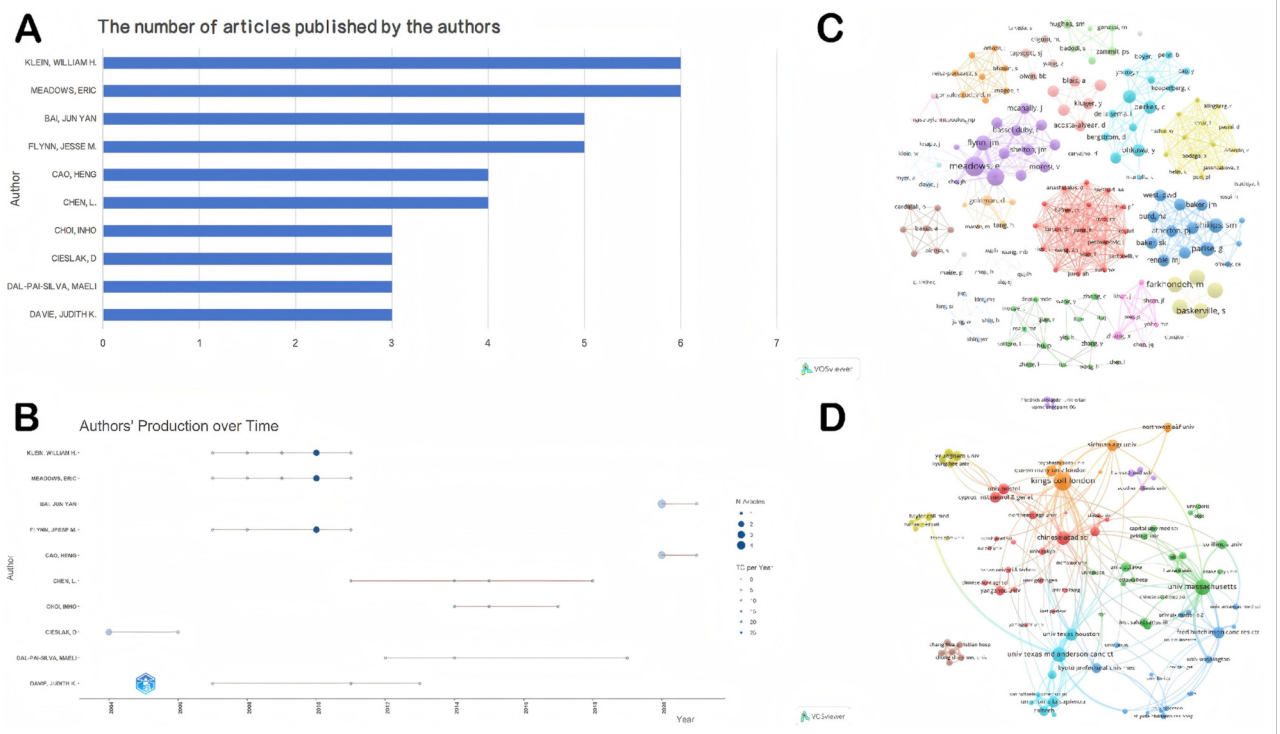

FIGURE 3
Visualizations of author productivity and collaborative networks in MyoG research. **(A)** Top ten authors ranked by publication count, highlighting the most productive contributors in the field. **(B)** Publication timeline of the top ten authors, illustrating patterns of research activity over time. **(C)** Author collaboration network, depicting partnerships and scientific interactions among researchers in the MyoG domain. **(D)** Institutional collaboration network, showing inter-institutional connections and contributions within the MyoG research landscape.

Further integration with the institutional collaboration network visualization in Figure 3D, which displays the top 100 most-cited institutions, shows that node size reflects institutional centrality within the collaborative network. Despite its high publication output, Sichuan Agricultural University occupies a peripheral position in the network. In contrast, institutions such as King's College London, the University of Massachusetts, and the University of Texas MD Anderson Cancer Center occupy central hub positions by establishing dense collaborative networks.

The visualization also reveals several representative collaboration clusters.

King's College London and Queen Mary University of London form a strong partnership, focusing primarily on key genes and signaling pathways involved in skeletal muscle development as well as the mechanisms underlying related pathologies such as muscle atrophy, muscle injury, and rhabdomyosarcoma. Their joint efforts also explore innovative gene therapy strategies based on gene editing and viral vectors [8, 9].

Knowledge exchange between the University of Texas MD Anderson Cancer Center and the University of Texas at Houston centers on integrating multidisciplinary expertise to investigate MyoG-mediated regulatory mechanisms during skeletal muscle development, as well as its roles in muscle metabolism and muscle disorders [10–12].

In terms of funding structures, MyoG research is predominantly supported by major public funding bodies in North America, East Asia and Europe. The top 20 funding agencies acknowledged in the 402 publications are summarised in Supplementary Material 3 Top 20 funding agencies supporting myogenin (MyoG) research. The US National Institutes of Health (NIH) and the US Department of Health and Human Services (HHS) together account for the largest share of funded papers, followed by the National Natural Science Foundation of China (NSFC), Japan's MEXT/KAKENHI programmes, and European and national research councils such as UKRI, DFG, CIHR and others.

Journal analysis

By analyzing journals with high publication output and high H-index values in the MyoG field, it becomes possible to accurately identify core academic platforms and provide strategic guidance for research dissemination and scholarly collaboration.

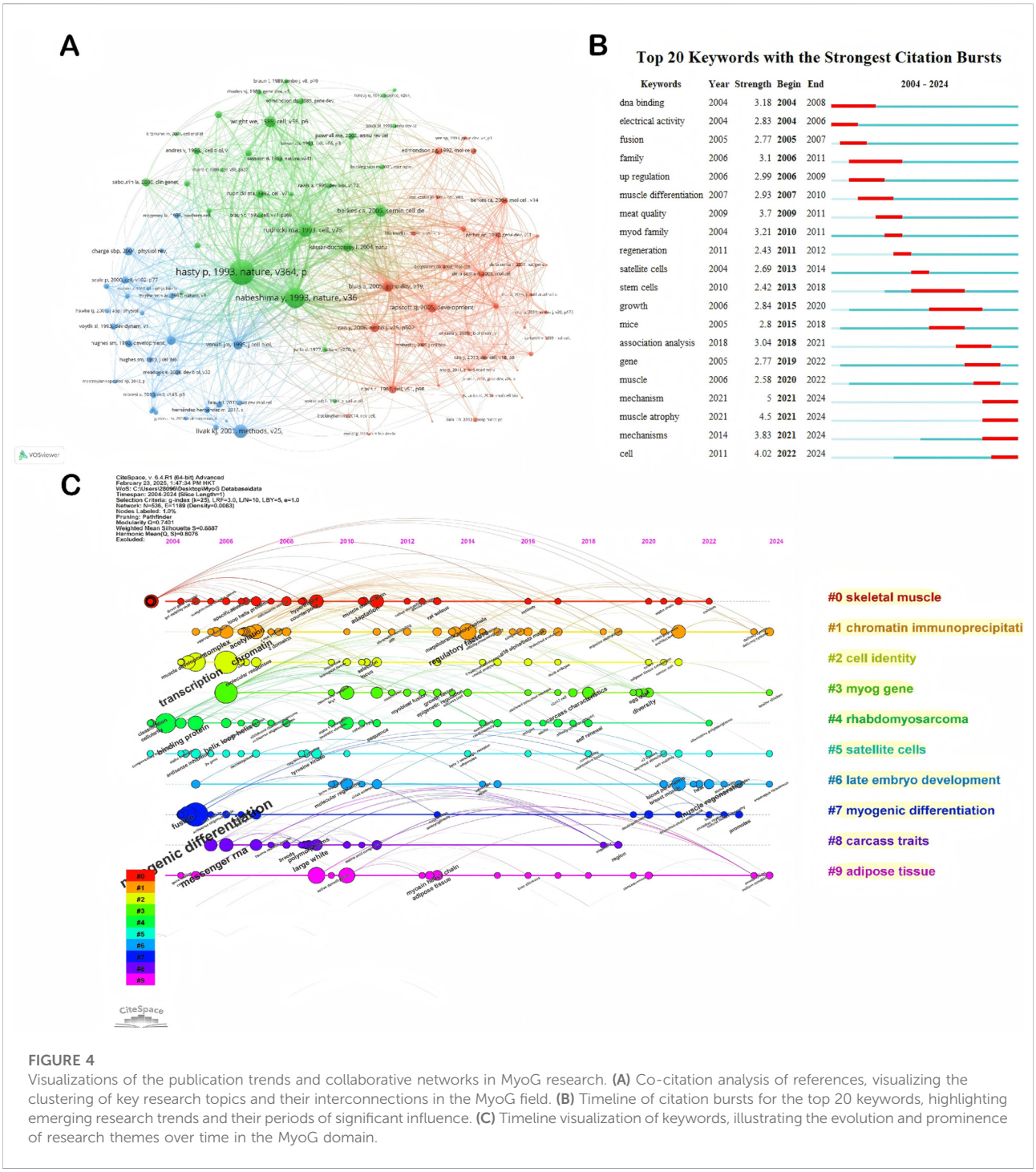

FIGURE 4
Visualizations of the publication trends and collaborative networks in MyoG research. **(A)** Co-citation analysis of references, visualizing the clustering of key research topics and their interconnections in the MyoG field. **(B)** Timeline of citation bursts for the top 20 keywords, highlighting emerging research trends and their periods of significant influence. **(C)** Timeline visualization of keywords, illustrating the evolution and prominence of research themes over time in the MyoG domain.

As shown in Supplementary Material 4 Publication Volume and Related Indices in the MyoG Field Journal of Biological Chemistry (United States) leads the field with an H-index of 15 and a total of 844 citations, supported by 18 publications that underscore its dual role as a central hub for knowledge production. PLOS ONE (United Kingdom) ranks second with a stable H-index of 12. Notably, the German journal Cell and Tissue Research demonstrates a striking "low-output, high-impact" pattern: despite an H-index of only 4, it has accumulated 678 total citations, yielding an exceptional average of 169.5 citations per article—surpassing even the leading journal's average of 46.9 citations. This phenomenon further highlights the asymmetric relationship between academic influence and publication quantity in the MyoG field,

emphasizing the pivotal role of high-quality, highly targeted studies in driving advances at the disciplinary frontier.

Experimental models used in MyoG research

To provide an accessible overview of how MyoG has been studied experimentally, we summarised the main experimental models used in the 402 publications (Table 2). C2C12 myoblasts were by far the dominant *in vitro* system (90/402, 22.4%), whereas other cell-based models, including primary mouse myoblasts/myotubes, human skeletal myoblasts/myotubes and rhabdomyosarcoma cell lines, were used only occasionally (1.5–2.0% of records each). Among *in vivo* approaches, denervation-induced atrophy models were the most frequently employed animal models (20/402, 5.0%), followed by disease-specific settings such as Duchenne muscular dystrophy (mdx) mice and chemical injury models using cardiotoxin or $BaCl_2$. Human skeletal muscle biopsies appeared in only a very small subset of studies (2/402, 0.5%), and no records in our dataset explicitly reported the use of rhabdomyosarcoma tumour specimens in the title, abstract or keyword fields.

Content theme analysis

Keyword analysis

Keyword burst detection provides a systematic means of revealing the dynamic evolution of research hotspots within the field. Figure 4B presents the top 20 keywords with the strongest citation bursts in MyoG research from 2004 to 2024. The year of first appearance and the duration of each burst period clearly reflect the stage-specific transitions in research focus over time.

Theme evolution

Using the keyword co-occurrence timeline shown in Figure 4C, the ten major thematic clusters in MyoG research can be visualized intuitively. Overall, studies in this field can be categorized into three overarching directions: molecular regulatory networks, developmental and regenerative mechanisms, and disease-related research.

As a core transcription factor governing skeletal muscle differentiation and development, foundational investigations of MyoG focus on its gene-regulatory characteristics (myog gene) and its interactions within the myogenic regulatory factor network, including myod. Techniques such as chromatin immunoprecipitation (ChIP) are frequently employed to elucidate its DNA-binding patterns and epigenetic regulatory mechanisms.

At the tissue-development level, research on satellite cell activation and the temporal regulation of late embryo development has identified key nodes through which MyoG orchestrates myogenic differentiation. In translational contexts, the scope extends to pathological mechanisms, such as the aberrant regulation of MyoG-related signaling pathways in rhabdomyosarcoma, underscoring its significant clinical relevance.

Citation and impact analysis

Literature citation analysis

Supplementary Material 5 Top 10 most cited MyoG-related papers (total citation counts). provides an intuitive overview of the most influential articles in the MyoG field. The 2006 publication by Rao, Prakash K and colleagues, entitled "Myogenic factors that regulate expression of muscle-specific microRNAs," ranks first, with a total of 573 citations and an average of 28.65 citations per year. This study demonstrated that the myogenic factors myogenin (MyoG) and MyoD regulate the expression of muscle-specific microRNAs (miRNAs)—including miR-1, miR-133, and miR-206—by directly binding to the upstream regulatory regions of their genes during muscle differentiation, thereby providing important mechanistic insights into the molecular regulation of myogenesis.

Co-citation analysis

Reference co-citation refers to the phenomenon in which two or more publications are cited together by subsequent articles, implying that these co-cited works may share similarities or relevance in terms of research topics, methodologies, or conceptual viewpoints. Through visualized clustering analysis of co-cited references (Figure 4A), it is possible to accurately identify foundational or breakthrough studies within the MyoG field. In this network, node size represents the citation frequency of a given reference, while the thickness of the connecting lines reflects the strength of the co-citation relationship between pairs of articles. In parallel, Supplementary Material 2, provides an intuitive ranking of citation counts, further underscoring the pivotal role of these references in MyoG research.

The analysis highlights, in particular, the landmark contribution of the 1993 study by Paul Hasty and colleagues published in Nature, which investigated the global phenotype of MyoG gene knockout mice and emphasized the essential role of MyoG in skeletal muscle differentiation and formation [13]. Similarly, the Nature paper by Yoko Nabeshima and co-workers focused on alterations in muscle tissues during embryonic development in MyoG knockout mice, underscoring the critical requirement of MyoG for proper muscle formation in the embryonic stage [14]. Together, these two gene knockout studies unequivocally demonstrated the indispensable role of MyoG in skeletal muscle development, and their complementary conclusions provide important clues for understanding the regulation of muscle-specific gene expression, the pathogenesis of muscle diseases, and the interplay between muscle and skeletal development.

Discussion

Using a bibliometric approach, this study analyzes nearly two decades of publications in the MyoG field, providing a comprehensive overview of global research collaboration, recent advances, and emerging trends. In particular, it visualizes current hotspots and developmental trajectories in MyoG research based on published records.

Historical development

This study analyzed publications in the MyoG field from 2004 to 2024 and examined in depth the three major peaks in annual output over this 20-year period. In combination with Supplementary Material 5, it is evident that each publication peak coincided with substantial theoretical or technological advances related to MyoG. From the perspective of thematic evolution, these three peaks delineate a clear trajectory of deepening research: initial efforts focused on elucidating the physiological functions of MyoG, subsequently expanding to the dissection of disease mechanisms, and ultimately converging on injury repair. This stepwise progression has gradually driven MyoG-related research toward clinical application.

The first peak occurred in 2006 (25 publications), when researchers intensively explored the molecular mechanisms by which MyoG regulates muscle differentiation, including the pivotal role of chromatin remodeling, transcriptional regulatory networks, and epigenetic control. Ohkawa et al. conducted a series of refined molecular biology experiments that clearly demonstrated how myogenin (MyoG) cooperates with other transcription factors such as MyoD and MEF2 to regulate the expression of muscle-specific genes, thereby elucidating in depth the mechanistic role of MyoG in myogenic differentiation [15, 16]. In addition, de la Serna et al. showed that MyoD recruits the SWI/SNF chromatin-remodeling complex to the myogenin locus, promoting chromatin structural changes that create a permissive environment for MyoG expression [17]. This finding further underscored the critical importance of chromatin remodeling in muscle differentiation and clarified the interaction between chromatin-remodeling complexes (such as SWI/SNF) and muscle regulatory factors.

Building on this, Blais et al. reconstructed the transcriptional regulatory network governing muscle differentiation, revealing how muscle regulatory factors drive myogenesis through multilayered control mechanisms [18]. Collectively, these studies greatly deepened our understanding of the molecular basis of muscle differentiation and provided new potential targets and strategies for the treatment of muscle-related diseases, such as muscular dystrophies.

The second pronounced peak occurred between 2011 and 2014, with an average of 23 publications per year. As indicated by the highly cited articles summarized in Supplementary Material 1 research during this period primarily focused on breakthroughs in epigenetic regulation, deeper elucidation of molecular mechanisms, and the disease relevance and therapeutic potential of MyoG. Studies by Stojic et al. and Huang et al. provided new conceptual support for the role of epigenetic regulation in muscle development [19, 20]. In the context of disease association and therapeutic implications, Moresi et al. demonstrated that myogenin (MyoG) promotes muscle atrophy by activating E3 ubiquitin ligases, with HDAC4 and HDAC5 serving as critical regulatory nodes in this process [7]. These findings not only broadened the functional spectrum of MyoG but also offered new theoretical foundations and potential targets for the treatment of muscle disorders.

From 2020 onward, interest in MyoG research has risen once again, culminating in a new peak of 25 publications in 2022. As shown in Supplementary Material 7 Top 10 MyoG-related papers ranked by normalised citation counts, this recent surge is largely driven by growing attention to the interface between epigenetic regulation, muscle development, and disease. While researchers continue to refine our understanding of the classical role of myogenin in skeletal muscle development, increasing emphasis has been placed on its potential in cardioprotection and cardiac regeneration. In the cardiac field, our previous work demonstrated that myogenin can attenuate oxidative stress–induced apoptosis by modulating DUSP13 and p38 MAPK signaling, thereby reducing myocardial injury and promoting tissue repair [21]. Furthermore, studies centered on angiotensin II have revealed additional anti-apoptotic effects of myogenin in cardiovascular disease models, opening new avenues for therapeutic intervention [22]. Together, these emerging hotspots indicate that myogenin not only plays a pivotal role in muscle growth and development but also holds substantial promise in muscle injury repair and the treatment of cardiovascular and muscle-related diseases.

Thematic evolution

Systematic analysis of keyword bursts (Figure 4B) intuitively illustrates how research themes in the MyoG field have progressively deepened over time.

In the early stage (2004–2011), studies primarily focused on elucidating the molecular mechanisms and fundamental functions of MyoG. Key advances included the repeated validation of DNA binding as core evidence for MyoG's activity as a transcription factor [23]. The emergence of keywords such as MyoD family and other family-related terms reflected systematic efforts to dissect the regulatory networks and evolutionary relationships of the gene family to which MyoG

belongs. During this period, investigations into molecular interactions and signaling pathways laid the theoretical foundation for understanding the mechanisms of muscle differentiation.

During this period, basic research centered on skeletal muscle entered a peak phase. Around 2004, the main focus was on MyoG-mediated regulation and activation of skeletal muscle–specific genes. High-frequency occurrence of keywords such as MyoD and activation, together with terms like acetylcholine receptor (AChR) and citrate synthase, reflected growing interest in both transcriptional control and muscle metabolism. These studies showed that MyoG serves as the sole bridge through which muscle LIM protein (MLP) participates in the regulation of the AChR gene, and plays a specialized role in the selective control of AChR expression. At the same time, the involvement of enzymes such as citrate synthase indicated that research had begun to extend into neuromuscular junction function and muscle energy metabolism. Collectively, these findings established an initial link between MyoG and skeletal muscle physiological function and challenged the earlier notion that MyoG expression is restricted to the embryonic period [24, 25].

From 2005 to 2013, the focus gradually shifted from basic transcriptional regulation to mechanisms of skeletal muscle differentiation and regeneration. The clustered emergence in 2009 of keywords such as satellite cell, hypertrophy, and beta 1 integrin directly reflected growing interest in satellite cell regulation and the mechanisms of muscle hypertrophy, and further uncovered the role of MyoG in initiating muscle regeneration [26–31]. By 2011, attention turned to the fine-tuning of the regenerative process itself. The appearance of keywords such as regeneration, methylation, and adaptation signaled that MyoG-related research had entered the epigenetic level, with the field beginning to explore how epigenetic modifications—particularly DNA methylation—regulate MyoG function and shape adaptive responses during muscle regeneration [12, 32–34].

In the intermediate phase (2013–2018), the thematic evolution of the field was characterized by a clear technological and conceptual shift toward regenerative medicine. The concentrated emergence of keywords such as satellite cells, stem cells, and regeneration indicated that the research focus had moved toward mechanisms of muscle injury repair. Notably, the high frequency of the keyword mice underscored the central role of *in vivo* animal models as a critical platform for validating the roles of MyoG in stem cell regulation and muscle regeneration.

As a key regulator of muscle-specific gene transcription, myogenin (MyoG) exerts indispensable functions across multiple stages of the muscle injury–repair process. On one hand, MyoG drives the core repair program by precisely recruiting transcription initiation complexes—such as TATA-binding protein (TBP) and RNA polymerase II—to the promoters of repair-related target genes, thereby directly activating downstream gene expression and initiating the regenerative response following muscle injury [35]. On the other hand, MyoG promotes myofiber regeneration by facilitating myocyte fusion. It does so by directly binding to and activating the myomaker gene, a critical effector of myoblast fusion whose encoded protein is essential for this process. Loss of MyoG results in a permanent defect in myocyte fusion, which in turn impedes myofiber formation and regeneration [36].

MyoG also plays a central role in regulating satellite cell function and maintaining muscle homeostasis. As illustrated in Figure 4C, satellite cells constitute one of the core themes in MyoG-related research. Current evidence indicates that MyoG exerts complex but crucial control over satellite cell behavior, not only promoting terminal stages of myogenic differentiation (such as myocyte fusion) but also helping to preserve the quiescent state of satellite cells. MyoG deletion leads to premature exit from quiescence, dysregulation of the mTORC1 signaling pathway, and aberrant interactions between satellite cells and their myofiber niche [35, 37].

In the recent phase (2019–2024), the field has increasingly shifted toward clinical translation and precision medicine. Strong citation bursts for keywords such as muscle atrophy (strength 4.5) and mechanism (strength 5.0) point to intensified efforts to dissect the pathophysiological mechanisms underlying age-related muscle degenerative diseases. Concurrently, the prominence of terms such as association analysis and gene reflects the widespread application of multi-omics technologies and gene association analyses in elucidating disease mechanisms. This stage is characterized by a clear transition from purely mechanistic studies toward research explicitly driven by clinical diagnostic and therapeutic needs.

Consistent with this late-stage shift toward clinically oriented research, analysis of disease-related research themes in the MyoG literature (Table 1) further highlighted the dominance of clinically focused topics. Among these topics, “Duchenne muscular dystrophy” alone accounted for almost half of all records (47.8%), followed by “Muscle wasting” (8.2%) and “Sarcoma research”, which includes rhabdomyosarcoma-related studies (4.0%). Together, these categories indicate that a substantial proportion of MyoG work has moved downstream from developmental biology into degenerative muscle disease, inherited dystrophies and muscle cancers. At the same time, mechanistically oriented topics such as “Epigenetic regulation”, “lncRNA”, “Hippo pathway” and “HIF in cancer” remain highly represented, suggesting that disease-oriented studies are tightly coupled to investigations of MyoG-centred regulatory pathways rather than being purely descriptive.

Within this context, rhabdomyosarcoma (RMS) has emerged as a particularly prominent focus. RMS is a muscle-derived sarcoma that occurs predominantly in children, whose tumor cells aberrantly express myogenic regulatory factors such as MYOD1 and MYOG. Functional suppression of MyoG blocks

TABLE 1 Distribution of disease-related research themes in myogenin (MyoG) publications (2004–2024).

Citation Topics Micro	Records (n)	Proportion of all 402 records (%)
Duchenne muscular dystrophy	192	47.761
Muscle wasting	33	8.209
Sarcoma research	16	3.98
Epigenetic regulation	16	3.98
Microrna in cancer	8	1.99
Nicotinic receptors	7	1.741
Lncrna	6	1.493
Neural crest	4	0.995
Hippo pathway	4	0.995
Gh/igf axis	3	0.746
Bacterial gene regulation	3	0.746
Protease inhibitors	3	0.746
Heart failure management	2	0.498
Hif in cancer	2	0.498
Tgf-beta	2	0.498

the myogenic differentiation program and locks tumor cells in a proliferative state, constituting one of the key mechanisms driving RMS pathogenesis [38, 39]. Building on this central mechanism, multiple targeted therapeutic strategies have been developed. Leveraging the high expression of MYOG in RMS cells, researchers have engineered MYOG promoter–driven oncolytic viruses—such as Ad5/3-pMYOG (S)-mMEF2—to achieve selective oncolysis of RMS cells [40]. In parallel, therapeutic approaches that interfere with negative regulators of MYOG, such as TRPS1 and SNAI2, and modulate associated signaling pathways, including the ERK/MAPK axis, can relieve repression of MYOG function and promote the differentiation of RMS cells toward a more normal myogenic phenotype [41, 42]. Furthermore, studies on MYOG-related RNA molecules—for example, the natural antisense transcript MYOG-NAT—have begun to elucidate how RNA-based mechanisms regulate MYOG protein stability, providing a theoretical foundation for novel RNA-targeted therapeutic strategies [43].

Collectively, these advances not only substantiate MYOG and its regulatory network as promising therapeutic targets for RMS but also propel concrete gene therapy approaches—particularly oncolytic virotherapy—into the experimental stage. Future research should focus on optimizing the specificity, efficacy, and clinical safety of these strategies to develop effective MYOG-centered interventions for RMS and related malignancies [38].

The experimental landscape summarised in Table 2 further contextualises these thematic trajectories. The field remains heavily reliant on a limited set of preclinical systems, with more than one fifth of all publications using C2C12 myoblasts and a substantial fraction relying on rodent denervation models for *in vivo* validation. By contrast, human skeletal muscle biopsies and clinically proximate disease models are used only sporadically. This imbalance highlights both the strength and the limitation of current MyoG research: mechanistic insights are largely derived from tractable rodent and cell-line models, whereas translation to human pathology still depends on relatively few studies. Future work will therefore need to expand the use of human tissue, advanced genetic disease models and clinically annotated cohorts to fully exploit the translational potential outlined by our bibliometric mapping.

Overall, MyoG research from 2004 to 2024 exhibits a clear pattern of staged evolution: early work concentrated on transcription factor function and gene regulatory networks; intermediate studies shifted toward mechanisms of muscle regeneration; and recent efforts have delved into the pathogenesis of muscle atrophy and driven advances in clinical translation. The regulatory axis centered on MyoG—DNA binding → MyoD family → muscle differentiation → muscle atrophy—integrates molecular interactions with disease phenotypes into a coherent dynamic continuum.

Taken together, the observed thematic evolution of MyoG research appears to mirror broader scientific and clinical drivers in muscle biology. The early dominance of transcriptional regulation and chromatin remodelling reflects the rapid

TABLE 2 Experimental models used in myogenin (MyoG) research (2004–2024).

Model category	Representative models	No. of publications (n, %)
Cell lines	C2C12 myoblasts	90 (22.4%)
	Primary mouse myoblasts/myotubes	8 (2.0%)
	Human skeletal myoblasts/myotubes	6 (1.5%)
	Rhabdomyosarcoma cell lines (e.g., RD, RH30, RH41)	8 (2.0%)
Animal models	Conventional MyoG knockout mice	2 (0.5%)
	Conditional MyoG knockout/knockdown mice	2 (0.5%)
	Duchenne muscular dystrophy (mdx) models	4 (1.0%)
	Denervation-induced atrophy models	20 (5.0%)
	Chemical injury models (cardiotoxin/$BaCl_2$)	4 (1.0%)
Human samples	Human skeletal muscle biopsies	2 (0.5%)

expansion of molecular genetics and epigenetics in the early 2000s, when establishing MyoG as an indispensable regulator of myogenic differentiation was a central conceptual goal. The subsequent shift toward satellite cell biology and regenerative mechanisms coincides with the emergence of stem cell–based regenerative medicine and increasing interest in functional recovery after muscle injury. More recently, the prominence of keywords related to muscle atrophy, Duchenne muscular dystrophy and rhabdomyosarcoma suggests a field-level realignment toward clinically salient phenotypes, driven by population ageing, the unmet need in degenerative muscle disease and advances in genetic and cellular therapies. This trajectory—from basic regulatory circuits to regeneration and disease-focused applications—is consistent with bibliometric trajectories reported in sarcopenia, exercise and mental health research, where early mechanistic work progressively gives way to translational and precision medicine–oriented themes [44].

Core authors

In scientific research, core teams within a field often serve as the driving force behind continuous advances at the academic frontier. Based on the visualized author collaboration network in Figure 3C, several key research clusters can be identified in the MyoG domain. Among them, Eric Meadows from The University of Texas emerges as a major central node, with seven publications and a total of 797 citations. His work primarily focuses on the functions of MyoG in muscle biology and its underlying regulatory mechanisms. Using a range of genetic approaches—including gene knockout, gene knockdown, and conditional knockout—his group has systematically dissected the roles of MyoG in muscle denervation, muscle atrophy, adult muscle stem cell function, exercise capacity and metabolism, and Duchenne muscular dystrophy models [7, 10–12, 45].

Another important research network is centered around S.J. Tapscott and C.A. Berkes at the Massachusetts Institute of Technology (MIT), whose four key publications have collectively received 702 citations. Tapscott's work focuses on the molecular mechanisms of muscle differentiation, elucidating the sequential regulation of shared target genes by MyoD and MyoG during myogenesis. Subsequent studies from this group proposed a two-step model in which MyoD activates MyoG gene expression, thereby clarifying the dynamic changes in gene regulation that occur during muscle differentiation and providing important insights into how myogenic cells achieve differentiation through precisely orchestrated molecular programs [17, 46–48].

The joint team of S.M. Phillips and G. Parise at McMaster University in Canada also stands out, with two publications that have accumulated 519 citations, making them another major source of high-impact knowledge production in North America. Although these core teams are geographically dispersed, their highly influential contributions collectively form an implicit academic coordinate system that structures the intellectual landscape of MyoG research.

Future perspectives

Our findings also need to be interpreted in the context of the wider bibliometric landscape of muscle and ageing research. Recent mapping studies on sarcopenia, exercise and frailty, and mental health–related digital research have consistently reported a similar macro-structure, with a small number of high-income countries and specialised centres dominating knowledge production and collaboration networks, and emerging regions contributing growing but comparatively lower-impact outputs. Within this pattern, MyoG research

appears to occupy a more upstream, mechanism-focused niche that feeds into downstream themes such as sarcopenia, muscle wasting and functional decline. The pronounced "quantity–quality imbalance" we observed in East Asian outputs therefore echoes imbalances reported in sarcopenia and exercise bibliometrics, and reinforces the need for strategic investment in cross-centre collaboration, longitudinal cohorts and multi-omics platforms if mechanistic insights around MyoG are to translate into clinically meaningful gains.

Drawing on the bibliometric analysis of MyoG-related literature from 2004 to 2024, which reveals clear patterns of thematic evolution, core bottlenecks, and potential breakthrough points, and considering the practical demands of muscle development regulation, regenerative medicine, and clinical translation, future research on MyoG should advance in a coordinated manner along three interconnected axes—mechanistic deepening, technological innovation, and clinical implementation. Such an integrated strategy will be essential to fully realize the central value of MyoG in both fundamental research and disease intervention.

Currently, MyoG research has shifted from basic functional exploration toward a stronger focus on pathological mechanisms, yet the integrity and specificity of disease-related regulatory networks remain incomplete. Future work should prioritize major conditions such as age-related muscle atrophy, Duchenne muscular dystrophy, and rhabdomyosarcoma (RMS), with particular emphasis on the following directions.

First, epigenomic approaches such as chromatin immunoprecipitation sequencing (ChIP-seq) and assay for transposase-accessible chromatin using sequencing (ATAC-seq) should be leveraged to dissect the dynamic interactions between MyoG, histone modifications, and DNA methylation. This will help identify "switch-like" regulatory nodes through which MyoG controls disease progression, with a special focus on clarifying the cascade regulation between MyoG and the HDAC4/5–E3 ubiquitin ligase axis in denervation-induced injury, thereby providing novel targets for the selective inhibition of muscle atrophy [49].

Second, the mechanisms underlying functional suppression of MyoG in RMS require deeper investigation. Future studies should concentrate on the cooperative effects of inhibitory factors such as TRPS1 and SNAI2 with the ERK/MAPK signaling pathway, and delineate how the natural antisense transcript of MyoG (MYOG-NAT) regulates MyoG protein stability. Deciphering these processes will be key to resolving the "differentiation block" characteristic of tumor cells and will provide a mechanistic basis for precisely relieving MyoG inhibition in RMS [41–43].

Existing MyoG research is still constrained by limitations in dissecting cellular heterogeneity and in modeling disease-relevant phenotypes, and these gaps will require technological innovation to overcome. Moving forward, the integration of single-cell, spatial, and genome-editing technologies should be actively promoted. On the one hand, combining single-cell RNA sequencing (scRNA-seq) with spatial transcriptomics will enable construction of spatiotemporal expression atlases of MyoG under distinct physiological and pathological conditions—such as quiescent versus activated satellite cells and different stages of myofiber injury and repair—thereby resolving cell subtype–specific regulatory networks and helping to reconcile the apparent paradox between maintaining satellite cell homeostasis and ensuring efficient myocyte fusion [37]. On the other hand, CRISPR-Cas9–based gene editing can be used to generate conditional MyoG knockout or mutation animal models that recapitulate clinically relevant genetic alterations (e.g., MyoG promoter mutations in RMS), providing a more precise alternative to traditional germline knockout models and enhancing the fidelity of drug screening and mechanistic validation [50]. In parallel, the application of artificial intelligence to MyoG regulatory network prediction—through integrative modeling of multi-omics datasets (genomics, transcriptomics, metabolomics)—may accelerate the discovery of previously unrecognized MyoG-interacting molecules and signaling pathways.

The complexity of MyoG-centered regulatory networks extends beyond the protein level; the potential contributions of noncoding RNAs and metabolic pathways remain insufficiently explored. Future work should therefore systematically advance along two major lines. First, with respect to noncoding RNAs—including microRNAs (miRNAs), long noncoding RNAs (lncRNAs), and circular RNAs (circRNAs)—RNA sequencing (RNA-seq) combined with RNA pull-down assays should be employed to identify and validate key molecules that regulate MyoG expression, and to clarify their roles in muscle regeneration (e.g., satellite cell activation) and disease (e.g., muscle atrophy). Particular emphasis should be placed on deepening our understanding of the interactions between miR-1/133 and MyoG, with the goal of developing RNA interference–or mimetic-based tools for precise modulation of MyoG activity [41, 43]. Second, the interplay between metabolic reprogramming and MyoG function warrants in-depth investigation. Future studies should focus on how glycolysis and fatty acid oxidation pathways influence MyoG-mediated myocyte differentiation and fusion, and determine whether metabolic signaling cascades such as AMP-activated protein kinase (AMPK) and mechanistic target of rapamycin complex 1 (mTORC1) contribute to muscle homeostasis by modulating MyoG activity. Such insights could provide a new conceptual framework for improving muscle function through metabolic interventions, including exercise and nutritional modulation [51].

The translation of advances in the MyoG field into clinical applications remains at an early stage, and future efforts must focus on overcoming key bottlenecks along the translational continuum

of technology optimization–efficacy validation–safety evaluation. In terms of targeted therapy, existing oncolytic viral vectors—such as Ad5/3-pMYOG (S)-mMEF2—require further refinement to enhance tumor tropism and infection efficiency while minimizing toxicity to normal myocytes. In parallel, gene therapy vectors driven by the MyoG promoter should be developed to achieve selective expression of therapeutic genes in diseased muscle cells [42].

For diagnosis and prognostic assessment, large-scale clinical datasets are needed to validate the feasibility of MyoG mRNA and protein expression levels as diagnostic biomarkers and prognostic indicators for muscle diseases such as rhabdomyosarcoma (RMS) and muscle atrophy. By integrating these molecular markers with imaging modalities, including magnetic resonance imaging (MRI) and ultrasound, a combined "molecular biomarker–imaging phenotype" evaluation system could be established to enable early disease screening and dynamic monitoring of therapeutic responses.

The complexity of MyoG research and its extensive connections to multiple biological systems make interdisciplinary collaboration and international cooperation indispensable. Future work should further integrate developmental biology, immunology, metabolomics, and clinical medicine to expand the conceptual and translational boundaries of MyoG research. For example, it will be important to elucidate the role of MyoG in cardioprotection—such as its ability to suppress cardiomyocyte apoptosis via regulation of the DUSP13–p38 MAPK pathway—and in neuromuscular interactions, including neural regulation of muscle regeneration following nerve injury, thereby uncovering its potential relevance in cardiovascular and neurodegenerative diseases. In parallel, a globally accessible MyoG data-sharing platform should be established to aggregate clinical samples, experimental datasets, and research outputs from different countries and regions. Such an infrastructure would help to resolve the "quantity–quality mismatch" observed in some emerging research communities, promote more rational allocation and efficient utilization of global MyoG research resources, and accelerate overall progress in the field.

In summary, future MyoG research should be explicitly guided by the goal of addressing real-world clinical problems, driven by technological innovation, and sustained by robust interdisciplinary collaboration. By advancing mechanistic understanding and translational application in tandem, MyoG research can progressively move from basic science toward clinical implementation, providing essential support for precision therapy of muscle diseases and for the continued development of regenerative medicine.

From a translational perspective, the bibliometric patterns identified here provide a practical roadmap rather than a purely descriptive overview. The concentration of highly cited work around MyoG-dependent atrophy pathways and rhabdomyosarcoma biology suggests that future experimental studies should prioritise dissecting MyoG-centred regulatory axes that are directly druggable (e.g., HDAC–E3 ligase cascades, ERK/MAPK signalling, MYOG-NAT–mediated RNA regulation) and testing these in disease-relevant *in vivo* models. At the clinical and multidisciplinary level, our collaboration and hotspot maps highlight at least three actionable priorities: (i) building multi-centre networks that link basic myogenesis laboratories with neuromuscular, oncology and geriatric units; (ii) embedding MyoG-related biomarkers into longitudinal cohorts and interventional trials for muscle wasting and paediatric muscle tumours; and (iii) fostering cross-talk with digital and imaging sciences to integrate molecular readouts with functional and imaging phenotypes. Explicitly aligning future experimental and clinical agendas with these mapped hotspots and gaps may accelerate the translation of MyoG biology into tangible benefits for patients with muscle disease.

Strengths and limitations

Bibliometric analysis provides a valuable window for researchers to gain an in-depth understanding of knowledge dynamics within a specific field and has become an important tool for exploring the intrinsic structure of scientific knowledge. However, this methodological approach also has several limitations. First, the literature search in this study was initially restricted to the Web of Science Core Collection and to publications in English. Such constraints may introduce selection bias; for example, the exclusion of Chinese-language publications could lead to an underestimation of contributions from Chinese researchers. Second, this work relied on multiple software tools, including CiteSpace, bibliometrics-related packages in R, and VOSviewer. Although these tools can generate broadly consistent results, some key information may still be inadvertently overlooked due to differences in algorithms or parameter settings.

In addition, bibliometric analysis itself carries inherent limitations. (i) It primarily focuses on the retrieval, screening, and organization of publications to provide a macroscopic overview of the literature, and therefore may lack sufficient depth for nuanced interpretation of scientific content. (ii) Citation-based indicators may be influenced by factors such as self-citation, language bias, and discipline-specific citation practices, which can compromise the reliability and validity of the findings. (iii) Journal-level metrics, such as the journal impact factor, may not accurately reflect the true influence of individual researchers or specific articles when used inappropriately at the micro level and can, in some cases, be misleading.

Despite these limitations, bibliometric analysis still enables a clear visualization of the complex interactions among authors,

institutions, and countries, and helps to identify emerging trends and future directions in the MyoG field.

Conclusion

This bibliometric analysis delineates the evolutionary trajectory of MyoG research from 2004 to 2024. The global scientific landscape in this field exhibits a multipolar collaborative pattern: traditional research powerhouses continue to dominate the innovative frontier, whereas emerging countries are rapidly increasing their output but still lag behind in academic influence, reflecting structural differences between basic research–driven and technology application–oriented systems. Research hotspots have progressively shifted from molecular mechanisms—such as DNA binding and interactions with MyoD—toward regenerative medicine, particularly satellite cell regulation, and more recently toward clinical translation, including the elucidation of muscle atrophy mechanisms. Landmark studies have continued to shape the conceptual foundation of the field, while recent breakthroughs have expanded the pathological and translational relevance of MyoG.

Future work should focus on deepening the understanding of molecular mechanisms underlying muscle degenerative diseases, integrating emerging technologies such as single-cell sequencing and spatial transcriptomics, and clarifying the interplay between MyoG, noncoding RNAs, and metabolic reprogramming, with the ultimate goal of advancing MyoG-targeted therapeutic strategies into clinical practice. Although this study is constrained by potential data source bias and methodological limitations—such as reliance on a single primary database and specific software tools—it nonetheless provides a panoramic overview of the MyoG research landscape. Moving forward, the integration of multiple databases, development of more refined evaluation frameworks, and reinforcement of interdisciplinary and international collaboration will be essential to optimize research pathways and unlock the full potential of MyoG in muscle development regulation, disease intervention, and regenerative medicine.

Author contributions

LH and WZ contributed to conceptualization and methodology and curated the bibliometric data. LH drafted the original manuscript. SY implemented the software, performed the formal analysis and validated the results. WC provided resources and contributed to data curation. SC and XW carried out the investigation and assisted with data curation. QG and JC critically reviewed and edited the manuscript and acquired funding. All authors contributed to the article and approved the submitted version.

Data availability

The bibliometric data used in this study were retrieved from the Web of Science Core Collection (https://www.webofscience.com) on 14 February 2025. The raw records are subject to licence restrictions and cannot be shared directly by the authors, but can be obtained by any qualified researcher with institutional access to Web of Science using the search strategy described in the Methods section. Processed data (e.g., aggregated country-, institution- and keyword-level matrices) and analysis scripts are available from the corresponding author on reasonable request.

Funding

The author(s) declared that financial support was received for this work and/or its publication. This work was partially supported by the 2024 Guangdong Provincial Research Institute Innovation Capacity Construction Stability Support Project (No. KD022024023) and the National Key Research and Development Program of China (No. 2022YFC2407406; 2022YFB4600600).

Acknowledgements

The authors would like to thank their colleagues for helpful discussions and technical support during the course of this work.

Conflict of interest

The author(s) declared no potential conflicts of interest with respect to the research, authorship, and/or publication of this article.

Generative AI statement

The author(s) declared that generative AI was not used in the creation of this manuscript.

Any alternative text (alt text) provided alongside figures in this article has been generated by Frontiers with the support of artificial intelligence and reasonable efforts have been made to ensure accuracy, including review by the authors wherever possible. If you identify any issues, please contact us.

Supplementary material

The Supplementary Material for this article can be found online at: https://www.ebm-journal.org/articles/10.3389/ebm.2026.10929/full#supplementary-material

References

1. Davis RL, Weintraub H, Lassar AB. Expression of a single transfected cDNA converts fibroblasts to myoblasts. *Cell* (1987) **51**(6):987–1000. doi:10.1016/0092-8674(87)90585-x

2. Wright WE, Sassoon DA, Lin VK. Myogenin, a factor regulating myogenesis, has a domain homologous to MyoD. *Cell* (1989) **56**(4):607–17. doi:10.1016/0092-8674(89)90583-7

3. Sassoon D, Lyons G, Wright WE, Lin V, Lassar A, Weintraub H, et al. Expression of two myogenic regulatory factors myogenin and MyoD1 during mouse embryogenesis. *Nature* (1989) **341**(6240):303–7. doi:10.1038/341303a0

4. Rantanen J, Hurme T, Lukka R, Heino J, Kalimo H. Satellite cell proliferation and the expression of myogenin and desmin in regenerating skeletal muscle: evidence for two different populations of satellite cells. *Lab Investigation; a Journal Technical Methods Pathology* (1995) **72**(3):341–7.

5. Azizan A. Exercise and frailty in later life: a systematic review and bibliometric analysis of research themes and scientific collaborations. *Int J Popul Stud* (2024) **11**(1):1. doi:10.36922/ijps.3282

6. Azizan A. Mapping the muscle mass: a birds-eye view of sarcopenia research through bibliometric network analysis. *Int J Disabilities Sports and Health Sci* (2024) **7**(1):134–43. doi:10.33438/ijdshs.1362539

7. Moresi V, Williams AH, Meadows E, Flynn JM, Potthoff MJ, McAnally J, et al. Myogenin and class II HDACs control neurogenic muscle atrophy by inducing E3 ubiquitin ligases. *Cell* (2010) **143**(1):35–45. doi:10.1016/j.cell.2010.09.004

8. Calhabeu F, Hayashi S, Morgan JE, Relaix F, Zammit PS. Alveolar rhabdomyosarcoma-associated proteins PAX3/FOXO1A and PAX7/FOXO1A suppress the transcriptional activity of MyoD-target genes in muscle stem cells. *Oncogene* (2013) **32**(5):651–62. doi:10.1038/onc.2012.73

9. Hinits Y, Osborn DPS, Hughes SM. Differential requirements for myogenic regulatory factors distinguish medial and lateral somitic, cranial and fin muscle fibre populations. *Development* (2009) **136**(3):403–14. doi:10.1242/dev.028019

10. Meadows E, Cho JH, Flynn JM, Klein WH. Myogenin regulates a distinct genetic program in adult muscle stem cells. *Developmental Biol* (2008) **322**(2):406–14. doi:10.1016/j.ydbio.2008.07.024

11. Flynn JM, Meadows E, Fiorotto M, Klein WH. Myogenin regulates exercise capacity and skeletal muscle metabolism in the adult mouse. *PLoS One* (2010) **5**(10):e13535. doi:10.1371/journal.pone.0013535

12. Meadows E, Flynn JM, Klein WH. Myogenin regulates exercise capacity but is dispensable for skeletal muscle regeneration in adult mdx mice. *PLoS One* (2011) **6**(1):e16184. doi:10.1371/journal.pone.0016184

13. Hasty P, Bradley A, Morris JH, Edmondson DG, Venuti JM, Olson EN, et al. Muscle deficiency and neonatal death in mice with a targeted mutation in the myogenin gene. *Nature* (1993) **364**(6437):501–6. doi:10.1038/364501a0

14. Nabeshima Y, Hanaoka K, Hayasaka M, Esumi E, Li S, Nonaka I, et al. Myogenin gene disruption results in perinatal lethality because of severe muscle defect. *Nature* (1993) **364**(6437):532–5. doi:10.1038/364532a0

15. Ohkawa Y, Marfella CGA, Imbalzano AN. Skeletal muscle specification by myogenin and Mef2D via the SWI/SNF ATPase Brg1. *Embo J* (2006) **25**(3):490–501. doi:10.1038/sj.emboj.7600943

16. Rao PK, Kumar RM, Farkhondeh M, Baskerville S, Lodish HF. Myogenic factors that regulate expression of muscle-specific. *microRNAs. Proc Natl Acad Sci U S A.* (2006) **103**(23):8721–6. doi:10.1073/pnas.0602831103

17. de la Serna IL, Ohkawa Y, Berkes CA, Bergstrom DA, Dacwag CS, Tapscott SJ, et al. MyoD targets chromatin remodeling complexes to the myogenin locus prior to forming a stable DNA-bound complex. *Mol Cell Biol* (2005) **25**(10):3997–4009. doi:10.1128/mcb.25.10.3997-4009.2005

18. Blais A, Tsikitis M, Acosta-Alvear D, Sharan R, Kluger Y, Dynlacht BD. An initial blueprint for myogenic differentiation. *Genes Dev* (2005) **19**(5):553–69. doi:10.1101/gad.1281105

19. Stojic L, Jasencakova Z, Prezioso C, Stützer A, Bodega B, Pasini D, et al. Chromatin regulated interchange between polycomb repressive complex 2 (PRC2)-Ezh2 and PRC2-Ezh1 complexes controls myogenin activation in skeletal muscle cells. *Epigenetics and Chromatin* (2011) **4**:16. doi:10.1186/1756-8935-4-16

20. Huang MB, Xu H, Xie SJ, Zhou H, Qu LH. Insulin-like growth Factor-1 receptor is regulated by microRNA-133 during skeletal myogenesis. *PLoS One* (2011) **6**(12):e29173. doi:10.1371/journal.pone.0029173

21. Luo J, Gao Q, Qiu HL, Zhang S, Zou WW, Wang P, et al. Myogenin regulates DUSP13 to inhibit apoptosis induced by reactive oxygen species. *Front Bioscience-Landmark* (2024) **29**(2):49. doi:10.31083/j.fbl2902049

22. Gao Q, Wang P, Qiu HL, Qiu B, Yi WJ, Tu WC, et al. Myogenin suppresses apoptosis induced by angiotensin II in human induced pluripotent stem cell-derived cardiomyocytes. *Biochem Biophysical Res Commun* (2021) **552**:84–90. doi:10.1016/j.bbrc.2021.03.031

23. Zhang L, Wang C. Identification of a new class of PAX3-FKHR target promoters: a role of the Pax3 paired box DNA binding domain. *Oncogene* (2007) **26**(11):1595–605. doi:10.1038/sj.onc.1209958

24. Lu PY, Taylor M, Jia HT, Ni JH. Muscle LIM protein promotes expression of the acetylcholine receptor γ-subunit gene cooperatively with the myogenin-E12 complex. *Cell Mol Life Sci* (2004) **61**(18):2386–92. doi:10.1007/s00018-004-4213-x

25. Fraterman S, Khurana TS, Rubinstein NA. Identification of acetylcholine receptor subunits differentially expressed in singly and multiply innervated fibers of extraocular muscles. *Invest Ophthalmol and Vis Sci* (2006) **47**(9):3828–34. doi:10.1167/iovs.06-0073

26. Chen DH, Chen SC, Wang W, Liu F, Zhang CS, Zheng HL. Modulation of satellite cells in rat facial muscle following denervation and delayed reinnervation. *Acta Oto-Laryngologica* (2010) **130**(12):1411–20. doi:10.3109/00016489.2010.496464

27. Yajima H, Motohashi N, Ono Y, Sato S, Ikeda K, Masuda S, et al. Six family genes control the proliferation and differentiation of muscle satellite cells. *Exp Cell Res* (2010) **316**(17):2932–44. doi:10.1016/j.yexcr.2010.08.001

28. Lindström M, Pedrosa-Domellöf F, Thornell LE. Satellite cell heterogeneity with respect to expression of MyoD, myogenin, Dlk1 and c-Met in human skeletal muscle: application to a cohort of power lifters and sedentary men. *Histochem Cell Biol* (2010) **134**(4):371–85. doi:10.1007/s00418-010-0743-5

29. Riuzzi F, Sorci G, Sagheddu R, Donato R. HMGB1-RAGE regulates muscle satellite cell homeostasis through p38-MAPK- and myogenin-dependent repression of Pax7 transcription. *J Cell Sci* (2012) **125**(6):1440–54. doi:10.1242/jcs.092163

30. McFarland DC, Pesall JE, Coy CS, Velleman SG. Effects of 17β-estradiol on Turkey myogenic satellite cell proliferation, differentiation, and expression of glypican-1, MyoD and myogenin. *Comp Biochem Physiol A-Molecular and Integr Physiol* (2013) **164**(4):565–71. doi:10.1016/j.cbpa.2013.01.001

31. Chisada S, Okamoto H, Taniguchi Y, Kimori Y, Toyoda A, Sakaki Y, et al. Myostatin-deficient medaka exhibit a double-muscling phenotype with hyperplasia and hypertrophy, which occur sequentially during post-hatch development. *Developmental Biol* (2011) **359**(1):82–94. doi:10.1016/j.ydbio.2011.08.027

32. Le Grand F, Grifone R, Mourikis P, Houbron C, Gigaud C, Pujol J, et al. Six1 regulates stem cell repair potential and self-renewal during skeletal muscle regeneration. *J Cell Biol* (2012) **198**(5):815–32. doi:10.1083/jcb.201201050

33. Steffens AA, Hong GM, Bain LJ. Sodium arsenite delays the differentiation of C2C12 mouse myoblast cells and alters methylation patterns on the transcription factor myogenin. *Toxicol Appl Pharmacol* (2011) **250**(2):154–61. doi:10.1016/j.taap.2010.10.006

34. Campos C, Valente LMP, Conceiçao LEC, Engrola S, Fernandes JMO. Temperature affects methylation of the myogenin putative promoter, its expression and muscle cellularity in Senegalese sole larvae. *Epigenetics* (2013) **8**(4):389–97. doi:10.4161/epi.24178

35. Adhikari A, Kim W, Davie J. Myogenin is required for assembly of the transcription machinery on muscle genes during skeletal muscle differentiation. *PLoS One* (2021) **16**(1):e0245618. doi:10.1371/journal.pone.0245618

36. Ganassi M, Badodi S, Quiroga HPO, Zammit PS, Hinits Y, Hughes SM. Myogenin promotes myocyte fusion to balance fibre number and size. *Nat Commun* (2018) **9**:1–17. doi:10.1038/s41467-018-06583-6

37. Ganassi M, Badodi S, Wanders K, Zammit PS, Hughes SM. Myogenin is an essential regulator of adult myofibre growth and muscle stem cell homeostasis. *Elife* (2020) **9**:9doi. doi:10.7554/eLife.60445

38. Hsu JY, Danis EP, Nance S, O'Brien JH, Gustafson AL, Wessells VM, et al. SIX1 reprograms myogenic transcription factors to maintain the rhabdomyosarcoma undifferentiated state. *Cell Rep* (2022) **38**(5):110323. doi:10.1016/j.celrep.2022.110323

39. Pruller J, Hofer I, Ganassi M, Heher P, Ma MT, Zammit PS. A modified human Myogenin promoter that is highly active in alveolar rhabdomyosarcoma. *Cancer Gene Ther* (2021) **28**(5):427–41. doi:10.1038/s41417-020-00225-0

40. Yoshida H, Sato-Dahlman M, Hajeri P, Jacobsen K, Koodie L, Yanagiba C, et al. Mutant myogenin promoter-controlled oncolytic adenovirus selectively kills PAX3-FOXO1-positive rhabdomyosarcoma cells. *Translational Oncol* (2021) **14**(2):100997. doi:10.1016/j.tranon.2020.100997

41. Huettner SS, Henze H, Elster D, Koch P, Anderer U, von Eyss B, et al. A dysfunctional miR-1-TRPS1-MYOG axis drives ERMS by suppressing terminal myogenic differentiation. *Mol Ther* (2023) **31**(9):2612–32. doi:10.1016/j.ymthe.2023.07.003

42. Yohe ME, Gryder BE, Shern JF, Song YK, Chou HC, Sindiri S, et al. MEK inhibition induces MYOG and remodels super-enhancers in RAS-driven rhabdomyosarcoma. *Sci Translational Med* (2018) **10** (448):1–14. doi:10.1126/scitranslmed.aan4470

43. Yin YQ, Chen GH, Lin ZT, Zhang DL, Lin WJ, Luo W. Natural antisense transcript of MYOG regulates development and regeneration in skeletal muscle by shielding the binding sites of MicroRNAs of MYOG mRNA 3'UTR. *Biochem Biophysical Res Commun* (2023) **662**:93–103. doi:10.1016/j.bbrc.2023.04.050

44. Azizan A, Centre of Physiotherapy FoHSUTMPASM, Clinical, Rehabilitation Exercise Research Group FoHSUTMPASM. Mapping the knowledge structure of online learning research in health sciences education: a bibliometric network analysis. *Education Med J* (2025) **17**(3):1–15. doi:10.21315/eimj2025.17.3.1

45. Tang HB, Macpherson P, Marvin M, Meadows E, Klein WH, Yang XJ, et al. A histone deacetylase 4/Myogenin positive feedback loop coordinates denervation-dependent gene induction and suppression. *Mol Biol Cell* (2009) **20**(4):1120–31. doi:10.1091/mbc.E08-07-0759

46. Cao Y, Kumar RM, Penn BH, Berkes CA, Kooperberg C, Boyer LA, et al. Global and gene-specific analyses show distinct roles for Myod and Myog at a common set of promoters. *Embo J* (2006) **25**(3):502–11. doi:10.1038/sj.emboj.7600958

47. Yang ZJP, Broz DK, Noderer WL, Ferreira JP, Overton KW, Spencer SL, et al. p53 suppresses muscle differentiation at the myogenin step in response to genotoxic stress. *Cell Death Differ* (2015) **22**(4):560–73. doi:10.1038/cdd.2014.189

48. Olguin HC, Yang ZH, Tapscott SJ, Olwin BB. Reciprocal inhibition between Pax7 and muscle regulatory factors modulates myogenic cell fate determination. *J Cell Biol* (2007) **177**(5):769–79. doi:10.1083/jcb.200608122

49. Ma WJ, Cai Y, Shen YT, Chen X, Zhang LL, Ji YA, et al. HDAC4 knockdown alleviates denervation-induced muscle atrophy by inhibiting myogenin-dependent atrogene activation. *Front Cell Neurosci* (2021) **15**:663384. doi:10.3389/fncel.2021.663384

50. Long KR, Li XK, Su D, Zeng S, Li HK, Zhang Y, et al. Exploring high-resolution chromatin interaction changes and functional enhancers of myogenic marker genes during myogenic differentiation. *J Biol Chem* (2022) **298**(8):102149. doi:10.1016/j.jbc.2022.102149

51. Prince LM, Rand MD. Methylmercury exposure causes a persistent inhibition of myogenin expression and C2C12 myoblast differentiation. *Toxicology* (2018) **393**:113–22. doi:10.1016/j.tox.2017.11.002

EBM Experimental Biology and Medicine

TYPE Original Research
PUBLISHED 17 April 2026
DOI 10.3389/ebm.2026.10827

OPEN ACCESS

*CORRESPONDENCE
Xiaomin Chen,
chenxm7301@126.com

RECEIVED 18 September 2025
REVISED 24 February 2026
ACCEPTED 31 March 2026
PUBLISHED 17 April 2026

CITATION
Tong B, Wang J, Chen J, Zhang Q, Xu Z, Yang K and Chen X (2026) Elevated ApoC3 levels in cerebrospinal fluid predict poor outcomes in patients with aneurysmal subarachnoid hemorrhage. *Exp. Biol. Med.* 251:10827. doi: 10.3389/ebm.2026.10827

Elevated ApoC3 levels in cerebrospinal fluid predict poor outcomes in patients with aneurysmal subarachnoid hemorrhage

Bin Tong[1], Junjie Wang[2], Jiarui Chen[2], Qia Zhang[2], Zhouhan Xu[2], Kaichuang Yang[3] and Xiaomin Chen[4]*

[1]Department of the Operating Room, Zhejiang Provincial People's Hospital, Affiliated People's Hospital, Hangzhou Medical College, Hangzhou, China, [2]Department of Neurosurgery, Second Affiliated Hospital, School of Medicine, Zhejiang University, Hangzhou, China, [3]Center for Rehabilitation Medicine, Department of Neurosurgery, Zhejiang Provincial People's Hospital, Affiliated People's Hospital, Hangzhou Medical College, Hangzhou, China, [4]Department of Nursing, Zhejiang Provincial People's Hospital, Affiliated People's Hospital, Hangzhou Medical College, Hangzhou, China

Abstract

Aneurysmal subarachnoid hemorrhage (aSAH) is a devastating condition associated with approximately 30% mortality and 20% severe disability among survivors. Delayed cerebral ischemia due to cerebral vasospasm and hydrocephalus significantly contribute to poor neurological outcomes. Currently, reliable biomarkers for early prediction of these complications remain lacking. In this study, 63 patients with a mean age of 59.7 ± 11.53 years were enrolled. Functional outcomes were assessed by the modified Rankin Scale (mRS). Cerebrospinal fluid (CSF) samples were obtained through lumbar drainage (LD) or external ventricular drainage (EVD) and analyzed by ELISA. The predictive value of biomarkers was evaluated using receiver operating characteristic (ROC) curve analysis. Elevated Apolipoprotein C-III (ApoC3) levels in CSF of aSAH patients were observed. Furthermore, increased ApoC3 concentrations were significantly associated with poor prognosis and an elevated risk of severe complications. At an optimal cutoff value of 4,463 ng/mL, patients with high ApoC3 levels exhibited significantly worse 3-month functional outcomes and a higher incidence of delayed cerebral ischemia and hydrocephalus. Monitoring ApoC3 levels in CSF may be beneficial for predicting complications such as delayed cerebral ischemia and hydrocephalus in patients with aSAH.

KEYWORDS
aneurysmal subarachnoid hemorrhage, ApoC3, cerebrospinal fluid, delayed cerebral ischemia, hydrocephalus

Impact statement

Although surgical clipping or endovascular coiling, alongside vasospasm management have improved survival rates, the rates of morbidity and mortality of Subarachnoid hemorrhage (SAH) patients remain unacceptably high. Early diagnosis and timely intervention are paramount for optimizing outcomes. In our study, we found that CSF ApoC3 levels in aSAH patients were significantly negative correlated with clinical scores. This study may improve prognostic assessments, enable early identification of high-risk patients,

and potentially guide personalized treatment strategies, ultimately reducing the morbidity and mortality associated with SAH and uncovering new therapeutic targets for managing this condition.

Introduction

SAH is a severe form of stroke characterized by bleeding into the subarachnoid space, usually caused by the rupture of an intracranial aneurysm. Although SAH represents only 5%–10% of all stroke cases, it is associated with disproportionately high mortality and long-term disability rates [1]. Globally, the incidence of SAH ranges from 6 to 10 cases per 100,000 people annually, typically occurring between ages 50 and 60, with a slight predominance in females [1]. Despite advances in medical treatment, the case-fatality rate remains alarmingly high, with 40%–50% of patients succumbing within the first month following SAH [2]. Even with current therapeutic strategies, survivors have significantly different prognoses. Approximately 10%–20% of patients experience severe disabilities, including lasting cognitive and physical impairments that limit independence and quality of life. In contrast, about 63.3% of patients without infarction achieve excellent outcomes (mRS scores of 0–1) within 1 year [2, 3]. Currently, clinical management strategies are uniform across SAH patients. Given the substantial variability in outcomes and the clear relationship between excellent outcomes and the absence of infarction, reliable prognostic biomarkers are essential. Such biomarkers could identify patients at high risk for poor outcomes and facilitate early interventions to manage brain edema and prevent vasospasm, thereby altering disease progression and improving prognosis. However, reliable biomarkers are currently lacking.

The pathophysiology of SAH is complex, involving primary and secondary mechanisms of injury. The initial hemorrhagic event initiates multiple complications, including cerebral vasospasm, brain edema, intracranial hypertension, and a robust inflammatory response due to blood accumulation in the subarachnoid space. Vasospasm occurs in up to 70% of patients, resulting from endothelial dysfunction, and leads to delayed cerebral ischemia in 30%–40% of cases, significantly contributing to poor neurological outcomes [4, 5]. Additionally, brain edema and elevated intracranial pressure further exacerbate secondary injuries, complicating clinical management [5].

ApoC3 is a glycoprotein primarily involved in lipid metabolism, particularly the regulation of triglyceride-rich lipoproteins (TRLs) such as very low-density lipoproteins (VLDL) and chylomicrons [6]. ApoC3 slows the catabolism of these lipoproteins by inhibiting lipoprotein lipase (LPL) activity, contributing to hypertriglyceridemia [6]. Beyond its metabolic functions, ApoC3 is implicated in inflammation and endothelial dysfunction, crucial mechanisms in cardiovascular and cerebrovascular diseases [6, 7].

As mentioned previously, vasospasm significantly contributes to poor neurological outcomes [8]; however, no reliable biomarkers currently exist to predict vasospasm in SAH patients. Considering ApoC3's established role in inflammation and endothelial dysfunction, ApoC3 may serve as a promising prognostic biomarker.

Given its known involvement in cerebrovascular diseases, we hypothesize that ApoC3 levels represent effective biomarkers for predicting vasospasm and overall prognosis in SAH patients. Specifically, ApoC3 may influence recovery by regulating inflammation, oxidative stress, and endothelial repair, processes essential for vascular healing and neurological improvement. To test this hypothesis, we aimed to evaluate the correlation between CSF ApoC3 levels and clinical outcomes in SAH patients, including the mRS score, cerebral vasospasm, and hydrocephalus. Since SAH frequently requires invasive procedures such as CSF analysis for diagnosis and monitoring, identifying CSF ApoC3 levels as a prognostic biomarker could offer valuable insights into disease progression and potentially reduce repeated invasive procedures. Results demonstrated that ApoC3 levels were an independent biomarker for SAH prognosis and significantly correlated with vasospasm and hydrocephalus. Early identification of SAH patients with elevated CSF ApoC3 levels and targeted interventions, such as enhanced vasospasm prevention, close monitoring of hydrocephalus through CT imaging, and prompt treatment, may help alter disease progression and improve patient prognosis.

Materials and methods

Study overview

This prospective observational cohort study enrolled patients with spontaneous aneurysmal SAH admitted to the Second Affiliated Hospital of Zhejiang University and Zhejiang Provincial People's Hospital between October 2021 and October 2023 (ClinicalTrials.gov NCT06009016). Eligible patients were required to be ≥18 years old, diagnosed with aneurysmal SAH, and have a modified Fisher score (mFS) of 2-4 by Computed Tomography Angiography (CTA) within 24 h of symptom onset. Exclusion criteria included: (1) non-aneurysmal SAH (e.g., trauma, arteriovenous malformations, angiogram-negative SAH); (2) previous central nervous system (CNS) disorders (stroke, traumatic brain injury, CNS infections); (3) severe comorbidities within 6 months prior to SAH (e.g., malignancies, drug-resistant cardiovascular diseases, coagulation disorders, or organ dysfunction). Patients with normal pressure hydrocephalus (NPH) aged ≥18 years were enrolled as the control group, presenting at least two symptoms of the Hakim-Adams triad (gait disturbance, urinary incontinence, and cognitive decline), CSF pressure <200 mm H_2O, normal CSF content, and exclusion of other medical causes [9]. Ethical approval was granted by the Institutional Review Board of the Second Affiliated Hospital of Zhejiang University (Approval No. 2023-059). Informed consent was obtained from participants or their family members, or waived by the board.

Treatment protocol

Digital subtraction angiography (DSA) was performed within 24 h of admission to identify the responsible aneurysm, followed by embolization or clipping by experienced neurointerventional or neurosurgical teams. LD was routinely performed for patients with an mFS of 3-4, except when acute hydrocephalus necessitated EVD. Postoperative brain CT scans were initially performed, with follow-up scans every 1–3 days, as clinically indicated, until discharge. Nimodipine was administered to

10.3389/ebm.2026.10827

TABLE 1 Demographic and Clinical Data of 63 patients with aSAH.

Variable		Average/median/N	SD/IQR/%
Hospital LOS, d		12	(10–22)
Sex (F)		34	54%
Age, y		59.7	±11.53
Systolic blood pressure, mmHg		150	(137–168)
Systolic blood pressure >190		11	17.5%
Admission GCS	13–15	39	61.9%
	6–12	11	17.5%
	3–5	13	20.6%
WFNS grade (3-5)		29	46%
Hunt & hess grade (3-4)		28	44.4%
NSICU LOS, d		6	(2–18)
Duration of mechanical ventilation, d		5	(2–12)
Drinking		20	31.7%
Smoking		21	33.3%
Hypertension		36	57.1%
Diabetes		4	6.3%
BMI	<18.5	4	6.3%
	<24	12	50.8%
	<28	24	38.1%
	≥28	3	4.8%
CSF examination	ApoC3, ng/mL	3,149.5	(1,174.77–7,768.51)
	RBC, 10⁶/L	83,000	(29,000–102000)
	Lymphocytes, %	29.26	(13–38)
	Nucleated cells, 10⁶/L	442	(169–1,487)
	Glucose, mmol/L	3.82	(2.93–4.25)
	Protein level, mg/dL	128.3	(69–157.6)
	Cl^-, mmol/L	129.5	(125.2–131.4)
mFS (3-4)		41	65.1%
SEBES (3-4)		46	73%
IVH		44	69.8%
mGS		2	(0–9)
Aneurysm Location	Internal carotid artery	5	7.9%
	Anterior cerebral artery	31	49.2%
	Middle cerebral artery	11	17.5%
	Posterior circulation	16	25.4%

(*Continued*)

TABLE 1 Continued

Variable		Average/median/N	SD/IQR/%
Aneurysm size	1–5 mm	24	38.1%
	5.1–10 mm	33	52.4%
	Greater than 10 mm	6	9.5%
Coiling		21	33.3%
Clipping		42	66.7%
Decompression		11	17.5%
LD		43	68.3%
EVD		15	23.8%
Clinical vasospasm		23	36.5%
Delayed infarction		27	42.9%
Hydrocephalus		21	33.3%
3-month mRS (3–6)		30	47.6%

prevent cerebral vasospasm, and intravenous rehydration was used to maintain normal blood volume.

Sample size calculation

Sample size estimation was conducted by G*Power (version 3.1) to determine the number of patients of SAH (one-sample case), with an α error probability of 0.05, effect size [d] of 0.4, study power (1-β) of 0.9. The result was 55 aSAH patients. We totally enrolled 63 patients to ensure the study's statistical power.

mRS outcome assessment

Functional outcomes assessed by the mRS were collected via telephone calls or hospital and clinic visits 3 months after discharge. mRS scores of 0–2 were considered good outcomes, while scores of 3–6 indicated poor outcomes. Assessments were conducted by independent, trained investigators blinded to study details to minimize bias.

Data collection

Baseline characteristics (age, gender, BMI, medical history, and social history) were assessed by the treating physician. Clinical data upon admission, including the Glasgow Coma Scale (GCS), Hunt and Hess (HH) grade, and World Federation of Neurosurgeons Scale (WFNS), were recorded. Treatment-related data, such as surgical approaches, ICU length of stay, and duration of mechanical ventilation, were also documented. SAH-related complications, including seizures and delayed cerebral ischemia (DCI), were monitored. DCI was defined as focal neurological deficits or a ≥2-point decline in GCS, caused by cerebral vasospasm or infarction (new infarcts on CT or MRI, excluding those occurring within 48 h post-surgery). Functional outcomes were evaluated at 3 months post-discharge using the mRS, with good prognosis defined as mRS scores of 0–3 and poor prognosis as scores of 4–6. Radiological data collected from head CT scans included mFS, Subarachnoid Hemorrhage Early Brain Edema Score (SEBES), intraventricular hemorrhage (IVH), and the highest Hounsfield unit (HU) in the hemorrhagic area. CSF samples were collected via LD or EVD within 72 h postoperatively. Following collection, samples were centrifuged at 3,000 rpm for 10 min at 4 °C to remove erythrocytes and immune cells, and stored at −80 °C until ELISA analysis.

ELISA detection

CSF ApoC3 concentrations were determined using the Human Apolipoprotein CIII ELISA Kit (ab154131, Abcam, Cambridge, MA, USA) according to the manufacturer's protocol. The intra-assay coefficient of variation (CV) is 6% and the inter-assay CV is 11%. All samples were tested in duplicate, and mean values were calculated for further analysis. Samples were analyzed on two plates within the same day to minimize variability between assays. A standard curve was generated using a four-parameter logistic regression model, and ApoC3 concentrations were calculated by interpolation. All experiments and analyses were conducted by separate investigators, blinded to patients' clinical information and 3-month outcome status. Sample identifiers were anonymized prior to analysis.

Statistical analysis

Descriptive statistics are presented as counts (n) and percentages (%) for categorical variables, and mean ± standard deviation (SD) for continuous variables. Differences in patient characteristics were evaluated using unpaired Student's t-tests or non-parametric Mann-Whitney U tests for continuous variables, and Pearson chi-square or Fisher's exact tests for categorical variables. Normality of the data was assessed using the Shapiro-Wilk test. The predictive value of

TABLE 2 Univariate analysis of poor outcome at 3 months after discharge.

Variable		3-month mRS		
		Favourable 0-2	Unfavourable 3-6	*p*-value
Hospital LOS, d		11 (9.5–13.5)	18.5 (11–33.5)	**0.002**
Sex (F)		18 (54.5)	16 (53.3)	0.923
Age, y		56.55 ± 9.60	63.17 ± 12.61	**0.022**
Systolic blood pressure, mmHg		147 (132.5–156)	160 (140.5–196.75)	**0.037**
Systolic blood pressure >190		2 (6.1)	9 (30)	**0.012**
Admission GCS	13–15	30 (90.9)	9 (30)	**<0.001**
	6–12	2 (6.1)	9 (30)	
	3–5	1 (3)	12 (40)	
WFNS grade (3-5)		8 (24.2)	21 (70)	**<0.001**
Hunt & hess grade (3-4)		5 (15.2)	23 (76.7)	**<0.001**
NSICU LOS, d		3 (1.5–5.5)	15 (7–26.5)	**<0.001**
Duration of mechanical ventilation, d		2 (1–3.5)	11 (5–28)	**<0.001**
Drinking		14 (42.4)	6 (20)	0.056
Smoking		12 (36.4)	9 (30)	0.593
Hypertension		18 (54.5)	18 (60)	0.662
Diabetes		1 (3)	3 (10)	0.538
BMI	<18.5	2 (6.1)	2 (6.7)	0.101
	<24	20 (60.6)	12 (40)	
	<28	11 (33.3)	13 (43.3)	
	≥28	0 (0)	3 (10)	
CSF examination	ApoC3, ng/mL	1,464.70 (641.40–3,201.46)	7,179.49 (2000.65–13915.86)	**<0.001**
	RBC, 10^6/L	62,100 (28,500–115000)	88,500 (32,688–101928)	0.61
	Lymphocytes, %	29.26 (15–41.5)	29.26 (12.75–34)	0.643
	Nucleated cells, 10^6/L	330 (149.5–1886.5)	590 (210.25–1,486.57)	0.825
	Glucose, mmol/L	3.59 (2.63–4.03)	4.00 (3.55–5.99)	0.059
	Protein level, mg/dL	83.3 (51.85–135.05)	135.05 (94.7–208.23)	**0.017**
	Cl^-, mmol/L	128 (124.05–129.55)	130.2 (129.36–135.33)	**0.001**
mFS (3-4)		13 (39.4)	28 (93.3)	**<0.001**
SEBES (3-4)		18 (54.5)	28 (93.3)	**0.001**
IVH		16 (48.5)	28 (93.3)	**<0.001**
mGS		0 (0–2)	8.5 (2–19)	**<0.001**
Aneurysm Location	Internal carotid artery	3 (9.1)	2 (6.7)	0.161
	Anterior cerebral artery	20 (60.6)	11 (36.7)	
	Middle cerebral artery	5 (15.2)	6 (20)	
	Posterior circulation	5 (15.2)	11 (36.7)	

(*Continued*)

TABLE 2 Continued

Variable		3-month mRS		
		Favourable 0-2	Unfavourable 3-6	*p*-value
Aneurysm size	1–5 mm	15 (45.5)	9 (30)	0.113
	5.1–10 mm	17 (51.5)	16 (53.3)	
	Greater than 10 mm	1 (3)	5 (16.7)	
Coiling		11 (33.3)	10 (33.3)	1
Clipping		22 (66.7)	20 (66.7)	1
Decompression		1 (3)	10 (33.3)	**0.002**
LD		27 (81.8)	16 (53.3)	**0.015**
EVD		1 (3)	14 (46.7)	**<0.001**
Clinical vasospasm		6 (18.2)	17 (56.7)	**0.002**
Delayed infarction		5 (15.2)	22 (73.3)	**<0.001**
Hydrocephalus		3 (9.1)	18 (60)	**<0.001**

Bold values indicates the p-value that less than 0.05.

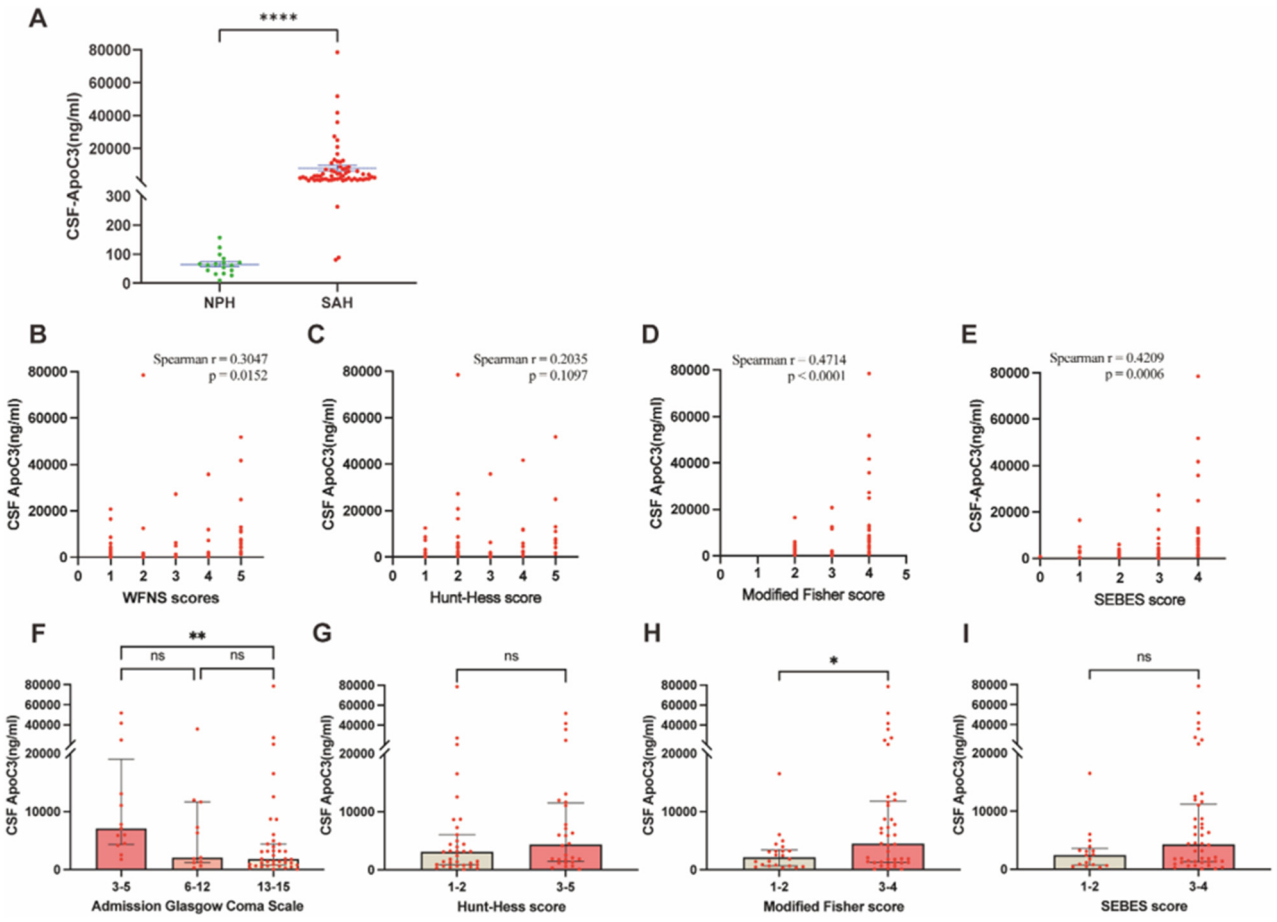

FIGURE 1
Comparison of CSF ApoC3 concentrations between NPH patients and clinical grades of aSAH. **(A)** Comparison of CSF ApoC3 levels between 63 patients with aSAH and 17 patients with NPH. **(B–E)** Spearman correlation analyses of CSF ApoC3 concentrations and clinical grades of SAH among patients with aSAH. **(F–I)** Correlation analyses between CSF ApoC3 concentrations and graded clinical scores of SAH.

TABLE 3 Multivariate logistic regression analysis of poor outcome 3 months after discharge.

Independent variable	OR	95% CI	*p*-value
Age, y	1.05	0.91–1.22	0.488
Admission GCS	21.33	0.77–594.34	0.071
WFNS grade (3-5)	110.04	1.404–8,623.27	**0.035**
Hunt & hess grade (3-4)	198.88	2.158–17235.48	**0.022**
mFS (3-4)	1.562	0.035–69.274	0.818
SEBES (3-4)	5.826	0.133–254.59	0.36
CSF-ApoC3 (>4,463 ng/mL)	132.29	3.08–5,673.96	**0.011**
Hydrocephalus	32.07	1.25–820.85	**0.036**

Bold values indicates the p-value that less than 0.05.

ApoC3 for mRS outcomes was assessed by ROC curve analysis, with optimal cutoff points determined by the Youden index. Statistical analyses were conducted using GraphPad Prism 8.2.1 (GraphPad Software, San Diego, CA, USA) and SPSS 23.0 (IBM, Armonk, NY, USA). A p-value <0.05 was considered statistically significant.

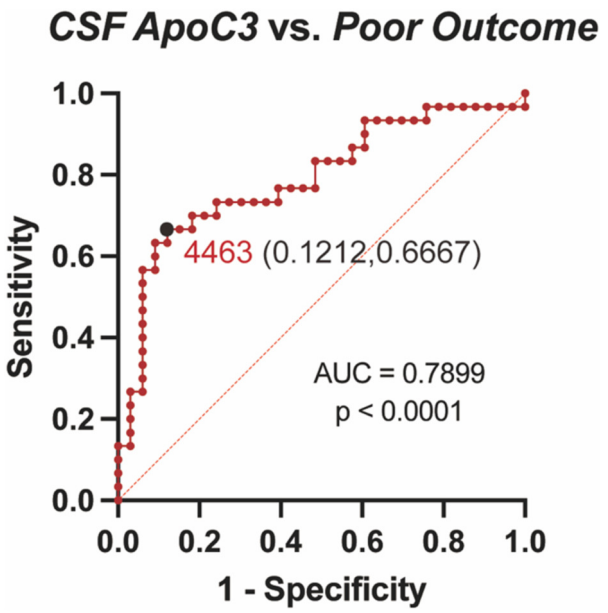

FIGURE 2
ROC curve analysis of CSF ApoC3 levels predicting poor outcomes (mRS scores 3–6) at 3 months. The results indicate that ApoC3 has strong predictive value for patient outcomes at 3 months (AUC = 0.7899, 95% CI 0.6739–0.9059). The optimal cutoff value yield a sensitivity of 0.6667 (95% CI 0.4878–0.8077) and a specificity of 0.8788 (95% CI 0.7267–0.9518).

Results

Study population

A total of 63 patients with aSAH were enrolled between June 2021 and March 2023. Of these, 54% were female, with a mean age of 59.7 ± 11.53 years. The median hospital length of stay (LOS) was 12 days (IQR: 10–22 days), and the median neurosurgical intensive care unit (NSICU) stay was 6 days (IQR: 2–18 days). At admission, 61.9% of patients had a Glasgow Coma Scale (GCS) score of 13–15, whereas 20.6% had scores of 3–5. Regarding severity scales, 46% of patients had WFNS grades 3–5, and 44.4% presented with Hunt & Hess grades 3-4. Smoking and hypertension were common comorbidities, observed in 33.3% and 57.1% of patients, respectively. CSF examination showed a median nucleated cell count of 442 × 10^6/L (IQR: 169–1,487) and a median protein level of 128.3 mg/dL (IQR: 69–157.6). The median CSF ApoC3 concentration was 3,149.5 ng/mL (IQR: 1,174.77–7,768.51). Aneurysms most frequently involved the anterior cerebral artery (49.2%), with sizes predominantly between 5.1 and 10 mm (52.4%). Regarding treatment, 66.7% underwent aneurysm clipping, and 33.3% received endovascular coiling. Post-treatment complications included clinical vasospasm in 36.5% and delayed infarction in 42.9% of patients. At 3-month follow-up, 47.6% of patients had poor outcomes (mRS scores 3–6). Detailed demographic and clinical data are presented in Table 1. The demographic characteristics of NPH patients are shown in Supplementary Table 1.

Risk factors for poor outcomes at 3 months after discharge

Univariate analysis showed that several clinical factors significantly correlated with poor outcomes (Table 2). Patients with unfavorable outcomes had significantly longer hospital (p = 0.002) and NSICU (p < 0.001) stays. Poor outcomes were also associated with advanced age (p = 0.022) and higher admission systolic blood pressure (p = 0.037). Patients with lower admission GCS scores (3–5) had significantly worse outcomes (p < 0.001). Higher WFNS grades (p < 0.001) and Hunt & Hess grades (p < 0.001) were also strongly linked to poor outcomes. Among CSF parameters, elevated ApoC3 levels (p < 0.001), increased protein levels (p = 0.017), and abnormal chloride (Cl-) concentrations (p = 0.001) were significantly associated with unfavorable outcomes. Severity scores, including mFS, SEBES, and mGS, were strongly predictive of poor prognosis (all p < 0.001). Complications such as clinical vasospasm (p = 0.002), delayed infarction (p < 0.001), and hydrocephalus (p < 0.001) were significantly more frequent among patients with poor outcomes. The Shapiro-Wilk test p-values for key continuous variables are present in Supplementary Table 2.

CSF ApoC3 as an indicator of clinical severity in aSAH patients

CSF ApoC3 concentrations were compared between 63 aSAH patients and 17 NPH controls (Figure 1A). ApoC3 levels were significantly higher in aSAH patients compared to controls (p < 0.0001). Univariate linear regression analysis indicated significant linear correlations between ApoC3 concentrations and various clinical scores, including WFNS (p = 0.0152, Figure 1B), mFS (p < 0.0001, Figure 1D), and SEBES (p = 0.006, Figure 1E). Higher CSF ApoC3 concentrations correlated significantly with worse GCS (p < 0.01, Figure 1F) and more severe mFS groups (p < 0.05, Figure 1H). Although several clinical scores aren't correlated with ApoC3 concentration (Figure 1C,G,I). To control

TABLE 4 Univariate analysis of different ApoC3 concentration groups and aSAH clinical features.

Variable		CSF-ApoC3		
		Low group ≤4,463 ng/mL	High group >4,463 ng/mL	*p*-value
Hospital LOS, d		12 (10–18)	17.5 (9.25–31.75)	0.31
Sex (F)		21 (53.8)	13 (54.2)	1
Age, y		59.23 ± 10.7	60.46 ± 12.96	0.685
Systolic blood pressure, mmHg		150 (133–163)	149 (139.5–192.25)	0.388
Systolic blood pressure >190		5 (12.8)	6 (25)	0.307
Admission GCS	13–15	30 (76.9)	9 (37.5)	**0.001**
	6–12	6 (15.4)	5 (20.8)	
	3–5	3 (7.7)	10 (41.7)	
WFNS grade (3-5)		12 (30.8)	17 (70.8)	**0.004**
Hunt & hess grade (3-4)		14 (35.9)	14 (58.3)	**0.118**
NSICU LOS, d		4 (2–11)	10.5 (5–23.5)	**0.018**
Duration of mechanical ventilation, d		2 (1–9)	7.5 (4–23.5)	**0.021**
Drinking		14 (35.9)	6 (25)	0.416
Smoking		14 (35.9)	7 (29.2)	0.784
Hypertension		25 (64.1)	11 (45.8)	0.194
Diabetes		3 (7.7)	1 (4.2)	0.657
BMI	<18.5	3 (7.7)	1 (4.2)	0.447
	<24	22 (56.4)	10 (41.7)	
	<28	13 (33.3)	11 (45.8)	
	≥28	1 (2.6)	2 (8.3)	
CSF examination	RBC, 10^6/L	50,000 (22,750–126000)	101,904 (58,000–101904)	0.207
	Lymphocytes, %	28 (13–39)	29.26 (11.5–37.5)	0.481
	Nucleated cells, 10^6/L	380 (130–2,364)	897.5 (210–1,486.6)	0.932
	Glucose, mmol/L	3.62 (2.59–4.03)	4.00 (3.62–5.62)	**0.016**
	Protein level, mg/dL	93.8 (48.7–157.6)	135.05 (98.78–177.28)	**0.033**
	Cl^-, mmol/L	128 (124.4–130.7)	129.55 (129.55–135.55)	**0.009**
mFS (3-4)		20 (51.3)	21 (87.5)	**0.006**
SEBES (3-4)		25 (64.1)	21 (87.5)	0.078
IVH		24 (61.5)	20 (83.3)	0.067
mGS		2 (0–4)	7 (1.25–18.25)	**0.006**
Aneurysm Location	Internal carotid artery	3 (7.7)	2 (8.3)	0.449
	Anterior cerebral artery	22 (56.4)	9 (37.5)	
	Middle cerebral artery	5 (12.8)	6 (25)	
	Posterior circulation	9 (23.1)	7 (29.2)	

(*Continued*)

TABLE 4 Continued

Variable		CSF-ApoC3		
		Low group ≤4,463 ng/mL	High group >4,463 ng/mL	*p*-value
Aneurysm size	1–5 mm	16 (41)	8 (33.3)	0.802
	5.1–10 mm	19 (48.7)	14 (58.3)	
	Greater than 10 mm	4 (10.3)	2 (8.3)	
Coiling		12 (30.8)	9 (37.5)	0.784
Clipping		27 (69.2)	15 (62.5)	0.784
Decompression		3 (7.7)	8 (33.3)	**0.015**
LD		29 (74.4)	14 (58.3)	0.265
EVD		9 (23.1)	6 (25)	1
Clinical vasospasm		12 (30.8)	11 (45.8)	0.285
Delayed infarction		10 (25.6)	17 (70.8)	**0.001**
Hydrocephalus		8 (20.5)	13 (54.2)	**0.012**
3-month mRS (3–6)		10 (25.6)	20 (83.3)	**<0.001**

Bold values indicates the p-value that less than 0.05.

for confounding factors and assess ApoC3 as an independent predictor of prognosis, multivariable logistic regression was performed, including ApoC3, age, WFNS score, Fisher score, and hydrocephalus (Table 3). The results indicated that elevated CSF ApoC3 levels were independently correlated with poor 3-month outcomes.

CSF ApoC3 is associated with the outcome of aSAH patients

ROC curve analysis was performed to evaluate the predictive ability of CSF ApoC3 concentrations for 3-month outcomes (Figure 2). The results demonstrated that ApoC3 levels effectively predicted poor outcomes (AUC = 0.7899, 95% CI: 0.6739–0.9059). The optimal cutoff value, determined by the Youden index, was 4,463 ng/mL, with a sensitivity of 0.6667 (95% CI: 0.4878–0.8077) and specificity of 0.8788 (95% CI: 0.7267–0.9518).

Subsequently, the optimal cutoff (4,463 ng/mL) was used to classify 63 aSAH patients into high ApoC3 and low ApoC3 groups. Univariate analysis of clinical factors between these groups is presented in Table 4.

Patients in the high ApoC3 group exhibited significantly worse clinical scores upon admission. Specifically, they showed lower GCS scores ($p = 0.001$), higher WFNS grades ($p = 0.004$), higher mFS scores ($p = 0.006$), and higher mGS scores ($p = 0.006$). Moreover, patients with elevated ApoC3 experienced significantly longer NSICU stays ($p = 0.018$) and longer durations of mechanical ventilation ($p = 0.021$). Regarding surgical interventions, no significant differences existed between the two groups in the rates of coiling, clipping, or LD/EVD drainage. However, patients undergoing decompression were significantly more likely to have elevated ApoC3 ($p = 0.015$). CSF analysis revealed significantly increased glucose, protein, and Cl^- levels in the high ApoC3 group. Notably, the high ApoC3 group exhibited significantly worse 3-month functional outcomes ($p < 0.001$). Additionally, complications such as delayed infarction ($p = 0.001$) and hydrocephalus ($p = 0.012$) occurred significantly more often in the high ApoC3 group.

aSAH patients with elevated ApoC3 experienced worse outcomes at discharge and three months

Three months post-discharge, the proportion of patients with poor outcomes (mRS 3–6) decreased from 96.9% at discharge to 47.6% at 3 months (Figure 3A). However, patients in the high ApoC3 group (CSF ApoC3 >4,463 ng/mL) had consistently poor mRS scores at discharge, with 100% scoring 3–6 (Figure 3B). Even after 3 months of rehabilitation, poor outcomes remained prevalent (83.3%) in the high ApoC3 group, while decreasing to 25.6% in the low ApoC3 group (Figure 3C).

Discussion

In this study, experimental and clinical data demonstrated that among CSF parameters, elevated ApoC3 levels were significantly associated with adverse prognosis and an increased risk of complications. Using an optimal cutoff value of 4,463 ng/mL, patients in the high ApoC3 group exhibited significantly worse functional outcomes at 3 months ($p < 0.001$) and experienced more complications, particularly delayed infarction ($p = 0.001$) and hydrocephalus ($p = 0.012$). Therefore, promptly monitoring CSF ApoC3 levels and taking appropriate preventive and therapeutic measures may enhance outcomes for patients with aSAH.

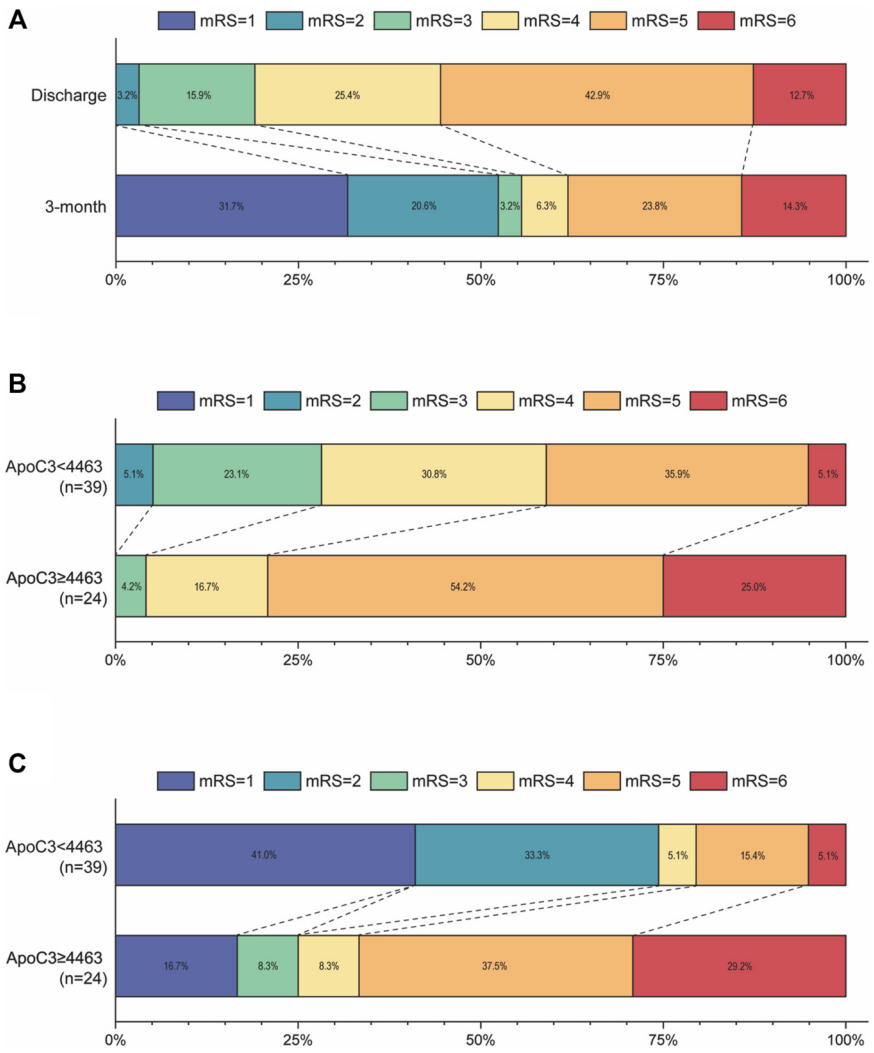

FIGURE 3
Stacked bar charts illustrating outcomes of aSAH patients based on mRS scores at discharge and at 3 months. **(A)** Distribution of mRS scores among 63 aSAH patients at discharge and at 3 months. **(B)** Percentage distribution of mRS scores at discharge among aSAH patients stratified by ApoC3 levels. **(C)** Percentage distribution of mRS scores at 3 months among aSAH patients stratified by ApoC3 levels.

It has long been recognized that lipid metabolism is associated with the formation and rupture of intracranial aneurysms, contributing to aSAH [10–13]. Several studies have indicated that blood lipid levels are significant predictors of prognosis in patients with aSAH15. ApoC3, a glycoprotein primarily synthesized in the liver, is a crucial regulator of TRL metabolism [11]. ApoC3 is a glycoprotein primarily synthesized in the liver and serves as a key regulator of TRL metabolism. Previous studies have demonstrated that ApoC3 is significantly involved in the pathogenesis, progression, and prognosis of vascular diseases. For instance, loss-of-function mutations in ApoC3 can decrease the risk of atherosclerotic cardiovascular disease by approximately 40% and protect against coronary heart disease, consequently increasing longevity [14]. However, the relationship between ApoC3 and aSAH remains unclear.

In our study, we found that CSF ApoC3 levels in aSAH patients were significantly negatively correlated with clinical scores, including the WFNS score ($p = 0.0152$), mFS ($p < 0.0001$), and SEBES score ($p = 0.006$), indicating that elevated CSF ApoC3 may reflect more severe clinical symptoms in patients with aSAH. Moreover, univariate analysis of various clinical factors confirmed that CSF ApoC3 levels above 4,463 ng/mL effectively predicted poor 3-month outcomes after discharge, yielding an area under the curve (AUC) of 0.7899. Our findings are consistent with previous studies indicating that elevated blood lipid levels predict adverse outcomes in aSAH patients [11].

Future directions

The negative correlation observed between elevated CSF ApoC3 levels and poor prognosis may be related to inflammation, oxidative stress, and dysregulated lipid ratios. Previous studies have demonstrated that ApoC3 mediates NLRP3 inflammasome activation in human monocytes and induces reactive oxygen species production via caspase-8 activation and Toll-like receptor (TLR) 2 and 4 dimerization, processes that impede endothelial regeneration and promote kidney injury [15], and previous study

has shown that elevated inflammatory level in the CSF are associated with the development of complication following SAH [16]. Thus, elevated CSF ApoC3 may exacerbate inflammatory responses and oxidative stress, thereby aggravating brain injury in aSAH patients. Additionally, ApoC3 accumulates in circulating blood and performs an essential function in TRL metabolism. Elevated CSF ApoC3 may suggest increased penetration of peripheral substances into the brain, contributing to more severe pathology. Changes in lipid ratios associated with elevated CSF ApoC3 levels may also contribute to secondary injury following SAH [10].

Moreover, it is recognized that lipid metabolites in CSF are associated with the risk, complications, and outcomes in patients with aSAH. Levels of lipid peroxides are positively correlated with an increased incidence of symptomatic vasospasm [17]. Total cholesterol levels negatively correlate with the risk of delayed infarction and mortality in aSAH patients [18]. Elevated CSF ApoC3 may increase the prevalence of complications (particularly delayed infarction and hydrocephalus) in aSAH patients by altering lipid metabolism, leading to vasospasm, neuroinflammation, blood-brain barrier (BBB) disruption, and endothelial fragility [18–21]. Collectively, these mechanisms may explain how elevated CSF ApoC3 worsens clinical outcomes in aSAH patients.

Increased ApoC3 may originate from circulating blood, with ApoC3 levels rising in parallel with total protein or albumin quotients, reflecting the extent of BBB disruption. Regardless of whether ApoC3 is synthesized in the brain or derived from peripheral circulation, the clear correlation between ApoC3 levels and the prognosis of aSAH patients supports its utility as a valuable marker for clinical decision-making. In addition, considering that hydrocephalus and cerebral edema are crucial indicators for evaluating aSAH patients [16], we selected NPH patients with hydrocephalus and normal CSF composition as the control group. It should be noted that NPH patients might exhibit abnormal CSF dynamics. However, due to ethical constraints, obtaining CSF from healthy individuals is not feasible; thus, CSF form NPH patients is currently the most suitable control in clinical practice without increasing patient burden. And CSF sample from NPH patients is chosen as the standard control group in aSAH research [22].

Conclusion

This study indicates that ApoC3 may serve as a potential biomarker for predicting DCI and hydrocephalus. With an AUC of 0.7899 and an optimal cutoff value of 4,463 ng/mL, measuring CSF ApoC3 levels during the acute stage of aSAH could help clinicians determine the timing and type of preventive and therapeutic interventions, thereby potentially reducing complication rates and improving patient outcomes. However, given the limited sample size and coarse sampling time, further validation through larger sample sizes, continuous monitoring ApoC3 level in CSF, and multicenter studies is necessary before clinical application.

Author contributions

XC had full access to all the data in the study and takes responsibility for the integrity of the data and the accuracy of the data analysis. Funding acquisition, Methodology, Software, Investigation, Formal analysis, Data curation: BT; Software, Validation, Formal analysis, Resources: JW; Validation, Investigation: JC; Data curation, Writing – original draft: QZ; Visualization: ZX; Writing – review and editing: KY; Conceptualization, Methodology, Project administration: XC. All authors contributed to the article and approved the submitted version.

Data availability

The datasets for this article are not publicly available due to concerns regarding patient anonymity. Requests to access the datasets should be directed to the corresponding author.

Ethics statement

This study was conducted according to the guidelines of the Declaration of Helsinki and approved by the Institutional Review Board of the Second Affiliated Hospital of Zhejiang University (Approval No. 2023-059).

Funding

The author(s) declared that financial support was received for this work and/or its publication. This research was funded by General Program of Medical and Pharmaceutical Science and Technology Projects by Zhejiang Provincial Health Commission, grant number 2021KY031.

Conflict of interest

The author(s) declared no potential conflicts of interest with respect to the research, authorship, and/or publication of this article.

Generative AI statement

The author(s) declared that generative AI was not used in the creation of this manuscript.

Any alternative text (alt text) provided alongside figures in this article has been generated by Frontiers with the support of artificial intelligence and reasonable efforts have been made to ensure accuracy, including review by the authors wherever possible. If you identify any issues, please contact us.

Supplementary material

The Supplementary Material for this article can be found online at: https://www.ebm-journal.org/articles/10.3389/ebm.2026.10827/full#supplementary-material

References

1. Collaborators GS. Global, regional, and national burden of stroke and its risk factors, 1990-2019: a systematic analysis for the global burden of disease study 2019. *Lancet Neurol* (2021) 20:795–820. doi:10.1016/s1474-4422(21)00252-0

2. Hop JW, Rinkel GJ, Algra A, van Gijn J. Case-fatality rates and functional outcome after subarachnoid hemorrhage: a systematic review. *Stroke* (1997) 28:660–4. doi:10.1161/01.str.28.3.660

3. Tawk RG, Hasan TF, D'Souza CE, Peel JB, Freeman WD. Diagnosis and treatment of unruptured intracranial aneurysms and aneurysmal subarachnoid hemorrhage. *Mayo Clinic Proceedings* (2021) 96:1970–2000. doi:10.1016/j.mayocp.2021.01.005

4. Cahill J, Calvert JW, Zhang JH. Mechanisms of early brain injury after subarachnoid hemorrhage. *J Cereb Blood Flow Metab* (2006) 26:1341–53. doi:10.1038/sj.jcbfm.9600283

5. Lauzier DC, Jayaraman K, Yuan JY, Diwan D, Vellimana AK, Osbun JW, et al. Early brain injury after subarachnoid hemorrhage: incidence and mechanisms. *Stroke* (2023) 54:1426–40. doi:10.1161/strokeaha.122.040072

6. Norata GD, Tsimikas S, Pirillo A, Catapano AL. Apolipoprotein C-III: from pathophysiology to pharmacology. *Trends Pharmacol Sci* (2015) 36:675–87. doi:10.1016/j.tips.2015.07.001

7. Kawakami A, Aikawa M, Alcaide P, Luscinskas FW, Libby P, Sacks FM. Apolipoprotein CIII induces expression of vascular cell adhesion molecule-1 in vascular endothelial cells and increases adhesion of monocytic cells. *Circulation* (2006) 114:681–7. doi:10.1161/circulationaha.106.622514

8. Pegoli M, Mandrekar J, Rabinstein AA, Lanzino G. Predictors of excellent functional outcome in aneurysmal subarachnoid hemorrhage. *J Neurosurgery* (2015) 122:414–8. doi:10.3171/2014.10.JNS14290

9. Yalcin A, Akkus T, Tezcan A, Usta B, Yalcin R, Simsek F, et al. Diagnostic performance of Black tent sign on 3D T2 SPACE in the diagnosis of idiopathic normal-pressure hydrocephalus. *Jpn J Radiol* (2025) 43:1090–6. doi:10.1007/s11604-025-01757-x

10. Yang BSK, Blackburn SL, Lorenzi PL, Choi HA, Gusdon AM. Metabolomic and lipidomic pathways in aneurysmal subarachnoid hemorrhage. *Neurotherapeutics* (2024) 22:e00504. doi:10.1016/j.neurot.2024.e00504

11. Yajun Z, Diqing O, Xingwei L, Liuyang T, Xiaofeng Z, Xiaoguo L, et al. High levels of blood lipid and glucose predict adverse prognosis in patients with aneurysmal subarachnoid hemorrhage. *Heliyon* (2024) 10:e38601. doi:10.1016/j.heliyon.2024.e38601

12. Pan T, Shi Y, Yu G, Mamtimin A, Zhu W. Intracranial aneurysms and lipid metabolism disorders: from molecular mechanisms to clinical implications. *Biomolecules* (2023) 13:1652. doi:10.3390/biom13111652

13. Can A, Castro VM, Dligach D, Finan S, Yu S, Gainer V, et al. Lipid-lowering agents and high HDL (High-Density lipoprotein) are inversely associated with intracranial aneurysm rupture. *Stroke* (2018) 49:1148–54. doi:10.1161/strokeaha.117.019972

14. Ballantyne CM, Vasas S, Azizad M, Clifton P, Rosenson RS, Chang T, et al. Plozasiran, an RNA interference agent targeting APOC3, for mixed hyperlipidemia. *N Engl J Med* (2024) 391:899–912. doi:10.1056/NEJMoa2404143

15. Zewinger S, Reiser J, Jankowski V, Alansary D, Hahm E, Triem S, et al. Apolipoprotein C3 induces inflammation and organ damage by alternative inflammasome activation. *Nat Immunol* (2020) 21:30–41. doi:10.1038/s41590-019-0548-1

16. Fang Y, Liu Y, Chen L, Wang J, Zhang J, Zhang H, et al. Cerebrospinal fluid markers of neuroinflammation and coagulation in severe cerebral edema and chronic hydrocephalus after subarachnoid hemorrhage: a prospective study. *J Neuroinflammation* (2024) 21:237. doi:10.1186/s12974-024-03236-y

17. Kang J, Tian S, Zhang L, Yang G. Ferroptosis in early brain injury after subarachnoid hemorrhage: review of literature. *Chin Neurosurg J* (2024) 10:6. doi:10.1186/s41016-024-00357-4

18. Kirkpatrick PJ, Turner CL, Smith C, Hutchinson PJ, Murray GD, STASH Collaborators. Simvastatin in aneurysmal subarachnoid haemorrhage (STASH): a multicentre randomised phase 3 trial. *Lancet Neurol* (2014) 13:666–75. doi:10.1016/s1474-4422(14)70084-5

19. Spiegel S, Milstien S. The outs and the ins of sphingosine-1-phosphate in immunity. *Nat Rev Immunol* (2011) 11:403–15. doi:10.1038/nri2974

20. Altay O, Suzuki H, Hasegawa Y, Ostrowski RP, Tang J, Zhang JH. Isoflurane on brain inflammation. *Neurobiol Dis* (2014) 62:365–71. doi:10.1016/j.nbd.2013.09.016

21. Tseng MY, Czosnyka M, Richards H, Pickard JD, Kirkpatrick PJ. Effects of acute treatment with pravastatin on cerebral vasospasm, autoregulation, and delayed ischemic deficits after aneurysmal subarachnoid hemorrhage: a phase II randomized placebo-controlled trial. *Stroke* (2005) 36:1627–32. doi:10.1161/01.STR.0000176743.67564.5d

22. Magid-Bernstein J, Yan J, Herman AL, He Z, Johnson CW, Beatty H, et al. Early CSF inflammatory markers after aneurysmal subarachnoid hemorrhage and their relationship to disease severity and shunt placement. *J Stroke Cerebrovasc Dis* (2025) 34:108395. doi:10.1016/j.jstrokecerebrovasdis.2025.108395

EBM Experimental Biology and Medicine

TYPE Original Research
PUBLISHED 12 March 2026
DOI 10.3389/ebm.2026.10679

OPEN ACCESS

*CORRESPONDENCE
Fadi T. Khasawneh,
fkhasawneh@tamu.edu

RECEIVED 22 May 2025
REVISED 06 February 2026
ACCEPTED 16 February 2026
PUBLISHED 12 March 2026

CITATION
Badejo PO, Alarabi AB, Ali HEA, Millican L, De La Paz R, Umphres SS, Kamal S, Alshbool FZ and Khasawneh FT (2026) Low dose thirdhand smoke exposure enhances platelet functional responses in mice.
Exp. Biol. Med. 251:10679.
doi: 10.3389/ebm.2026.10679

Low dose thirdhand smoke exposure enhances platelet functional responses in mice

Precious O. Badejo[1], Ahmed B. Alarabi[1], Hamdy E. A. Ali[1], Lanam Millican[2], Reina De La Paz[2], Shelby S. Umphres[1], Sadia Kamal[1], Fatima Z. Alshbool[3] and Fadi T. Khasawneh[1]*

[1]Department of Pharmaceutical Sciences, Irma Lerma Rangel College of Pharmacy, Texas A&M University, Kingsville, TX, United States, [2]Irma Lerma Rangel College of Pharmacy, Texas A&M University, Kingsville, TX, United States, [3]Department of Pharmacy Practice, Irma Lerma Rangel College of Pharmacy, Texas A&M University, Kingsville, TX, United States

Abstract

Although cigarette smoking is the most preventable cause of cardiovascular diseases, most researchers have focused on either direct/firsthand or secondhand smoke exposures. Recently though, attention has shifted to an emerging/indirect exposure trend-known as thirdhand smoke (THS)- which was previously "overlooked." This phenomenon, which was/is thought to be harmless, has been identified as a serious health risk, including in the context of thrombogenesis/platelets. However, whether low dose THS exposure has the capacity to modulate platelets has not been investigated. Two sets of household materials were exposed to 20 cigarettes/day for a week on an alternating basis, with controls exposed to clean air. After the first set of exposed materials is placed in mice cages, exposure of the second set is initiated. The materials were interchanged weekly, for a total exposure duration of 1 month. Mice were then subjected to multiple platelet function assays. THS exposed mice exhibited shortened tail bleeding and occlusion times, indicating a prothrombotic phenotype. Moreover, we also observed that platelets from the exposed mice exhibited an enhanced aggregation response. However, we did not observe any gender differences in our *in vivo* as well as aggregation experiments; hence, subsequent characterization was carried out on male mice. It was also found that dense granules release, integrin activation, and PS exposure were also potentiated in the exposed platelets compared to the controls. Finally, we observed for the first time that the tobacco-specific nitrosamine and THS toxicant NNK enhanced platelet aggregation and thrombus formation. Collectively, we provide documentation that low dose of THS exposure is detrimental to health by increasing the risk of thrombosis through a hyperactive platelet phenotype that involves the toxicant NNK.

KEYWORDS

cardiovascular disease, novel tobacco exposure, platelets, thirdhand smoke, thrombosis

Impact statement

We document for the very first time that exposure to THS, even under low dose conditions, could modulate platelets hemostatic responses, thereby promoting a thrombogenic phenotype in exposed mice. This suggests that even a relatively short and small amount of exposure can be extremely harmful, which is alarming for susceptible populations who are mostly unaware when exposed. Importantly, THS phenomenon-albeit indirect-is viewed as harmless with little/no attention paid to it. Our work also highlights the impact that this preventable risk factor has on the leading cause of death worldwide, namely cardiovascular disease. Bearing in mind that mice tobacco studies have been shown to "map" very well with humans, we believe that our studies should serve as a guide for future research, public enlightenment and policy guidance. We aim to educate the public on these health risks which could lead to reduced disease states and mortality caused from smoking.

Introduction

Cigarette smoking, which remains the single most preventable cause of death globally, accounts for approximately 10 years reduction in the life expectancy of smokers when compared to non-smokers [1]. In fact, in 2019, a report by the World Health Organization (WHO) revealed that tobacco products kill about 50% of users, which accounted for more than 8 million deaths annually [2]. Among these, 7 million died because of direct exposure or firsthand smoke (FHS), while 1.2 million deaths were attributed to secondhand smoke (SHS) [2]. Additionally, a more recent report from the National Health Interview Survey (NHIS) in 2021 revealed that 46 million US adults were current tobacco users with the highest percentage using traditional cigarettes [3]. Smoking is associated with a range of cardiovascular diseases (CVDs), including heart failure, and atherosclerosis [4–6]. Additionally, multiple studies documented that cigarette smoking could modulate platelet reactivity, resulting in thrombotic episodes [7]. To this end, the toxicant profile of the smoke of cigarettes-which is responsible for the cigarette smoke-associated disease phenotypes-involves over 7,000 toxicants, including nicotine, carbon monoxide and tar. These, amongst potentially other toxicants, contribute to the pathogenesis of CVDs by inducing inflammation, endothelial dysfunction, and thrombus formation [8, 9]. As such, there is growing interest in investigating the contribution of other tobacco/THS toxicants to the thrombosis phenotype, such as tobacco-specific nitrosamines, including NNK [(4-(methylnitrosamino)-1-(3-pyridyl)-1-butanone]. Indeed, our findings indicate that NNK could enhance platelet reactivity and thus might contribute to the prothrombotic impact of third-hand smoke exposures.

In this connection, "third hand smoke" (THS), which is an emerging health risk, has been a topic of interest and continues to be studied by several research groups, not only in the USA, but also worldwide. THS is defined as tobacco smoke residues and contaminants that may linger on smokers' clothing, skin, and hair as well as carpets, curtains long after exposure to SHS [10, 11]. THS is difficult to eliminate and can remain embedded in indoor environments—such as homes and vehicles—for months after smoking has ceased [12, 13]. To this end, a number of reports confirmed significant levels of THS are present in the cars and residence of non-smokers whose houses were previously occupied by smokers [12–14]. Consequently, THS has been established as playing a significant part in exposure of non-smokers to tobacco products, even many years after smoking cessation in homes of smokers [15]. This is attributed, at least in part, to the fact that exposure to THS creates secondary toxins that remain "indoors", even when doors and windows are opened to eliminate the "stench" [11, 16]. Additionally, the concentration of these toxins continues to increase in the blood, gradually over time, which further increases the dangers of THS to health due to this continuous exposure [17]. This theory was first described at a Children's hospital located in Boston in 2009 [18]. Indeed, recent data points to the fact that THS can impair development, cause cytotoxicity, as well as DNA damage, which increases the risk of cancer, in mice [19].

With regards to sex differences in cigarette use, men generally use tobacco products more than women, with about 942 million men reportedly smoking globally relative to 175 million women. Although smoking has been dominated by men for decades, the rate of cigarette usage has escalated among women. According to a WHO report on prevalence/future tobacco use from 2000–2025, the rate of use was highest among European women (19%) globally. Even with the decline in smoking worldwide, it is projected that in 2025, the prevalence in women who smoke would be 18%, which is quite worrisome. An interesting body of evidence revealed that smoking affects men and women differentially in the context of CVD and lung diseases, with the risk of lung cancer found to be elevated in women more than in men [20]. Regarding CVDs, cigarette smoking significantly increased risk of coronary artery disease by 25% in women as compared to men [21]. However, these reports were based on direct cigarette exposure. To this end, we have previously documented that *in utero*, as well as long-, and short-term exposure to THS increases the risk of thrombosis [22–24]. Regarding *in utero* THS, our previous study revealed sex-related differences in integrin activation, dense and α-granules secretions, as well as PS exposure, whereas no difference were observed in bleeding and occlusion times. Moreover, sex differences were also observed in our THS 3-month study in which we used 40 cigarettes/day exposure protocol [24]. Additionally, our very recent study showed that even when the exposure to 40 cigarettes/day is for 1 month, THS can still exert occlusive effects [25]. In that study, our findings

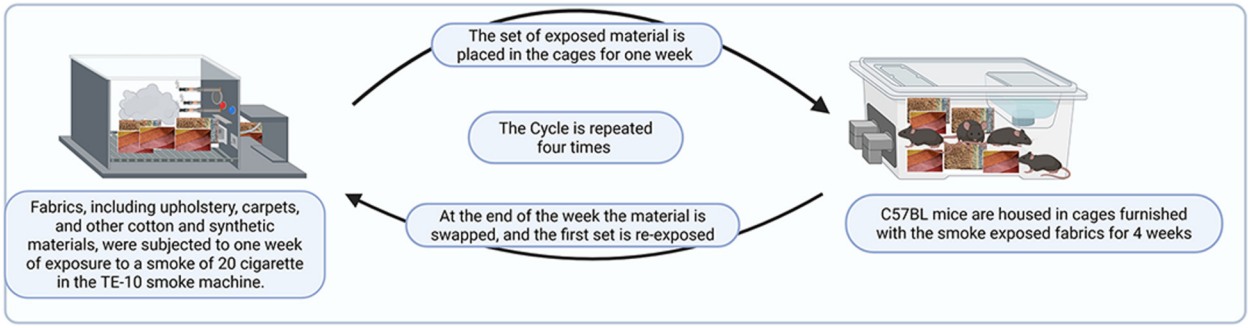

FIGURE 1
Illustration of the THS exposure protocol.

show a shortened bleeding and occlusion times in the exposed male and female mice, which was more striking in the females. However, whether these effects manifest under low "cigarette dose" experimental settings are yet to be determined.

Based on these considerations, we sought to investigate the effects of low dose THS, namely 20 cigarettes/day, on platelet reactivity and thrombus formation, in a sex-dependent manner under short term/1 month exposure settings [24].

Materials and methods

Thirdhand smoke (THS) exposure protocol

Mice were randomly divided into 2 groups and exposed to either THS or clean air as previously described [22]. Materials, which included upholstery (12in × 3.5in), cotton (7.5in × 5.5in), and square-sized carpets (2in × 2in), were exposed to cigarette smoke by being placed in the smoking machine. The exposure duration was for 1 month (4 weeks), using low dose/20 cigarettes/day for 1 week, and involved two sets of material, such that the exposure of the second set is initiated at the same time the first one is placed into the cages (after 1 week) to start the exposure. At the end of the 1 week of exposure, the material is swapped, and the first set is re-exposed, and this cycle is repeated (please see Figure 1 for an illustration of the exposure protocol). In other words, employing two sets of material that were exposed on an alternating-week basis ensures that mice are constantly exposed to THS or clean air. Of note, mice were exposed starting at 6 weeks of age, and the exposure was conducted on each sex separately.

Reagents and materials

Thrombin and stir bars were purchased from Chronolog Corporation (Havertown, PA), whereas adenosine diphosphate (ADP), Avertine [(2,2,2-Tribromoethanol) and ferric chloride] were from Sigma Aldrich (St Louis, MO). The antibody for P-Selectin (Fluorescein isothiocyanate/FITC-conjugated P-selectin) was purchased from Cell Signaling Technology, Inc. (Danvers, MA), phycoerythrin-conjugated GPIIb-IIIa (αIIbβ3) antibody was from Emfret Analytics (Würzburg, Germany) and Annexin V (Phosphatidylserine PS) antibody was purchased from BD BioSciences (Franklin Lakes, NJ). The cotinine enzyme-linked immunosorbent assay (ELISA) kit was purchased from Calbiotech (El Cajon, CA). NNK was purchased from MedChemExpress (Monmouth Junction, NJ).

Animals

C57BL/6J (6-week-old male) mice were purchased from the Jackson Laboratory (Bar Harbor, ME) and housed 5 mice per cage under 12/12 light/dark cycles. Each cage had uninterrupted access to water and food except when mice were being exposed. All protocols were approved by the Institutional Animal Care and Use Committee of Texas A&M University, College Station.

Cotinine assay

To ensure that our THS exposure protocol systemically and effectively exposes mice to THS toxicants, we measured the serum levels of cotinine, a metabolite of nicotine, in both the THS and clean air–exposed mice, using the Cotinine Direct ELISA kit as per the manufacturer's instructions.

Tail bleeding time

The tail bleeding time assay was carried out as we described in another report [26]. Briefly, mice exposed to either THS or

clean air for 1 month were anesthetized using 2.5% isoflurane. The tail of each mouse was cut 5 mm from the tip using a sterile scalpel and placed in 37 °C saline solution and the bleeding time was recorded until the bleeding stopped.

In vivo $FeCl_3$ carotid artery injury–induced thrombosis model

The *in vivo* thrombosis model was performed as described previously [26]. Thus, both THS and clean air–exposed mice were anesthetized with avertin, and the left carotid artery was isolated. Thereafter, 1 μL of 7.5% ferric chloride was applied to a 1 mm in diameter filter paper disc, which was immediately placed on top of the artery for 3 min. The Transonic Micro flow probe was used to establish the occlusion time.

Mouse platelet rich plasma (PRP) preparation

Blood was collected from the heart of each mouse after anesthesia using 0.38% w/v sodium citrate solution as the anti-coagulant (Fisher Scientific, Hampton, NH). The pooled blood sample for each group was centrifuged at 180 g for 11 min, and the supernatant was harvested (platelet-rich plasma; PRP). Platelets were counted with the HEMAVET 950FS Multi-species Hematology System before each experiment.

Human blood and platelet rich plasma (PRP) preparation

Blood samples were obtained from healthy adult volunteers/donors (3 males, age range between 24 and 48 years) after approval by the Institutional Review Board at Texas A&M University (IRB Reference Number: IRB2020-0385D). Informed consent was provided by all participants prior to phlebotomy. Venous blood (3–10 mL) was collected into tubes containing either citrate-phosphate-dextrose (1:9 v/v) or Benzylsulfonyl-D-Arg-Pro-4-amidinobenzylamide (BAPA) as the anticoagulant. For PRP preparation, blood from each donor was centrifuged at 180 g for 11 min, and the supernatant was harvested (PRP). Platelets were counted with the HEMAVET 950FS Multi-species Hematology System and counts adjusted before each experiment.

Mouse washed platelet preparation

Blood was collected from each mouse as described above. Equal amounts of blood were mixed with modified HEPES Tyrodes buffer of pH 7.4 in a 2 mL Eppendorf tube. This mixture was centrifuged at 180 × g for 7 min at room temperature. PRP was recovered and centrifuged a second time at 400 × g for 10 min at room temperature. The recovered pellets were resuspended in 1 mL of HEPES Tyrodes and centrifuged again at 400 g for 10 min. The washed pellets were resuspended in 1 mL of Tyrodes buffer, before platelets were counted using the HEMAVET 950FS Multi-species Hematology System and adjusted to the concentrations indicated elsewhere.

In vitro platelet aggregation

The PRP from THS-, and clean air–exposed mice was activated with the agonists ADP (1 μM) or thrombin (0.05 U/mL). In a separate set of experiments using human PRP, platelets were activated with ADP (0.25 μM) or thrombin (0.025 U/mL). Aggregation was measured using a model 700 aggregometer with each experiment repeated at least 3 times with blood pooled from at least 5 mice each time.

Dense granule release

PRP was placed in cuvettes at 37 °C, with the aggregometer set at 1,200 rpm, after which 12.5 μL of the luciferase mixture was added. Next, PRP was activated using the agonists ADP (1 μM) or thrombin (0.05 U/mL). Release of ATP was measured using a model 700 aggregometer. Each experiment was repeated at least 3 times with blood pooled from at least 5 mice each time.

Flow cytometric analysis

Briefly, washed platelets from clean air or THS exposed male mice were prepared as described above and 1 μL of 1 mM Ca^{2+} was added to Eppendorf tubes in triplicates for both groups. Afterwards, washed platelets at a concentration of 100,000 platelets/μL was added and incubated with FITC-conjugated CD62P (P-selectin), Annexin V (PS exposure) or JON/A (integrin activation) antibodies at room temperature for 30 min in the dark. Finally, platelets were stimulated with the agonist thrombin (0.5 U/ml) and fluorescent intensities were measured using a BD Accuri C6 flow cytometer. Each experiment was repeated 3 times from pooled blood samples of 5 mice for each group.

Platelet thrombus formation measurement

Platelet thrombus formation under flow conditions was evaluated using the T-TAS01 system (Fujimori Kogyo, Japan)

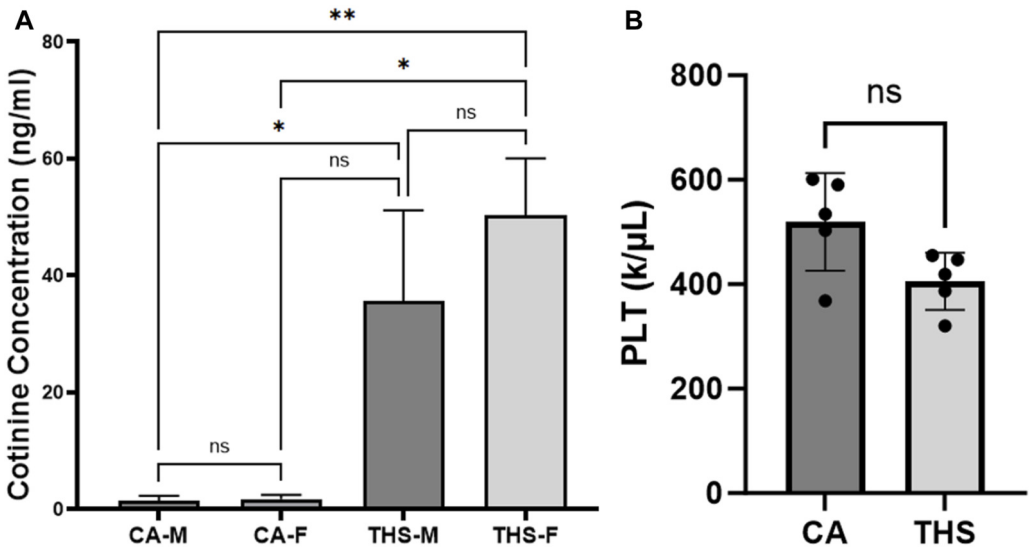

FIGURE 2
Low dose THS exposure results in systemic delivery of nicotine (cotinine) with no impact on platelet counts. **(A)** The concentrations of cotinine were measured in serum from THS and clean air–exposed mice. **(B)** Bar chart of platelet count showing comparison between THS vs. CA. Each bar represents the mean ± SD (**p < 0.01, *p < 0.05, NS: not significant).

as described before [27]. Briefly, 400 μL of whole blood from healthy donors, anticoagulated with 50 μM BAPA, was incubated for 5 min with vehicle Dimethyl sulfoxide (DMSO) or 2 μM NNK. The treated blood was then perfused through PL-chip collagen-coated microchannels at a shear rate of 1,500 s–1. The increase in flow pressure across the microchip was recorded as a measure of platelet thrombus formation, and platelet thrombogenicity was quantified as the area under the flow pressure curve (AUC) over a 10 min period.

Immunoblotting

Washed platelets were prepared before being stimulated with thrombin (0.1 U/mL) for 3 min and lysed in a suitable volume of sample buffer (1×, BioRad). About 15 μg of protein lysates prepared from the clean air- and the THS- exposed groups were resolved onto a 4–20% SDS-PAGE gel (Bio-Rad, Hercules, CA) under reducing conditions. The fractionated proteins were transferred onto nitrocellulose membranes (Bio-Rad, Hercules, CA) and subsequently blocked with 5% bovine serum albumin for 1 h at room temperature. The blocked membranes were incubated overnight at 4 °C with primary antibodies against total/phosphorylated Akt, total/phosphorylated ERK, and β-actin. Total Akt, ERK, and β-actin, were used as an internal protein loading control. The membranes were washed thoroughly and incubated with the proper HRP-conjugated secondary antibodies for 1 h at room temperature and detected using ECL (Thermo Scientific, Rockford, IL). Images were obtained with ChemiDoc MP Imaging System (Bio-Rad, Hercules, CA).

Statistical analysis

All experimental analysis was carried out using GraphPad Prism Version 7. A normality test was performed before each analysis and based on this result, the Mann Whitney test was used to evaluate differences in bleeding and occlusion times; whereas the differences in aggregation and secretion were analyzed using Student's t-test and represented as mean ± SEM. Flow cytometry data was analyzed using one-way ANOVA with Tukey's multiple comparison test as *post hoc*. All sex differences analysis was analyzed using two-way ANOVA with Tukey's multiple comparison test. Statistical significance was fixed at $p < 0.05$ for all analysis.

Results

THS exposure systemically delivers nicotine to exposed mice

Our data showed a significant increase in the level of cotinine in the THS exposed mice in comparison to clean air, in both males and females (Figure 2A). This confirms that our THS exposure model enables the delivery of toxicants, including nicotine to the mice's circulatory system.

TABLE 1 Total blood counts obtained from THS and clean air exposed male and female mice.

Cell type	CA-M	THS-M	P-value	CA-F	THS-F	P-value
Platelets (k/μL)	488.5 ± 28.25	350.8 ± 90.31	0.20	230.3 ± 24.42	268.3 ± 13.38	0.20
MPV (fL)	3.88 ± 0.05	5.00 ± 0.66	0.14	4.29 ± 0.17	4.07 ± 0.05	0.24
RBC (M/μL)	9.61 ± 0.14	9.66 ± 0.21	0.87	8.9 ± 0.33	8.56 ± 0.31	0.50
LY (k/μL)	77.87 ± 1.44	76.88 ± 0.33	0.44	1.94 ± 0.18	2.11 ± 0.36	0.68
MO (k/μL)	4.56 ± 0.90	4.11 ± 0.31	0.65	3.08 ± 0.74	2.75 ± 0.30	0.69
WBC (k/μL)	4.81 ± 0.40	6.82 ± 1.33	0.20	2.30 ± 0.20	2.71 ± 0.47	0.44

Comparison of the levels of cotinine between the exposed male and female mice showed no statistical significance between the two sexes (Figure 2A), which is important when determining sex differences.

THS exposure does not impact blood cell counts in mice

We first examined the total blood counts for the male and female mice and observed no difference in platelets and other blood cells from the THS-exposed and clean air groups (Table 1: data is presented as mean ± SEM; and Figure 2B). Blood cell count was assessed to rule out potential hematological effects that could confound interpretation of platelet functional outcomes. Specifically, alterations in platelet count, platelet size (MPV), or other blood cell populations could independently influence hemostasis and thrombosis, making it essential to confirm that the observed hyperactive platelet phenotype was not secondary to THS-induced changes in circulating cell numbers or bone marrow output [28]. Also, many platelet function assays are impacted by any change (drop) in platelet counts or quality [29]. Blood collected from the heart was analyzed using a Hemavet Hematology Analyzer. Representative data of platelet count comparison between THS vs. CA is shown in a bar chart in Figure 2B.

THS exposure modulates hemostasis in mice

We next sought to determine the effect of our low dose exposure *in vivo* by investigating the hemostasis function of platelets utilizing the tail bleeding time test. As can be seen in Figures 3A,B, there is a significant decrease in the bleeding time in both male and female THS-exposed mice, respectively, in comparison with the clean air-exposed group, suggesting a platelet hyperactive phenotype. For the male group, the average bleeding time for THS-exposed was 79.25 ± 14.28 s, while the clean air exposed was 197.5 ± 14.28 s. For the females, THS-exposed mice had an average bleeding time of 123.1 ± 29.23 s relative to 290.1 ± 60.26 s in those exposed to clean-air. To assess sex differences, we compared the bleeding times between the male and female group. While the average bleeding time was slightly different (shorter in males relatives to females; Figure 3C), it did not reach statistical significance (p value of 0.8431).

THS exposure modulates thrombosis in mice

Given that smoking is the main cause of cardiovascular mortality [8], we sought to investigate if our mice were prone to thrombosis by carrying out the ferric chloride carotid artery thrombosis model. Figures 4A,B show a reduction in the occlusion times of THS-exposed male and female mice as compared to clean air controls, respectively. For the male group, the average occlusion time for THS-exposed was 133.7 ± 23.56 s, while the clean air exposed was 305.8 ± 59.47 s. In terms of the females, THS-exposed mice had an average occlusion time of 164.6 ± 41.97 s, compared to an occlusion time of 332.6 ± 52.07 s in the clean-air exposed group. We also compared the occlusion times between the male and female group (Figure 4C) but did not observe any differences (p = 0.9671).

THS exposure modulates in vitro platelet aggregation and dense granule secretion in mice

To determine if our THS low dose exposure would affect platelet function *in vitro*, we studied its effect on platelet functional responses, starting with platelet aggregation, which is the gold standard for assessing platelet function [30]. Our results show enhanced aggregation in the THS-exposed mice, in both males and females, in comparison to the clean air-exposed when platelets were stimulated with the agonists ADP (Figures 5A,B) and thrombin (Figures 5C,D); with data quantification for

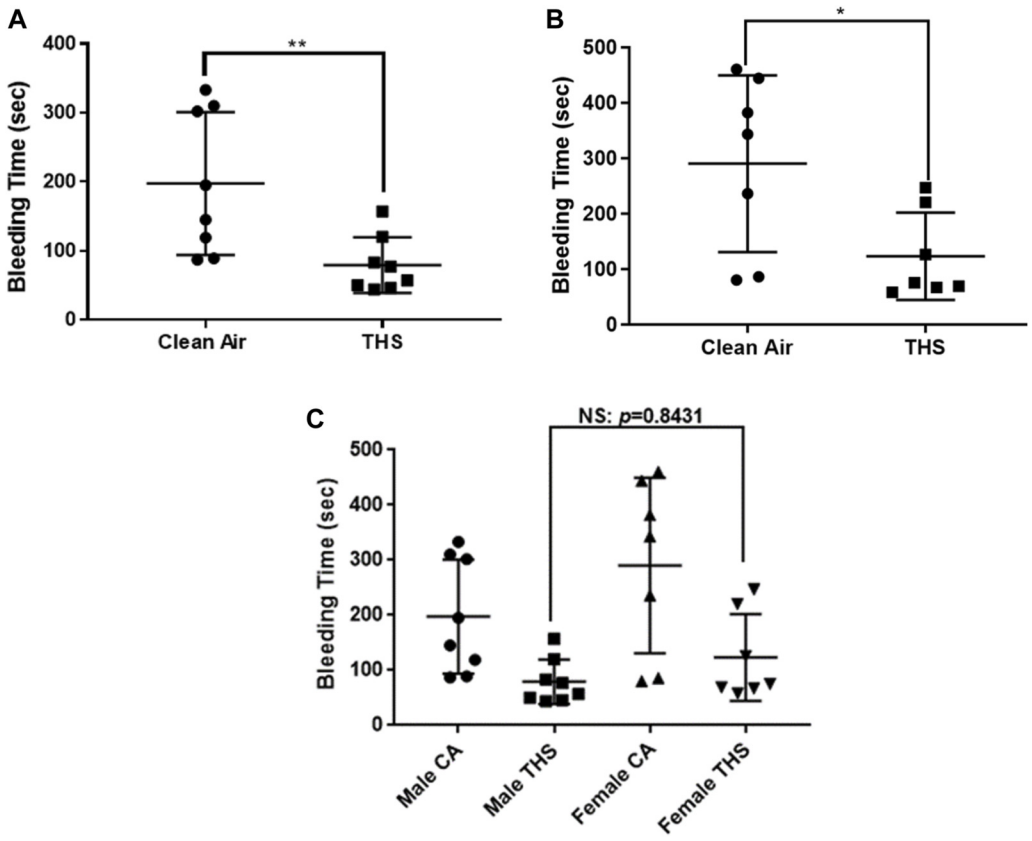

FIGURE 3
Low dose THS exposed mice exhibit shortened tail bleeding time, in both males and females. Both THS-exposed and clean air exposed male, n = 8 **(A)** and female, n = 7 **(B)** mice were anesthetized before being subjected to the tail bleeding time test. Each point represents the bleeding time from a single animal. Sex differences analysis is shown in panel **(C)**. Data was analyzed using Mann-Whitney test on GraphPad Prism version 7. (**p < 0.01, *p < 0.05, NS: not significant).

both sexes shown in Figures 5E,F, for ADP and thrombin, respectively. In line with the platelet aggregation result, dense granule release was also more enhanced in the THS-exposed platelets for male (Figures 6A,B) and female (Figures 6C,D) mice for both agonists. In terms of sex differences, we did not observe any, whether in the aggregation or dense granule secretion responses, as was the case with the *in vivo* phenotype.

THS exposure increases integrin activation (αIIbβ3), α-granule secretion and phosphatidylserine expression in male mice

Based on our enhanced aggregation and dense granule results, we investigated if separate platelet activation markers were also enhanced due to the THS exposure. These experiments were performed only on male mice since we have not observed any gender differences *in vivo* or *in vitro* thus far. Using flow cytometry analysis, our results revealed that integrin activation, α-granule secretion and phosphatidylserine exposure were all enhanced in THS-exposed male mice in response to thrombin (Figures 7A–C). These results are all consistent with our *in vivo* results, suggesting a hyperactive platelet phenotype due to the exposure.

NNK enhances platelet aggregation and *ex vivo* thrombus formation

Although there has been interest in investigating the toxicants that underlie tobacco effects, including in the context of THS, with tar, carbon monoxide, and nicotine receiving significant attention, NNK has largely been ignored, especially concerning its role in CVD. Nonetheless, based on the published work [31] and our *in silico* analysis using the comparative toxicogenomic database (CTD) (not shown),

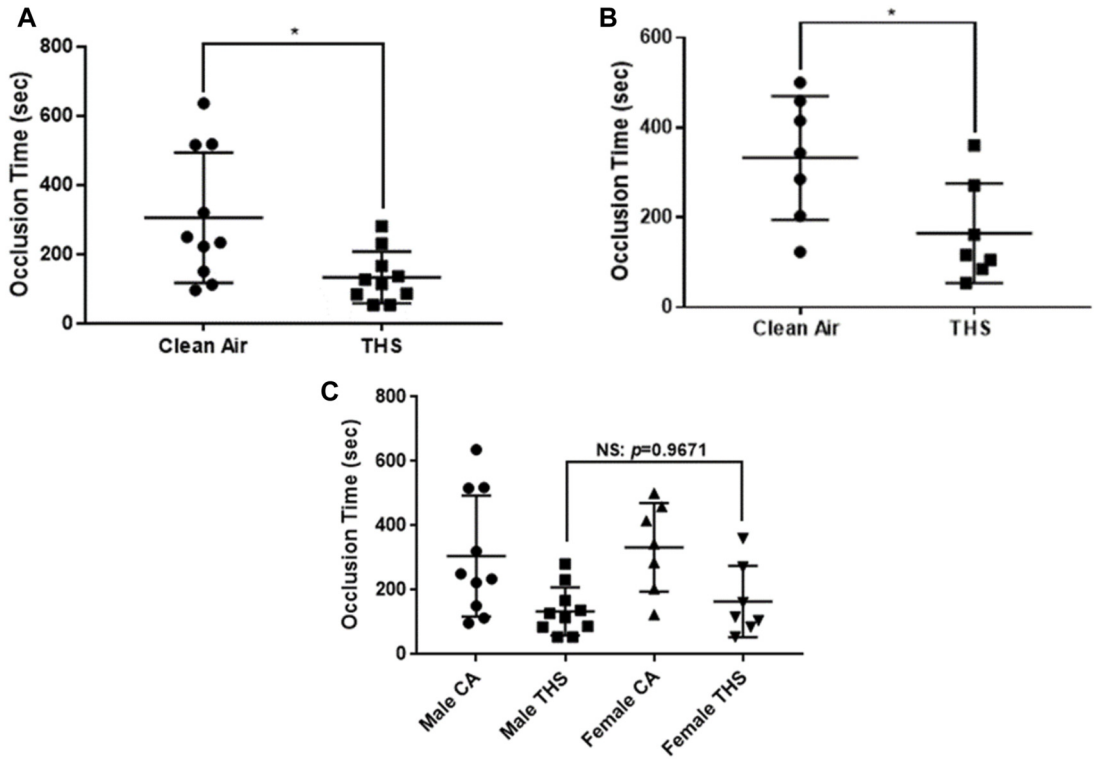

FIGURE 4
Low dose THS mice exhibit shortened occlusion time. Both THS-exposed and clean air exposed male, n = 10 **(A)** and female, n = 7 **(B)** mice were subjected to ferric chloride carotid artery thrombosis model. Sex differences analysis is shown in panel **(C)**. Data was analyzed using Mann-Whitney test on GraphPad Prism version 7. Each point represents the occlusion time from a single animal (*p < 0.05, NS: not significant).

NNK seems to be associated with pathways that might be involved in CVD. Our data showed, for the first time, that platelets incubated with NNK exhibit enhanced aggregation when activated by a low dose of ADP and thrombin (Figures 8A,B). Furthermore, NNK was also found to enhance thrombus formation *ex vivo*, as shown by the increase in the AUC using the T-TAS01 system (Figure 8C). Together, our results provide evidence that NNK is involved in instigating/contributes to a hyperactive platelet state as a result of exposure to THS.

Low dose THS exposure enhance thrombin-induced Akt and ERK phosphorylation

There is evidence that phosphorylation of Akt and ERK proteins is a critical signaling mechanism in platelet function and thrombus formation [32]. Therefore, we investigated whether THS exposure would enhance phosphorylation of Akt and ERK in platelets. Our data showed that Akt and ERK phosphorylation are indeed enhanced in the THS-exposed platelets, relative to controls after stimulation with thrombin (Figure 9). These results provide biochemical evidence and indicate even at low dose, Akt and ERK are an essential component in the THS-mediated modulation of platelets toward a hyperactive state.

Discussion

The negative and public health consequences of indirect inhalation of cigarette smoke by non-smokers (and smokers) in the form of THS is yet to be fully understood and hence remains an active area of interest/investigation. Thus, while much progress has been made in the last several decades highlighting the pathogenesis associated with FHS and SHS, the same cannot be said regarding the adverse effects of THS [33]. One of the main differences between THS and other patterns of smoke exposure (FHS and SHS) is that while exposure to the latter is short and transient, THS exposure could go on for a very long period [34]. And the major pathways of exposure are thought to mainly be inhalation and uptake through skin and hair, when in contact with contaminated surfaces or clothing of smokers [17, 35]. The toxins emitted can remain on surfaces and react with other compounds to generate secondary pollutants, which could be

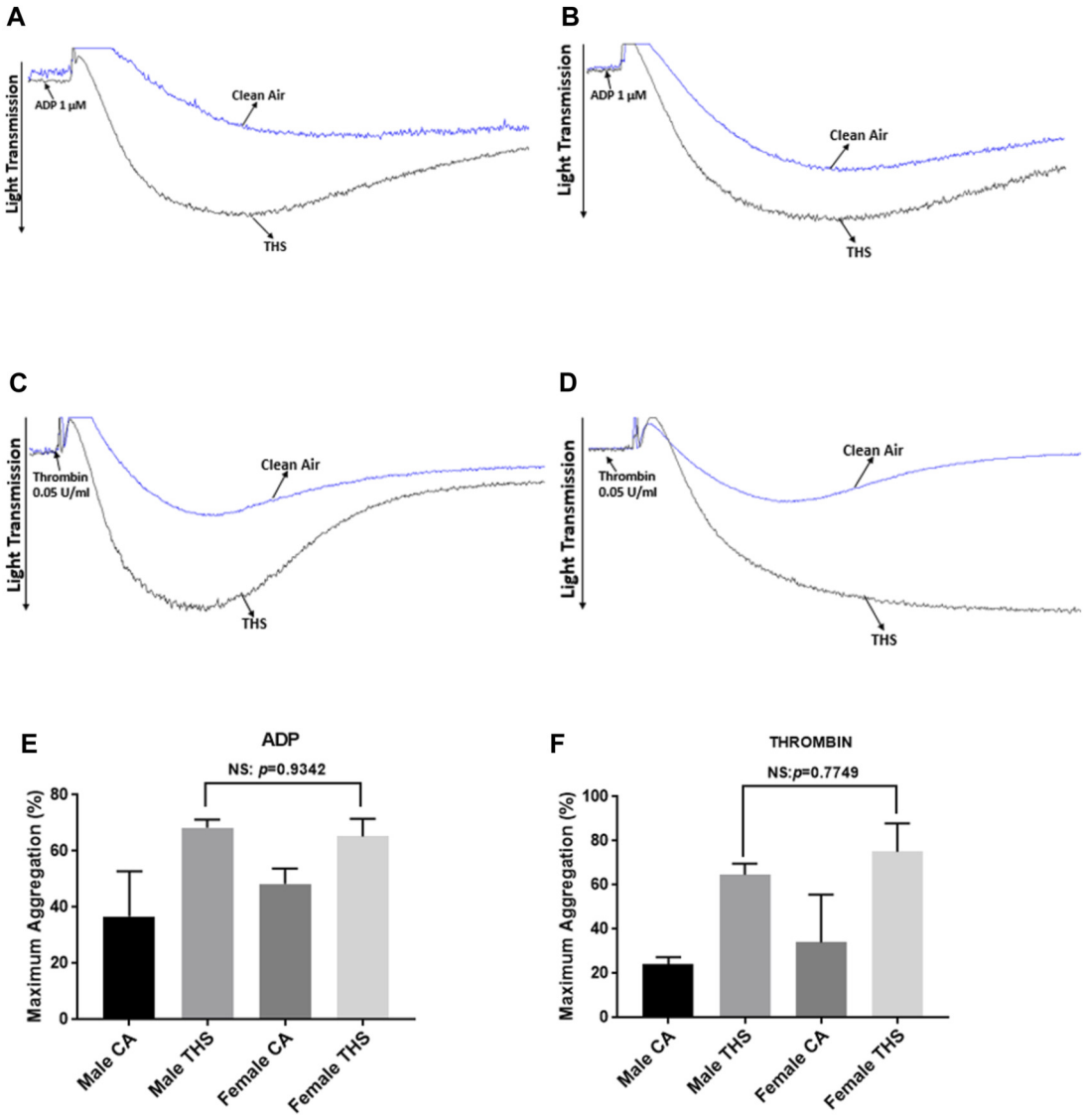

FIGURE 5
Low dose THS exposed mice show enhanced platelet aggregation. Both THS-exposed and clean air-exposed platelets from male **(A,C)** and female **(B,D)** mice were stimulated with either 1 µM ADP or 0.05 U/mL thrombin. Experiments were performed on at least 5 mice for each group and repeated at least twice. Sex differences as shown for ADP and thrombin in panel **(E, F)** respectively. Data was analyzed using student's t-test on GraphPad Prism version 7.

released back into the air and inhaled [17]. Therefore, even the most vulnerable of our population-which includes toddlers and pregnant females who stay in houses with people who smoke-are exposed to some of these toxins. As a matter of fact, there is evidence showing that children residing in households with smokers have higher levels of NNK/nicotine ratios because of THS exposure, when compared to adults [36]. This is very likely because toddlers have the tendency to put objects in their mouth and spend a lot of time "on the floor". Additionally, toddlers breathe very fast and have thinner skin layers, thereby increasing absorption through the skin [37].

Based on the nature and gravity of THS exposure, coupled with the deficiency in the knowledge regarding its effects, we recently investigated its impact on platelet function and thrombus formation, including under maternal/*in utero* exposure settings and in the context of sex, by employing a validated mouse model. Regarding its *in utero* effects, our results documented that it modulates platelet function and increases the risk of thrombosis in the offspring mice, in a sex-dependent manner [23]. In addition, we have also documented that exposure of "adult" mice to both intermediate and long-term THS (3- and 6-month, respectively) affected the hemostasis

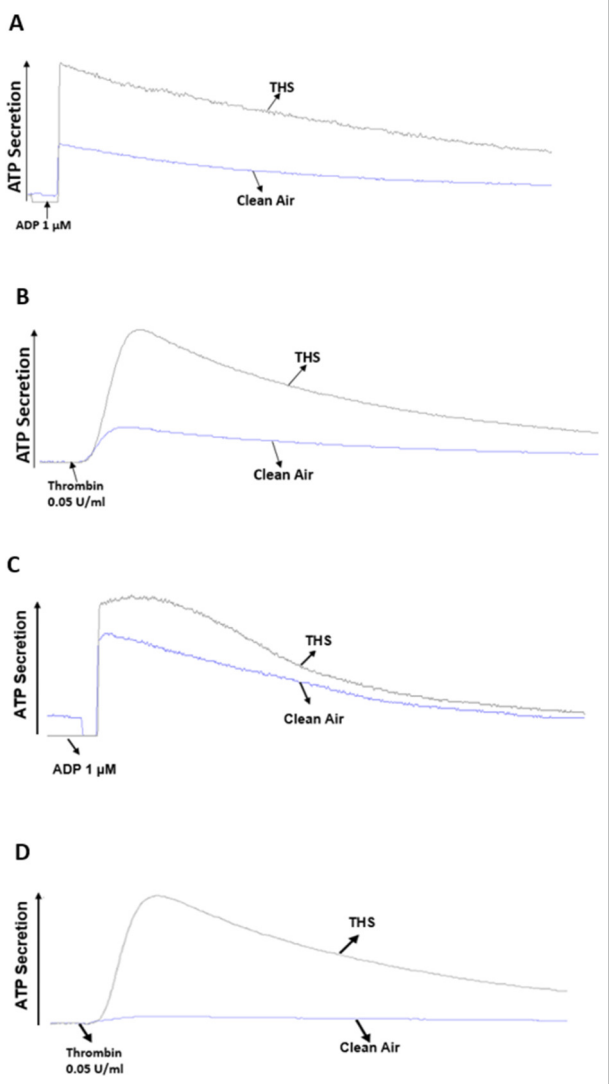

FIGURE 6
Low dose THS exposed mice show enhanced platelet dense granule secretion. Both THS and clean air exposed platelets from male **(A,B)** and female **(C, D)** mice were stimulated with either 1 µM ADP or 0.05 U/mL thrombin. Experiments were performed at least twice with pooled blood samples from at least 5 mice per group.

function of platelets and rendered mice susceptible to thrombosis [22, 24]. Indeed, there is interest in investigating the effects of THS/cigarette smoking on platelets under short- and long-term conditions [38]. To this end, interestingly, a separate study by our team [25] revealed that even when the exposure is relatively short, namely 1 month, THS still triggers a state of hyperactive platelets and thrombogenesis. Given that the aforementioned studies involved a high dose of THS, specifically 40 cigarettes, we do not know if the same results would be obtained when a low dose, specifically 20 cigarettes, is used (that is, dose dependent effects of THS in the context of platelets). This issue was examined under the 1-month exposure time frame. It is important to note that others have also studied this concept through diverse approaches. For example, a study showed that THS can affect mice *in vivo* by increasing blood sugar levels and delaying wound healing in mice [17, 39].

Before evaluating the platelet functional consequences of low-dose THS, it was essential to confirm that our exposure protocol produced measurable systemic uptake of tobacco-derived toxicants. Therefore, we quantified circulating (serum) cotinine and found significantly elevated levels in THS-exposed mice compared to clean-air controls, verifying that even a reduced THS burden (equivalent to 20 cigarettes) delivers nicotine metabolites into the bloodstream. Moreover, no statistically significant sex differences were detected when comparing the levels in males and females. Importantly, this validation strengthens the interpretability of our subsequent platelet and thrombosis findings, as it demonstrates that the observed phenotypes are linked to quantifiable internal exposures rather than merely environmental contact with THS residues.

Consequently, first, we investigated the effect of 1-month exposure to low dose of THS by carrying out the tail bleeding assay, on male and female mice. Notably, our results showed that the tail bleeding time was significantly shortened in both THS-exposed male and female mice, relative to the clean air-exposed controls. This result is consistent with our recently published data in which we observed that a high dose (40 cigarettes) of THS under 1-month exposures can modulate platelet activity *in vivo*. Based on the aforementioned finding, we hypothesized that these exposed mice may be more prone to thrombosis, which we tested utilizing the widely used ferric chloride-induced thrombosis model. Consistent with our tail bleeding data, our results showed a shortened occlusion time in the THS exposed mice, in both male and female mice. We also investigated the total blood count in the exposed mice, which is a known/standardized test for evaluating general health [40]. We observed no significant differences in both sexes indicating that the platelet and other blood cell life cycle may not have been impacted as a result of the low dose THS exposure. Therefore, the observed phenotype does not appear to involve any changes in blood count, at least under the present experimental conditions.

Based on our *in vivo* findings, we hypothesized that THS produces a hyperactive platelet phenotype that underlies their tendency towards thrombosis. To address this hypothesis, and investigate the mechanism of the observed phenotype, we initially carried out platelet aggregometry experiments. It is important to note that platelet aggregation is shown to be enhanced in smokers, compared to non-smokers [41]. Indeed, the aggregation response was found to be more enhanced in THS exposed platelets regardless of the sex of the mice they were obtained from, and this was the case in response to both ADP and thrombin. These results are all consistent with our previous findings [23, 24], including those done using 40 cigarettes under 1 month of exposure to THS [25]. These data are consistent with work by Hung et al., which investigated the effect of cigarette smoking on platelet reactivity and documented that it enhances platelet aggregation and makes platelets prone to thrombosis [42]. We also investigated the

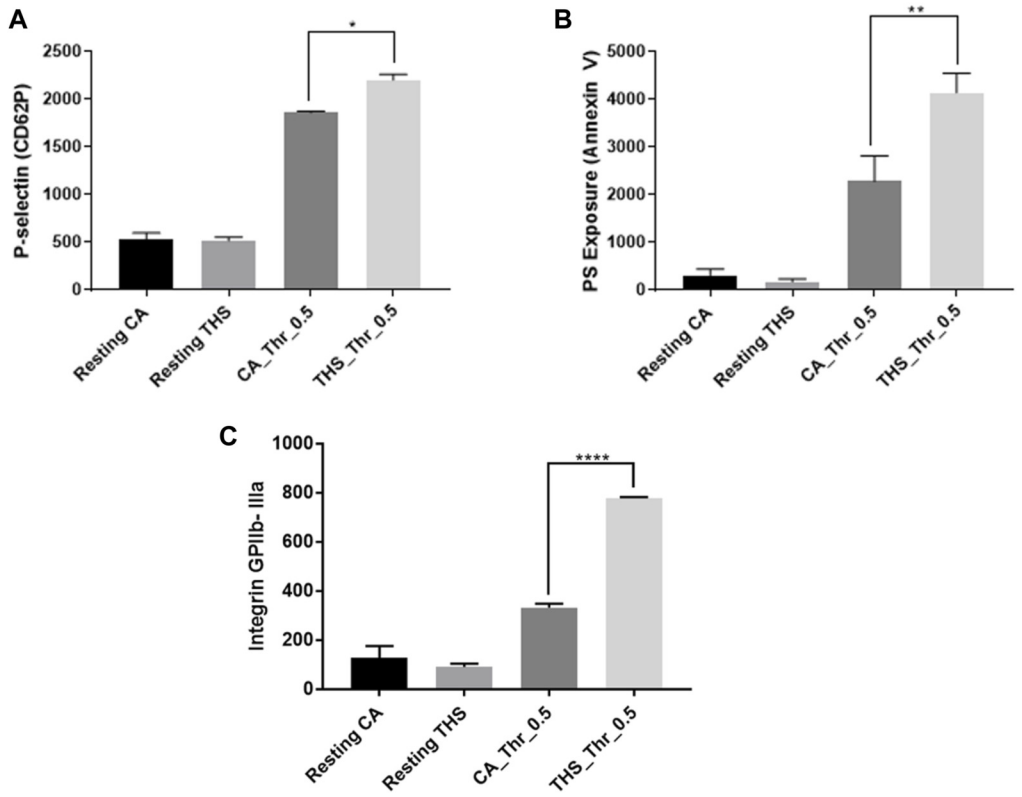

FIGURE 7
Low dose THS exposed mice show enhanced platelet activation markers. Both THS and clean air exposed platelets from male mice were stimulated with 0.5 U/mL of thrombin agonist before P-selectin **(A)**, PS exposure **(B)** and integrin GPIIb-IIIa **(C)** activation were assessed using flow cytometry. Experiments were performed at least twice with pooled blood from 5 male mice for each group (*p < 0.05, **p < 0.01, ****p < 0.0001). Data was analyzed using one-way ANOVA with Tukey's multiple comparison test.

effect of our exposures on both alpha (α) and dense granule secretion. The α-granules' P-selectin is mostly released upon platelet activation and can be measured with flow cytometric analysis. Interestingly, p-selectin was previously found to be expressed at much higher levels in smokers, when compared to non-smokers [43]. Concerning our low dose THS exposure, we found p-selectin expression levels to be enhanced in response to agonist stimulation in male mice. Furthermore, we also observed a more enhanced dense granule release in both male and female mice, in response to agonist stimulation. These results are consistent with our previous findings [23, 25]. Since we didn't observe any sex differences in our *in vivo* assays as well as platelet aggregation and dense granule secretion, we decided to carry out the rest of the experiments on only male mice. Next, we investigated the effect of our exposure on agonist-induced integrin activation, which was more enhanced in THS-exposed mice (males), which is in line with our aggregation results.

Platelets stimulated by agonists rapidly expose phosphatidylserine (PS) on their surfaces, which serves as a platform for the assembly of the coagulation cascade [44]. Hence, it serves as a marker of platelet activation *in vitro* [45] and can be measured with flow cytometry. Our results showed higher agonist-triggered PS exposure in the THS exposed platelets. Moreover, our biochemical results revealed enhanced phosphorylation of Akt and ERK in response to low dose THS exposure. It is to be noted that Akt and ERK phosphorylation were also found to be enhanced in other forms of tobacco and/or types of exposures [46, 47].

Finally, we also examined the role of one of the key THS toxicants, NNK as a potential suspect in modulating platelet reactivity. NNK has indeed been identified as one of the major toxic constituents of THS residues, where it accumulates at high levels on indoor surfaces and persists long after active smoking has ceased [17]. Both NNK and NNA (tobacco-specific nitrosamines) have been previously documented to possess mutagenic properties *in vitro*, resulting in DNA damage through transcription and replication impairment, thereby contributing to significant cellular changes, similar to real life THS exposures [48]. Our results suggest that NNK could have a role, at least in part, in promoting thrombosis.

In regard to the possible mechanism of THS induced phenotype, a study carried out on humans have shed light on

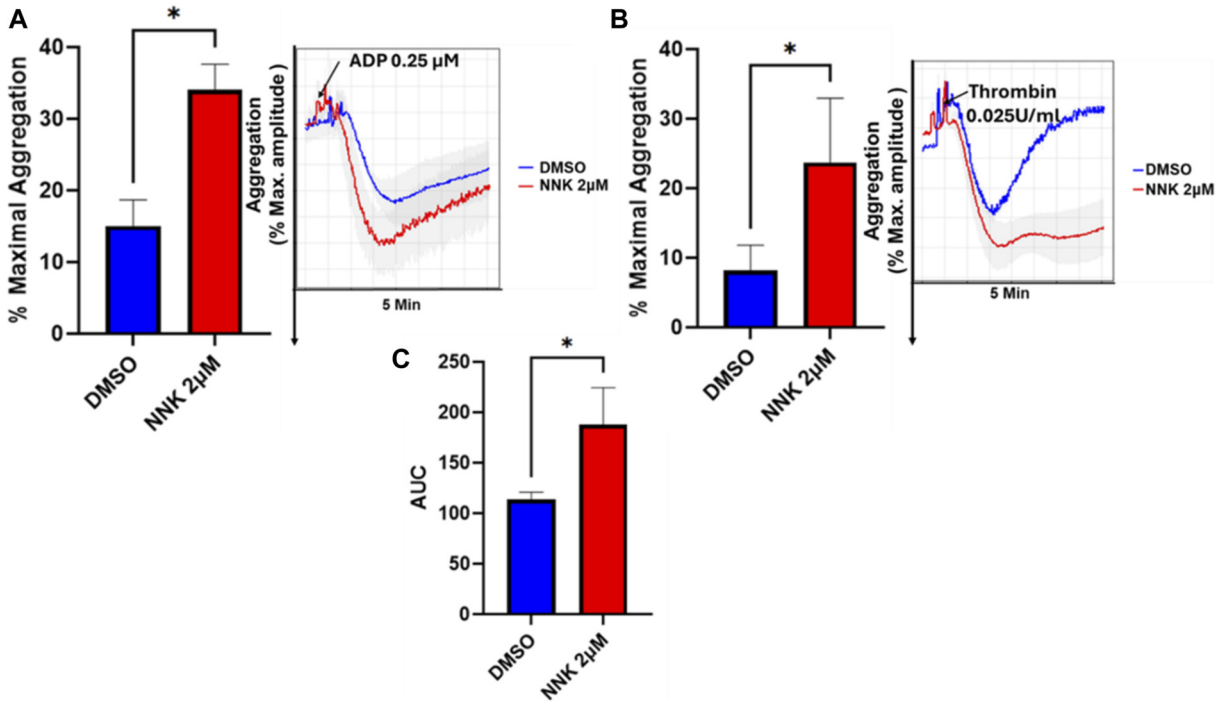

FIGURE 8
The THS toxicant NNK modulates platelet aggregation and platelets thrombus formation *ex vivo*. PRP or Blood was collected from healthy human subjects, treated with 2 μM NNK or the vehicle (DMSO) for 5 min before being subjected to either aggregation or T-TAS01 system analysis (PL chip flow under arterial shear stress conditions on a collagen coated surface). Platelet aggregation **(A,B)** was measured in response to stimulation with ADP **(A)** or thrombin **(B)**. The area under the curve/AUC10 comparing NNK vs. the vehicle DMSO was also assessed **(C)**. These data were obtained from healthy human subjects. Data were compared by running the student t-test using GraphPad Prism (*$p < 0.05$).

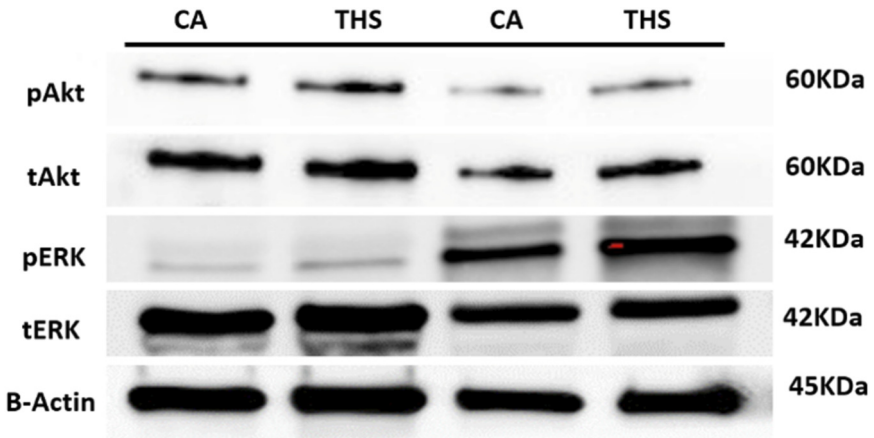

FIGURE 9
Low dose THS exposed mice show enhanced platelet Akt and ERK activation (phosphorylation). Platelets from low dose THS and clean air–exposed mice were prepared and washed. Platelets were either resting or stimulated with 0.1 U/mL thrombin for 3 min before being subjected to immunoblotting with anti-Akt, anti-pAkt, anti-ERK, and anti-pERK antibodies. Each experiment was repeated at least three times with blood pooled from a group of six to eight mice each time.

the potential molecular pathways associated with THS exposure [49]. To this end, THS was found to activate pathways associated with enhanced leukocyte migration and immune cells proliferation-both as a result of upregulation of the Rho family of GTPases-which led to an increase in oxidative stress. Importantly, the RhoA GTPases regulate the reorganization of the actin cytoskeleton, which is a key step in platelet spreading and activation [50], further validating our current and previous findings [25], which showed that THS exposure potentiates platelet spreading.

In a recent study, we also identified a plausible mechanistic pathway by which *in utero* THS exposure promoted a prothrombotic phenotype, by modulating the platelet transcriptome [51]. The results revealed a significant amount of differentially expressed genes and miRNAs controlling platelet signaling and activation as well as other cellular pathways. Bearing in mind that these mice were maternally exposed to THS, it would be worth investigating in the future if direct THS exposure has similar effects on the platelet transcriptome.

Regarding the integrated mechanism underlying the observed phenotype, it is possible that nicotine and tobacco-specific nitrosamines converge on redox and Ca^{2+} pathways that prime platelets for hyperreactivity. In vascular cells, nicotine activates nicotinic acetylcholine receptors (notably α7/α3), raising intracellular Ca^{2+} and driving NOX-dependent oxidative stress and mediating vesicles release [52]. Because human platelets themselves express α7-nAChRs [53], that could provide a direct route to modulate platelet signaling. Consistent with this notion, the α7-nAChR antagonist MG624 was previously found to reverse pathobiologic effects of tobacco toxicants [54], and our unpublished data shows it has the capacity to reverse the prothrombotic phenotype induced by THS. Downstream, platelet NOX isoforms couple ROS to the classical activation machinery, thus, ROS generated by these enzymes promotes platelet activation via the Syk/phospholipase Cγ2/calcium signaling pathway [55]. In parallel, the tobacco carcinogen NNK, which is also an nAChR ligand, is well documented to trigger Ca^{2+} influx through voltage-dependent Ca^{2+} channels [56], a mechanism entirely consistent with modulation of platelet Ca^{2+} handling. Collectively, the aforementioned evidence reinforces the link between tobacco exposure (through its toxic profile), oxidative stress, and heightened platelet responsiveness.

Our study, however, has some limitations, for example, not all experiments could be carried out on both male and female mice due to limited samples, albeit no sex differences were observed in any of the experiments in which male and female mice were used. Similarly, the sample size for our human subjects was very small, and although we took account of subjects' present medications and health status, we did not take into account the presence of other confounding factors that may impact our results. Finally, our exposure scheme also considered only 1 month (4 weeks) exposure and therefore, potential longer-term effects remain undefined.

Collectively, we document for the first time that 1-month low dose exposure to THS can cause a hyperactive platelet phenotype, as evident by the host of platelet functional studies carried out. Although we did not observe any sex difference with our low dose exposure, it may be possible that a "longer" exposure timeline may show such difference in the observed phenotype, which will be the focus of future research. Nevertheless, our results should serve as the foundation for regulations to restrict tobacco exposure in all its forms.

In summary, our results show that THS exposure negatively impacts health, at least in part, through increasing the risk of occlusive disorders, and involves the toxicant NNK. Also, considering our short exposure time and low dose of cigarettes used, our findings underscore the notion that the negative effects of THS on health do not necessarily require "chronic" exposure, and suggest that it may even be detrimental to people who are subjected to "lower" levels of exposure.

Author contributions

PB, AA, and HA: performed experiments and wrote the manuscript. LM, RD, SU, and SK performed experiments. FA and FK conceptualized and edited the manuscript. All authors contributed to the article and approved the submitted version.

Data availability

The original contributions presented in the study are included in the article/supplementary material, further inquiries can be directed to the corresponding author.

Ethics statement

The studies involving humans were approved by Institutional Review Board of Texas A&M University. The participants provided their written informed consent to participate in this study. The animal study was approved by Institutional Animal Care and Use Committee of Texas A&M University. The study was conducted in accordance with the local legislation and institutional requirements.

Funding

The author(s) declared that financial support was received for this work and/or its publication. This work was supported by the National Institute of Environmental Health Sciences, the National Heart, Lung, And Blood Institute and the Eunice Kennedy Shriver National Institute of Child Health and Human Development of the National Institutes of Health under Awards Number R03ES030486, R01HL145053, R21ES029345, R56HL158730, R21HD105187, R21ES034512 and. The content is solely the responsibility of the authors and does not necessarily represent

the official views of the National Institutes of Health. This research was also supported by startup funds provided by the School of Pharmacy, Texas A&M University (to FK and FA).

Conflict of interest

The author(s) declared no potential conflicts of interest with respect to the research, authorship, and/or publication of this article.

Generative AI statement

The author(s) declared that generative AI was not used in the creation of this manuscript.

Any alternative text (alt text) provided alongside figures in this article has been generated by Frontiers with the support of artificial intelligence and reasonable efforts have been made to ensure accuracy, including review by the authors wherever possible. If you identify any issues, please contact us.

References

1. Kondo T, Nakano Y, Adachi S, Murohara T. Effects of tobacco smoking on cardiovascular disease. *Circ J* (2019) **83**(10):1980–5. doi:10.1253/circj.CJ-19-0323

2. Münzel T, Hahad O, Kuntic M, Keaney JF, Deanfield JE, Daiber A. Effects of tobacco cigarettes, e-cigarettes, and waterpipe smoking on endothelial function and clinical outcomes. *Eur Heart J* (2020) **41**(41):4057–70. doi:10.1093/eurheartj/ehaa460

3. Martell BN, Garrett BE, Caraballo RS. Disparities in adult cigarette smoking - united States, 2002-2005 and 2010-2013. *MMWR Morb Mortal Wkly Rep* (2016) **65**(30):753–8. doi:10.15585/mmwr.mm6530a1

4. Suskin N, Sheth T, Negassa A, Yusuf S. Relationship of current and past smoking to mortality and morbidity in patients with left ventricular dysfunction. *J Am Coll Cardiol* (2001) **37**(6):1677–82. doi:10.1016/s0735-1097(01)01195-0

5. He J, Ogden LG, Bazzano LA, Vupputuri S, Loria C, Whelton PK. Risk factors for congestive heart failure in US men and women: NHANES I epidemiologic follow-up study. *Arch Intern Med* (2001) **161**(7):996–1002. doi:10.1001/archinte.161.7.996

6. Kamimura D, Cain LR, Mentz RJ, White WB, Blaha MJ, DeFilippis AP, et al. Cigarette smoking and incident heart failure: insights from the Jackson heart study. *Circulation* (2018) **137**(24):2572–82. doi:10.1161/circulationaha.117.031912

7. Mobarrez F, Antoniewicz L, Bosson JA, Kuhl J, Pisetsky DS, Lundbäck M. The effects of smoking on levels of endothelial progenitor cells and microparticles in the blood of healthy volunteers. *PLoS One* (2014) **9**(2):e90314. doi:10.1371/journal.pone.0090314

8. Barua RS, Ambrose JA. Mechanisms of coronary thrombosis in cigarette smoke exposure. *Arterioscler Thromb Vasc Biol* (2013) **33**(7):1460–7. doi:10.1161/atvbaha.112.300154

9. Zaid M, Miura K, Okayama A, Nakagawa H, Sakata K, Saitoh S, et al. Associations of high-density lipoprotein particle and high-density lipoprotein cholesterol with alcohol intake, smoking, and body mass index - the INTERLIPID study. *Circ J* (2018) **82**(10):2557–65. doi:10.1253/circj.CJ-18-0341

10. Matt GE, Quintana PJ, Destaillats H, Gundel LA, Sleiman M, Singer BC, et al. Thirdhand tobacco smoke: emerging evidence and arguments for a multidisciplinary research agenda. *Environ Health Perspect* (2011) **119**(9):1218–26. doi:10.1289/ehp.1103500

11. Wu JX, Lau ATY, Xu YM. Indoor secondary pollutants cannot be ignored: third-hand smoke. *Toxics* (2022) **10**(7):363. doi:10.3390/toxics10070363

12. Matt GE, Quintana PJ, Zakarian JM, Fortmann AL, Chatfield DA, Hoh E, et al. When smokers move out and non-smokers move in: residential thirdhand smoke pollution and exposure. *Tob Control* (2011) **20**(1):e1. doi:10.1136/tc.2010.037382

13. Matt GE, Quintana PJ, Hovell MF, Chatfield D, Ma DS, Romero R, et al. Residual tobacco smoke pollution in used cars for sale: air, dust, and surfaces. *Nicotine Tob Res* (2008) **10**(9):1467–75. doi:10.1080/14622200802279898

14. Fortmann AL, Romero RA, Sklar M, Pham V, Zakarian J, Quintana PJE, et al. Residual tobacco smoke in used cars: futile efforts and persistent pollutants. *Nicotine Tob Res* (2010) **12**(10):1029–36. doi:10.1093/ntr/ntq144

15. Singer BC, Hodgson AT, Guevarra KS, Hawley EL, Nazaroff WW. Gas-phase organics in environmental tobacco smoke. 1. Effects of smoking rate, ventilation, and furnishing level on emission factors. *Environ Sci Technol* (2002) **36**(5):846–53. doi:10.1021/es011058w

16. Protano C, Vitali M. The new danger of thirdhand smoke: why passive smoking does not stop at secondhand smoke. *Environ Health Perspect* (2011) **119**(10):A422. doi:10.1289/ehp.1103956

17. Jacob P, 3rd, Benowitz NL, Destaillats H, Gundel L, Hang B, Martins-Green M, et al. Thirdhand smoke: new evidence, challenges, and future directions. *Chem Res Toxicol* (2017) **30**(1):270–94. doi:10.1021/acs.chemrestox.6b00343

18. Winickoff JP, Friebely J, Tanski SE, Sherrod C, Matt GE, Hovell MF, et al. Beliefs about the health effects of "thirdhand" smoke and home smoking bans. *Pediatrics* (2009) **123**(1):e74–9. doi:10.1542/peds.2008-2184

19. Hang B, Sarker AH, Havel C, Saha S, Hazra TK, Schick S, et al. Thirdhand smoke causes DNA damage in human cells. *Mutagenesis* (2013) **28**(4):381–91. doi:10.1093/mutage/get013

20. Freedman ND, Leitzmann MF, Hollenbeck AR, Schatzkin A, Abnet CC. Cigarette smoking and subsequent risk of lung cancer in men and women: analysis of a prospective cohort study. *Lancet Oncol* (2008) **9**(7):649–56. doi:10.1016/s1470-2045(08)70154-2

21. Huxley RR, Woodward M. Cigarette smoking as a risk factor for coronary heart disease in women compared with men: a systematic review and meta-analysis of prospective cohort studies. *Lancet* (2011) **378**(9799):1297–305. doi:10.1016/s0140-6736(11)60781-2

22. Karim ZA, Alshbool FZ, Vemana HP, Adhami N, Dhall S, Espinosa EVP, et al. Third-hand smoke: impact on hemostasis and thrombogenesis. *J Cardiovasc Pharmacol* (2015) **66**(2):177–82. doi:10.1097/fjc.0000000000000260

23. Ali HEA, Alarabi AB, Karim ZA, Rodriguez V, Hernandez KR, Lozano PA, et al. In utero thirdhand smoke exposure modulates platelet function in a sex-dependent manner. *Haematologica* (2022) **107**(1):312–5. doi:10.3324/haematol.2021.279388

24. Villalobos-García D, Ali HEA, Alarabi AB, El-Halawany MS, Alshbool FZ, Khasawneh FT. Exposure of mice to thirdhand smoke modulates *in vitro* and *in vivo* platelet responses. *Int J Mol Sci* (2022) **23**(10). doi:10.3390/ijms23105595

25. Qadri S, Maia ACG, Ali HEA, Alarabi AB, Alshbool FZ, Khasawneh FT. Sex dependent occlusive cardiovascular disease effects of short-term thirdhand smoke exposure. *Nicotine Tob Res* (2024) **26**:1225–33.

26. Qasim H, Karim ZA, Silva-Espinoza JC, Khasawneh FT, Rivera JO, Ellis CC, et al. Short-term E-Cigarette exposure increases the risk of thrombogenesis and enhances platelet function in mice. *J Am Heart Assoc* (2018) **7**(15). doi:10.1161/JAHA.118.009264

27. Lozano PA, Alarabi AB, Garcia SE, Boakye ET, Kingbong HT, Naddour E, et al. The antidepressant duloxetine inhibits platelet function and protects against thrombosis. *Int J Mol Sci* (2022) **23**(5):2587. doi:10.3390/ijms23052587

28. Morowski M, Vogtle T, Kraft P, Kleinschnitz C, Stoll G, Nieswandt B. Only severe thrombocytopenia results in bleeding and defective thrombus formation in mice. *Blood* (2013) **121**(24):4938–47. doi:10.1182/blood-2012-10-461459

29. Lawrie AS, Kobayashi K, Lane PJ, Mackie IJ, Machin SJ. The automation of routine light transmission platelet aggregation. *Int J Lab Hematol* (2014) **36**(4):431–8. doi:10.1111/ijlh.12161

30. Vinholt PJ, Frederiksen H, Hvas AM, Sprogøe U, Nielsen C. Measurement of platelet aggregation, independently of patient platelet count: a flow-cytometric approach. *J Thromb Haemost* (2017) **15**(6):1191–202. doi:10.1111/jth.13675

31. Merianos AL, Matt GE, Stone TM, Jandarov RA, Hoh E, Dodder NG, et al. Contamination of surfaces in children's homes with nicotine and the potent carcinogenic tobacco-specific nitrosamine NNK. *J Expo Sci Environ Epidemiol* (2024) **34**(4):727–34. doi:10.1038/s41370-023-00629-8

32. Senis YA, Sangrar W, Zirngibl RA, Craig AW, Lee DH, Greer PA. Fps/fes and fer non-receptor protein-tyrosine kinases regulate collagen- and ADP-induced platelet aggregation. *J Thromb Haemost* (2003) **1**(5):1062–70. doi:10.1046/j.1538-7836.2003.t01-1-00124.x

33. Giovino GA, Mirza SA, Samet JM, Gupta PC, Jarvis MJ, Bhala N, et al. Tobacco use in 3 billion individuals from 16 countries: an analysis of nationally representative cross-sectional household surveys. *Lancet* (2012) **380**(9842):668–79. doi:10.1016/s0140-6736(12)61085-x

34. Matt GE, Quintana PJE, Hoh E, Zakarian JM, Chowdhury Z, Hovell MF, et al. A casino goes smoke free: a longitudinal study of secondhand and thirdhand smoke pollution and exposure. *Tob Control* (2018) **27**(6):643–9. doi:10.1136/tobaccocontrol-2017-054052

35. Adhami N, Starck SR, Flores C, Martins Green M. A health threat to bystanders living in the homes of smokers: how smoke toxins deposited on surfaces can cause insulin resistance. *PLoS One* (2016) **11**(3):e0149510. doi:10.1371/journal.pone.0149510

36. Hovell MF, Zakarian JM, Matt GE, Liles S, Jones JA, Hofstetter CR, et al. Counseling to reduce children's secondhand smoke exposure and help parents quit smoking: a controlled trial. *Nicotine Tob Res* (2009) **11**(12):1383–94. doi:10.1093/ntr/ntp148

37. Drehmer JE, Walters BH, Nabi-Burza E, Winickoff JP. Guidance for the clinical management of thirdhand smoke exposure in the child health care setting. *J Clin Outcomes Manag* (2017) **24**(12):551–9.

38. Pamukcu B, Oflaz H, Onur I, Cimen A, Nisanci Y. Effect of cigarette smoking on platelet aggregation. *Clin Appl Thromb Hemost* (2011) **17**(6):E175–80. doi:10.1177/1076029610394440

39. Martins-Green M, Adhami N, Frankos M, Valdez M, Goodwin B, Lyubovitsky J, et al. Cigarette smoke toxins deposited on surfaces: implications for human health. *PLoS One* (2014) **9**(1):e86391. doi:10.1371/journal.pone.0086391

40. Hang B, Snijders AM, Huang Y, Schick SF, Wang P, Xia Y, et al. Early exposure to thirdhand cigarette smoke affects body mass and the development of immunity in mice. *Sci Rep* (2017) **7**:41915. doi:10.1038/srep41915

41. Fusegawa Y, Goto S, Handa S, Kawada T, Ando Y. Platelet spontaneous aggregation in platelet-rich plasma is increased in habitual smokers. *Thromb Res* (1999) **93**(6):271–8. doi:10.1016/s0049-3848(98)00184-4

42. Hung J, Lam JY, Lacoste L, Letchacovski G. Cigarette smoking acutely increases platelet thrombus formation in patients with coronary artery disease taking aspirin. *Circulation* (1995) **92**(9):2432–6. doi:10.1161/01.cir.92.9.2432

43. Pernerstorfer T, Stohlawetz P, Stummvoll G, Kapiotis S, Szekeres T, Eichler HG, et al. Low-dose aspirin does not lower *in vivo* platelet activation in healthy smokers. *Br J Haematol* (1998) **102**(5):1229–31. doi:10.1046/j.1365-2141.1998.00883.x

44. Reddy EC, Rand ML. Procoagulant phosphatidylserine-exposing platelets *in vitro* and *in vivo*. *Front Cardiovasc Med* (2020) **7**:15. doi:10.3389/fcvm.2020.00015

45. Rand ML, Wang H, Bang KW, Packham MA, Freedman J. Persistence of phosphatidylserine exposure on activated platelets *in vivo* in rabbits. *Thromb Haemost* (2007) **98**(2):477–8.

46. Alarabi AB, Karim ZA, Ramirez JEM, Hernandez KR, Lozano PA, Rivera JO, et al. Short-term exposure to waterpipe/hookah smoke triggers a hyperactive platelet activation state and increases the risk of thrombogenesis. *Arterioscler Thromb Vasc Biol* (2020) **40**(2):335–49. doi:10.1161/ATVBAHA.119.313435

47. Badejo PO, Umphres SS, Ali HEA, Alarabi AB, Qadri S, Alshbool FZ, et al. Exposure to electronic waterpipes increases the risk of occlusive cardiovascular disease in C57BL/6J mice. *J Cardiovasc Pharmacol Ther* (2024) **29**:10742484241242702. doi:10.1177/10742484241242702

48. Tang X, Benowitz N, Gundel L, Hang B, Havel CM, Hoh E, et al. Thirdhand exposures to tobacco-specific nitrosamines through inhalation, dust ingestion, dermal uptake, and epidermal chemistry. *Environ Sci Technol* (2022) **56**(17):12506–16. doi:10.1021/acs.est.2c02559

49. Sakamaki-Ching S, Schick S, Grigorean G, Li J, Talbot P. Dermal thirdhand smoke exposure induces oxidative damage, initiates skin inflammatory markers, and adversely alters the human plasma proteome. *EBioMedicine* (2022) **84**:104256. doi:10.1016/j.ebiom.2022.104256

50. Sorrentino S, Conesa JJ, Cuervo A, Melero R, Martins B, Fernandez-Gimenez E, et al. Structural analysis of receptors and actin polarity in platelet protrusions. *Proc Natl Acad Sci U S A.* (2021) **118**(37):118. doi:10.1073/pnas.2105004118

51. Ali HEA, Alarabi AB, Alshbool FZ, Khasawneh FT. Alterations in the platelet transcriptome mediate prenatal thirdhand smoke exposure associated thrombogenicity *via* integrated miRNA-mRNA regulatory networks. *Int J Mol Sci.* (2025) **26**(15):7633. doi:10.3390/ijms26157633

52. Petsophonsakul P, Burgmaier M, Willems B, Heeneman S, Stadler N, Gremse F, et al. Nicotine promotes vascular calcification *via* intracellular Ca2+-mediated, Nox5-induced oxidative stress, and extracellular vesicle release in vascular smooth muscle cells. *Cardiovasc Res* (2022) **118**(9):2196–210. doi:10.1093/cvr/cvab244

53. Schedel A, Thornton S, Schloss P, Kluter H, Bugert P. Human platelets express functional alpha7-nicotinic acetylcholine receptors. *Arterioscler Thromb Vasc Biol* (2011) **31**(4):928–34. doi:10.1161/ATVBAHA.110.218297

54. Arredondo J, Chernyavsky AI, Grando SA. The nicotinic receptor antagonists abolish pathobiologic effects of tobacco-derived nitrosamines on BEP2D cells. *J Cancer Res Clin Oncol* (2006) **132**(10):653–63. doi:10.1007/s00432-006-0113-9

55. Delaney MK, Kim K, Estevez B, Xu Z, Stojanovic-Terpo A, Shen B, et al. Differential roles of the NADPH-oxidase 1 and 2 in platelet activation and thrombosis. *Arterioscler Thromb Vasc Biol* (2016) **36**(5):846–54. doi:10.1161/ATVBAHA.116.307308

56. Boo HJ, Min HY, Jang HJ, Yun HJ, Smith JK, Jin Q, et al. The tobacco-specific carcinogen-operated calcium channel promotes lung tumorigenesis *via* IGF2 exocytosis in lung epithelial cells. *Nat Commun* (2016) **7**:12961. doi:10.1038/ncomms12961

EBM Experimental Biology and Medicine

TYPE Original Research
PUBLISHED 28 April 2026
DOI 10.3389/ebm.2026.10946

OPEN ACCESS

*CORRESPONDENCE
Hui Huang,
huanghuiHH13@163.com
Min Xu,
jd16298@163.com

†These authors have contributed equally to this work

RECEIVED 23 December 2025
REVISED 20 March 2026
ACCEPTED 23 March 2026
PUBLISHED 28 April 2026

CITATION
Liu P, Yang H, Li R, Huang H and Xu M (2026) Sacubitril valsartan combined with bisoprolol reduces doxorubicin-induced cardiotoxicity in rats by attenuating oxidative stress. *Exp. Biol. Med.* 251:10946. doi: 10.3389/ebm.2026.10946

Sacubitril valsartan combined with bisoprolol reduces doxorubicin-induced cardiotoxicity in rats by attenuating oxidative stress

Ping Liu[1†], Hui Yang[2†], Runqi Li[3], Hui Huang[4*] and Min Xu[5*]

[1]Laboratory Department, Xinhua Hospital of Ili Kazak Autonomous Prefecture, Yining, Xinjiang, China, [2]Department of Cardiology, The First Affiliated Hospital of Shihezi University, Shihezi, Xinjiang, China, [3]Department of Nephrology, The First Affiliated Hospital of Shihezi University, Shihezi, Xinjiang, China, [4]Department of Cardiology, Xinhua Hospital of Ili Kazak Autonomous Prefecture, Yining, Xinjiang, China, [5]Department of Critical Care Medicine, Xinhua Hospital of Ili Kazak Autonomous Prefecture, Yining, Xinjiang, China

Abstract

Doxorubicin-induced cardiotoxicity remains a leading cause of mortality among cancer patients, with oxidative stress serving as a central pathogenic mechanism. This study investigated whether combination therapy with sacubitril valsartan and bisoprolol attenuates doxorubicin-induced cardiotoxicity through modulation of oxidative stress pathways. Sixty male Sprague-Dawley rats were randomized into five groups: control, doxorubicin (DOX), bisoprolol (1.0 mg/kg/d), sacubitril valsartan (30 mg/kg/d), and combination therapy. All groups except control received intraperitoneal DOX (2.5 mg/kg weekly for 5 weeks). Cardiac function was assessed by echocardiography, myocardial injury by histopathology and enzyme levels (CK-MB, cTnI, BNP), and oxidative stress by ROS fluorescence, MDA, and SOD. Protein expression of Nrf2, HO-1, and Keap1 was analyzed by Western blot. DOX administration significantly impaired cardiac function, induced myocardial structural damage, elevated cardiac enzymes and oxidative stress markers, and downregulated Nrf2 pathway proteins compared to controls (all $P < 0.05$). All treatment groups significantly attenuated these abnormalities versus DOX (all $P < 0.05$), with combination therapy demonstrating superior cardioprotection evidenced by greatest improvement in LVEF (68.74 $\pm$ 6.87% vs. 50.26 $\pm$ 6.11%, $P < 0.05$), lowest cardiac enzyme levels, and most robust restoration of Nrf2 pathway expression. These findings demonstrate that sacubitril valsartan combined with bisoprolol effectively reduces doxorubicin-induced cardiotoxicity in rats by activating Nrf2-mediated antioxidant responses, providing experimental evidence for a potentially synergistic prophylactic strategy.

KEYWORDS

adriamycin, bisoprolol, cardiotoxicity, oxidative stress, sacubitril valsartan

Impact statement

Chemotherapy with doxorubicin saves lives, but its heart-damaging side-effects limit how much medicine patients can safely receive. We show that a simple, low-cost pill combining two common heart drugs—sacubitril/valsartan and bisoprolol—prevents this damage in rats by switching on the body's own antioxidant defense system. This is the first demonstration that the duo works better than either drug alone, restoring heart function and lowering injury markers after just 18 days of treatment. The findings give clinicians an immediately translatable strategy to protect cancer patients' hearts without altering the tumor-killing power of doxorubicin, potentially allowing higher, more effective doses while reducing heart failure risk.

Introduction

Anthracyclines are widely used chemotherapeutic agents for the treatment of both solid tumours and haematological malignancies, yet anthracycline-induced cardiotoxicity remains one of the leading causes of mortality among patients with cancer [1–3]. Doxorubicin, one of the most commonly prescribed anthracyclines, has potent antitumour efficacy; however, its clinical use is substantially limited by dose-dependent and largely irreversible cardiotoxic effects. These effects lead to myocardial injury and may ultimately result in arrhythmias, myocardial infarction, and ventricular hypertrophy, thereby markedly increasing long-term cardiovascular mortality [4–6]. Current clinical guidelines recommend the prophylactic use of cardioprotective agents in patients receiving anticancer therapies with established cardiotoxic potential [7, 8]. Nevertheless, effective prevention and treatment strategies for doxorubicin-induced cardiotoxicity remain under active investigation. Previous studies have suggested that angiotensin-converting enzyme inhibitors, statins, and β-adrenergic blockers may confer varying degrees of cardioprotection, although stronger evidence from well-designed studies is still required [9, 10]. Sacubitril/valsartan, an angiotensin receptor–neprilysin inhibitor, has been shown to improve cardiac pump function, and experimental studies indicate that it can attenuate anthracycline-induced cardiotoxicity in rats by modulating oxidative stress–related pathways [11]. Bisoprolol, a selective β-adrenergic blocker widely used in the treatment of chronic heart failure [12], has also demonstrated cardioprotective effects. Ma Yuru et al. [13] reported that bisoprolol alleviates myocardial fibrosis, reduces ventricular hypertrophy, and improves cardiac function in rats with chronic heart failure through inhibition of pathological signalling pathways. Despite these findings, evidence regarding the combined effects of bisoprolol and sacubitril/valsartan on doxorubicin-induced cardiotoxicity is lacking. The mechanisms underlying doxorubicin-associated cardiac injury have not yet been fully elucidated and are believed to involve multiple pathological processes, including oxidative stress, mitochondrial dysfunction, ferroptosis, autophagy, and apoptosis. Among these mechanisms, oxidative stress is widely regarded as a central contributor to doxorubicin-induced cardiotoxicity [14–16]. Against this background, the present study aimed to investigate whether the combination of sacubitril/valsartan and bisoprolol mitigates doxorubicin-induced cardiotoxicity in rats through modulation of oxidative stress pathways. The findings are intended to provide mechanistic insight and experimental evidence to support novel combination strategies for the prevention of anthracycline-related cardiotoxicity.

Materials and methods

Experimental animals

A total of 60 male Sprague–Dawley rats were obtained from the Guangdong Institute for Product Quality Supervision and Inspection (license no. SYXK [Yue] 2023-0181). The animals were 6–8 weeks old and weighed 180–220 g; they were housed in groups at the institutional animal experimental centre under controlled conditions (temperature 23–27 °C, relative humidity 50%–60%, and a 12-h light/12-h dark cycle). All rats were allowed a one-week acclimatisation period before the start of the experiment. Throughout the study, animals had free access to standard chow and water.

Reagents and instruments

Doxorubicin was purchased from Zhejiang Hisun Pharmaceutical Co., Ltd.; bisoprolol from Hangzhou Minsheng Pharmaceutical Co., Ltd.; and sacubitril/valsartan from Novartis (China) Biomedical Research Co., Ltd. Haematoxylin–eosin staining reagents were obtained from Beyotime Biotechnology (Shanghai, China). Commercial ELISA kits for CK-MB, SOD, BNP, cTnI, and MDA were purchased from Shanghai Enzyme-linked Biotechnology Co., Ltd. The catalog numbers and specifications were as follows: CK-MB ELISA kit (Cat# ML037723), SOD ELISA kit (Cat# ML077379), BNP ELISA kit (Cat# ML059422), cTnI ELISA kit (Cat# 059111), MDA ELISA kit (Cat# ML077384). Primary antibodies against nuclear factor erythroid 2-related factor 2 (Nrf2), haem oxygenase-1 (HO-1), Kelch-like ECH-associated protein 1 (Keap1), and GAPDH were obtained from Abcam (Cambridge, UK). The following antibodies were used: anti-Nrf2 (ab137550, rabbit monoclonal, 1:1000, validated for rat), anti-HO-1 (ab68477, rabbit monoclonal, 1:1000, validated for rat), anti-Keap1 (ab227828, rabbit monoclonal, 1:1000, validated for rat), and anti-GAPDH (ab181602, rabbit monoclonal, 1:5000,

validated for rat). HRP-conjugated secondary antibody (ab205718, goat anti-rabbit IgG, 1:5000) was also purchased from Abcam.

Cardiac function was assessed using a VisualSonics Vevo 2100 high-resolution small-animal ultrasound system (FUJIFILM VisualSonics, Canada). Flow cytometric analyses were performed with an Attune™ NxT flow cytometer (Thermo Fisher Scientific, USA).

Experimental grouping and model establishment

Sixty rats were randomly assigned to five groups (n = 12 per group): normal control (Control), doxorubicin (DOX), bisoprolol (Bisoprolol), sacubitril/valsartan (Valsartan), and combination therapy (Combine). Rats in the Bisoprolol, Valsartan, and combination groups received daily oral gavage of the respective drugs for five consecutive weeks, starting 1 week prior to the first doxorubicin administration and continuing throughout the entire experimental period. Specifically, the Bisoprolol group received bisoprolol (1.0 mg/kg), the Valsartan group received sacubitril/valsartan (30 mg/kg), and the combination group received both sacubitril/valsartan (30 mg/kg) and bisoprolol (1.0 mg/kg) once daily by oral gavage. Rats in the Control and DOX groups received an equivalent volume of 0.9% normal saline by oral gavage by oral gavage daily during the same period.

This pretreatment period was designed to ensure that steady-state plasma concentrations of the cardioprotective agents were achieved before the first doxorubicin dose, consistent with standard prophylactic protocols for preventing chemotherapy-induced cardiotoxicity.

One hour after gavage, rats in all groups except the Control group were administered doxorubicin intraperitoneally at a dose of 2.5 mg/kg once weekly for 5 weeks (cumulative dose 15 mg/kg). Rats in the Control group received an equivalent volume of 0.9% normal saline by intraperitoneal injection, and general health status was monitored throughout the experimental period.

Transthoracic echocardiography

Twenty-four hours after the final gavage, rats were fasted for 6 h before echocardiographic assessment. Anaesthesia was induced by intraperitoneal injection of 2% sodium pentobarbital (3 mL/kg), after which the chest hair was removed and the animals were placed supine with limbs secured to the examination platform to optimise intercostal access. Cardiac function was evaluated using a high-resolution small-animal echocardiography system.

Two-dimensional guided M-mode images were obtained from the parasternal long-axis view at the level of the papillary muscles. Left ventricular end-systolic diameter (LVESD) and left ventricular end-diastolic diameter (LVEDD) were measured according to the American Society of Echocardiography guidelines. Left ventricular ejection fraction (LVEF) was calculated using the Teichholz formula: LVEF (%) = $[(LVEDD^3 - LVESD^3)/LVEDD^3] \times 100$. Left ventricular fractional shortening (LVFS) was calculated as: LVFS (%) = [(LVEDD - LVESD)/LVEDD] × 100. All measurements were averaged over three consecutive cardiac cycles.

Haematoxylin–eosin (H&E) staining

Following echocardiographic examination, rats were euthanised by exsanguination under deep anaesthesia induced by an intraperitoneal injection of 2% sodium pentobarbital (100 mg/kg body weight). Following the confirmation of deep anesthesia (absence of pedal reflexes), the thoracic cavity was opened, blood samples were collected from the inferior vena cava, and the heart was rapidly excised to isolate myocardial tissue. Approximately 50 mg of left ventricular myocardium from each rat was fixed in paraformaldehyde, embedded, and sectioned at a thickness of 4 μm. For each animal, three non-consecutive sections were collected and stained with hematoxylin and eosin (H&E) for histopathological evaluation.

After deparaffinisation in xylene and rehydration through graded ethanol, sections were stained with haematoxylin for 10 min, differentiated briefly in acid alcohol, blued, and counterstained with eosin for 2 min. After dehydration and mounting with neutral resin, histopathological changes in myocardial tissue were examined under light microscopy.

For semi-quantitative analysis, myocardial injury was scored based on the following criteria modified from previous studies [Reference]: 0 = normal myocardium with regularly arranged cardiomyocytes and no visible damage; 1 = mild focal myofibrillar loss or cytoplasmic vacuolization involving <25% of the field; 2 = moderate multifocal myofibrillar loss, cytoplasmic vacuolization, or interstitial edema involving 25–50% of the field; 3 = severe confluent myofibrillar disorganization, nuclear pyknosis, karyorrhexis, or inflammatory cell infiltration involving >50% of the field. Five randomly selected fields per section (15 fields per animal) were evaluated, and the average score was calculated for each rat.

Measurement of myocardial enzymes and oxidative stress markers by ELISA

Myocardial tissue (30 mg) and blood samples were collected from rats in each group following the procedures described above. Blood samples were allowed to clot at room

temperature for 30 min before centrifugation at 3,000 × g for 10 min (radius 12 cm) to obtain the supernatan. All samples were processed within 2 h of collection to ensure optimal analyte stability. The supernatants from myocardial homogenates and serum samples were used for quantitative determination of CK-MB, MDA, cTnI, BNP and SOD. All measurements were performed using commercially available ELISA kits, strictly according to the manufacturers' instructions. All ELISA assays were completed within 4 weeks of sample collection, and samples were stored at −80 °C during this period.

Assessment of reactive oxygen species by flow cytometry

Serum samples: Blood samples were centrifuged at 3,000 × g for 10 min (radius 12 cm) to obtain serum within 1 h of collection. To detect reactive oxygen species (ROS) levels in circulating extracellular vesicles (EVs) enriched fractions, we adapted a previously published method [17]. Briefly, 50–100 μL of serum was incubated with an equal volume of DCFH-DA working solution (diluted in serum-free PBS, final concentration 10 μmol/L) in the dark at 37 °C for 30 min. After incubation, samples were diluted with PBS and immediately analyzed by flow cytometry using an Attune™ NxT flow cytometer (Thermo Fisher Scientific, USA). The EV-enriched particle population was gated based on characteristic forward and side scatter properties, as previously described [17]. It should be noted that this scatter-based gating approach, while widely used for EV-rich fractions, cannot definitively exclude potential contributions from other submicron particles such as lipoproteins or protein aggregates that may share similar scatter characteristics. DCF fluorescence intensity within this gate was quantified to represent serum ROS levels. A total of 10,000 EV events were acquired per sample, and results were expressed as mean fluorescence intensity.

Myocardial tissue samples: Fresh myocardial tissue was enzymatically dissociated using type II collagenase and trypsin, followed by incubation at 37 °C for 30 min with gentle agitation every 10 min. Digestion was terminated by the addition of serum-containing medium, and the cell suspension was filtered through a 40 μm cell strainer to remove undigested tissue fragments, then centrifuged at 3,000 × g for 10 min (radius 12 cm). The total processing time from tissue collection to cell isolation was approximately 45 min. The resulting cell pellet was resuspended in pre-cooled PBS and incubated with DCFH-DA working solution (final concentration 10 μmol/L) at 37 °C for 45 min, with gentle mixing every 10 min. After incubation, cells were washed twice with PBS, resuspended in 500 μL PBS, and intracellular ROS fluorescence was measured by flow cytometry. The entire procedure from tissue collection to flow cytometry analysis was completed within 90 min. A total of 10,000 live cell events were acquired per sample, and results were expressed as mean fluorescence intensity. The analysis was performed on total live cells gated based on forward/side scatter properties, without discrimination of specific cardiac cell subtypes.

Western blot analysis of Nrf2, HO-1, and Keap1

Approximately 30 mg of myocardial tissue from each rat was lysed in ice-cold lysis buffer for 30 min on ice. Lysates were centrifuged at 12,000 × g for 15 min (radius 12 cm), and the supernatant was collected for protein quantification using the BCA assay within 2 h of extraction. Equal amounts of protein (30 μg per lane) were mixed with loading buffer at a 1:4 ratio, denatured at 95 °C for 5 min, and separated by SDS–PAGE using stacking and resolving gels. Electrophoresis was performed at 80 V until proteins entered the resolving gel and then continued at 120 V until clear separation of the molecular weight marker was achieved. Proteins were transferred onto PVDF membranes, which were blocked with 5% non-fat milk for 60 min at room temperature. Membranes were then incubated overnight at 4 °C with primary antibodies against Nrf2 (1:1,000), HO-1 (1:1,000), Keap1 (1:1,000), and GAPDH (1:5,000), followed by incubation with appropriate secondary antibodies (1:5,000) for 60 min at room temperature. Protein bands were visualised using enhanced chemiluminescence, and band intensities were quantified using ImageJ software.

Statistical analysis

All data were analysed using SPSS software (version 25.0). Continuous variables that conformed to a normal distribution are presented as mean($\bar{x}$ ±s). Comparisons among multiple groups were performed using one-way analysis of variance (ANOVA), followed by the least significant difference (LSD) t-test for *post hoc* pairwise comparisons. A two-sided P value <0.05 was considered to indicate statistical significance.

Results

General condition of rats in each group

Rats in the Control group exhibited a glossy coat, normal food intake and activity, rapid responses, normal defecation, and good overall vitality. In contrast, rats in the DOX group showed dull fur, markedly reduced food intake and spontaneous activity, sluggish responses, and an overall lethargic appearance. Compared with the DOX group, general condition was

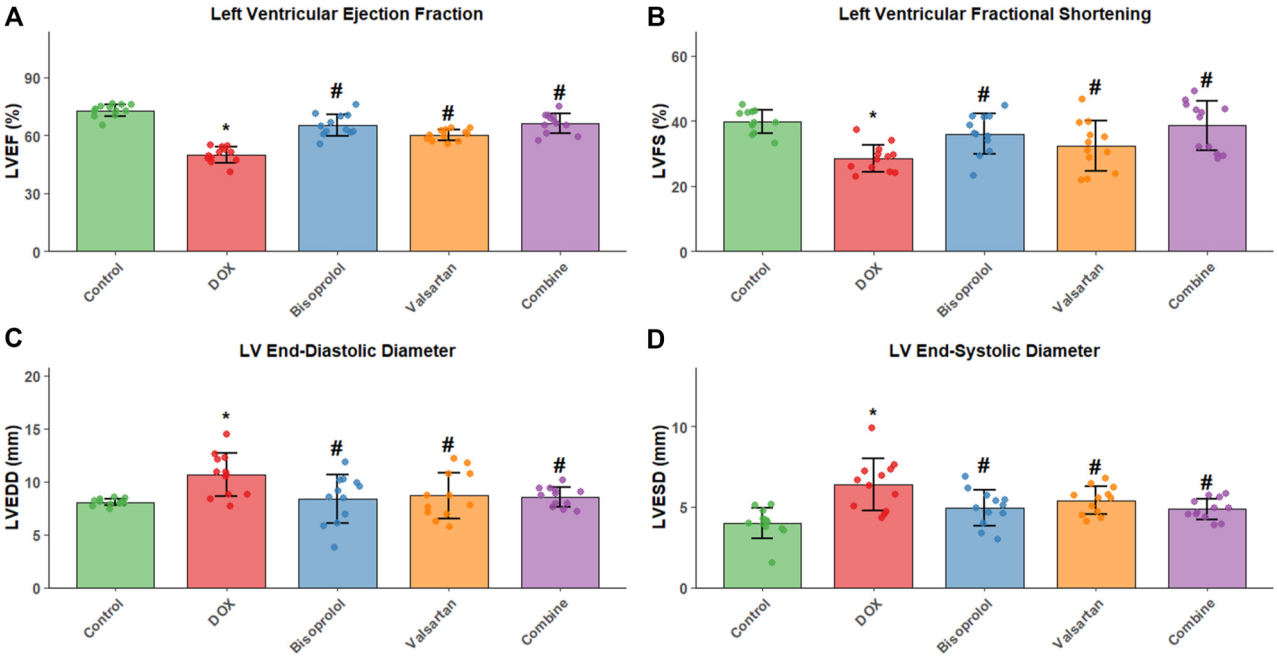

FIGURE 1
Echocardiographic assessment of left ventricular function in each group. Bar graphs showing **(A)** left ventricular end-diastolic diameter (LVEDD), **(B)** left ventricular end-systolic diameter (LVESD), **(C)** left ventricular ejection fraction (LVEF), and **(D)** left ventricular fractional shortening (LVFS) in Control, DOX, Bisoprolol, Valsartan, and combination groups (n = 12 per group). Data are presented as mean ± SD. *P < 0.05 vs. Control group; #P < 0.05 vs. DOX group. The combination therapy significantly improved cardiac function compared to monotherapy groups.

noticeably improved in the Bisoprolol, Valsartan, and combination groups. The most pronounced improvement was observed in the combination group.

Echocardiographic parameters

Compared with the Control group, rats in the DOX group showed significant increases in left ventricular end-diastolic diameter (LVEDD) and left ventricular end-systolic diameter (LVESD), accompanied by marked reductions in left ventricular fractional shortening (LVFS) and left ventricular ejection fraction (LVEF) (all $P < 0.05$). Relative to the DOX group, LVEDD and LVESD were significantly reduced in the Bisoprolol, Valsartan, and combination groups, whereas LVFS and LVEF were significantly increased (all $P < 0.05$). Among these treatments, the combination therapy produced the greatest improvement in cardiac function (Figure 1).

Histopathological changes in myocardial tissue

HE staining revealed normal myocardial architecture in the Control group, with regularly arranged cardiomyocytes, clear striations, and well-defined nuclei and cytoplasm, without evidence of edema or inflammatory infiltration (Figure 2, Control panel). In contrast, the DOX group exhibited severe myocardial injury characterized by disorganized myofibrils, nuclear pyknosis or fragmentation, extensive cardiomyocyte necrosis, marked interstitial edema, and prominent inflammatory cell infiltration (Figure 2, DOX panel).

Myocardial damage was attenuated to varying degrees in the Bisoprolol, Valsartan, and combination groups compared with the DOX group (Figure 2, Bisoprolol, Valsartan, and Combine panels). Semi-quantitative histological scoring confirmed these observations: the DOX group showed significantly higher myocardial injury scores compared with the Control group (2.85 ± 0.42 vs. 0.32 ± 0.18, $P < 0.001$). All treatment groups significantly reduced injury scores versus the DOX group (Bisoprolol: 1.68 ± 0.35; Valsartan: 1.54 ± 0.31; Combine: 0.86 ± 0.24; all $P < 0.05$ vs. DOX), with the combination therapy showing the most substantial histological improvement and the lowest injury score among treatment groups ($P < 0.05$ vs. monotherapy groups). The most substantial histological improvement was observed in the combination group, with near-normal myocardial architecture and minimal residual damage (Figure 2, Combine panel).

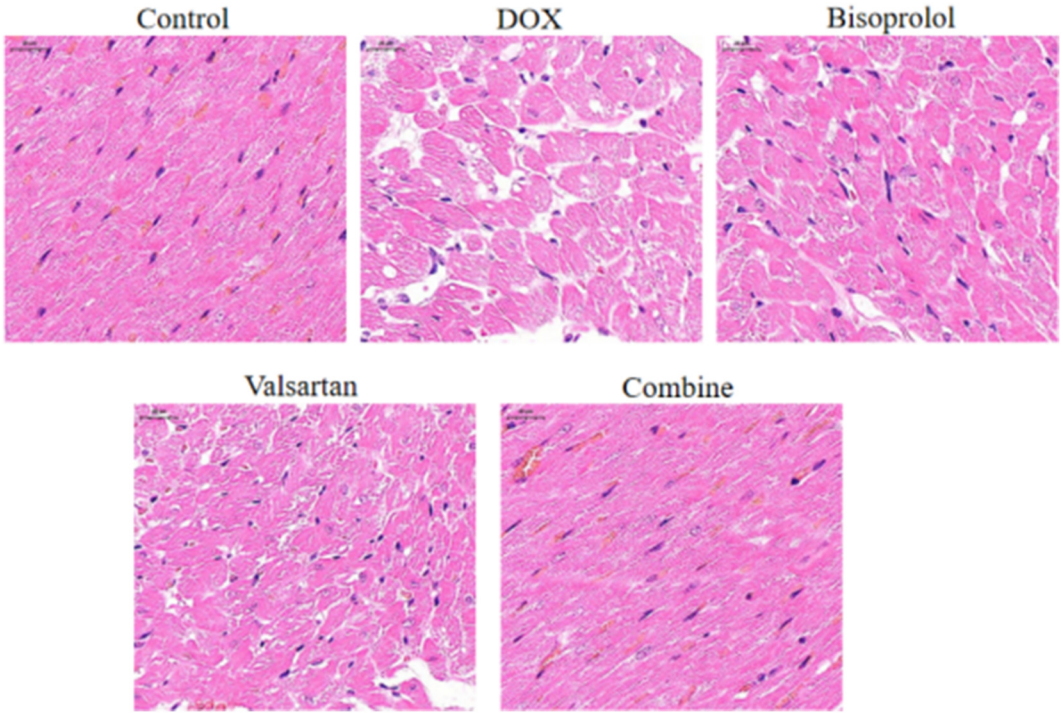

FIGURE 2
Histopathological assessment of doxorubicin-induced myocardial injury and the protective effects of bisoprolol, sacubitril/valsartan, and their combination. Representative hematoxylin and eosin (H&E) stained sections of left ventricular myocardium from each experimental group (n = 6 per group; 3 sections per animal). The Control group shows normal myocardial architecture with regularly arranged cardiomyocytes, clear striations, and well-defined nuclei and cytoplasm. The DOX group exhibits severe myocardial injury characterized by disorganized myofibrils, extensive cardiomyocyte necrosis, nuclear pyknosis/fragmentation, and prominent inflammatory cell infiltration. The Bisoprolol group shows moderate improvement with reduced myofibrillar disorganization. The Valsartan group demonstrates similar moderate improvement. The combination group shows the most substantial histological improvement with near-normal architecture and minimal residual damage. Scale bar = 50 μm. The lower panel shows semi-quantitative myocardial injury scores. Data are presented as mean ± SD (n = 6 per group). $P < 0.05$ vs. Control group; #$P < 0.05$ vs. DOX group; †$P < 0.05$ vs. Bisoprolol and Valsartan groups (one-way ANOVA followed by LSD t-test).

Myocardial enzyme levels in cardiac tissue

Compared with the Control group, levels of creatine kinase-MB (CK-MB), cardiac troponin I (cTnI), and brain natriuretic peptide (BNP) were significantly elevated in the DOX group (all $P < 0.05$). In contrast, CK-MB, cTnI, and BNP levels were significantly reduced in the Bisoprolol, Valsartan, and combination groups relative to the DOX group (all $P < 0.05$). Consistent with the functional and histological findings, the greatest reduction in myocardial enzyme levels was observed in the combination group (Figure 3).

ROS fluorescence intensity in myocardial tissue and serum

Compared with the Control group, rats in the DOX group exhibited significantly increased reactive oxygen species (ROS) fluorescence intensity in both myocardial tissue and the EV-enriched serum fraction ($P < 0.05$). In contrast, ROS fluorescence intensity was markedly reduced in the Bisoprolol, Valsartan, and combination groups compared with the DOX group (all $P < 0.05$), with the combination therapy showing the most pronounced reduction (Figure 4). Myocardial ROS levels represent the average fluorescence of total live cells, as specific cell-type markers were not used in this study.

Oxidative stress markers in myocardial tissue and serum

Relative to the Control group, myocardial and serum malondialdehyde (MDA) levels were significantly elevated in the DOX group, whereas superoxide dismutase (SOD) activity was significantly reduced ($P < 0.05$). Compared with the DOX group, MDA levels were significantly decreased and SOD activity was significantly increased in the Bisoprolol, Valsartan, and combination groups (all $P < 0.05$). Consistent with other findings, the most substantial improvement in oxidative stress status was observed in the combination group (Figure 5).

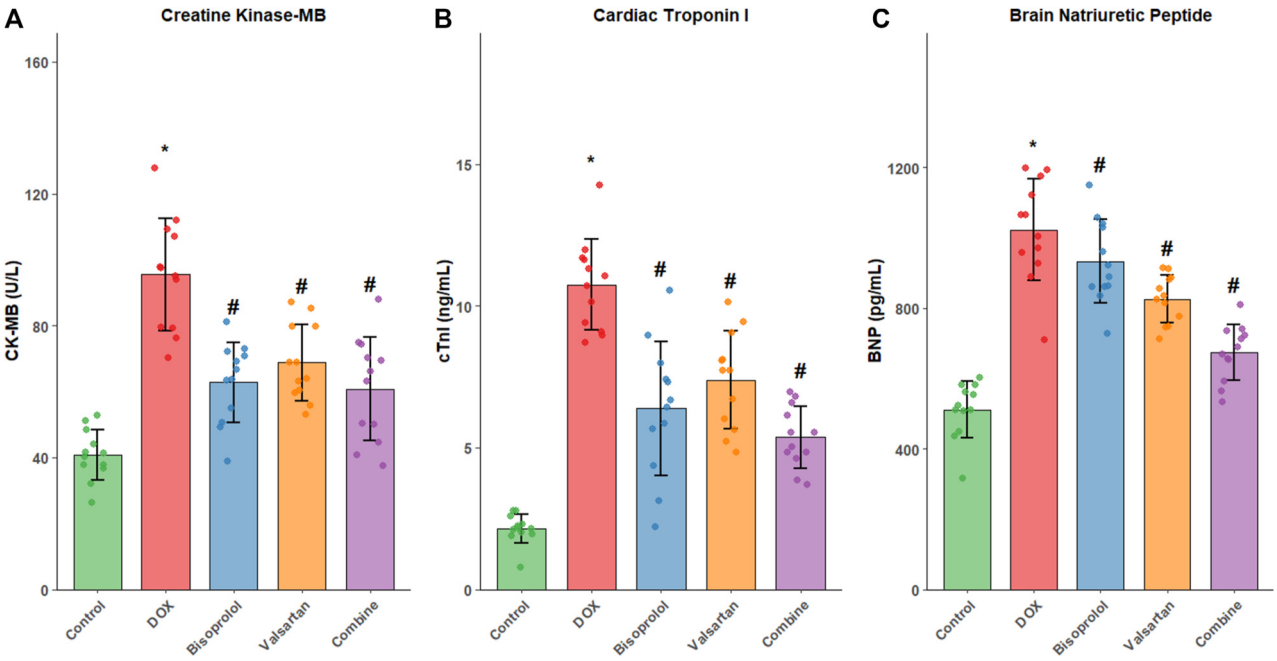

FIGURE 3
Myocardial enzyme levels in cardiac tissue across experimental groups. **(A)** Levels of creatine kinase-MB (CK-MB), **(B)** cardiac troponin I (cTnI), and **(C)** brain natriuretic peptide (BNP) were measured by ELISA in myocardial homogenates from Control, DOX, Bisoprolol, Valsartan, and combination groups (n = 12 per group). Data are expressed as mean ± SD. *P < 0.05 vs. Control group; #P < 0.05 vs. DOX group. The combination treatment resulted in the most pronounced reduction in cardiac enzyme levels.

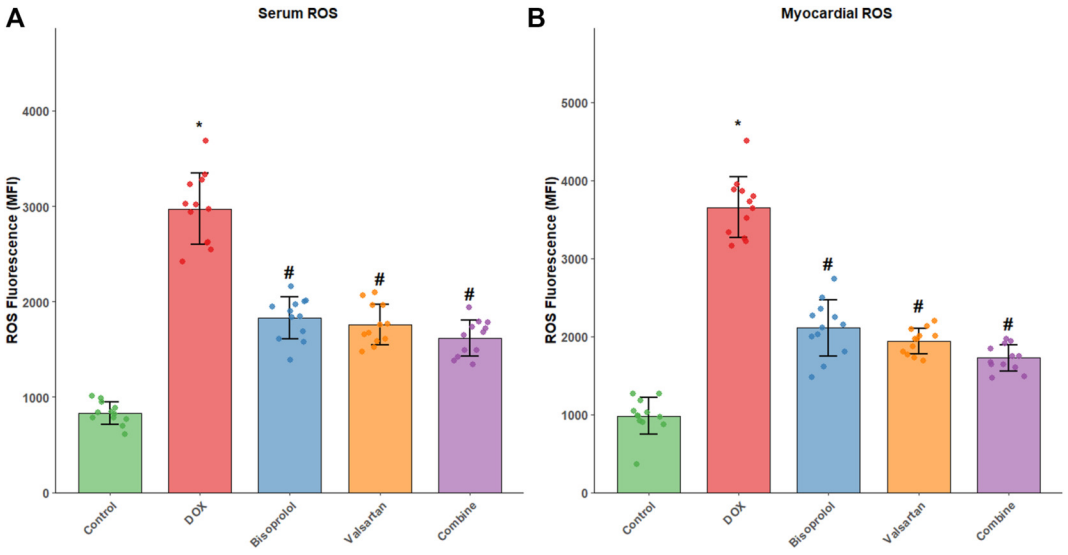

FIGURE 4
Reactive oxygen species (ROS) levels in serum and myocardial tissue. **(A)** ROS fluorescence intensity in serum-derived extracellular vesicles; **(B)** ROS fluorescence intensity in myocardial cells. ROS fluorescence intensity was measured by flow cytometry in serum-derived extracellular vesicles and myocardial cells from each group (n = 12 per group). Data are shown as mean fluorescence intensity ± SD. *P < 0.05 vs. Control group; #P < 0.05 vs. DOX group. The combination therapy exhibited the greatest reduction in ROS levels in both compartments.

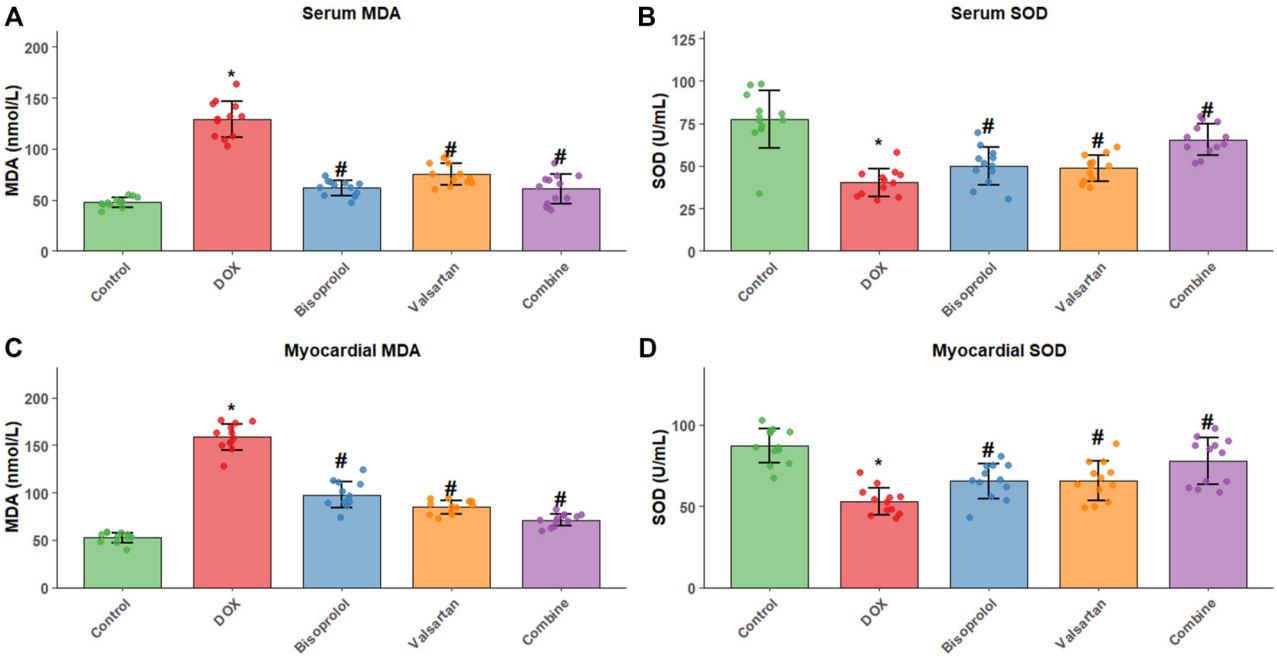

FIGURE 5
Oxidative stress markers in serum and myocardial tissue. **(A)** Serum MDA, **(B)** serum SOD, **(C)** myocardial MDA, and **(D)** myocardial SOD. Malondialdehyde (MDA) levels and superoxide dismutase (SOD) activity were measured in serum and myocardial tissue from all groups (n = 12 per group). Data are presented as mean ± SD. *P < 0.05 vs. Control group; #P < 0.05 vs. DOX group. The combination group showed the most significant improvement in oxidative stress parameters.

Expression of oxidative stress–related proteins in myocardial tissue

Compared with the Control group, protein expression levels of nuclear factor erythroid 2-related factor 2 (Nrf2), haem oxygenase-1 (HO-1), and Kelch-like ECH-associated protein 1 (Keap1) were significantly reduced in the DOX group ($P < 0.05$). In contrast, expression of Nrf2, HO-1, and Keap1 was significantly upregulated in the Bisoprolol, Valsartan, and combination groups compared with the DOX group (all $P < 0.05$). The greatest increase in protein expression was again observed in the combination group (Figure 6).

Discussion

Doxorubicin is an effective chemotherapeutic agent for the treatment of various malignancies; however, its clinical application is significantly limited by severe cardiotoxicity, which adversely affects patients' quality of life and long-term prognosis [18–20]. In this study, a rat model of doxorubicin-induced cardiotoxicity was established. Following doxorubicin administration, rats exhibited markedly reduced food intake and spontaneous activity, slowed responsiveness, and lethargy. Cardiac dysfunction was evident, accompanied by abnormal myocardial enzyme levels and varying degrees of oxidative stress in myocardial tissue. Histological analysis with H&E staining showed disordered myocardial fibre arrangement and extensive cardiomyocyte necrosis, consistent with previous findings [21], confirming the successful establishment of the cardiotoxicity model. Oxidative stress is a well-recognized mechanism underlying doxorubicin-induced cardiotoxicity. Doxorubicin acts as a highly redox-active substrate; during its metabolism, the quinone moiety undergoes redox cycling, generating excessive reactive oxygen species. These free radicals cause sarcoplasmic reticulum calcium leakage and structural damage to DNA, RNA, proteins, and lipids. Through activation of oxidative stress pathways, doxorubicin disrupts cardiomyocyte integrity, promotes apoptosis and myocardial fibrosis, impairs cardiac function, and ultimately leads to irreversible myocardial injury [22–24].

Several studies have demonstrated that early prophylactic administration of cardioprotective agents can effectively improve cardiac function and prolong survival in patients receiving doxorubicin, particularly with β-adrenergic blockers and angiotensin-converting enzyme inhibitors [25]. Sacubitril/valsartan improves cardiac function through a dual mechanism of neprilysin inhibition and angiotensin receptor blockade, thereby reducing vasoconstriction and attenuating myocardial fibrosis and hypertrophy [26, 27]. Experimental

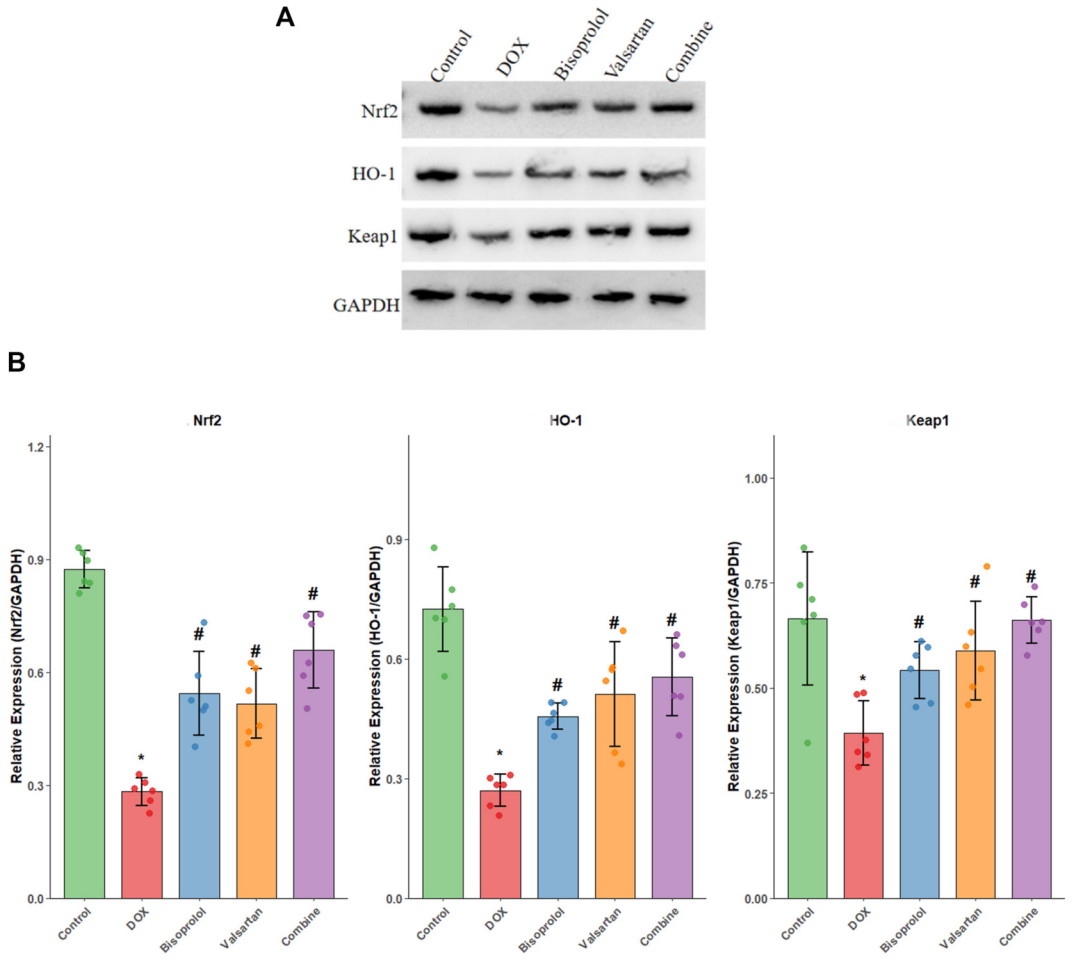

FIGURE 6
Protein expression of Nrf2, HO-1, and Keap1 in myocardial tissue. **(A)** Representative Western blot bands showing protein expression of Nrf2, HO-1, Keap1, and GAPDH (loading control) in left ventricular tissue from Control, DOX, Bisoprolol, Valsartan, and Combination groups. Each lane represents a sample from each experimental group (n = 6 per group). **(B)** Quantitative analysis of Western blot results showing relative protein expression levels of Nrf2, HO-1, and Keap1 normalized to GAPDH. Individual data points represent the quantified protein expression levels for each experimental animal (n = 6 per group), demonstrating the distribution and variability within each group. Data are presented as mean ± SD. *P < 0.05 vs. Control group; #P < 0.05 vs. DOX group (one-way ANOVA followed by LSD t-test). The combination therapy showed the most significant upregulation of all three antioxidant pathway proteins compared to the DOX group.

evidence has confirmed that sacubitril/valsartan can alleviate doxorubicin-induced myocardial fibrosis in rats, likely through modulation of oxidative stress pathways [28]. Bisoprolol, a selective β-adrenergic blocker, reduces myocardial oxygen consumption and improves cardiac perfusion by blocking cardiac β-receptors [29, 30]. Previous studies have shown that bisoprolol improves cardiac function and ventricular remodelling in heart failure models by regulating oxidative stress and apoptosis, thereby delaying myocardial fibrosis [31, 32]. However, evidence regarding the combined effects of bisoprolol and sacubitril/valsartan on doxorubicin-induced cardiotoxicity is limited. In the present study, analysis of the combination therapy revealed that, compared with the DOX group, rats in the Bisoprolol, Valsartan, and combination groups exhibited significant improvements in general condition and cardiac function. Histopathological examination further showed attenuation of myocardial injury, with the combination therapy producing the most pronounced protective effect. The observed synergy may be attributed to the dual neurohormonal modulation by sacubitril/valsartan, which inhibits angiotensin II receptors and enhances neprilysin activity to reduce vasoconstriction and promote vasodilation [33]. Meanwhile, bisoprolol, as a highly selective β-blocker, directly suppresses sympathetic activation induced by doxorubicin, thereby reducing myocardial oxygen demand [34]. The combination of these mechanisms likely cooperatively attenuates myocardial fibrosis and improves cardiac function in doxorubicin-treated rats.

Abnormal myocardial enzyme levels and oxidative stress imbalance are closely associated with doxorubicin-induced cardiotoxicity. During its metabolism, doxorubicin generates excessive reactive oxygen species (ROS), disrupting the myocardial oxidative–antioxidative balance. This imbalance compromises the integrity of cardiomyocyte membranes, leading to elevated myocardial enzymes and, ultimately, impaired cardiac function [35]. These observations underscore the pivotal role of oxidative stress in doxorubicin-induced cardiotoxicity.

In the present study, treatment with Bisoprolol, Valsartan, or their combination significantly reduced myocardial CK-MB, cTnI, and BNP levels, as well as ROS fluorescence intensity and malondialdehyde (MDA) content in both myocardial tissue and serum, while superoxide dismutase (SOD) activity was markedly increased. Importantly, the detection of ROS in circulating EV-enriched fractions by flow cytometry provided a complementary "liquid biopsy" assessment of systemic oxidative stress. It should be acknowledged that this method, based on scatter gating, cannot definitively distinguish extracellular vesicles from other submicron particles such as lipoproteins or protein aggregates, and therefore the results should be interpreted as ROS associated with an EV-enriched particle population rather than pure EVs. Nevertheless, the observed correlation between serum particle-associated ROS and intramyocardial oxidative status supports the utility of this method as a complementary indicator of systemic oxidative stress. Among the treatments, the combination therapy produced the most pronounced improvements, indicating that co-administration effectively attenuates myocardial injury. Although single-drug interventions improved oxidative stress and myocardial enzyme profiles, the combined therapy was superior, likely due to its synergistic reduction of ROS generation, inhibition of lipid peroxidation, and enhancement of antioxidant enzyme activity, thereby mitigating oxidative injury to cardiomyocytes and normalizing myocardial enzyme expression. The Nrf2/HO-1 signalling pathway is a key regulator of oxidative stress, and previous studies have shown that its activation can ameliorate doxorubicin-induced cardiotoxicity and delay the progression of myocardial fibrosis in rats [36–37]. Consistently, in this study, Bisoprolol, Valsartan, and their combination upregulated Nrf2, HO-1, and Keap1 protein expression, further demonstrating that the combined therapy mitigates doxorubicin-induced cardiotoxicity through modulation of oxidative stress pathways.

In summary, sacubitril/valsartan combined with bisoprolol attenuates doxorubicin-induced cardiotoxicity in rats via regulation of oxidative stress, thereby improving cardiac function and myocardial enzyme profiles. These findings provide experimental support for potential clinical strategies to prevent doxorubicin-related cardiac injury.

Author contributions

PL: Conceptualization, Methodology, Investigation, Formal Analysis, Data Curation, Writing – Original Draft. HY: Conceptualization, Methodology, Investigation, Formal Analysis, Data Curation, Writing – Original Draft. RL: Data Curation, Validation, Writing – Review and Editing. HH: Supervision, Resources, Validation, Project Administration, Writing – Review and Editing. MX: Supervision, Project Administration, Visualization, Writing – Review and Editing. All authors contributed to the article and approved the submitted version.

Data availability

The original contributions presented in the study are included in the article/supplementary material, further inquiries can be directed to the corresponding authors.

Ethics statement

This study was approved by the Ethics Committee of Xinhua Hospital of ili Kazak Autonomous Prefecture (XHYY-LW-2025003). All applicable institutional and governmental regulations concerning the ethical use of animals were followed. The study was conducted in accordance with the local legislation and institutional requirements.

Funding

The author(s) declared that financial support was received for this work and/or its publication. This work was supported by the (2023 Zhanjiang Non-Funded Science and Technology Research Program (Project No. : 2023B01081)), but received no specific financial grant. This work was supported by the (2023 Zhanjiang Non-Funded Science and Technology Research Program (Project No. : 2023B01191)), but received no specific financial grant.

Conflict of interest

The author(s) declared no potential conflicts of interest with respect to the research, authorship, and/or publication of this article.

Generative AI statement

The author(s) declared that generative AI was not used in the creation of this manuscript.

Any alternative text (alt text) provided alongside figures in this article has been generated by Frontiers with the support of artificial intelligence and reasonable efforts have been made to ensure accuracy, including review by the authors wherever possible. If you identify any issues, please contact us.

References

1. Li LY, He WB, Hao YX, Li SM. Clinical significance of the albumin-to-alkaline phosphatase ratio in evaluating anthracycline-induced cardiotoxicity following surgery for breast cancer. *Clin Misdiagnosis and Mistherapy* (2023) **36**(3):50–3. doi:10.3969/j.issn.1002-3429.2023.03.012

2. Vaitiekus D, Muckiene G, Verikas D, Vaitiekiene A, Astasauskaite S, Gerbutavicius R, et al. Drugs metabolism-related genes variants impact on anthracycline-based chemotherapy induced subclinical cardiotoxicity in breast cancer patients. *Int J Mol Sci* (2025) **26**(9):4051. doi:10.3390/ijms26094051

3. Qiao X, van der Zanden SY, Li X, Tan M, Zhang Y, Song JY, et al. Diversifying the anthracycline class of anti-cancer drugs identifies aclarubicin for superior survival of acute myeloid leukemia patients. *Mol Cancer* (2024) **23**(1):120. doi:10.1186/s12943-024-02034-7

4. Tai P, Chen X, Jia G, Chen G, Gong L, Cheng Y, et al. WGX50 mitigates doxorubicin-induced cardiotoxicity through inhibition of mitochondrial ROS and ferroptosis. *J Transl Med* (2023) **21**(1):823. doi:10.1186/s12967-023-04715-1

5. Ye C, Yan C, Bian SJ, Li XR, Li Y, Wang KX, et al. Momordica charantia L.-derived exosome-like nanovesicles stabilize p62 expression to ameliorate doxorubicin cardiotoxicity. *J Nanobiotechnology* (2024) **22**(1):464. doi:10.1186/s12951-024-02705-z

6. Wu L, Wang L, Du Y, Zhang Y, Ren J. Mitochondrial quality control mechanisms as therapeutic targets in doxorubicin-induced cardiotoxicity. *Trends Pharmacol Sci* (2023) **44**(1):34–49. doi:10.1016/j.tips.2022.10.003

7. Dobson R, Ghosh AK, Ky B, Marwick T, Stout M, Harkness A, et al. British society for echocardiography and British cardio-oncology society guideline for transthoracic echocardiographic assessment of adult cancer patients receiving anthracyclines and/or trastuzumab. *Echo Res Pract* (2021) **8**(1):G1–G18. doi:10.1530/ERP-21-0001

8. Shi YK, Ba Y, Feng JF, Lyu Y, Xu JP, He XH, et al. Chinese expert consensus on the characteristics of anthracyclines. *Chin J Clin Oncol* (2018) **45**(3):109–12. doi:10.3969/j.issn.1000-8179.2018.03.955

9. Keshavarzian E, Sadighpour T, Mortazavizadeh SM, Soltani M, Motevalipoor AF, Khamas SS, et al. Prophylactic agents for preventing cardiotoxicity induced following anticancer agents: a systematic review and meta-analysis of clinical trials. *Rev Recent Clin Trials* (2023) **18**(2):112–22. doi:10.2174/1574887118666230118102252

10. Lewinter C, Nielsen TH, Edfors LR, Linde C, Bland JM, LeWinter M, et al. A systematic review and meta-analysis of beta-blockers and renin-angiotensin system inhibitors for preventing left ventricular dysfunction due to anthracyclines or trastuzumab in patients with breast cancer. *Eur Heart J* (2022) **43**(27):2562–9. doi:10.1093/eurheartj/ehab843

11. Liu JQ, Yao Yi, Sui Q, Li K, Huang F, Cao YQ. Mechanisms of sacubitril/valsartan in the prevention of doxorubicin-induced cardiotoxicity. *The J Pract Med* (2024) **40**(2):188–94. doi:10.3969/j.issn.1006-5725.2024.02.011

12. Devereux G, Cotton S, Nath M, McMeekin N, Campbell K, Chaudhuri R, et al. Bisoprolol in patients with chronic obstructive pulmonary disease at high risk of exacerbation: the BICS randomized clinical trial. *JAMA* (2024) **332**(6):462–70. doi:10.1001/jama.2024.8771

13. Ma YR, Zhao L. Effects of bisoprolol on cardiomyocyte function and the MAPK/ERK1/2 signaling pathway in rats with chronic heart failure. *China J Mod Med* (2020) **30**(23):6–10. doi:10.13753/j.issn.1007-6611.2020.23.002

14. Zhang H, Xie S, Deng W. Mitophagy in doxorubicin-induced cardiotoxicity: insights into molecular biology and novel therapeutic strategies. *Biomolecules* (2024) **14**(12):1614. doi:10.3390/biom14121614

15. Vitale R, Marzocco S, Popolo A. Role of oxidative stress and inflammation in doxorubicin-induced cardiotoxicity: a brief account. *Int J Mol Sci* (2024) **25**(13):7477. doi:10.3390/ijms25137477

16. Chen Y, Guo X, Zeng Y, Mo X, Hong S, He H, et al. Oxidative stress induces mitochondrial iron overload and ferroptotic cell death. *Sci Rep* (2023) **13**(1):15515. doi:10.1038/s41598-023-42760-4

17. Žėkas V, Kurg R, Kurg K, Bironaitė D, Radzevičius M, Karčiauskaitė D, et al. Oxidative properties of blood-derived extracellular vesicles in 15 patients after myocardial infarction. *Med Sci Monit* (2022) **28**:e935291. doi:10.12659/MSM.935291

18. He W, Sun Z, Tong G, Zeng L, He W, Chen X, et al. FUNDC1 alleviates doxorubicin-induced cardiotoxicity by restoring mitochondrial-endoplasmic reticulum contacts and blocked autophagic flux. *Theranostics* (2024) **14**(9):3719–38. doi:10.7150/thno.92771

19. Al-Chlaihawi M, Janabi A. Azilsartan improves doxorubicin-induced cardiotoxicity via inhibiting oxidative stress,proinflammatory pathway, and apoptosis. *J Med Life* (2023) **16**(12):1783–8. doi:10.25122/jml-2023-0106

20. Zhang H, Wang Y, Wang R, Yi Q, Xu H, Tan B, et al. Kartogenin improves doxorubicin-induced cardiotoxicity by alleviating oxidative stress and protecting mitochondria. *Int J Mol Sci* (2025) **26**(6):2434. doi:10.3390/ijms26062434

21. Li RQ, Zhai ZH, Du QQ, Wang Z. Protective effect of TBHQ against chronic doxorubicin-induced cardiotoxicity in rats. *J Shanxi Med Univ* (2024) **55**(7):835–41. doi:10.13753/j.issn.1007-6611.2024.07.004

22. Lin Z, Wu C, Song D, Zhu C, Wu B, Wang J, et al. Sarmentosin alleviates doxorubicin-induced cardiotoxicity and ferroptosis via the p62-Keap1-Nrf2 pathway. *Redox Rep* (2024) **29**(1):2392329. doi:10.1080/13510002.2024.2392329

23. Yang D, Chen YH, Chen YK, Zeng YL, Ling ZY. Tirzepatide alleviates doxorubicin-induced cardiotoxicity via inhibiting HRD1-mediated Nrf2 ubiquitination. *Cardiovasc Res* (2025) **121**(12):1865–82. doi:10.1093/cvr/cvaf033

24. Mao M, Zheng W, Deng B, Wang Y, Zhou D, Shen L, et al. Cinnamaldehyde alleviates doxorubicin-induced cardiotoxicity by decreasing oxidative stress and ferroptosis in cardiomyocytes. *PLoS One* (2023) **18**(10):e0292124. doi:10.1371/journal.pone.0292124

25. Chen YF, Shen YH, Cheng LL, Lin JY, Zhang H, Wang XJ, et al. Differential preventive effects of four cardioprotective agents against doxorubicin-induced cardiotoxicity in mice. *Chin J Cancer* (2022) **32**(10):936–47. doi:10.19401/j.cnki.1007-3639.2022.10.002

26. Le D, Grams ME, Coresh J, Shin JI. Sacubitril-valsartan in patients requiring hemodialysis. *JAMA Netw Open* (2024) **7**(8):e2429237. doi:10.1001/jamanetworkopen.2024.29237

27. Morrow DA, Velazquez EJ, Desai AS, DeVore AD, Lepage S, Park JG, et al. Sacubitril/valsartan in patients hospitalized with decompensated heart failure. *J Am Coll Cardiol* (2024) **83**(12):1123–32. doi:10.1016/j.jacc.2024.01.027

28. Song XY, Li JF, Cheng XH, Chen YJ. Mechanism of action of sacubitril/valsartan in inhibiting doxorubicin-induced myocardial fibrosis in rats. *Chin J Integr Med Cardio/Cerebrovascular Dis* (2023) **21**(17):3154–9. doi:10.12102/j.issn.1672-1349.2023.17.009

29. Sharma K, Sathe S, Desai B, Manchanda S, Mohan J, Bansal M, et al. Optimizing cardiovascular outcomes with bisoprolol: an evidence-based perspective. *Cureus* (2025) **17**(8):e89579. doi:10.7759/cureus.89579

30. Kittleson MM. Guidelines for treating heart failure. *Trends Cardiovasc Med* (2025) **35**(3):141–50. doi:10.1016/j.tcm.2024.10.002

31. Belenichev I, Goncharov O, Bukhtiyarova N, Kuchkovskyi O, Ryzhenko V, Makyeyeva L, et al. Beta-blockers of different generations: features of influence on the disturbances of myocardial energy metabolism in doxorubicin-induced chronic heart failure in rats. *Biomedicines* (2024) **12**(9):1957. doi:10.3390/biomedicines12091957

32. Lyu XY, Ma AQ, Wang TZ, Feng ZB, Yuan B, Liu ML. Effects of bisoprolol on calcium-handling proteins in ventricular myocytes of rats with volume-overload heart failure. *Chin J Geriatr Heart Brain Vasc Dis* (2017) **19**(2):184–7. doi:10.3969/j.issn.1009-0126.2017.02.019

33. Wu JB, Ye XH, Xian SX, Dong MG. Effects of bisoprolol combined with perindopril on myocardial endoplasmic reticulum stress in rats with doxorubicin-induced heart failure. *Chin J Pathophysiology* (2016) **32**(11):1939–44. doi:10.3969/j.issn.1000-4718.2016.11.004

34. Hu F, Yan S, Lin L, Qiu X, Lin X, Wang W. Correction to: sacubitril/valsartan attenuated myocardial inflammation, fibrosis, apoptosis and promoted autophagy in doxorubicin-induced cardiotoxicity mice via regulating the AMPKα-mTORC1 signaling pathway. *Mol Cell Biochem* (2025) **480**(5):3217. doi:10.1007/s11010-024-05159-x

35. Chen S, Chen J, Du W, Mickelsen DM, Shi H, Yu H, et al. PDE10A inactivation prevents doxorubicin-induced cardiotoxicity and tumor growth. *Circ Res* (2023) **33**(2):138–57. doi:10.1161/CIRCRESAHA.122.322264

36. Hu S, Liu B, Yang M, Mao S, Ju H, Liu Z, et al. Carnosic acid protects against doxorubicin-induced cardiotoxicity through enhancing the Nrf2/HO-1 pathway. *Food Funct* (2023) **14**(8):3849–62. doi:10.1039/d2fo03904d

37. Li D, Zhang W, Fu H, Wang X, Tang Y, Huang C. DL-3-n-butylphthalide attenuates doxorubicin-induced acute cardiotoxicity via Nrf2/HO-1 signaling pathway[J]. *Heliyon* (2024) **10**(5):e27644. doi:10.1016/j.heliyon.2024.e27644

EBM Experimental Biology and Medicine

TYPE Original Research
PUBLISHED 30 March 2026
DOI 10.3389/ebm.2026.10850

OPEN ACCESS

*CORRESPONDENCE
John J. Kopchick,
kopchick@ohio.edu

RECEIVED 03 October 2025
REVISED 22 January 2026
ACCEPTED 06 March 2026
PUBLISHED 30 March 2026

CITATION
Walsh C, Kirstein M, Wagner E, Scott E, Walsh J, Reddy S, Hoggard N, Ahmad A, Basu R, Mathes S, Qian Y and Kopchick JJ (2026) Lymphatic pumping technique in mice alters blood parameters and metastatic melanoma in an age-dependent manner. *Exp. Biol. Med.* 251:10850. doi: 10.3389/ebm.2026.10850

Lymphatic pumping technique in mice alters blood parameters and metastatic melanoma in an age-dependent manner

Christopher Walsh[1,2], Matthew Kirstein[3], Elise Wagner[3], Emily Scott[3], Jerome Walsh[1], Shashank Reddy[1], Nathan Hoggard[1], Arshad Ahmad[2], Reetobrata Basu[1,2], Sam Mathes[2], Yanrong Qian[1,2] and John J. Kopchick[1,2]*

[1]Heritage College of Osteopathic Medicine, Ohio University, Athens, OH, United States, [2]Institute for Molecular Medicine and Aging, Ohio University, Athens, OH, United States, [3]Department of Biological Sciences, Ohio University, Athens, OH, United States

Abstract

Therapeutic touch applied to primary tumors can increase metastasis. The goal of this project was to determine whether touch applied to metastatic tumors also increases metastasis. We evaluated touch on a mouse model of experimental metastasis using a manual treatment called Lymphatic Pumping Technique (LPT), which increases lymphatic fluid flow and is contraindicated in patients with cancer. The LPT, or a sham treatment, was administered for 5 minutes while the mice were anesthetized with vaporized isoflurane. Young adult (3 months old) and aged (20–24 months old) mice received daily sham or LPT treatments for 7 days prior to the injection of 200k B16F10-luc2 mouse melanoma cells into the tail vein, then treated every other day for 21 days. In middle-aged (9–11 months old) mice, we waited 8 days after tumor injection to start treatments and assessed the effect of LPT on immunotherapy efficacy. These mice also received either LPT or sham every other day, along with four doses of 200 μg anti–PD-1 or isotype control antibody. LPT did not increase tumor growth or spread in any of the experiments. Surprisingly, LPT was negatively associated with metastasis in young and middle-aged mice, without enhancing or diminishing the efficacy of immunotherapy. In mice without cancer, LPT rapidly elevated red blood cell, white blood cell, and platelet counts in young, but not middle-aged, animals. Taken together, these findings suggest that therapeutic touch near metastatic tumors does not worsen disease and may confer an age-dependent benefit.

KEYWORDS

lymphatic pumping technique, manual therapy, melanoma, metastasis, osteopathy

Impact statement

Current clinical guidelines broadly discourage therapeutic touch near all tumors based on evidence derived almost exclusively from primary tumor models. This study is the first to directly evaluate the effect of touch on metastatic disease. Using mouse models of experimental metastasis and the lymphatic pumping technique, a form of touch that maximizes theoretical risk, we demonstrate that touch does not increase metastatic growth or spread and, in fact, reduces it in an age-dependent manner. These findings reveal that the biological impact of touch on cancer is not uniform but varies with age and disease stage. By showing that therapeutic touch can be safe and potentially beneficial in diffuse metastatic disease, this work challenges long-standing assumptions in oncology. Integrating osteopathic manual medicine with molecular cancer biology, this study bridges two traditionally separate fields and identifies a novel, non-pharmacologic avenue for adjunctive cancer therapy.

Introduction

Metastatic tumors growing outside of the primary tumor are the leading cause of death in patients with cancer [1]. Surgical and radiation-based treatments are highly effective for localized tumors but become limited in metastatic disease, which can present with many tumors in multiple organs. Systemic chemical therapies remain the standard approach for the treatment of metastatic disease, yet survival declines precipitously after metastasis. For example, the 5-year survival rate after the diagnosis of melanoma drops from nearly 100% for localized disease to 35% for patients with tumors that have grown in distant organs [2]. These stark disparities underscore the importance of specifically studying and targeting metastatic disease.

An essential stage of cancer metastasis is colonization, during which newly arrived cancer cells remodel the local organ interstitium into a permissive tumor microenvironment [3]. An important driver of this transformation is the disruption of the organ's fascial network. Fascia, a connective tissue continuum that organizes and mechanically integrates organs and their microenvironments, exerts biomechanical forces that influence cell behavior. When dysregulated, the fascia can promote tumorigenesis and metastatic progression [4]. Emerging work focused on manual techniques has introduced the concept that physical manipulation of the fascia could be used to study, and potentially disrupt, the tumor microenvironment [5].

Despite this potential, the effects of touch on metastatic disease remain largely unexplored. In contrast, physical manipulation near primary tumors has been associated with increased metastatic spread in both animal and large-scale observational studies [6–8]. These findings have shaped clinical guidelines, which broadly recommend against the use of manual therapies near any tumor [9]. While appropriately cautious, such recommendations are largely extrapolated from studies of primary tumors and may inadvertently limit beneficial supportive care. Therapeutic touch has demonstrated value in oncology [10], including reductions in cancer-associated pain [11], chemotherapy-induced constipation [12], and post mastectomy lymphedema [13]. Osteopathic manipulative medicine is a form of manual medicine capable of addressing cancer comorbidities, but patients with diffuse metastatic disease are often excluded due to a theoretical risk of promoting tumor spread.

One osteopathic technique of particular concern is the lymphatic pumping technique (LPT), which is a commonly used manipulation that increases lymph production and flow through rhythmic compression and release of tissue spaces. This mechanical force distorts the interstitium, opening primary lymphatic valves, and increasing perivascular lymphatic pressure, thereby enhancing lymph production and flow through the lymphatic system [14]. Because LPT increases tissue fluid movement, it is presumed to pose a heightened risk for facilitating cancer dissemination and is specifically contraindicated in patients with cancer [9]. For this reason, we believed LPT could be used to study the risk posed by physical manipulation of the metastatic tumor.

We designed the experiments, detailed in Figure 1, to assess the effect of LPT on melanoma growth and spread in a mouse model of experimental metastasis using young adult and aged mice. Ageing increases tissue stiffness [15] and the accumulation of dysregulated immune mechanisms [16]. Since LPT relies on tissue distortion to activate the lymphatic system, we hypothesized that the stiffer tissue in older animals would be less responsive to LPT. Likewise, the depressed capacity of the aged immune system to mount a successful immune response could limit any immune benefit brought by LPT in the aged cohort. Following the observation of a beneficial impact of LPT in young mice, we investigated whether LPT could further enhance the anti-tumor immune response induced by immune checkpoint blockade in middle-aged mice. In addition to *in vivo* and *ex vivo* measures of tumor burden, we assessed the effect of LPT on the tumor microenvironment by measuring the expression of proteins associated with epithelial-to-mesenchymal transition and lymphangiogenesis. Lastly, we evaluated the influence of age on LPT's ability to move non-cancerous cells by measuring the complete blood cell count in whole blood collected from mice before and immediately after LPT.

Materials and methods

Lymphatic pumping technique (LPT)

The LPT used in this study is a series of manual therapies designed to increase whole-body lymphatic flow by relaxing

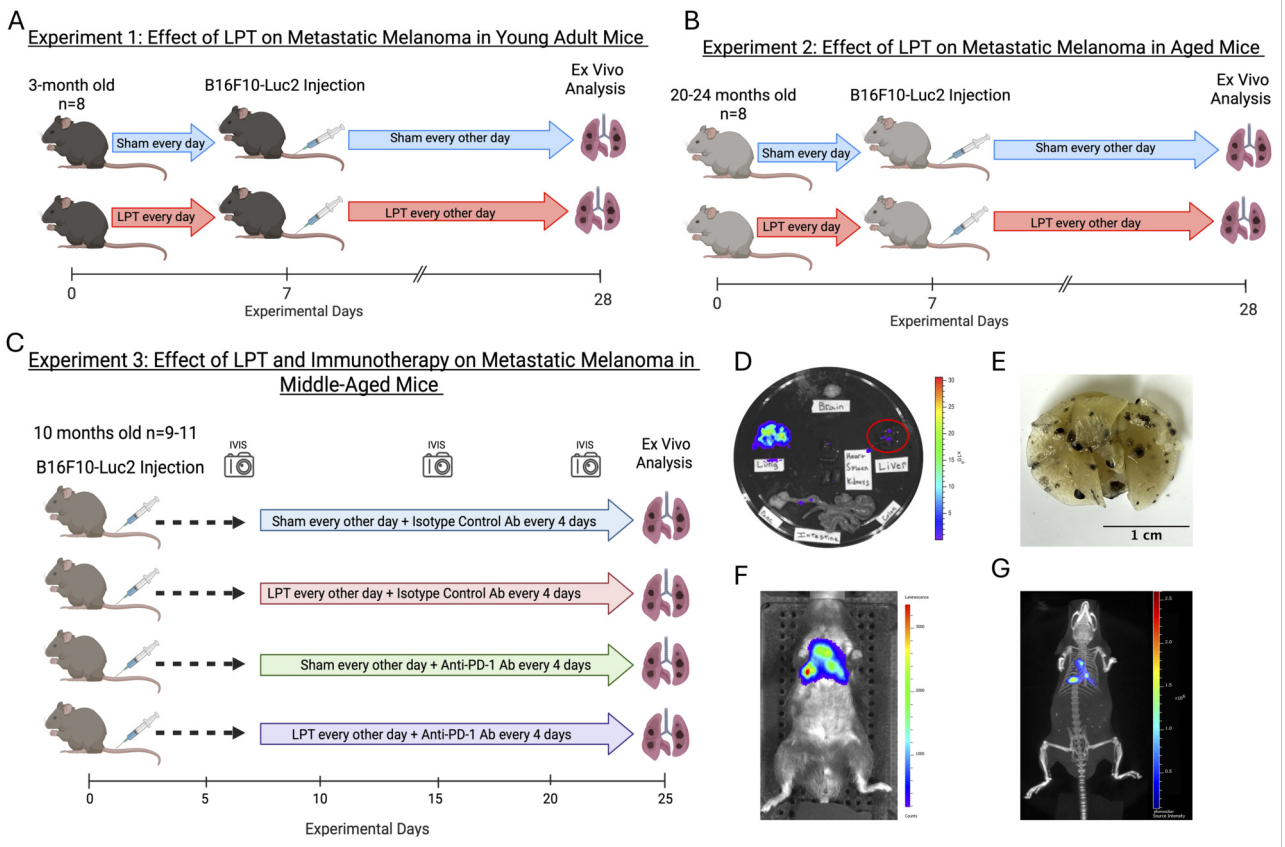

FIGURE 1
Methods and experimental design. An illustrated workflow for the first experiment with young adult mice **(A)**, the second experiment with aged mice **(B)**, and the third experiment with middle-aged mice and the addition of immunotherapy **(C)**. The lymphatic pumping technique (LPT) sequence used in the treatment group **(D)**, along with the hand placement **(G)** used during thoracic LPT. Example of the 2D bioluminescent imaging used to measure tumor burden *in vivo* **(H)** and *ex vivo* **(E)**. **(F)** A photo of formalin-fixed lungs from mice bearing B16F10-Fluc metastatic tumor growth. **(I)** Example of the 3D bioluminescent imaging of B16F10-Fluc lung metastasis. The graphics in A, B, and C were created in BioRender. Walsh, C. (2026) https://BioRender.com/m1cz62o.

myofascial tension at transition areas around the thorax and abdomen, followed by lymphatic pumping of the thoracic and abdominal cavities. Similar thoracic and abdominal LPTs have been used separately in preclinical rodent models of pneumonia [17] and inflammatory bowel disease [18]. The LPT and sham treatments were performed under general anesthesia using 2.0–2.5% isoflurane and prewarmed heating pads. Mice in the control group received a sham treatment consisting of 5 minutes of general anesthesia only. Mice in the LPT group received the following series of manual therapies: a 1-min soft-tissue massage, 2 min of thoracic LPT, and 2 min of abdominal LPT. To allow time for normal respirations, the mouse was not touched for 15 seconds between the rounds of thoracic LPT. The soft tissue massage consisted of medial-to-lateral kneading of the diaphragm and circular massaging of the axilla and inguinal areas. Thoracic lymphatic pumping was performed by placing the thumb on one side of the rib cage and an index and middle finger on the opposite rib cage, specifically, 1 cm lateral and cranial to the xiphoid cartilage. Then, with the index finger of the opposite hand, light pressure is exerted over the sternum in a dorsal-caudal direction until rib cage compression is appreciated and then released. Similarly, abdominal lymphatic pumping was performed by placing the thumb and forefinger on the lateral edge of the abdomen, then compressing the abdomen with the finger of the opposite hand in a dorsal-cranial direction until counterpressure from the ribs against the diaphragm was appreciated. This pressure is applied at a rate of 1 compression per second for both techniques. The same 5-min LPT sequence was used for all experiments in this study. A video of the LPT treatment is available in Supplementary Video S1.

Melanoma lung metastasis model

A widely used method for studying metastatic tumors is the experimental lung metastasis model, which mimics the metastatic

process by injecting cancer cells into the mouse's tail vein. The cells used were B16F10-Fluc-Puro mouse melanoma cells (Imanis Cat# CL052, RRID:CVCL_QZ90), which were maintained in T75 flasks with regular media changes consisting of Dulbecco's modified Eagle's medium containing 10% fetal bovine serum, 1% Penicillin/Streptomycin, and 1ug/mL puromycin and injected into the mice before cell passage 9. Luciferase expression was checked in the cell passage before injection by plating cells at increasing concentrations on a 12-well plate. The following day, the cells were washed with warm phosphate-buffered saline (PBS) and incubated in PBS containing 15 μg/mL of IVISbrite D-Luciferin (#122799, Revity), then imaged with an IVIS imaging unit. On the day of tumor injection, cells from the same passage number were washed twice, dissociated from their flask using 0.25% trypsin-EDTA, centrifuged, resuspended in cold PBS at 2 million cells/mL, and kept on ice until tail vein injection. Before injection, mice were warmed under a heat lamp for 1 min and then placed under general anesthesia as previously described. The injection location over the lateral tail vein was wiped with 70% alcohol, then punctured with a 29 G needle to intravenously inject 200,000 melanoma cells in 100 μL of PBS. The number of cells was selected based on a standard protocol, which states that metastatic tumors can be measured for 3 weeks after cancer cell injection and before death is expected due to pulmonary congestion [19].

Wild-type male C57BL/6J mice were used in all cancer experiments (RRID:IMSR_JAX:000664). We used 3-month-old mice for the young group, 10-month-old mice for the middle-aged group, and 20–24-month-old mice for the aged group, roughly corresponding to humans aged 20, 45, and 80 years, respectively [20]. Mice were randomly assigned to groups before the experiment, and each cage received the same treatment. If a mouse died before the experimental endpoint, the animal was removed from the study. Only one mouse died early and was removed from the study: a middle-aged mouse in the control group.

The experimental design of the four *in vivo* experiments reported in this study is shown in Figure 1. The goals of Experiments 1 (Figure 1A) and 2 (Figure 1B) were to assess how increased lymphatic flow affects tumor metastasis at both young adult and advanced ages. Therefore, we performed LPT before and after the injection of cancer cells. Specifically, the sham and LPT treatments were administered daily on days 1–7; the cancer cells were injected on day 8; and the animals were treated every other day on days 7–27. On day 28, mice were euthanized with carbon dioxide inhalation. In Experiment 3 (Figure 1C), we aimed to increase the clinical translatability of the study by initiating LPT after cancer cell injection and combining it with a commonly used treatment for metastatic melanoma, an immune checkpoint inhibitor. In addition to the sham and LPT treatments, the mice were treated with anti-mouse programmed cell death protein 1 (PD1) antibody (#PA007163.m2cLA, Syd Labs) or an isotype control antibody (#PA007141, Syd Labs). Four treatments of 200 μg of antibody diluted in 100 μL of PBS (2 mg/mL) were administered intraperitoneally between days 9 and 21 of the experiment. The anti-PD1 dosing regimen of 200 ug per injection was selected based on established murine immunotherapy protocols rather than allometric scaling from human doses, consistent with prior studies demonstrating biological efficacy at this dose [21, 22]. Mice were divided into four treatment groups: group 1 received sham treatment and isotype control antibodies; group 2 received LPT and isotype control antibodies; group 3 received sham treatment and anti-PD1 antibodies; and group 4 received LPT treatment and anti-PD1 antibodies. The cancer cells were injected on experimental day 0, treatments started on day 8, ended on day 22, and the mice were euthanized with carbon dioxide inhalation and on day 25.

At the end of each experiment, ex vivo bioluminescent imaging was performed to quantify tumor growth and spread. Prior to euthanasia, mice were injected with D-luciferin (#88292, Thermo Fisher Scientific) at 150 mg/kg of body weight, dissolved in PBS, into the peritoneum. After 7 min, the mice were euthanized by carbon dioxide inhalation, and the organs (brain, lungs, heart, spleen, kidneys, liver, pancreas, and small and large intestines) were removed, placed on a plastic dish, and immediately imaged. An ROI was drawn around each individual organ to calculate the total signal for each mouse. Figure 1 depicts examples of ex vivo imaging (Figure 1D), formalin-fixed lungs (Figure 1E), 2D imaging (Figure 1F), 3D imaging (Figure 1G) generated using the techniques described above. For experiments 1 and 2, tumors were imaged using the Xenogen IVIS 100 Imaging System (RRID:SCR_020901), and the images were analyzed with Living Image 3.50 software (RRID:SCR_014247). A new IVIS imaging unit (IVIS SpectrumCT 2, #CLS158737, Revvity) was used for Experiment 3, offering improved tumor visualization and a standardized alternative method for calculating the bioluminescent signal, called counts, using Living Image 4.8 Software (Revvity). During weekly in vivo imaging sessions, mice were intraperitoneally injected with 4.5 mg of diluted IVISbrite D-Luciferin (#122799, Revvity) in 150 μL and imaged using auto-exposure settings, with 2D and 3D CT-assisted image reconstruction.

Saphenous bleeding and CBC

By collecting whole blood, we were able to assess the ability of LPT to flux non-cancerous cells into the bloodstream. For this, we used young adult and middle-aged male and female mice. They were warmed under a heat lamp for 1 min and then placed under general anesthesia using vaporized isoflurane as described previously. The skin above the lateral saphenous vein was shaved, wiped with 70% ethanol, and coated with a small amount of petroleum jelly. The vein was pierced with a 27-

gauge needle, and 100 μL of blood was collected into an EDTA-coated polypropylene blood collection tube (Microvette, Sarstedt). After achieving hemostasis using finger pressure, 5 minutes of sham or LPT treatment were performed. After the intervention, a subsequent blood sample was collected from the opposite leg. After blood collection, each sample was placed on a blood rocker for 10 min and then analyzed using an automated hematology system (Hemavet 950FS, Drew Scientific, USA). For each mouse, the blood parameters before LPT were subtracted from those after LPT. A two-tailed t-test was then performed for each parameter. The blood parameters measured were white blood cells, neutrophils, lymphocytes, monocytes, eosinophils, basophils, red blood cells, hemoglobin, hematocrit, mean corpuscular volume, mean corpuscular hemoglobin, mean corpuscular hemoglobin concentration, red blood cell distribution width, and platelet count.

Western blot analysis

After dissection, the heart and lungs were snap frozen in liquid nitrogen. Proteins were extracted from 35 mg of tissues using a 2x RIPA protein extraction buffer with 1:100 protease/phosphatase inhibitor and 1:100 phenylmethylsulfonyl fluoride. A Precellys tissue homogenizer was used to create a lysate, which was then centrifuged and sonicated at 4 °C for 15 min to purify the protein. Protein concentrations were determined using the Bradford assay, allowing for the separation of 50 μg of each sample via SDS-PAGE. Proteins were transferred from the gel to PVDF membranes using a Trans-Blot Turbo Transfer System (BIO-RAD). Total protein transferred to the blot was measured using AdvanStain Ponceau protein staining (#R-03021-D50, Advansta). Membranes were blotted overnight with the following primary antibodies against lymphatic vessel hyaluronic receptor 1(LYVE1) (Goat, 1:1000, R and D Systems Cat# AF2125, RRID:AB_2297188), podoplanin (PDPN) (Rat, 1:1000, Abcam Cat# ab256559, RRID:AB_2936436), prospero homeodomain protein 1 (PROX1) (Rabbit, 1:1000, Abcam Cat# ab199359, RRID:AB_2868427), vascular endothelial growth factor receptor 3 (VEGFR3) (Rat, 1:1000, Thermo Fisher Scientific Cat# 14–5988-82, RRID:AB_467795), platelet endothelial cell adhesion molecule (CD31) (Rabbit, 1:500, Proteintech Cat# 28083-1-AP, RRID:AB_2881055), E-cadherin (ECAD) (Rabbit, 1:1000, Cell Signaling Technology Cat# 3195, RRID:AB_2291471), N-cadherin (NCAD) (Rabbit, 1:1000, Cell Signaling Technology Cat# 13116, RRID:AB_2687616), vimentin (VIM) (Rabbit, 1:1000, Cell Signaling Technology Cat# 5741, RRID:AB_10695459), slug (Rabit, 1:1000, Cell Signaling Technology Cat# 9585, RRID:AB_2239535), programmed death ligand 1 PDL1(Rabbit, 1:1000, Cell Signaling Technology Cat# 60475, RRID:AB_2924680) and programmed death ligand 2 (PDL2) (Rabbit, 1:1000, Cell Signaling Technology Cat# 82723, RRID:AB_2799999). After multiple washes, the blots were incubated for 1 hour with secondary antibodies linked to horseradish peroxidase (HRP), including an anti-rat-HRP (Goat, 1:2000, Thermo Fisher Scientific Cat# 31470, RRID:AB_228356), an anti-goat-HRP (Chicken, 1:2000, R and D Systems Cat# HAF019, RRID:AB_573132), and an anti-rabbit-HRP (Goat, 1:2000, Cell Signaling Technology Cat# 7074, RRID:AB_2099233). Blots were developed using luminol-based enhanced chemiluminescence HRP-substrate (SuperSignal West Dura Extended Duration Substrate, ThermoFisher # 34075) and imaged on an Azure 300. Densitometric analysis was performed using Image Studio. The signal of the target proteins was normalized to the total protein stain in that sample's lane by dividing the target signal by the normalized total protein signal.

Quantitative polymerase chain reaction (qPCR)

Total RNA was extracted from 50 mg of snap-frozen tissue using the GeneJET RNA Purification Kit (Thermo Scientific # K0731) according to the manufacturer's protocols. Equal amounts of total RNA, quantified with nanodrop, were then converted to cDNA using oligo-dT reverse transcription with the High-Capacity cDNA Reverse Transcription Kit (Thermo Scientific # 4368814). Quantitative PCR was performed using SYBR Green dye-based amplification and detection with SYBR Green Universal Master Mix (Applied Biosystems # 4309155) and a QuantStudio Real-Time PCR System 3 (Applied Biosystems). Target gene expression was normalized to actin and prostaglandin E receptor 2 expression and compared between treatment groups using the ΔΔ CT method. The KiCqStart primer (Millipore Sigma # KSPQ12012) sequence pairs used were for mouse prospero homeobox 1 (*Prox1*; Fwd: GACGTG AAGTTCAACAGATG and Rev: TTGTTGTAGTGCATGTTG AG), vascular endothelial growth factor receptor 3 (*Flt4*; Fwd: AGCTCTACATATCACCGAAG and Rev: CACAGTTGTAAT ATCTGGCTG), podoplanin (*Pdpn*; Fwd: AGATAAGAAAGATG GCTTGC and Rev: AACAACAATGAAGATCCCTC), lymphatic vessel hyaluronic acid receptor 1 (*Lyve1*; Fwd: ACG TGAAAAGGTATGTGAAG and Rev: CTCCTCTGGGTTTTT AATGG), collagen 1 (*Col1a1*; Fwd: CAGCGATTACTACTG GATTG and Rev: GATAGTCTCTCCTAACCAGAC), collagen 3 (*Col3a1*; Fwd: AACATGTTTCTTCTCTGCAC and Rev: ACT CAAGAGTGGAGAATACTG), collagen 4 (*Col4a1*; Fwd: CGG ATATTCATTCCTCATGC and Rev: CAGAAGCTGTACTTG TTAGC), collagen 18 (*Col18*; Fwd: GTAGATTCTATAGGA GCTGAGAC and Rev: CTCCCTTTTGTCCTTTCATAC), growth hormone (*Gh1*; Fwd: TCCAGTCTGTTTTCTAATGC and Rev: TCGAACTCTTTGTAGGTGTC), growth hormone receptor (*Ghr*; Fwd: ACTGTCCAGTGTACTCATTG and Rev: CTGGATATCTTCTTCACATGC), insulin-like growth factor receptor 1 (*Igf1r*; Fwd: AGAACCGAATCATCATAACG and Rev: TTTTAAATGGTGCCTCCTTG), firefly luciferase (*luc2*; Fwd: CACCGTCGTATTCGTGAGCA and Rev: AGTCGTACT

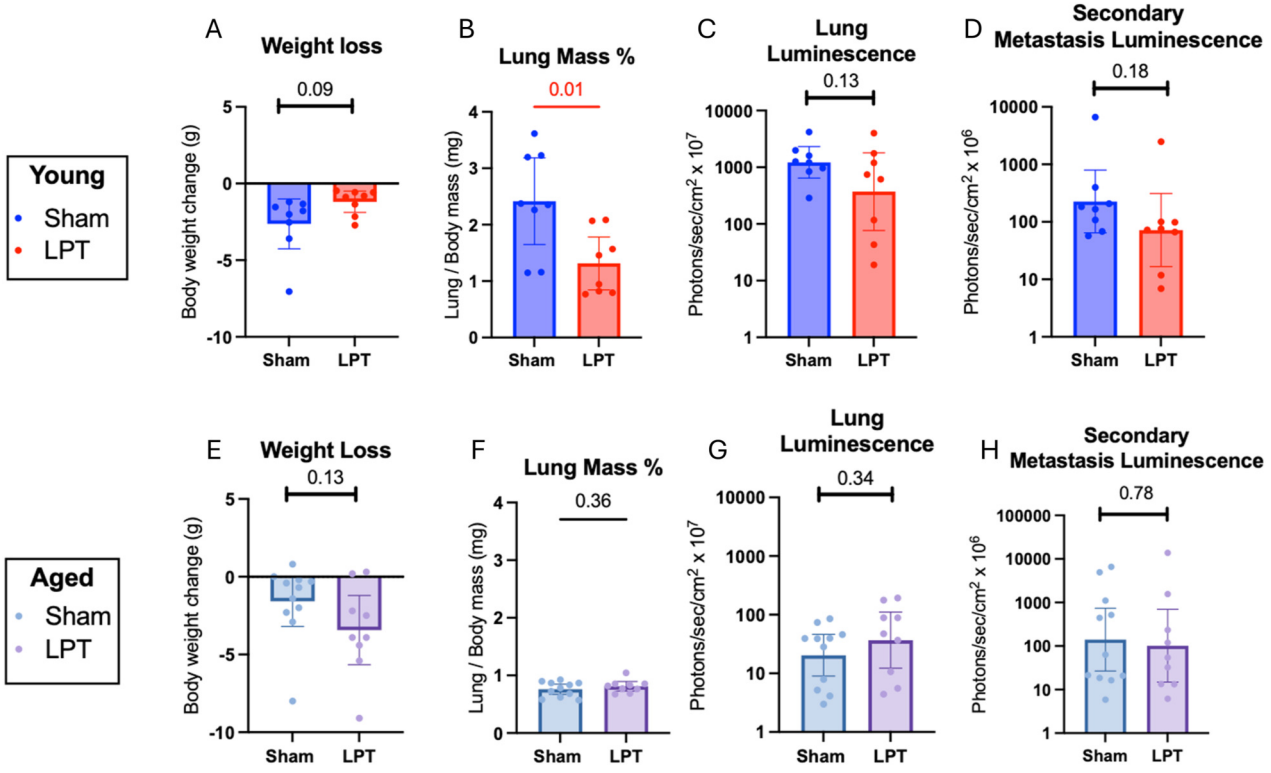

FIGURE 2
Increased lymphatic flow before and after metastasis from LPT did not increase tumor growth or spread in young adult or aged animals. Measures of tumor burden from the first two experiments with young adult and aged mice. The body weight changes for each young **(A)** and aged **(E)** mouse. The change in the percentage of body mass contributed to by the lung in the young **(B)** and aged cohorts **(F)**. *Ex vivo* luminescence in the primary site of metastasis, the lung, of the young **(C)** and aged **(G)** animals, and the secondary metastatic sites, including the brain, heart, spleen, kidneys, liver, and gastrointestinal tract of the young **(D)** and aged **(H)** animals. The statistical tests used were unpaired t-tests **(B,F)**, Welch's t-test in **(C,D,G,H)**, Mann-Whitney U-test **(E)**, and the KS test **(A)**. Bar graphs show the mean **(A,B,E,F)** or the geometric mean **(C,D,G,H)** with 95% CI. A red line and a number signify a significant change (p-value ≤0.05).

CGTTGAAGCCG), prostaglandin E receptor 2 (*Ptger2*; Fwd: CCT GCTGCTTATCGTGGCTG and Rev: GCCAGGAGAATGAGG TGGTC).

Statistics and data representation

The bioluminescent signal used to measure tumor burden in this study follows a lognormal distribution; therefore, geometric means were compared between groups, and the bioluminescent data were graphed on a log10 scale. The standard mean and linear scale were used to represent all other data. Error bars were expressed as the mean with the 95% confidence interval (CI) for error bars. The statistical test used to compare normal data was represented by a straight line, while a capped line indicated a comparison with nonparametric data or groups with unequal variances.

For each statistical comparison, we assessed normality and variance between biological groups using the Shapiro-Wilk and F-test for two-group comparisons and the Shapiro-Wilk and Brown-Forsythe tests for comparisons among multiple groups [23]. For comparisons between two independent groups, normally distributed data with homogeneous variances were analyzed with an unpaired two-tailed t-test, whereas normally distributed data with heterogeneous variances were analyzed with Welch's t-test, non-parametric data with equal variances were evaluated with the Mann–Whitney U test, and non-parametric data with unequal variances were examined with the Kolmogorov–Smirnov (KS) test. For comparisons among more than two groups, normally distributed data with equal variances were assessed by ordinary one-way ANOVA with the Tukey-Kramer *post hoc* test and displayed with capitalized compact letter display; non-parametric data, irrespective of variance homogeneity, were analyzed with the Kruskal–Wallis test with Dunn's *post hoc* analysis and displayed with lower-case compact letter display. For the ordinary two-way ANOVAs, the full model was used to assess the effects of age, treatment, and the interaction between age and treatment on the blood cell parameters. If the primary analysis indicated statistical significance, the Bonferroni *post hoc* test was then performed, and its p-value was displayed. P-values from each test were displayed on the corresponding graphs, colored red when statistically significant

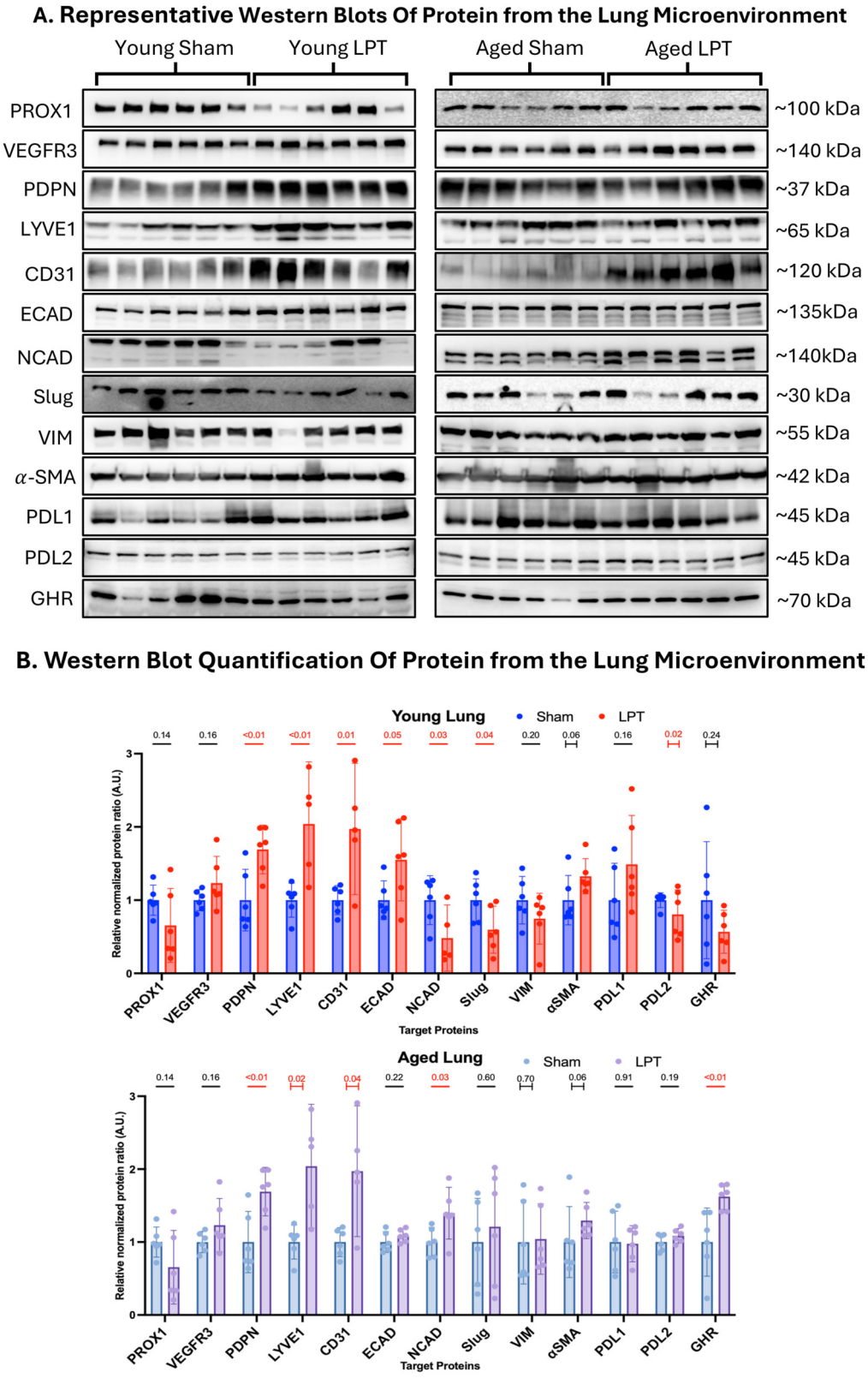

FIGURE 3
LPT altered gene expression in the lung microenvironment **(A)** Western blotting was performed on 50 mg of lung tissue taken at the time of

(*Continued*)

FIGURE 3 (Continued)
dissection for numerous target proteins. **(B)** The expression of these targets was normalized to the total protein stain and then graphed as fold change. The unpaired t-test was used for all comparisons, except for the young α SMA, aged α SMA, and aged VIM, which used the Mann-Whitney U-test; the young PDL2, young GHR, and aged LYVE1, which used Welch's t-test; and the young CD31 and aged CD31, which used the KS test. Bar graphs show the mean with the 95% CI. A red line and a number signify a significant change (p-value ≤0.05), and a capped line below the p-value indicates the use of a non-parametric test.

($p \leq 0.05$) and black when non-significant ($p > 0.05$). Graphical data and statistical analysis were performed using the statistical software Prism 10 (GraphPad Prism, RRID:SCR_002798).

Results

LPT before and after metastasis did not increase tumor growth or spread in young or aged animals

The impact of LPT on metastatic disease was assessed using four markers of tumor burden in old and young adult mice: weight loss, lung mass percent, lung luminescence, and secondary organ luminescence (Figure 2). LPT did not significantly increase tumor burden in young adult or old mice. Lung mass percent is a normalized measure of lung weight and a historical gross measure of tumor burden. In young animals that received LPT before and after the IV injection of cancer cells, lung mass percentage decreased significantly ($p = 0.01$). The luminescence from luciferase activity in cancer cells was quantified as a specific measure of tumor burden. LPT did not statistically affect luminescence in the lungs or organs outside of the lungs. Although this was true for both age groups, a trend of decreased luminescence in the lungs and secondary organs was observed in the younger animals that received LPT, with p-values of 0.13 and 0.18, respectively. LPT did not significantly affect weight loss in young adult or aged mice.

LPT altered gene and protein expression in the lung tumor microenvironment

The following proteins of interest (Figure 3) were selected to investigate three physiological events linked to (1) lymphangiogenesis (PROX1, VEGFR3, PDPN, LYVE1, CD31), (2) endothelial-to-mesenchymal transition (ECAD, NCAD, Slug, VIM, α-SMA, and (3) immune modulation (PDL1, PDL2, GHR). The most robust overlapping effect of LPT across the two ages was its impact on markers of lymphatic vessels. LPT nearly doubled the expression of CD31 ($p = 0.01$ and $p = 0.04$), LYVE1 ($p < 0.01$ and $p = 0.02$), and PDPN ($p < 0.01$ and $p < 0.01$) in both young adult and aged mice, respectively. The effect of LPT on markers of epithelial-to-mesenchymal transition was more pronounced in young animals. LPT increased the expression of the epithelial marker ECAD ($p = 0.05$) and decreased the expression of the pro-metastatic marker NCAD ($p = 0.03$) and Slug ($p = 0.04$) in the young animals. Only the pro-metastatic marker NCAD ($p = 0.03$) significantly changed in the aged animals after LPT treatment. Regarding immune modulation, LPT significantly decreased PDL2 expression ($p = 0.02$) in young adult mice and increased GHR expression ($p < 0.01$) in old mice.

Using qPCR to measure gene expression changes at the RNA level (Figure 4), we found that young adult animals receiving LPT had increased expression of the lymphangiogenesis-related RNA transcripts like *Lyve1*, *Flt4* (podoplanin), and *Prox1* compared to the sham treatment ($p < 0.01$, $p < 0.01$, $p = 0.04$, respectively). However, this effect was not observed in the aged group. Similarly, in the young cohort, there was an increased expression of *Ghr* ($p = 0.05$) and *Igf1r* ($p = 0.03$), but no significant change was observed in the aged cohort.

LPT did not alter LEC protein expression in the liver microenvironment

As with the lungs, liver protein samples were analyzed by western blot for expression of markers of the lymphatic system (Figure 5). LPT appeared to have little effect on the expression of LEC markers in both young and old animals. The only significant change caused by LPT was decreased PDPN expression in aged animals ($p = 0.04$).

LPT reduced tumor burden in middle-aged mice but did not enhance immunotherapy

The therapeutic effect of LPT was assessed in Experiment 3, which compared middle-aged mice from four treatment groups that received a sham treatment and isotype control antibodies (Control), LPT and isotype control antibodies (LPT), sham treatment and immunotherapy (Ix), and mice that received LPT and immunotherapy (LPT + Ix). Two-dimensional and three-dimensional bioluminescent images were captured at multiple time points, as shown in Figure 6.

To control for variability in tumor cells injected intravenously, two-dimensional whole-body luminescence was measured on day 7, the day before treatment started, and again on days 15 and 23 after treatment started. The pre-treatment signal on day 7 was used to normalize the post-treatment signals on days 15 and 23 for the individual mouse. Compared to the

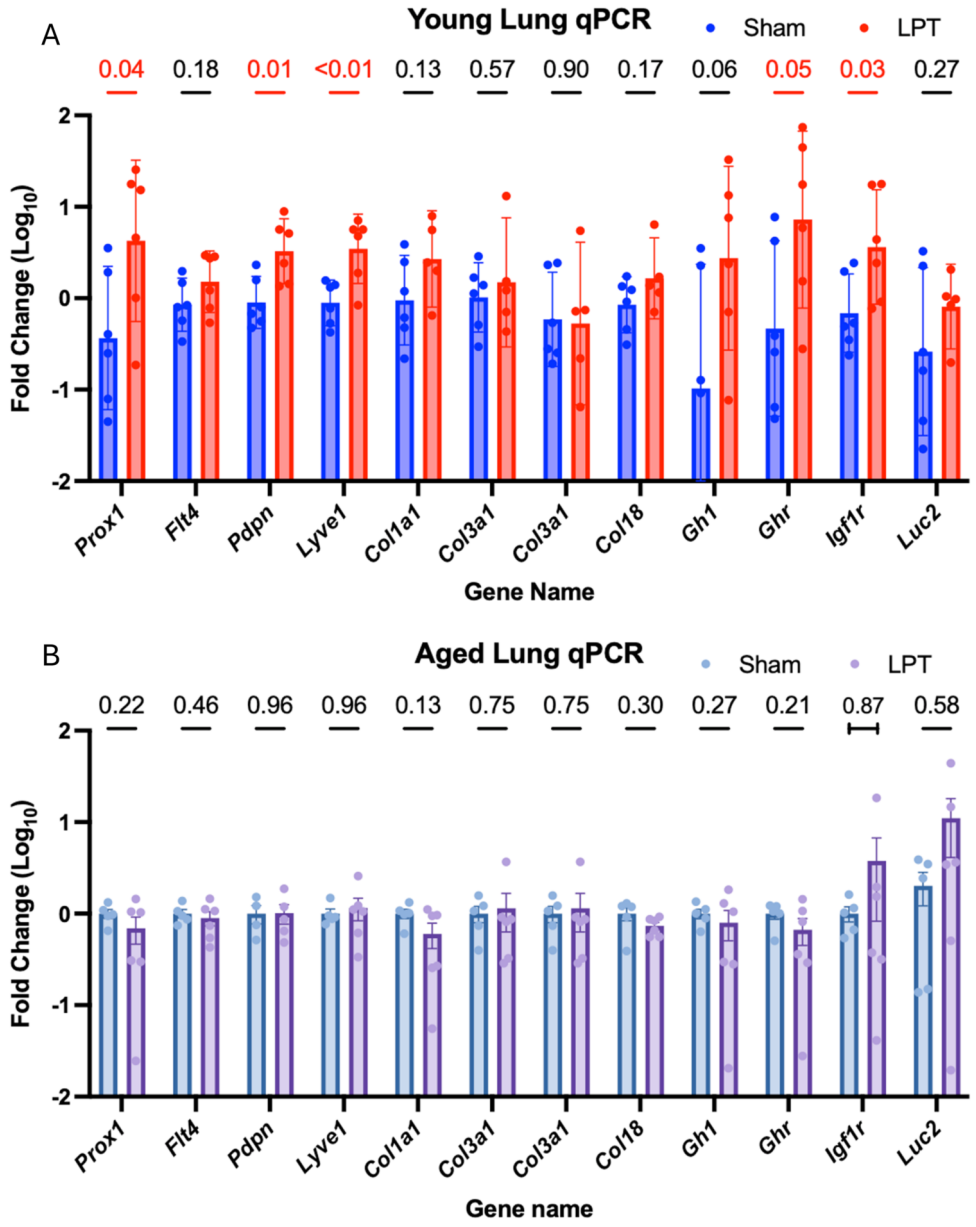

FIGURE 4
LPT altered the expression of mRNA in young but not aged lungs qPCR was performed on target genes in the lungs of young **(A)** and aged **(B)** animals, with results displayed as fold change, and bar graphs representing the geometric mean fold change (95% CI). A red line and a number signify a statistical change (p-value ≤0.05). The capped line below the p-value indicates the use of a non-parametric test.

control, the LPT group ($p = 0.04$), the Ix group ($p < 0.01$), and the LPT + Ix group ($p < 0.01$) all had significantly reduced *in vivo* luminescence on day 23. On day 25, *ex vivo* measures of tumor burden, including lung mass percentage, *ex vivo* lung luminescence, and *ex vivo* secondary organ luminescence, were collected, resulting in a bimodal distribution of tumor burden between mice treated with immunotherapy and those that were not. LPT did not interfere with the efficacy of immunotherapy in any of the measures.

To assess whether there were any metabolic effects, we tracked body weight throughout the experiment and changes in body composition parameters on day −1 (the day before cancer injection) and on day 24 (the day before dissection). LPT had little effect on weight loss and body composition. There was an insignificant trend that animals receiving immunotherapy had less weight loss. Among the mice receiving immunotherapy, those also receiving LPT showed greater fat loss (Supplementary Figure S1).

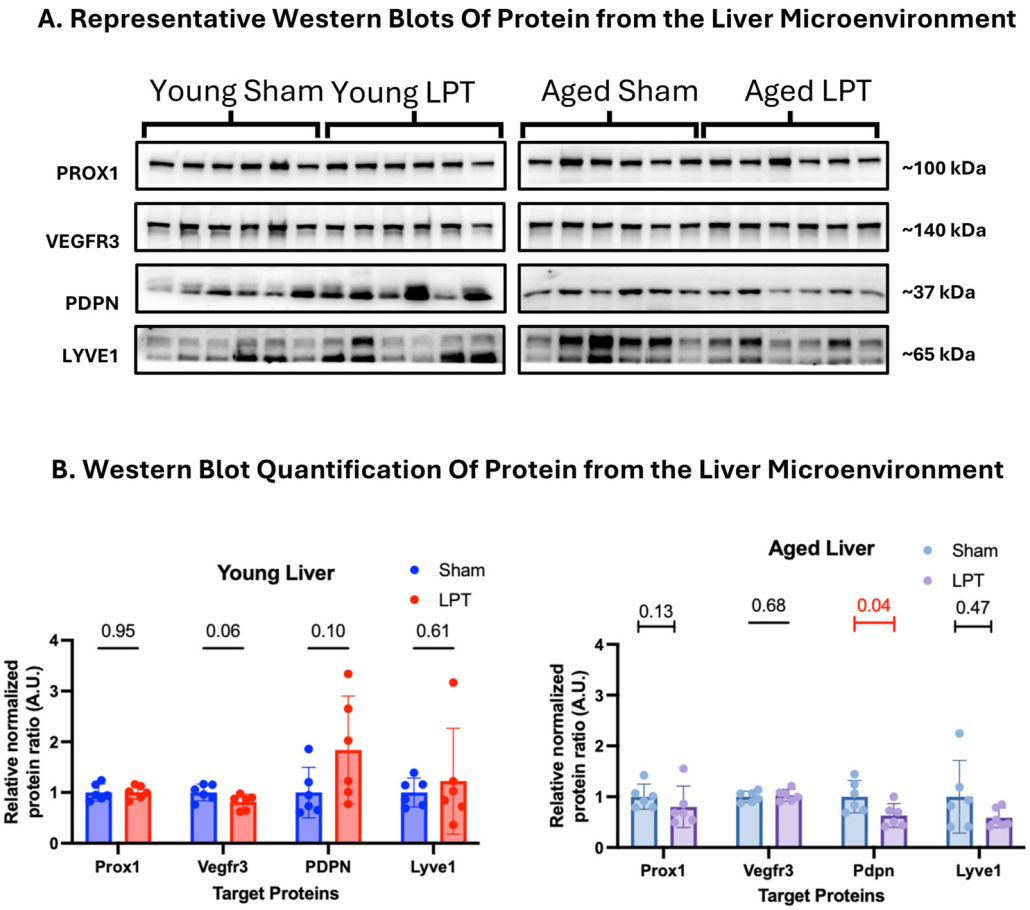

FIGURE 5
LPT did not alter protein expression in the liver microenvironment. Western blotting was performed on 50 mg of liver tissue taken at the time of dissection for lymphatic endothelial cell-specific protein expression **(A)**. The expression of these targets was normalized to the total protein stain and graphed as fold change **(B)**. The unpaired t-test was used for all comparisons aside from aged PROX1, which used the Mann-Whitney U-test; and the young LYVE1 and aged LYVE1, which used the KS test. The bar graphs represent the mean fold change with the 95% CI. A red line and a number signify a statistical change (p-value ≤0.05).

To assess immune-mediated effects, we measured the white blood cell count and differential on day 25, the day of dissection. Animals receiving immunotherapy had higher white blood cell counts than those that did not, primarily driven by increases in neutrophils and lymphocytes, with no significant change in monocyte, eosinophil, or basophil counts.

LPT immediately and significantly increased the white blood cell, red blood cell, and platelet counts in whole blood in young but not in middle-aged animals

To assess whether LPT can flux cells into or out of the circulatory system, we measured whole-blood parameters before and immediately after LPT. Figure 7 depicts the change in each blood parameter that was measured for young adult (3-month-old) and middle-aged (11-month-old) mice of both sexes (n = 16–18). Using a two-way ANOVA, it was found that LPT significantly increased red blood cell, white blood cell, platelet, and lymphocyte counts, as well as hemoglobin and hematocrit in whole blood. In the *post hoc* analysis, only the young animals' blood parameters changed significantly. LPT elicited a robust change in blood parameters in the young animals; for example, white blood cells, red blood cells, and platelets increased by 64%, 96%, and 53%, respectively.

Discussion

The primary motivation for this study was to assess the risks associated with physical manipulation in metastatic disease. Or

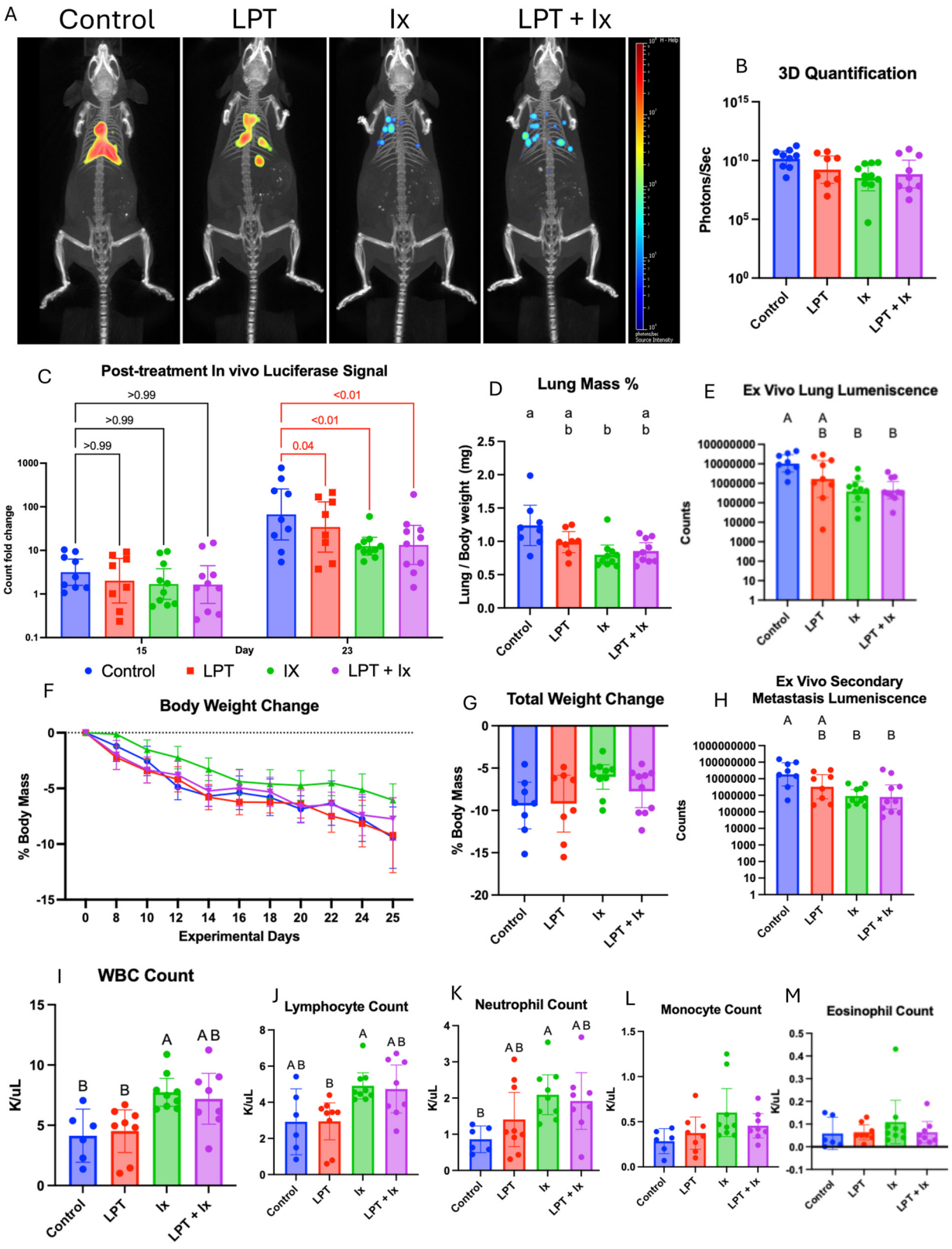

FIGURE 6
LPT reduced tumor burden in middle-aged mice and did not enhance or diminish the effect of immunotherapy. **(A)** Representative 3D
(*Continued*)

FIGURE 6 (Continued)
bioluminescent images from each treatment group, taken 23 days after the injection of cancer cells. **(B)** Quantification of 3D bioluminescent images taken on day 23. **(C)** Quantified 2D whole-body luminescence on days 15 and 23, normalized to day 7, before treatment started. The statistical difference between the control and each treatment group was evaluated using a two-way ANOVA with Dunnett's multiple comparisons test, and the results are indicated by a numeric p-value, which is highlighted in red if significant. **(D)** Statistical difference in lung mass percent was assessed with the Kruskal-Wallis test and *post hoc* analysis with Dunn's multiple comparisons test. Differences in *ex vivo* luminescence in the lung **(E)** and secondary metastatic sites **(H)**, including the brain, heart, spleen, kidneys, liver, and gastrointestinal tract, were assessed using a lognormal ordinary ANOVA with Tukey's multiple comparisons test. The mean percent change in each group's body weight throughout the experiment **(F)** and the final percent weight change **(G)**, which showed no significant difference between the groups when assessed with a one-way ANOVA. Whole blood was collected during the dissection, parameters were analyzed using a Hemavet 950FS, and the difference between groups was assessed with an ordinary one-way ANOVA and *post hoc* analysis with Tukey's multiple comparison test **(I–M)**. If the primary ANOVA analysis did not show a significant difference, the *post hoc* analysis to assess group differences was not performed, and the compact letter display was not created. Bar graphs show the mean **(D,F,G,I–M)** or the geometric mean **(B,C,E,H)** with 95% CI.

simply, *is it dangerous to touch metastatic tumors*? Because tissue compression increases interstitial and lymphatic flow [24], touch-based therapies are often presumed to carry the potential to promote tumor dissemination. To test this assumption, we employed a mouse model of experimental metastasis and intentionally accentuated mechanical stimulation using LPT. Across all experiments, repeated touch did not increase the growth or spread of metastatic melanoma. Notably, in the young and middle-aged animals, LPT was associated with a reduction in metastatic burden, directly contradicting predictions derived from studies of primary tumors. This protective effect was supported by protein expression profiles within the tumor microenvironment, which revealed LPT-induced shifts towards an anti-metastatic phenotype in young adult mice. In middle-aged mice, both LPT and immune checkpoint antagonism reduced tumor burden independently, whereas their combination conferred neither additive benefit nor detriment. Together, these findings indicate that mechanical touch influences metastatic disease in a manner distinct from primary tumors and may even confer a therapeutic benefit that wanes with advanced age.

We identified a robust effect of LPT on whole blood parameters in young, but not middle-aged, adult mice. By performing a complete blood count and differential before and immediately after 5 min of LPT, we could detect immediate changes in whole-blood parameters. We discovered that LPT increases the number of red blood cells, white blood cells, and platelets in the blood; however, this effect is lost with increasing age. The immediate rise in parameters immediately after LPT suggests that LPT mobilizes pre-existing cells residing outside the systemic circulation. This is supported by previous studies showing that abdominal LPT mobilizes T cells from the gut-associated lymphoid tissue [25]. Therefore, the source of the white blood cells in this LPT sequence could be lymphoid tissue in the abdominal cavity and the thorax. The LPT sequence also puts direct repeated pressure on the spleen, making it the likely source of red blood cells and platelets. Two rationales for why LPT did not increase blood parameters in middle-aged animals could be that their extravascular reserve of these blood components is lower, or that increased tissue stiffness reduces LPT's ability to flux cells. These preclinical results align with human data showing that LPT increases white blood cell counts in young, healthy males [26], while decreasing them in nursing home residents [27].

The only non-age-dependent result we found during this investigation was that LPT increased the expression of lymphatic-specific markers in the lung tumor microenvironment. This novel finding suggests that LPT either increases tumor-associated lymphangiogenesis or causes lung lymphangiogenesis. This is a unique presentation because tumor-induced lymphangiogenesis is often considered a negative prognostic factor. However, it has also been found that lymphatic endothelial cells can promote an anti-tumor immune response that enhances the effects of immunotherapy [28, 29]. For this reason, we hypothesized that LPT could enhance the efficacy of immunotherapy. Since LPT increased the expression of markers of the lymphatic system in both young adult and aged mice, we assumed the effect was shared with the middle-aged mice who received LPT in the immunotherapy study and were not measured. However, this assumed increase in lymphangiogenesis induced by LPT did not enhance immunotherapy efficacy. One possible explanation is that lymphangiogenesis could be a net benefit for metastatic disease, and both LPT and immunotherapy can serve as distinct stimuli to elicit tumor lymphangiogenesis. This hypothesis would suggest that the impact of tumor lymphangiogenesis is stage-dependent, causing a detriment in primary disease by facilitating lymphatic metastasis but providing a net benefit in the treatment of metastatic disease by enhancing anti-tumor immunity.

To determine the effect of touch on the growth and spread of metastatic tumors, we employed an experimental metastasis model in which melanoma cells are injected systemically, resulting in metastatic tumors without a primary tumor. This approach reduces animal use and experimental duration while avoiding the well-established risk of mechanically prompting dissemination from a primary lesion. Taken together, this preclinical evaluation found that: (1) mechanical pressure generated by human touch affects metastatic and primary cancer differently, supporting an improved safety profile for therapeutic touch in patients with diffuse metastatic disease; (2) enhancing lymphatic flow with LPT

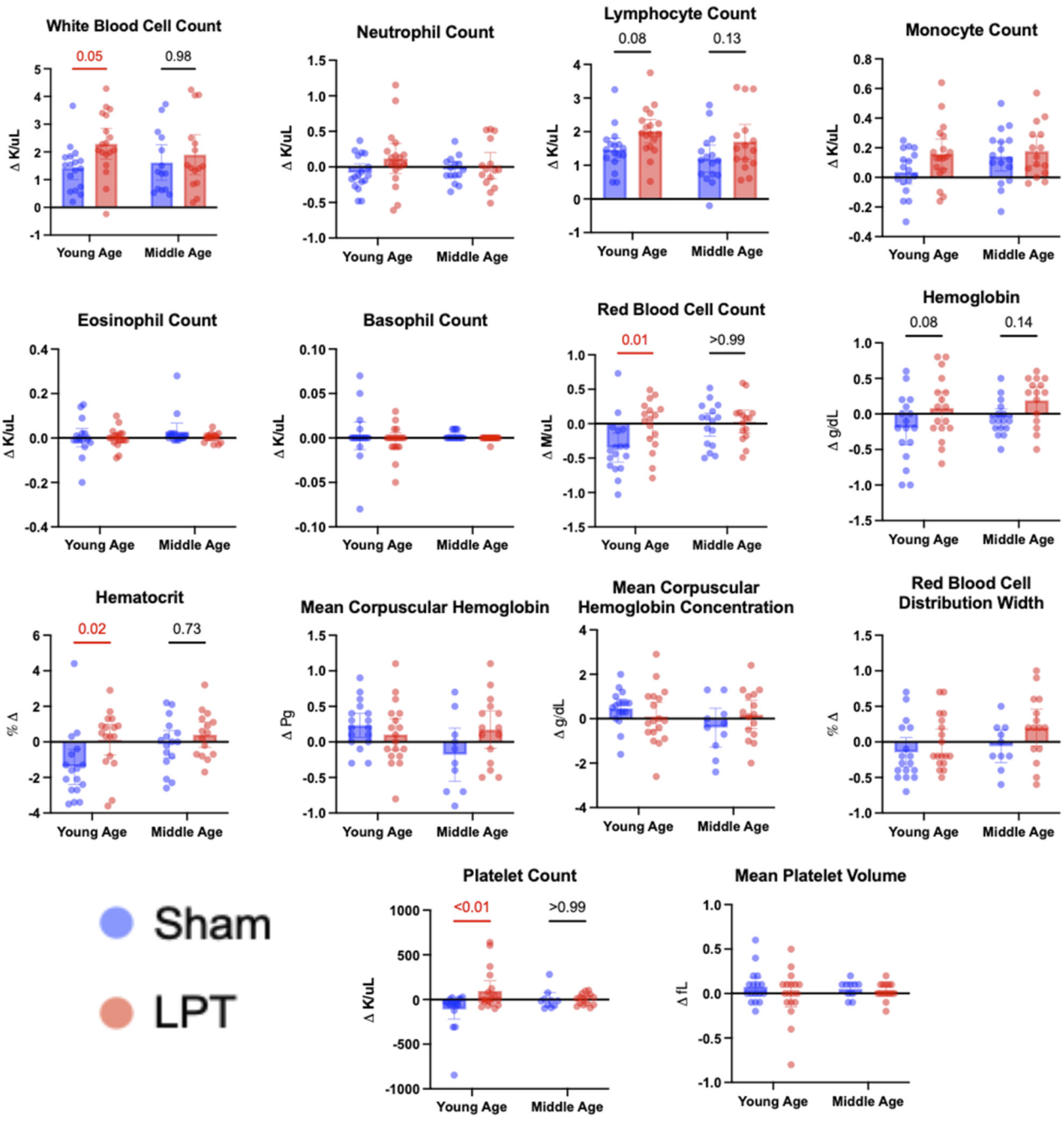

FIGURE 7
The effect of a 5-min LPT sequence on whole blood parameters in young adult and middle-aged mice. Whole blood collected immediately before and after a 5-min LPT sequence or sham treatment was analyzed using a Hemavet 950FS. The pre-treatment blood parameter was subtracted from the post-treatment parameter. The individual changes and the means of each group are represented as bar graphs with 95% CI. A statistical difference between the sham and LPT groups was assessed for both young and middle-aged animals using an ordinary two-way ANOVA, followed by *post hoc* analysis with Bonferroni's multiple comparisons test. If the treatment significantly contributed to the observed variation, a *post hoc* analysis was conducted, and the p-values were shown on the graphs. A red line and a number signify a significant change (p-value ≤0.05).

decreased various measures of tumor metastasis in young adult and middle-aged animals, but not in those at an advanced age; (3) LPT increases the expression of lymphatic-specific markers in the tumor microenvironment; and (4) age is negatively correlated with LPT's ability to mobilize white blood cells, red blood cells, and platelets into the circulation.

Several limitations temper the interpretation and clinical translation of these findings. This study relied on an experimental metastasis model that bypasses early stages of the metastatic cascade, including primary tumor formation, local invasion, and intravasation. These events could affect natural tumor behavior not accounted for in this study. In the first two experiments, LPT was administered to young adult and aged mice for 7 days before cancer cell injection, and every other day thereafter for 21 days. In the third experiment with middle-aged adult mice, LPT was administered only every other day after cancer cell injection. The intention of this approach was to simulate different clinical scenarios: 1) a patient receiving therapeutic touch before and after the metastatic event, and 2) a patient receiving therapeutic touch only after metastasis. Although we believe this increases the translatability of our findings, it is also a confounding mechanism. The observed effects of LPT in young adult and aged mice may have been caused by decreased seeding or increased clearance of circulating tumor cells rather than an anti-tumor immune response. Moreover, only one tumor type was evaluated, the B16F10 mouse melanoma cell line; this highly metastatic line is insufficient to draw conclusions about the behavior of human melanoma. Likewise, melanoma is a solid tumor type, so conclusions about blood-borne cancers cannot be drawn from this study. Accordingly, these results should be viewed as proof-of-concept within a constrained experimental framework, providing a foundation for future studies to more precisely define the safety and therapeutic potential of touch-based interventions in metastatic disease.

Author contributions

CW, JK, RB, and YQ designed the project. CW and JK coordinated the study and generated the hypothesis. CW, MK, EW, ES, JW, SR, SM, AA, and NH performed the experiments. JK and CW provided funding support. RB and YQ trained others to perform the experiments, analyze the data, and interpret the results. All authors contributed to the article and approved the submitted version.

Data availability

The original contributions presented in the study are publicly available. This data can be found here [https://doi.org/10.6084/m9.figshare.31129240].

Ethics statement

All animal procedures were carried out in accordance with the Animal Welfare Act, set forth by the National Institute of Health, and approved by the institutional animal care and use committees at Ohio University under protocol number 16-H-016.

Funding

The author(s) declared that financial support was received for this work and/or its publication. This research received no specific grant from any funding agency in the public, commercial, or not-for-profit sectors. It was supported by the John J. Kopchick Molecular and Cellular Biology/Translational Biomedical Sciences Research Fellowship Award, an internal award at Ohio University. This study was also supported by the Heritage College of Osteopathic Medicine, the Ohio Heritage Foundation, and the State of Ohio's Eminent Scholar Program, which includes a gift by Milton and Lawrence Goll.

Acknowledgements

Thank you to the groups and individuals who supported this project. This work would not have been possible without the financial support of Ohio University Graduate College, the Heritage College of Osteopathic Medicine, the Ohio Heritage Foundation, the John J. Kopchick Molecular and Cellular Biology/Translational Biomedical Science Research Fellowship Award, and the State of Ohio's Eminent Scholar Program, which includes a gift by Milton and Lawrence Goll. Similarly, thank you to Dr. Thomas Rosol, PhD, and Dr. Todd Fredricks, DO, for providing equipment for anesthesia and *in vivo* imaging. The blood machine was donated to our lab for this project by Andy Tucker at the Ohio University Innovation Center.

Conflict of interest

The author(s) declared no potential conflicts of interest with respect to the research, authorship, and/or publication of this article.

Generative AI statement

The author(s) declared that generative AI was not used in the creation of this manuscript.

Any alternative text (alt text) provided alongside figures in this article has been generated by Frontiers with the support of artificial intelligence and reasonable efforts have been made to ensure accuracy, including review by the authors wherever possible. If you identify any issues, please contact us.

Supplementary material

The Supplementary Material for this article can be found online at: https://www.ebm-journal.org/articles/10.3389/ebm.2026.10850/full#supplementary-material

References

1. Dillekås H, Rogers MS, Straume O. Are 90% of deaths from cancer caused by metastases? *Cancer Med* (2019) **8**:5574–6. doi:10.1002/cam4.2474

2. Siegel RL, Miller KD, Jemal A. Cancer statistics. *CA A Cancer J Clinicians* (2020) **70**:7–30. doi:10.3322/caac.21590

3. Gerstberger S, Jiang Q, Ganesh K. Metastasis. *Cell* (2023) **186**:1564–79. doi:10.1016/j.cell.2023.03.003

4. Shieh AC. Biomechanical forces shape the tumor microenvironment. *Ann Biomed Eng* (2011) **39**:1379–89. doi:10.1007/s10439-011-0252-2

5. Langevin HM, Keely P, Mao J, Hodge LM, Schleip R, Deng G, et al. Connecting (T)issues: how research in fascia biology can impact integrative oncology. *Cancer Res* (2016) **76**:6159–62. doi:10.1158/0008-5472.CAN-16-0753

6. Karda IWAM, Wan Ismail WF, Kamal AF. Massage manipulation and progression of osteosarcoma, does it really correlate: a combination of prospective and retrospective cohort study. *Sci Rep* (2023) **13**:18541. doi:10.1038/s41598-023-45808-7

7. Stoker TA. The effect of cortisone therapy and limb exercise on the dissemination of cancer via the lymphatic system. *Br J Cancer* (1969) **23**:132–5. doi:10.1038/bjc.1969.19

8. Wang J-Y, Wu PK, Chen PCH, Yen CC, Hung GY, Chen CF, et al. Manipulation therapy prior to diagnosis induced primary osteosarcoma metastasis—from clinical to basic research. *PLoS ONE* (2014) **9**:e96571. doi:10.1371/journal.pone.0096571

9. *Foundations of osteopathic medicine: philosophy, science, clinical applications, and research*. Philadelphia: Wolters Kluwer (2018).

10. Tabatabaee A, Tafreshi MZ, Rassouli M, Aledavood SA, AlaviMajd H, Farahmand SK. Effect of therapeutic touch in patients with cancer: a literature review. *Med Arh* (2016) **70**:142–7. doi:10.5455/medarh.2016.70.142-147

11. Arienti C, Bosisio T, Ratti S, Miglioli R, Negrini S. Osteopathic manipulative treatment effect on pain relief and quality of life in oncology geriatric patients: a nonrandomized controlled clinical trial. *Integr Cancer Ther* (2018) **17**:1163–71. doi:10.1177/1534735418796954

12. Belsky JA, Wolf K, Setty BA. A case of resolved vincristine-induced constipation following osteopathic medicine in a patient with infantile fibrosarcoma. *J Osteopathic Med* (2020) **120**:691–5. doi:10.7556/jaoa.2020.102

13. Goyal M, Goyal K, Narkeesh K, Samuel AJ, Arumugam N. Osteopathic manipulative treatment for post mastectomy lymphedema: a case report. *Int J Osteopathic Med* (2017) **26**:49–52. doi:10.1016/j.ijosm.2017.10.002

14. Schander A, Padro D, King HH, Downey HF, Hodge LM. Lymphatic pump treatment repeatedly enhances the lymphatic and immune systems. *Lymphat Res Biol* (2013) **11**:219–26. doi:10.1089/lrb.2012.0021

15. Sherratt MJ. Age-related tissue stiffening: cause and effect. *Adv Wound Care (New Rochelle)* (2013) **2**:11–7. doi:10.1089/wound.2011.0328

16. Demetrius L. Aging in mouse and human systems: a comparative study. *Ann New York Acad Sci* (2006) **1067**:66–82. doi:10.1196/annals.1354.010

17. Creasy C, Schander A, Orlowski A, Hodge LM. Thoracic and abdominal lymphatic pump techniques inhibit the growth of *S. pneumoniae* bacteria in the lungs of rats. *Lymphatic Res Biol* (2013) **11**:183–6. doi:10.1089/lrb.2013.0007

18. Schander A, Castillo R, Paredes D, Hodge LM. Effect of abdominal lymphatic pump treatment on disease activity in a rat model of inflammatory bowel disease. *J Osteopathic Med* (2020) **120**:337–44. doi:10.7556/jaoa.2020.052

19. Overwijk WW, Restifo NP. B16 as a mouse model for human melanoma. *CP Immunol* (2000) **39**:1–29. doi:10.1002/0471142735.im2001s39

20. Wang S, Lai X, Deng Y, Song Y. Correlation between mouse age and human age in anti-tumor research: significance and method establishment. *Life Sci* (2020) **242**:117242. doi:10.1016/j.lfs.2019.117242

21. Ozasa T, Nakajima M, Tsunedomi R, Goto S, Adachi K, Takahashi H, et al. Novel immune drug combination induces tumour microenvironment remodelling and reduces the dosage of anti-PD-1 antibody. *Sci Rep* (2025) **15**:8956. doi:10.1038/s41598-025-87344-6

22. Ontiveros CO, Garcia MG, Murray CE, Deng Y, Bai H, Tanner C, et al. Anti-PD-L2 immunotherapy is efficacious against melanoma in aged hosts through IL-17 and IFNγ signalling. *Nat Commun* (2025) **16**:10176. doi:10.1038/s41467-025-65025-2

23. Whitlock M, Schluter D. *The analysis of biological data*. Colo: Roberts and Co. Publishers, Greenwood Village (2009).

24. Olszewski WL, Cwikla J, Zaleska M, Domaszewska-Szostek A, Gradalski T, Szopinska S. Pathways of lymph and tissue fluid flow during intermittent pneumatic massage of lower limbs with obstructive lymphedema. *Lymphology* (2011) **44**:54–64. Available online at: https://journals.librarypublishing.arizona.edu/lymph/article/id/3699/.

25. Hodge LM, Bearden MK, Schander A, Huff JB, Williams A, Jr, King HH, et al. Lymphatic pump treatment mobilizes leukocytes from the gut associated lymphoid tissue into lymph. *Lymphatic Res Biol* (2010) **8**:103–10. doi:10.1089/lrb.2009.0011

26. Rivers WE, Treffer KD, Glaros AG, Williams CL. Short-term hematologic and hemodynamic effects of osteopathic lymphatic techniques: a pilot crossover trial. *J Am Osteopath Assoc* (2008) **108**:646–51. doi:10.7556/jaoa.2008.108.11.646

27. Noll DR. The short-term effect of a lymphatic pump protocol on blood cell counts in nursing home residents with limited mobility: a pilot study. *J Osteopathic Med* (2013) **113**:520–8. doi:10.7556/jaoa.2013.003

28. Sun M, Garnier L, Chevalier R, Roumain M, Wang C, Angelillo J, et al. Lymphatic-derived oxysterols promote anti-tumor immunity and response to immunotherapy in melanoma. *Nat Commun* (2025) **16**:1217. doi:10.1038/s41467-025-55969-w

29. Fankhauser M, Broggi MAS, Potin L, Bordry N, Jeanbart L, Lund AW, et al. Tumor lymphangiogenesis promotes T cell infiltration and potentiates immunotherapy in melanoma. *Sci Transl Med* (2017) **9**:eaal4712. doi:10.1126/scitranslmed.aal4712

EBM Experimental Biology and Medicine

TYPE Original Research
PUBLISHED 20 March 2026
DOI 10.3389/ebm.2026.10857

OPEN ACCESS

*CORRESPONDENCE
Chris S. Pridgeon,
christopher.pridgeon@helsinki.fi
Marjo Yliperttula,
marjo.yliperttula@helsinki.fi

RECEIVED 10 October 2025
REVISED 21 December 2025
ACCEPTED 16 February 2026
PUBLISHED 20 March 2026

CITATION
Koivunotko E, Monola J, Pridgeon CS, Linden J, Harjumäki R, Yatkin E, Madetoja M and Yliperttula M (2026) Towards a standardized diabetic prolonged wound healing model in hairless SKH1 mice.
Exp. Biol. Med. 251:10857.
doi: 10.3389/ebm.2026.10857

Towards a standardized diabetic prolonged wound healing model in hairless SKH1 mice

Elle Koivunotko[1], Julia Monola[1], Chris S. Pridgeon[1]*, Jere Linden[2,3], Riina Harjumäki[1], Emrah Yatkin[4], Mari Madetoja[5] and Marjo Yliperttula[1]*

[1]Division of Pharmaceutical Biosciences, Drug Research Program, Faculty of Pharmacy, University of Helsinki, Helsinki, Finland, [2]Finnish Centre for Laboratory Animal Pathology, HiLIFE, University of Helsinki, Helsinki, Finland, [3]Department of Veterinary Biosciences, Faculty of Veterinary Medicine, University of Helsinki, Helsinki, Finland, [4]Central Animal Laboratory, University of Turku, Turku, Finland, [5]Made Consulting Ltd, Turku, Finland

Abstract

Chronic wounds, particularly those associated with diabetes, pose a significant clinical challenge due to their impaired healing dynamics and lack of reliable and standardized preclinical models. This pilot study aimed to establish a diabetogenic, immunocompetent, hairless mouse model (SKH1 strain) to simulate prolonged wound healing. Diabetes was induced by streptozotocin administration, followed by the creation of full-thickness dorsal skin wounds. Wounds were treated with either saline or nanofibrillated cellulose hydrogel as a model treatment. Wound healing progression and blood glucose were monitored, and histopathological assessments were performed after a 14-day experiment. In addition, for the first time, the Thermidas thermal imaging system was used in an *in vivo* mouse model to evaluate skin temperature. Results demonstrated that diabetes induction successfully prolonged wound closure by 5 days compared with the previously described acute wound model in the same strain with the identical protocol without streptozotocin (STZ) induction. Histopathological analyses showed increased macrophage activity (16.2% vs. 2.2% in the treatment groups and 10.2% vs. 0.3% in the control groups) and decreased collagen deposition (12.2% vs. 43.2% in the treatment groups and 17.6% vs. 27.4% in the control groups), suggesting prolonged wound healing. These findings support the use of hairless SKH1 mice as a viable model for studying prolonged diabetic wound healing and evaluating future therapeutic candidates.

KEYWORDS

collagen deposition, diabetogenic SKH1 mice, *in vivo* prolonged wound healing model, macrophage activity, STZ induction

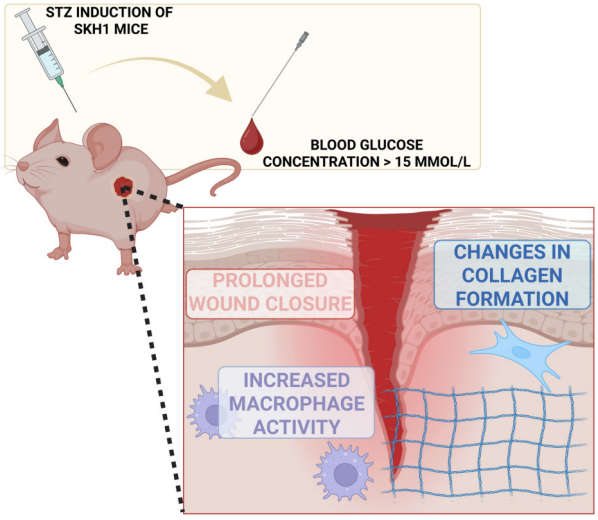

GRAPHICAL ABSTRACT

Impact statement

Chronic wounds are often referred to as a silent epidemic and represent a growing global challenge with increasing prevalence each year. The development of novel bioactive wound therapies is hindered by the lack of standardized pre-clinical models and limited understanding of prolonged wound-healing pathophysiology. In this study, together with our previous work, we provide new insights into the potential of the SKH1 nude mouse strain as a versatile model for both acute and chronic wound healing research. To our knowledge, this is the first methodological study directly comparing diabetogenic and healthy SKH1 mice in a full-thickness wound model, revealing important differences in wound-healing pathology and treatment candidate efficacy. Publication of this work offers the opportunity to advance more standardized, reproducible wound-healing models that can accelerate therapeutic development while adhering to the principles of the 3Rs.

Introduction

An aging population and the rising prevalence of chronic diseases, such as diabetes and cardiovascular disorders, present global challenges in managing chronic wounds. Chronic wounds have been reported to cost up to 97 billion USD annually [1] and increase the risk of mortality, particularly in patients with diabetic foot ulcers [2]. Insufficient homecare and the development of antibiotic resistance have led to a vicious cycle of chronic wound treatment [3], which will not be resolved without novel treatments and a better understanding of wound pathophysiology.

Diabetes is a leading systemic contributor to chronic wound development, primarily by inducing local ischemia, elevating protease activity, and impairing skin cell function due to persistent hyperglycemia [4, 5]. While the current standard of care (including wound cleansing, pressure offloading, and infection control) remains essential, alternative therapies are being explored to enhance oxygen delivery, stimulate angiogenesis, and restore cellular activity. These include negative pressure wound therapy, bioactive hydrogels, and the application of growth factors [6, 7]. However, despite their promise, these approaches have yielded inconsistent results and lack standardized protocols, limiting their integration into routine chronic wound management.

The development of effective wound therapies is hindered by the heterogeneity of chronic wounds and the complexity of the wound healing process, making it difficult to establish standardized and reproducible preclinical models. Acute and chronic wounds differ significantly in key biological processes, further complicating both *in vitro* and *in vivo* modeling. The classification of wounds as acute or chronic is primarily determined by their healing duration, which itself depends heavily on the wound's original size and location [8]. A wound is considered chronic if it fails to progress through the four partially overlapping healing phases (hemostasis, inflammation, proliferation, and maturation) within approximately 12 weeks. Beyond delayed or incomplete closure, chronic wounds are also characterized by persistent inflammation and impaired cellular function, often influenced by local or systemic conditions such as chronic diseases or

infections [9]. In diabetes, for instance, angiogenesis—the formation of new blood vessels from existing vasculature—is impaired, resulting in insufficient oxygen and nutrient delivery to the wound site and contributing to delayed healing [10]. This vascular deficiency disrupts the balance of growth factors and cytokines, impairs epithelialization, and delays wound closure [11, 12]. Elevated levels of reactive oxygen species and altered macrophage activity lead to prolonged inflammation, as macrophages in chronic wounds fail to undergo the normal transition from pro-inflammatory (M1) to pro-regenerative states (M2) [13]. This sustained inflammation negatively impacts the formation of fibrous tissue and angiogenic activity [14]. Additionally, later stages of healing, including proliferation and maturation, are disrupted. Increased metalloproteinase activity and altered fibroblast function lead to an imbalance in collagen production [15, 16]. Such disturbances can result in excessive or pathological scarring, for which no definitive treatment currently exists.

Although research has focused on reducing the use of *in vivo* models with versatile three-dimensional *in vitro* models, the use of animals remains the gold standard in medical device and medicinal drug development for wound treatment. From the anatomical perspective, porcine models provide the most similar skin structure to human skin when comparing skin thickness, layers, and hair density [17]. Conversely, a more standardized genetic background and established genetic modifications, lower cost, and simpler habitat maintenance mean that mouse models are the most common *in vivo* model. However, this causes difficulties when translating *in vivo* findings to the clinic due to the larger differences between mice and humans, such as differences in skin thickness and contraction and its attachment to underlying tissue [18]. The most common method to study diabetic wounds *in vivo* is with streptozotocin (STZ)-induced mice [19]. STZ is a chemotherapeutic agent for the treatment of pancreatic β-cell carcinoma, the cells in which normal insulin production occurs. In mice, STZ causes necrosis of the β-cells, decreasing insulin production as in type I diabetes [20]. Although STZ induction is widely used, the protocols differ substantially between laboratories in terms of the experimental setups, e.g., variations in STZ dosing protocol, animal strain, experimental endpoints, animal diet, and data monitoring. Additional challenges come from the lack of both acute and prolonged wound healing models in the same experimental modality, challenging the understanding of the pathological differences.

Although most studies using STZ induction in rodents are considered disease pathology models, the model has also been used in chronic wound healing research. However, most models are generated with strains with typical skin and hair, which decreases the similarity to humans [21]. This challenge can be addressed by using hairless mouse strains, where the lack of hair and hair-follicle–derived wound-healing stem cells may offer a more suitable foundation for developing an *in vivo* wound healing model [22, 23]. Although these strains retain certain biological limitations, like differences in skin structure [24] and the wound closure process [25, 26], they allow for easier wound creation, more consistent monitoring of the healing process, and improved capacity for thermographic assessment compared with other strains. Currently, there are few chronic wound models with immunocompetent hairless mouse strains, which encouraged us to generate a prolonged wound healing model in hairless SKH1 mice using a standardized STZ induction protocol. In addition, our previous study using SKH1 mice to generate an acute full-thickness wound model with an identical protocol to evaluate the efficacy and safety of wound treatment candidates was successful; it was carried out with good animal welfare, simplified wound creation, good monitoring of wound healing, and evaluation of possible changes in the skin during the experiment.

In this pilot study, our aim was to produce a tractable prolonged full-thickness wound healing model using STZ-induced hairless SKH1 mice, which has been used previously in our acute wound model study without diabetes induction [27]. For brevity, data in the prolonged wound healing model are henceforth referred to as "chronic wounds". Based on this study we emphasize the following: 1) the potential for future standardization of current *in vivo* wound models by using the same strain and experimental set up in both acute and prolonged wound healing experiments; 2) the use of non-invasive monitoring tools to evaluate the progression of wound healing and possible infection with thermograph analysis; and 3) the use of hairless mice for simplified wound monitoring, and avoidance of ethically contentious methods such as mechanical prevention of wound closure. Through comparison with data from the previous acute wound model, changes in wound healing physiology, including epithelialization, inflammation, angiogenesis, and collagen deposition, could be observed in response to the same treatments. We hypothesize that hyperglycemic SKH1 mice with prolonged wound healing characteristics, including longer wound closure time, induced macrophage activity, and reduced collagen deposition, can be produced using STZ induction. By considering both acute and prolonged wounds, this study indicates the importance of standardized preclinical models for future wound care development.

Materials and methods

Model treatment formulations

To illustrate the effects of the material candidate in the chronic wound model, medical-grade nanofibrillated cellulose (NFC) hydrogel (FibGel, UPM Biomedicals) [2.9% (m/v)] was

used as a model treatment as in our previous publication [27]. NFC hydrogel was diluted into 0.8% (m/v) with sterile water before use. 0.9% (m/v) NaCl was used as a control treatment.

Streptozotocin injection

Streptozotocin (STZ) (Sigma-Aldrich, batch 0661505.4, MO, USA) was solubilized in NaCl 0.9% (batch 214328131, Braun) into a final concentration of 8.0 mg/mL. STZ was prepared fresh daily and injected intraperitonially within 15 min of preparation. STZ bolus (40 mg/kg body weight) was administered daily for 5 consecutive days as previously described [28] using a Myjector 27Gx1/2″ Terumo 0.3–0.5 mL insulin syringe. The dosing volume was 5 mL/kg. The injection site of skin was wiped with 70% EtOH prior to injection. Animals were not fasted before STZ injection to avoid additional stress factors for mice.

Animals

STZ induction was performed on 10 male SKH1 mice (Crl: SKH1-Hrhr, SPF, Charles River) at age 8–9 weeks. In total, nine of the STZ-induced mice underwent the chronic wound model. The pilot animal experiments were approved by the National Project Authorization Board of Finland (license number ESAVI-25539-2024), and the study conformed to the following guidelines: DIRECTIVE 2010/63/EU of the European Parliament and the Council, Finnish Act (497/2013), Government Decree on the Protection of Animals Used for Scientific or Educational Purposes (564/2013), and Guidance document on the Recognition, Assessment and Use of Clinical Signs as Humane endpoints for Experimental Animals Used in Safety Evaluation, Environmental Health and Safety Monograph Series on Testing and Assessment (No 19. OECD 2000). The reporting of this animal research followed the ARRIVE 2.0 (Animal Research: Reporting *In Vivo* Experiments) guidelines [29] in the spirit of the pilot study.

This non-Good Laboratory Practices (GLP) animal experiment was performed in a GLP-certified Central Animal Laboratory, Turku University, Finland. The acclimatization period before the first experiment procedure was 6–13 days. The first STZ injection was given after the acclimatization period, and injections were given on 5 consecutive days. The mice were housed four to five animals per cage before experimentation and individually during the experiments, starting on study day 0. Cellulose paper and cardboard houses were used as environmental enrichment. Laboratory room temperature was 21 °C ± 3 °C, relative humidity was between 40% and 60%, and artificial lighting followed a 12-hour light, 12-hour dark cycle. A laboratory rodent chow diet (Teklad2920, Inotiv) and water were offered *ad libitum,* and the animals were cared for according to the standard operating procedures of Central Animal Laboratory.

TABLE 1 Glucose levels and the used insulin treatment dose.

Glucose level	Insulin treatment/day
<20 mmol/L	No insulin
20–25 mmol/L	0.5 IU
25–30 mmol/L	0.5–2 IU
>30 mmol/L	1–3 IU

The clinical status was checked twice daily during the experiment period. The animals were weighed on study days 0, 2, 5, 6, 8, 10, 12, and 14 after wound surgery without dressing.

Blood glucose monitoring

The blood glucose of the mice was measured for the first time after the first STZ injection using the ACCU Check Aviva glucose meter and Accu-Chek Aviva Blood Glucose Test Strips (lot 690720). The validity of the meter was checked by using Accu-Chek Guide control solutions (lot 24700675). Blood for glucose determination was taken from the tail vein by needle prick using a 27G needle and analyzed with a glucometer (0.6 µL of blood). When the blood glucose level was ≥15 mmol/L (corresponding to 270 mg/dL) in two consecutive measurements, a mouse was diagnosed with diabetes.

When blood glucose rose to ≥20 mmol/L, blood glucose was monitored daily, and insulin treatment was started at ≥25 mmol/L. The insulin doses were administered to mice once or twice a day, depending on the glucose level response (Lantus 100 IU/mL, 0.5 IU accuracy, batch 3F231A, insulin pen JuniorSTAR). The starting dose was 0.5 IU per mouse per day, after which the dose varied between 0.5 IU and 3.0 IU (Table 1).

Surgical procedure

Full-thickness wounds were created as described previously [27]. Briefly, 22 days after the last STZ injection, mice were preoperatively given a subcutaneous injection of buprenorphine (Bupaq multidose vet 0.1 mg/kg, Ritchter Pharma) and carprofen (Rimadyl vet 16 mg/kg, Zoetis) and anesthetized before the surgical procedure with isoflurane (3.5% Attane Vet 1,000 mg/g). Prior to incision, infiltrative local anesthesia of lidocaine (Lidocaine 4 mg/kg, Baxter) was applied under the skin. Rimadyl was also administered 6–8 h after surgery and every 10–13 h on study days 1 and 2 as a postoperative treatment. Surgical sites were disinfected with a skin disinfectant, and incisions were made on both sides of the animal's back with sterile scissors and tweezers, first to the right side and then to the left side. The veterinarian was blinded from the dosing sites of the treatment. The wounds were measured, and photographs were

taken immediately after surgery. After applying the model treatments on the right side and saline as a control on the left side, wounds were covered with transparent, non-occlusive polyurethane film.

A total of nine mice underwent surgery since one animal was hypoglycemic on the operation day (blood glucose <1.0 mmol/L) and had a decreased level of consciousness. The animal was treated with 0.5 mL of 10% sugar-water solution (D-sucrose, p.o.) and honey on the mouth mucous membranes. After 1 h, the animal was given 0.2 mL of 50% sugar solution. After 50 min of the last sugar application, the blood glucose level was 4.7 mmol/L. Subsequently, 10% sugar solution was provided *ad libitum*. After 3 h, the blood glucose level was 24.0 mmol/L. Blood sugar levels and insulin treatment were later performed in the same way as with animals that underwent surgery for welfare purposes, but are not plotted in the figures.

Wound monitoring

The length and width of the wounds were measured immediately after their creation and on study days 2, 5, 6, 8, 10, 12, and 14 using our previously published protocol with a calibrated digital caliper (Mitutoyo 0–150 mm) [27]. The analyst measured the wounds as a one-time method to keep the objectivity of the wound measurements. The wound area was calculated with the following equation according to Moreira et al. [30]:

$$(\text{Wound length}/2) \times (\text{wound width}/2) \times \pi \quad (1)$$

At the end of the study, mice were weighed, all macroscopic abnormalities at the wound site were recorded, and photographs of the wounds were taken. Blood samples (ca. 600 µL) were taken by heart puncture under isoflurane anesthesia in K2E Microtainer tubes (Becton Dickinson, United States, NJ, lot 4174515) for hematological analyses, which were implemented as blinded with sample coding without identifying the wound. Hematology test analyses were performed in EDTA blood tubes according to the protocol of Central Animal Laboratory using VetScan HM5 hematological analyses (Abaxis, United States). A piece of skin (1 cm^2), including the wound site, was removed and placed into 10% phosphate buffered neutral formalin (Oy Reagena Ltd, Finland, lot CB19/1). Subsequently, tissue samples were embedded in paraffin and cut into 4 µm sections for further histopathological analyses.

Thermal monitoring of the wounds

For wound temperature monitoring, a Thermidas IRT-384 Tablet (Vet VistaClinic, Software 1.4.2, Thermidas Oy, Tampere, Finland) was used. Images were taken in the same operating room (ambient temperature of 21–23 °C) within a 2-hour period on days 0, 2, 5, 6, 8, 10, 12, and 14 at the same time as the weight and wound measurements. Before imaging the mice, a blank image from the operating room table was taken to calibrate the temperature range. Images were taken approximately 15 cm from the animal. Animals were anesthetized before imaging, and the total operation time was approximately 4 min per animal. The thermal resolution of the images was 384 × 288 pixels. The temperature of the wounds was compared to healthy skin on the same animal.

Histopathology and immunohistochemistry

Wound tissue sections (4 µm thickness) were stained with hematoxylin and eosin (HE) for histological examination. A veterinary pathologist (J.L.) blinded to the sample identity assessed the staining. Masson's trichrome (MT) staining was used to evaluate collagen deposition by calculating the blue color intensity of the wound area.

Immunostaining was performed as reported previously by Koivuniemi et al. [31] and Koivunotko et al. [27]. Briefly, tissue sections were deparaffinized (3 × 2 min in xylene, 2 × 10 min in 100% ethanol, 2 × 10 min in 94% ethanol and 2 × 5 min in distilled H_2O). Antigen retrieval was carried out in 10 mM citrate buffer (Merck, Germany) with 0.05% Tween 20 solution (Merck) (pH 6) at 99 °C for 3 × 10 min. After antigen retrieval, endogenous peroxidase activity was blocked with 3% H_2O_2 (Merck) for 10 min. Sections were then blocked for 1 h in 5% bovine serum albumin (BSA, Merck) in Tris-buffered saline with Tween 20 (TBS-T, Merck). Next, sections were blocked with endogenous biotin (Avidin/Biotin blocking kit, Vector Laboratories, CA, USA) for 15 min with Avidin first and then 15 min with Biotin.

Tissue sections were incubated overnight at 4 °C with anti-rabbit CD31/platelet endothelial cell adhesion molecule (CD31/PECAM-1, 1:100, CAT: NB100–2284, Novus Biologicals, UK) or 1 h at room temperature with anti-rabbit ionized calcium-binding adaptor molecule 1 (Iba-1, 1:500, CAT: 019-19741, FujiFilm, USA) or anti-rabbit lysozyme (LZM, 1:1000, CAT: A0099, Agilent, CA, USA) as a primary antibody in 3% BSA/TBS-T. After washing with TBS-T, tissue sections were stained for 1 h at room temperature with goat anti-rabbit IgG as biotinylated secondary antibody (1:1000 for CD31 and 1:200 for Iba1 and LZM, Abcam, UK) in 3% BSA/TBS-T. VECTASTAIN Elite ABC reagents (Vector Laboratories) were used for antibody detection by staining the tissue sections for 30 min at room temperature, after which they were treated with 3,3′-diaminobenzidine (DAB) HRP substrate treatment (Vector Laboratories). All stained tissue sections were counterstained with hematoxylin, dehydrated, and covered with cover clips using a mounting medium (Coverquick 2000, VWR International, PA, USA).

Histoscanning was performed with a Pannoramic 250 Flash III brightfield digital slide scanner (3DHISTECH Ltd., Hungary) at the Histoscanner core facility (University of Helsinki) using the updated coding from the original one to increase the blindness of the image analyses. The thickness and length of the neo-epithelium and dermis were measured with CaseViewer (3DHISTECH Ltd., version 2.4). The intensity of the stained fibrous connective tissue and macrophage infiltration was evaluated using object and pixel classifications in QuPath 0.4.3 software [32]. To compare the results from the prolonged wound healing model with the previously described acute wound model using the same histopathological staining protocol [27], acute wound tissue section analyses were repeated with the same threshold settings. Thresholds in different analyses were as follows: 0.4 for iba-1 and LZM staining, 0.15 for CD-31 staining, 0.64 for MT staining.

Statistical analyses

The data are presented as mean standard deviation (STDEV). For the normally distributed data, statistical significance was determined with an unpaired t-test for two variables and a one-way ANOVA and Tukey HSD *post hoc* test for others. To evaluate the effects of glucose levels [defined as low (<23.4 mmol/L) and high (>23.4 mmol/L)] on the results, multivariate analyses were performed with a Wilks' Lambda test. Significance was concluded when $^{*}p < 0.05$, $^{**}p < 0.01$, $^{***}p < 0.001$, or $^{****}p < 0.0001$.

Results

Diabetes was successfully induced in all 10 animals

Diabetes was induced in all animals (blood glucose level ≥ 15 mmol/L) within 21 days after the first STZ bolus injection. In this study, animals were not fasted before STZ injections or before blood glucose measurements. The blood glucose measurements were performed daily or twice daily to ensure animal welfare and titrate the insulin dose for each animal. The mean blood glucose level on the last experimental day was 27 mmol/L (STDEV 4.1 mmol/L), which was significantly increased ($p < 0.001$) compared to the 16 days prior to surgery (Figure 1A). Based on clinical monitoring and weight (Figure 1B), even animals with high blood glucose levels (>30 mmol/L) were in good condition during the whole experiment. The non-significant weight decrease (3–9%) in some animals was correlated with higher blood glucose (>23.4 mmol/L) but was insignificant in multivariate analyses ($p = 0.085$).

Hematological analyses showed increased values in most of the measured parameters (Table 2) when compared with the acute wound model [27]. In the case of hematocrit, mean corpuscular hemoglobin, plateletcrit, and the total concentration of monocytes and neutrophils, no changes (less than 0.5-unit difference) were observed between the models. On the other hand, mean corpuscular volume, red blood cell distribution, and percentage of lymphocytes were decreased. However, no clinically relevant differences were observed.

Wounds were closed by day 14

The endpoint of the experiment was on day 14, during which the first closed wounds were observed (<5 mm^2) (Equation 1). No significant differences in wound closure, epithelialization, or fibrous tissue thickness between model treatment and control groups were observed (Figures 2A–C). The mean epithelium length in tissue samples was 1271 μm in treated wounds and 1207 μm in controls. The mean fibrous tissue thickness measured from the dermis site was 385 μm in treated wounds and 348 μm in control wounds. Histological evaluation of the HE-stained sections by the pathologist (J.L) showed regrown epidermis to cover the wound areas in all mice, often exhibiting minimal to mild epidermal hyperplasia. Model treatment was present extracellularly as large homogenous translucent depots occupying over half of the wound area in most treated samples.

The wound area treated with model treatment showed significantly decreased temperature during the first week compared with healthy skin temperatures (8 °C lower temperature on day 0, 2 °C on day 6, Figure 2D; Supplementary Material 1). In addition, treated wounds were 3 °C colder compared with control wounds on day 0.

Blood vessel formation at the wound site

The presence of newly formed blood vessels was measured from CD31 stained histopathological samples. The percentual contrast area of the CD31 staining in wounds was >5% in all wounds (Figure 3). In addition, the analyses were also performed for previous histopathological samples from the acute wound model on day 9 [27], but no significant differences were observed between CD31 stained tissue samples. In wounds with model treatment, standard deviation was higher than in control groups.

Increased infiltration of macrophages with higher activity in prolonged wound healing model

Macrophage cell infiltration was evaluated with both total macrophage staining (Iba-1) and active macrophage staining (LZM) (Figures 4A–D). The contrast analyses were also performed for previously obtained Iba-1 and LZM stained

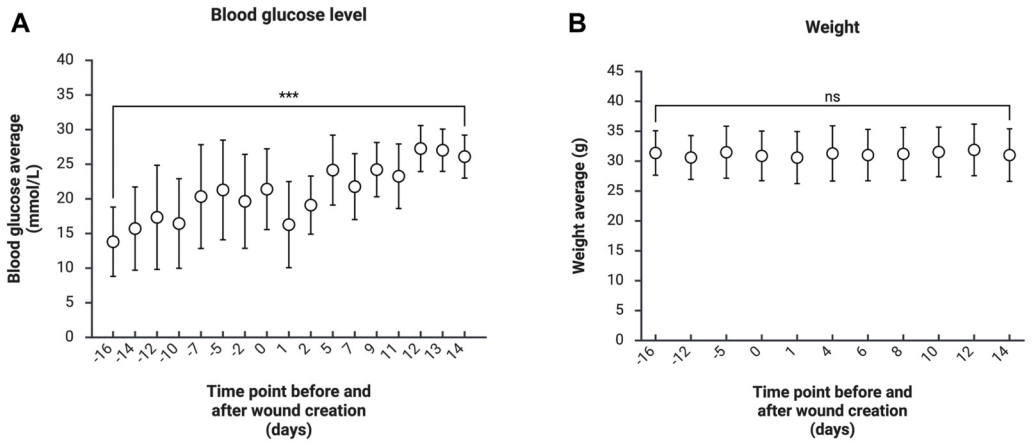

FIGURE 1
Mean blood glucose concentration (n = 9) **(A)** and mean weight (n = 9) **(B)** of animals throughout the experiment before and after surgery. Error bars indicate STDEV, and significance was calculated using one-way ANOVA (ns: $p \geq 0.05$, ***$p < 0.001$).

histopathological samples from the acute wound model on experimental day 9 [27] (Figures 4E,F). The treated chronic wound showed the highest presence of macrophages at the wound site [24.8% (± 6.6%)]. Despite the treatment conditions, chronic wounds showed significantly increased presence of macrophages with higher activity [10.2 (± 6.2%) and 16.23% (± 1.7%)] when compared with acute wounds [0.3% (± 0.2%) and 2.2% (± 0.9%); p = 0.003 between treatment groups, p = 0.009 between control groups, p = 0.0005 chronic treatment vs. acute control].

In the histological examination the treated wounds showed a stereotyped moderate inflammatory reaction, consisting of a thin rim of macrophages surrounding and infiltrating the hydrogel depots and single macrophages that contained modest amount of foamy hydrogel material as well as a moderate macrophage and lymphocyte infiltrate outside of the depots. Very few multinucleated giant cells were present. In comparison, most control wounds displayed mild to moderate mononuclear inflammatory cell infiltrate in the wound area.

Notably, most samples, regardless of treatment, exhibited pronounced, focally extensive hypodermal and deep dermal pyogranulomatous inflammation affecting damaged hair follicles and sebaceous glands (Supplementary Material 2). Granuloma formation was most prevalent at the wound borders and displayed a striking increase compared to the acute wound model [27].

Collagen deposition was slowed down in prolonged wound healing model

The blue color density of histopathological MT samples was measured to evaluate collagen deposition at wound sites (Figure 5). Based on the contrast analyses of chronic wounds on day 14 (Figures 5A,B) and acute wounds on day 9, collagen deposition was significantly lower (12.2 ± 0.09% and 23.7± 0.1%) in chronic wounds compared with treated acute wounds (43.2%± 18.6%; p = 0.003 between treatment groups, p = 0.004 chronic control vs. acute treatment) (Figure 5C). Higher blood glucose levels (>23.4 mmol/L) correlated with lower collagen deposition ($p < 0.01$).

Histological evaluation revealed plump horizontally orienting fibroblasts and palely staining collagen in the regenerating dermal connective tissue in both control and treated samples, suggesting maturing fibrous tissue with subjectively scarce collagen formation as well as sparse to moderate neovascularization (Supplementary Material 2). One control wound exhibited granulation tissue and one treated wound immature collagenous connective tissue.

Discussion

In this study, diabetes was successfully induced in all tested SKH1 mice. Furthermore, successfully prolonged full-thickness wound healing was observed in all surgical animals when compared to our previously described acute full-thickness wound model with the same surgical procedure and mouse strain [27]. SKH1 mouse is an outbred, euthymic, and immunocompetent strain and, due to the hairless skin, suitable as a wound model [23]. Male mice were used for their susceptibility to STZ induced cytotoxicity in pancreatic islet β-cells compared to females [36]. This likely enabled the successful induction of diabetes in all mice (blood glucose concentration ≥15 mmol/L). Normal blood glucose concentration in C57BL/6J mice is between 5.5 and 11 mmol/

TABLE 2 Hematological analyses of total blood samples after a prolonged wound healing model experiment. The results from the previous acute wound model in SKH1 [27] with informed reference values are presented on the right-hand side of the table.

Parameter	Unit	Value, mean (STDEV n = 9)	Previous acute wound model value (n = 3–6)	Reference value [33–35]
WBC- White blood cell	10^9/L	5.6 (2.5)	4.1 (1.5)	9.3 (1.8)
RBC- Red Blood Cell	10^{12}/L	11.1 (0.3)	9.9 (2.1)	9.4 (0.4)
HGB- Hemoglobin	g/L	157.6 (7.5)	142 (186.7)	120 (10.2)
HCT- Hematocrit	%	52.4 (4.0)	52.9 (4.1)	49.4 (2.2)
MCV- Mean Corpuscular Volume	fl	47.2 (3.0)	53.7 (2.3)	53.9 (2.4)
MCH- Mean Corpuscular Hemoglobin	pg	14.2 (0.4)	14.4 (0.6)	17.1 (0.4)
MCHC- Mean Corpuscular Hemoglobin Concentration	g/L	301.9 (15.5)	268 (16.6)	317.4 (9.8)
PLT- Platelet	10^9/L	431.2 (95.8)	335 (36.5)	285–890
PCT- Plateletcrit	%	0.3 (0.1)	0.2 (0.02)	N/Av
MPV- Mean Platelet Volume	fl	6.6 (0.4)	6.1 (0.9)	4.6 (0.1)
PDWs- Platelet Distribution Width	fl	7.4 (0.4)	6.4 (1.8)	7.7 (1.1)
PDWc- Platelet Distribution Width	%	28.4 (0.7)	26.6 (3.2)	N/Av
RDWs- Red blood cell Distribution	fl	32.7 (1.7)	38.3 (1.2)	29.1 (3.3)
RDWc- Red blood cell Distribution	%	21.6 (0.5)	19.9 (0.8)	16.4 (0.4)
LYM- Lymphocytes	10^9/L	4.1 (2.1)	3.6 (1.7)	5.7 (1.3)
MON- Monocytes	10^9/L	0.2 (0.1)	0.2 (0.1)	0.6 (0.2)
NE- Neutrophils	10^9/L	1.3 (0.6)	1.0 (0.1)	N/Av
LY%- Lymphocytes	%	71.9 (7.3)	73.8 (3.4)	61.5 (6.9)
MO%- Monocytes	%	4.8 (2.2)	4.9 (2.5)	6.1 (1.3)
NE%- Neutrophils	%	23.3 (6.0)	21.3 (10.2)	N/Av
EOS- Eosinophils EO%- Eosinophils BAS- Basophils BA%- Basophils	10^9/L % 10^9/L %	0.0	0.0	N/Av 0.6 (0.2) 0.0 (0.0) 0.0 (0.0)

L, which was used as a reference value [37]. Using a small needle and aspiration technique, no animals showed clinical symptoms due to failed STZ injection (The total number of STZ injections was 50, 5 per mouse). The repeated low STZ dose approach was chosen based on reported outcomes of single high-dose STZ (150–200 mg/kg IP), which induces a high acute mortality risk, often due to severe hypoglycemia and systemic toxicity [28]. The low-dose STZ approach only partially damages pancreatic islets, triggering an inflammatory process that causes the further loss of β-cell activity that ultimately results in insulin deficiency and hyperglycemia. The graphical summary comparing the outcomes of the previous acute wound model and prolonged wound healing model is presented in Figure 6.

In addition, animal welfare was closely monitored throughout the study by daily assessment of weight, behavior, and the risk of insulin dose-related hypoglycemia, all while maintaining on *ad libitum* diet. Since STZ induction has been reported to be equally diabetogenic to fed or fasted mice, fasting was not necessary in this model [38, 39]. This approach adheres to humane endpoints and ensures consistency across experimental conditions, facilitating reliable comparisons between prolonged and acute wound models under future standardized settings. However, it should be addressed that STZ induction produces hyperglycemic conditions similar to type 1 diabetes, while diabetic chronic wounds are often associated with type 2 diabetes due to metabolic syndrome, obesity, and insulin resistance. STZ induction of diabetes was selected in this case as it offers a controlled and non-transgenic approach, which helps to improve standardization when compared with genetically modified obese mouse strains or high-fat diet-based models alone. In future, a combined STZ induction and high-fat diet model could produce a diabetic

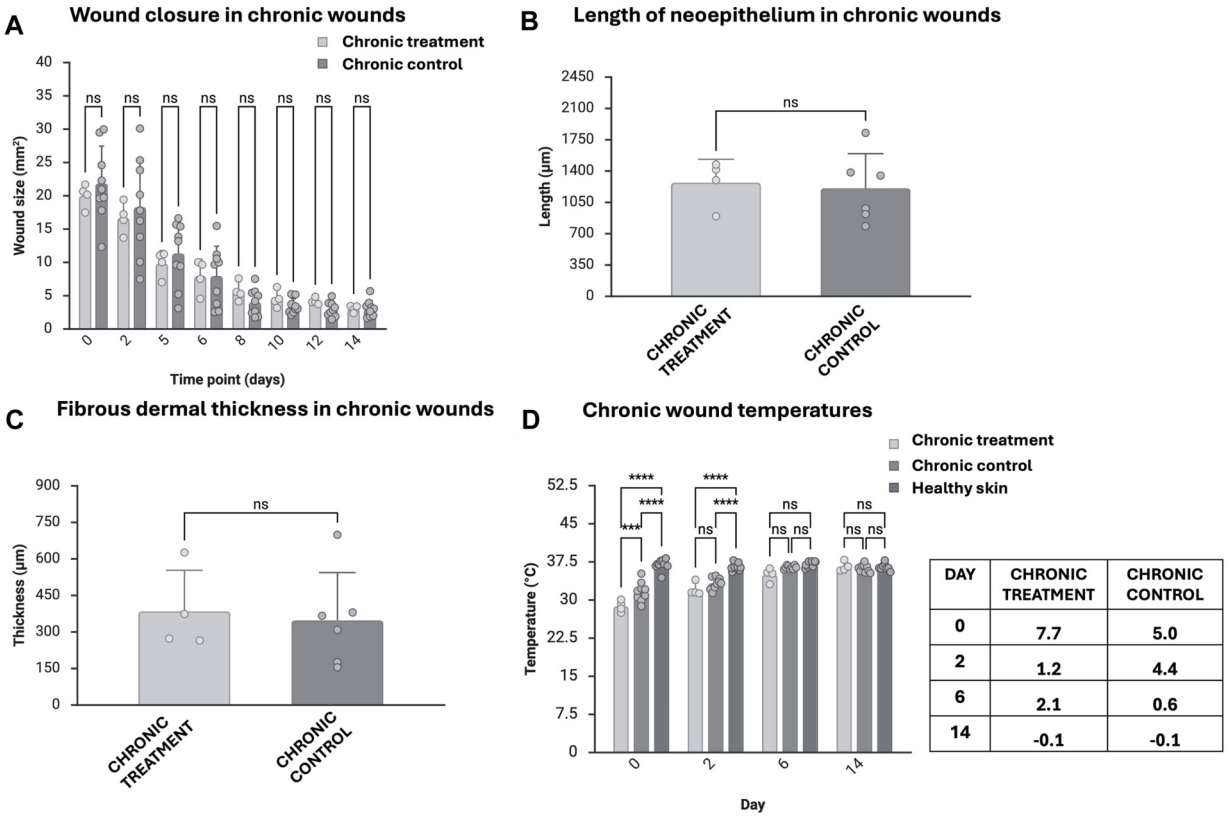

DAY	CHRONIC TREATMENT	CHRONIC CONTROL
0	7.7	5.0
2	1.2	4.4
6	2.1	0.6
14	-0.1	-0.1

FIGURE 2
Measurements of wound size over time (n = 4 in treatment group, n = 9 in control group) **(A)**, mean length of neo-epithelium (n = 4 in treatment group, n = 6 in control group) **(B)**, mean thickness of dermal fibrous tissue (n = 4 in treatment group, n = 6 in control group) **(C)**, and mean wound site temperature (n = 4 in treatment group, n = 9 in control group) with temperature differences (°C) compared with healthy skin presented in a table **(D)**. Error bars indicate STDEV, and significance was calculated using unpaired t-test and one-way ANOVA (ns: $p \geq 0.05$, ***$p < 0.001$, ****$p < 0.0001$).

chronic wound model with the characteristics of type-2 diabetes [40, 41].

In addition to blood glucose level monitoring, hematological parameters were measured at the end of the experiment. Based on the hematological parameters, a slight increase in the number of white blood cells, red blood cells and platelets were observed. However, these changes were not significantly different from our previous data [27] or reference values. A similar increase in these hematological values was observed in a study by Anggraeni et al. [42] where hematological parameters were studied in STZ induced diabetic mice with and without cogon grass treatment. However, most published *in vivo* models report inconsistent hematological data when comparing diabetic and healthy mice, making it difficult to draw definitive conclusions based on these parameters.

Higher blood glucose levels in SKH1 mice might have led to prolonged wound closure compared with similar size wounds in the acute wound healing model [27]. In prolonged wound healing models, wounds were only closed on day 14; this is 5 days longer than in acute wounds, which closed on day 9. The full-thickness wound creation was carried out as in our previous acute wound model reaching the muscle layer, partial destruction of which may lead to slower wound contraction. Similar observations have been made by Wyles et al. in which full-thickness wounds were created for C57BL/6 mice [43]. Chronic wounds were modeled by inducing oxidative stress with 3-amino-1,2,4-trizole and thiomalic acid as intraperitoneal injections, leading to slower wound contraction compared with non-injected mice. Although impaired wound closure is one characteristic in prolonged wound healing, wound closure in mice is affected by the *panniculus carnosus* and movement of the loose skin during surgical operation and wound covering. For this reason, other impaired wound healing-related factors, like re-epithelialization, reformation of extracellular matrix, angiogenesis and immunological changes are more reliable factors to study. The length of re-epithelialization and the thickness of the regenerating wound area were measured, which were not different to the acute wound healing model with or without model treatment. However, it is noteworthy that in the prolonged wound healing model, length and thickness

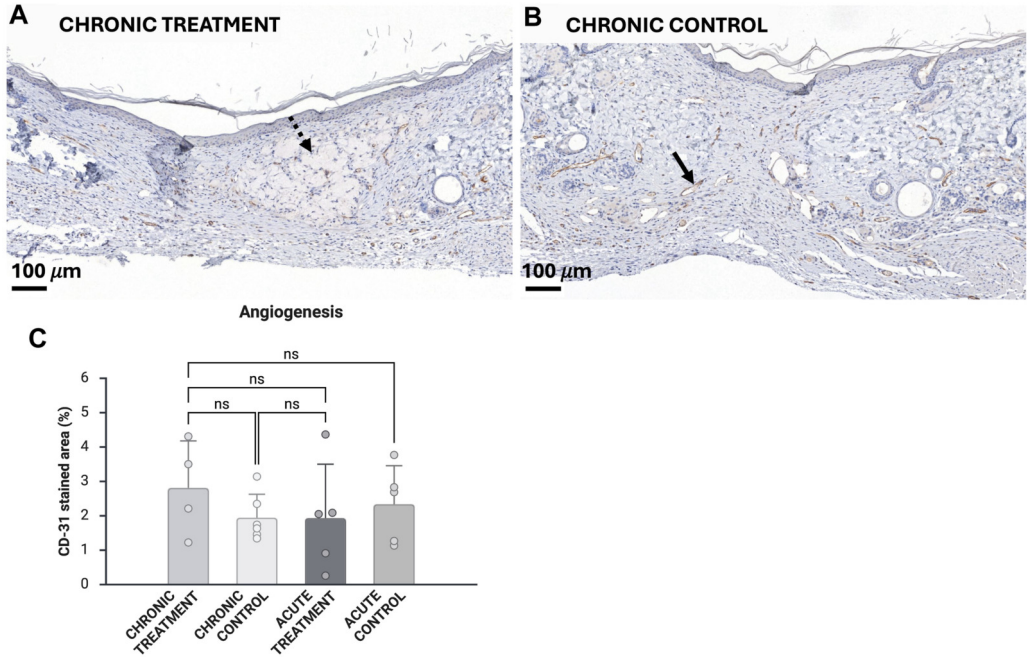

FIGURE 3
The contrast measurements of CD31-stained vessels in treated chronic wounds **(A)** and chronic control wounds **(B)**. The dotted arrow indicates model treatment (nanofibrillated cellulose hydrogel), and the solid arrow indicates an example of a stained vessel. Percentual area of the CD31-stained vessels (n = 4 for chronic treatment, n = 6 for chronic control) **(C)**. Analyses were also performed for previously obtained histopathological samples (n = 5 for acute treatment, n = 5 for acute control) [27]. Scale bar 100 μm. Error bars indicate STDEV, and significance was calculated using one-way ANOVA (ns: $p \geq 0.05$).

values were measured on day 14 but on day 9 in the acute wound, correlating with the slower wound closure and healing. Reduced collagen deposition in quantitative analysis using MT-stained slides, along with histologically detected maturing fibrous tissue that exhibited subjectively scarce collagen formation on day 14, further attest to delayed healing, which might be related to the higher blood glucose levels that correlated with lower collagen deposition. Additionally, while the treatment model enhanced epithelialization compared to control in acute wounds, there was no difference in the prolonged wound healing setting. This underscores the importance of incorporating both acute and prolonged wound healing models in early preclinical studies to accurately assess the therapeutic potential of candidate treatments across diverse wound types.

Thermidas thermal imaging system was used to measure temperature changes in differently treated wounds and healthy skin. In general, temperature monitoring can non-invasively detect early diagnosis of prolonged inflammation, the state of angiogenesis and the total progress of wound healing. In addition, thermal analyses indicate treatment candidate effects on wound site which may reflect on healing outcome [44–46]. In this study, temperature was significantly decreased in the treated wounds compared with healthy skin for 6 days after wound creation. Extreme temperature changes may perturb the progression of wound healing for instance by affecting cell functionality and degradation of proteins [47–49]. However, these effects were not observed in the wound healing outcomes of this study. Interestingly, the high water content of the hydrogel-based model treatment lowered local wound temperature, suggesting potential as a first-aid cooling agent for wounds, such as burns or acutely inflamed wounds [50]. The thermal imaging system was successfully used to measure temperature in this *in vivo* model with sufficient sensitivity to detect temperature variations between wounded and healthy skin. To our knowledge, Thermidas has not previously been used in *in vivo* models, for which reason this study highlights potential novel applications for the thermal imaging instruments in research and clinical settings.

A key issue in diabetic prolonged or chronic wounds is disturbed blood vessel formation due to the effects of high blood glucose concentration on the endothelial cell functions [51]. This leads to insufficient oxygen and nutrient supply at the wound site and prolongs wound healing. According to Shaterian et al. [52], the progression of angiogenesis in a full-thickness acute wound model in C57/B16 mice treated with a collagen-based wound dressing showed the greatest presence of blood vessels between days 10 and 14 after which wound maturation begins. In our study, angiogenesis was evaluated based on the CD31-positive area in tissue sections. No significant differences were observed between prolonged and acute wound models in

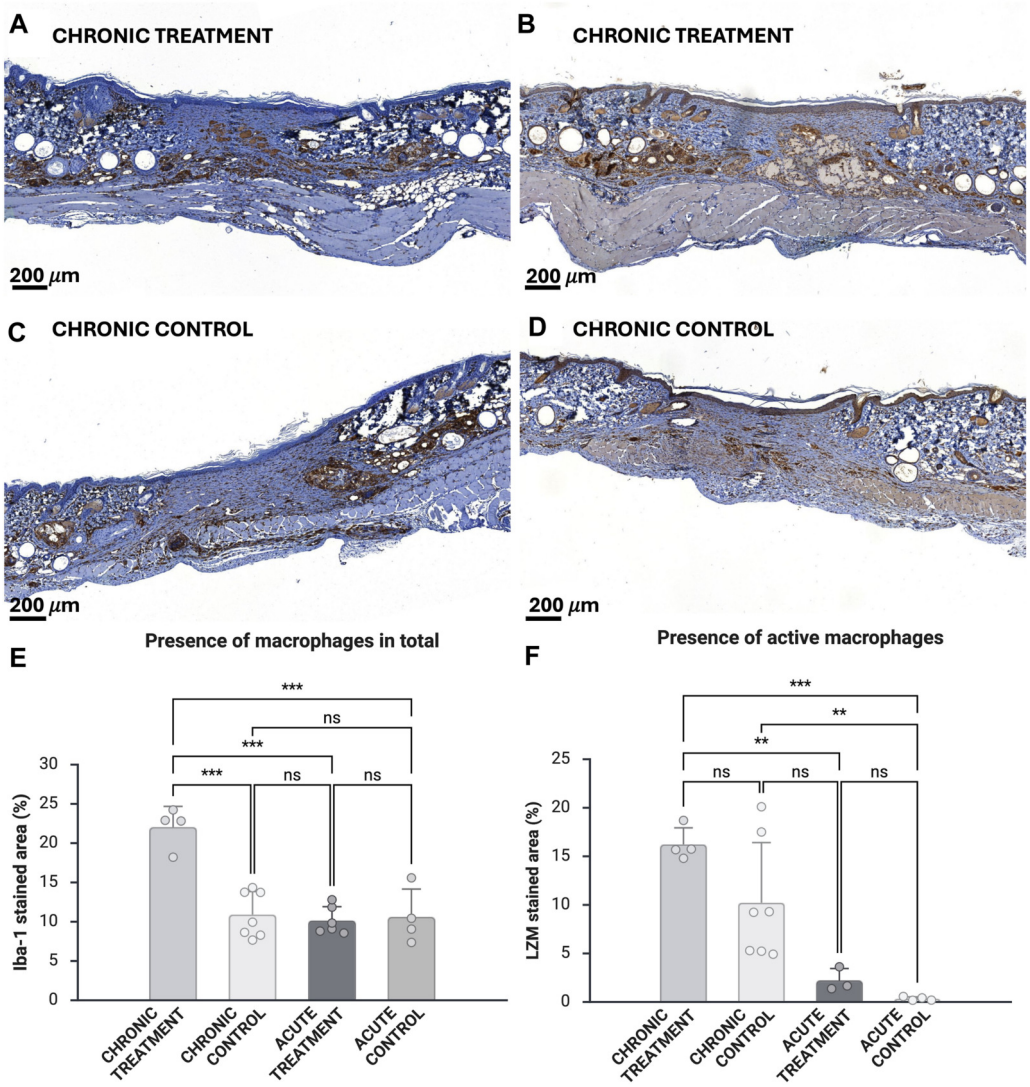

FIGURE 4
The presence of macrophages in total stained with Iba-1 **(A,C)** and active macrophages stained with LZM **(B,D)**. Upper tissue sample images are from treated chronic wounds and lower ones from chronic control wounds. Percentual area of the iba-1 stained macrophages (n = 4 for chronic treatment, n = 6 for chronic control, n = 6 for acute treatment, n = 4 for acute control) **(E)** and LZM stained macrophages (n = 4 for chronic treatment, n = 7 for chronic control) **(F)**. Analyses were also performed for previously obtained histopathological samples (n = 3 for acute treatment, n = 4 for acute control) [27] **(C)**. Scale bar 200 μm. Error bars indicate STDEV, and significance was calculated using one-way ANOVA (ns: $p \geq 0.05$, **$p < 0.01$, ***$p < 0.001$).

any treatment condition, and this similarity was also observed in the histological analysis. However, since the CD31 staining area was measured only after sacrifice of the animals (day 9 and 14 in the acute and prolonged wound healing models, respectively), a delay or a decrease in angiogenesis activity may only be inferred. Future studies should include all conditions in a single study and histologically compare angiogenesis on the same experimental day.

Another major factor in the progression of wound healing and activation of angiogenesis is the change in presence of pro-inflammatory macrophages into tissue regenerative ones, roughly categorized as M1 and M2 phenotypes [14, 53]. In diabetic wounds, due to the infection, and increased blood glucose concentration, the ratio between these phenotypes is disturbed, leading to persistence of M1 and prolonged inflammation [54]. Although the presence of specific macrophage phenotypes was not analyzed in this study, we observed significant increases in the macrophage-stained area (Iba-1) [55] with higher expression of the LZM enzyme, which may be related to enhanced macrophage activity [56], when

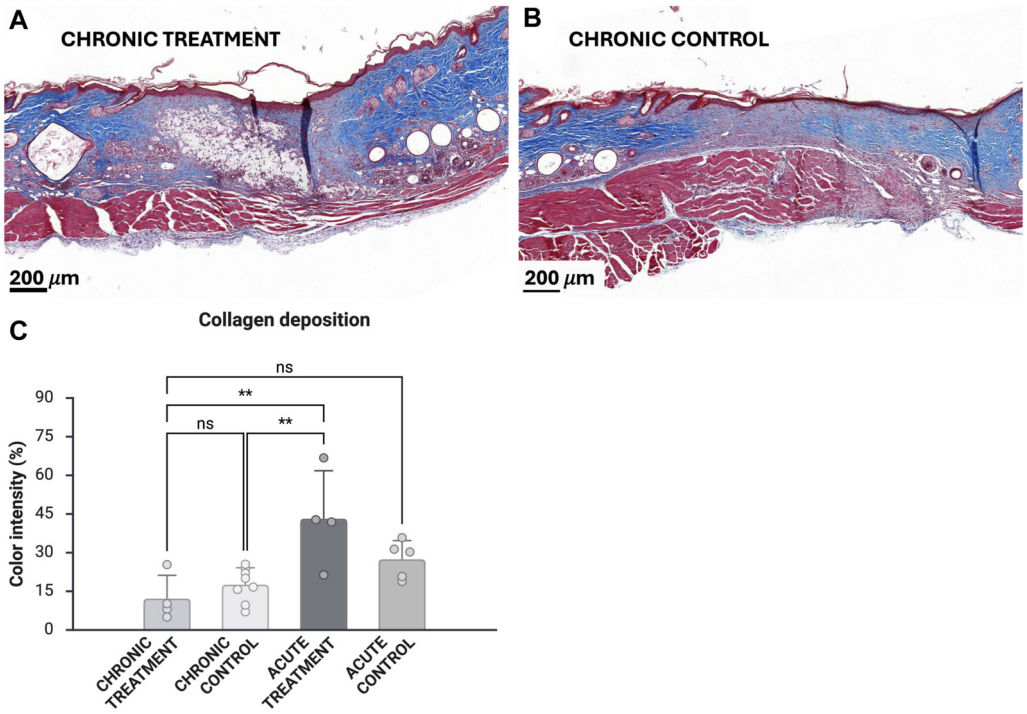

FIGURE 5
Masson trichrome analyses of treated chronic wounds **(A)** and control wounds **(B)**. Collagen deposition was measured from blue staining intensity (n = 4 for chronic treatment, n = 7 for chronic control) **(C)**. Analyses were also performed for previously obtained histopathological samples (n = 4 for acute treatment, n = 5 for acute control) [27]. Scale bar 200 μm. Error bars indicate STDEV, and significance was calculated using one-way ANOVA (ns: $p \geq 0.05$, **$p < 0.01$).

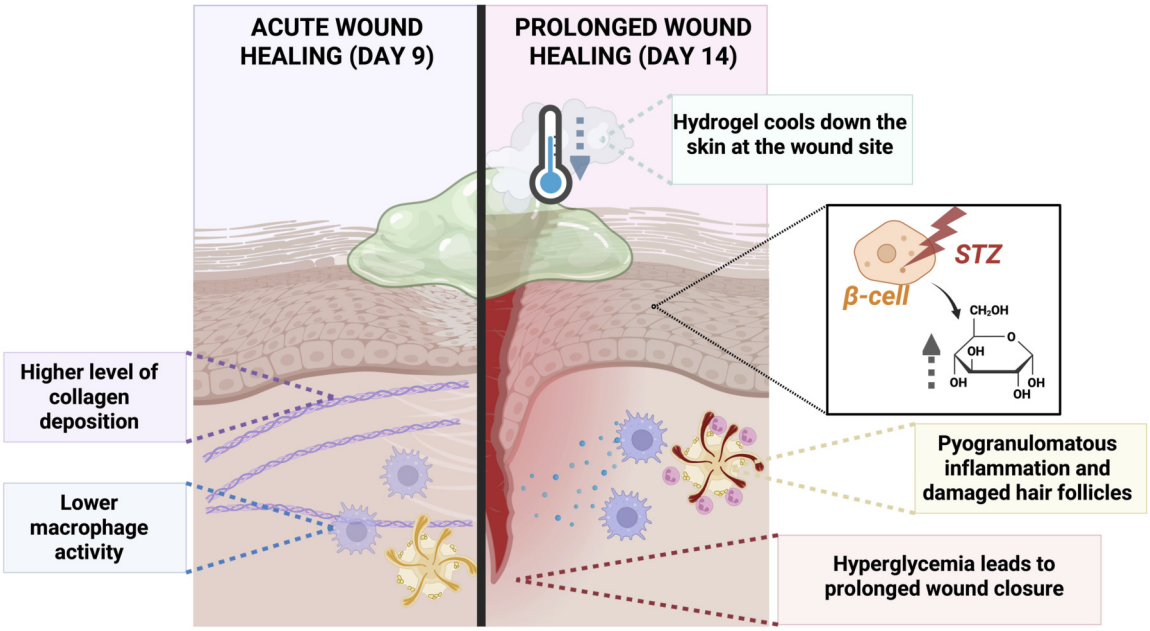

FIGURE 6
Graphical summary of the comparison between the acute wound model and prolonged wound healing model implemented in SKH1 mice.

compared to our previous acute wound model [27]. Increased LZM immunostaining may also be associated with increased presence of neutrophils at the wound site and/or in the pyogranulomatous inflammatory foci, which could lead to prolonged active neutrophilic inflammation [56]. Interestingly, in addition to a generally modest macrophage reaction to the NFC hydrogel, the prolonged wound healing model exhibited excessive pyogranulomatous inflammation affecting hair follicles. Granuloma formation was markedly more severe than that observed in our previous acute wound model [27] or the hair follicle granuloma formation typical of the SKH1 hairless mice [23]. This prolonged pyogranulomatous inflammation likely originated from the wounding trauma and corroborates the increased LZM immunostaining. These observations suggest that the diabetic full-thickness wound model more closely resembles the characteristics of prolonged, compromised wound healing than the previously published acute wound healing model.

The imbalance in macrophage activity in wound healing may lead to increased levels of reactive oxygen species damaging the ECM during re-modeling [57]. In addition, a hyperglycemic environment increases protease levels [53] and disturbs cell-level crosstalk between macrophages and fibroblasts that has a role in producing collagen at the wound site [58]. In this study, collagen deposition was significantly lower despite the treatment conditions when compared with the treated acute wounds indicating prolonged wound healing in diabetic mice. Furthermore, the markedly different outcomes observed between treatment groups suggest that prolonged wounds or wounds with chronic characteristics may require therapeutic strategies focused on enhancing cellular functionality, rather than solely providing mechanical support and an optimal wound bed environment. This study highlights the importance of creating comparable preclinical models in highly heterogenous wound research, which could reveal different physiological outcomes with varying treatment needs.

Conclusion

To our knowledge, no previous published work has compared acute wound healing and diabetic prolonged wound healing in hairless SKH1 mice. This pilot study may show the suitability of SKH1 mice for studying full-thickness wound healing under different conditions. Diabetes was induced in all mice using repeated STZ induction without complications. The markedly prolonged wound closure time, elevated macrophage activity, and reduced collagen deposition reflected key features of chronic wounds. However, establishing a fully representative chronic wound model requires additional considerations, like reduced oxygen availability, and the potential influence of infection; these factors were not examined in this study. With careful monitoring, SKH1 mice may be used in future wound healing studies as acute and prolonged wound healing models that are highly tractable for STZ-induced diabetes. The sample size of this proof-of-concept study was deliberately small and relies on wound healing in SKH1 mice in previously published data. Therefore, studies with a larger sample size, including healthy control groups and other treatment candidates, should be performed in future. By offering the opportunity to generate standardized and reproducible *in vivo* models, the development of wound treatment candidates can be enhanced while adhering to the 3Rs principles.

Author contributions

EK drafted the manuscript. EK, CP, and MM were responsible for validation. EK was responsible for visualization. EK, JM, and MM were responsible for methodology. EK, JM, JL, and MM conducted the investigation. EK, JL, and MM performed formal analysis. EK and JL were responsible for data curation. EK, CP, and MY conceptualized the experiments. RH and MY acquired funding and were responsible for supervision. MY was also responsible for resources and project administration. All authors contributed to the article and approved the submitted version.

Data availability

The raw data supporting the conclusions of this article will be made available by the authors, without undue reservation.

Ethics statement

The animal experiments were approved by the National Project Authorization Board of Finland (license number ESAVI-25539-2024) and the study conformed to the following guidelines: DIRECTIVE 2010/63/EU of the European Parliament and the Council, Finnish Act (497/2013), and Government Decree on the Protection of Animals Used for Scientific or Educational Purposes (564/2013), and Guidance document on the Recognition, Assessment and Use of Clinical Signs as Humane endpoints for Experimental Animals Used in Safety Evaluation, Environmental Health and Safety Monograph Series on Testing and Assessment (No 19. OECD 2000).

Funding

The author(s) declared that financial support was received for this work and/or its publication. EK acknowledges the Post Docs in Companies program 2025 funded by Jenny and Antti Wihuri Foundation. JM acknowledges the Doctoral Programme in

Materials Research and Nanosciences (University of Helsinki, Finland). CP acknowledges the Finnish Cultural Foundation (grant no. 00250755). RH and MY acknowledge the Academy of Finland, GeneCellNano flagship-project (grant no. 337430) and RH acknowledges the Finnish Cultural Foundation (grant no. 00220283).

Acknowledgements

The authors gratefully acknowledge the expert care provided by the personnel of Central Animal Laboratory, University of Turku. The authors also thank the Finnish Centre for Laboratory Animal Pathology (FCLAP) for histological sample processing and HE, MT, Iba-1, and LZM staining, as well as the Histoscanner core facility at the University of Helsinki for supporting histological analyses. Both FCLAP and the Histoscanner core facility are supported by HiLIFE and Biocenter Finland. The Figures were created with Biorender.com.

Conflict of interest

MM was employed by the company Made Consulting Ltd Oy. EK was part of the Postdocs in Companies project in collaboration with UPM Kymmene. UPM Kymmene was not involved in the study design, collection, analysis, interpretation of data, the writing of this article or the decision to submit it for publication.

The remaining author(s) declared no potential conflicts of interest with respect to the research, authorship, and/or publication of this article.

Generative AI statement

The author(s) declared that generative AI was not used in the creation of this manuscript.

Any alternative text (alt text) provided alongside figures in this article has been generated by Frontiers with the support of artificial intelligence and reasonable efforts have been made to ensure accuracy, including review by the authors wherever possible. If you identify any issues, please contact us.

Supplementary material

The Supplementary Material for this article can be found online at: https://www.ebm-journal.org/articles/10.3389/ebm.2026.10857/full#supplementary-material

References

1. Nussbaum SR, Carter MJ, Fife CE, DaVanzo J, Haught R, Nusgart M, et al. An economic evaluation of the impact, cost, and medicare policy implications of chronic nonhealing wounds. *Value in Health* (2018) **21**(1):27–32. doi:10.1016/j.jval.2017.07.007

2. Armstrong DG, Tan TW, Boulton AJM, Bus SA. Diabetic foot ulcers: a review. *JAMA* (2023) **330**:62–75. doi:10.1001/jama.2023.10578

3. Orfali R, Ghaffar S, AlAjlan L, Perveen S, Al-Turki E, Ameen F. Diabetes-related lower limb wounds: antibiotic susceptibility pattern and biofilm formation. *Saudi Pharm J* (2024) **32**(6):102069. doi:10.1016/j.jsps.2024.102069

4. Tobalem M, Lévigne D, Modarressi A, Atashi F, Villard F, Hinz B, et al. Hyperglycemia interacts with ischemia in a synergistic way on wound repair and myofibroblast differentiation. *Plast Reconstr Surg Glob Open* (2015) **3**(7):e471. doi:10.1097/GOX.0000000000000443

5. Dorf N, Maciejczyk M. Skin manifestations in diabetes—what is new? *Front Med* (2025) **12**:1640144. doi:10.3389/fmed.2025.1640144

6. Baltzis D, Eleftheriadou I, Veves A. Pathogenesis and treatment of impaired wound healing in diabetes mellitus: new insights. *Adv Ther* (2014) **31**:817–36. doi:10.1007/s12325-014-0140-x

7. Yadav JP, Singh AK, Grishina M, Pathak P, Verma A, Kumar V, et al. Insights into the mechanisms of diabetic wounds: pathophysiology, molecular targets, and treatment strategies through conventional and alternative therapies. *Inflammopharmacology* (2024) **32**:149–228. doi:10.1007/s10787-023-01407-6

8. Morton LM, Phillips TJ. Wound healing and treating wounds differential diagnosis and evaluation of chronic wounds. *J Am Acad Dermatol* (2016) **74**:589–605. doi:10.1016/j.jaad.2015.08.068

9. Guo S, DiPietro LA. Factors affecting wound healing REVIEW. *J Dent Res* (2010) **89** (3): 219–229. doi:10.1177/0022034509359125

10. Patel S, Srivastava S, Singh MR, Singh D. Mechanistic insight into diabetic wounds: pathogenesis, molecular targets and treatment strategies to pace wound healing. *Biomed Pharmacother* (2019) **112**:108615. doi:10.1016/j.biopha.2019.108615

11. Galkowska H, Wojewodzka U, Olszewski WL. Chemokines, cytokines, and growth factors in keratinocytes and dermal endothelial cells in the margin of chronic diabetic foot ulcers. *Wound Repair Regen* (2006) **14**(5):558–65. doi:10.1111/j.1743-6109.2006.00155.x

12. Linard C, Brachet M, Strup-Perrot C, L'homme B, Busson E, Squiban C, et al. Autologous bone marrow mesenchymal stem cells improve the quality and stability of vascularized flap surgery of irradiated skin in pigs. *Stem Cells Transl Med* (2018) **7**(8):569–82. doi:10.1002/sctm.17-0267

13. Hunt M, Torres M, Bachar-Wikstrom E, Wikstrom JD. Cellular and molecular roles of reactive oxygen species in wound healing. *Commun Biol* (2024) **7**:1534. doi:10.1038/s42003-024-07219-w

14. Hesketh M, Sahin KB, West ZE, Murray RZ. Macrophage phenotypes regulate scar formation and chronic wound healing. *Int J Mol Sci* (2017) **18**. doi:10.3390/ijms18071545

15. Hirota A, Ebihara T, Kusubata M, Kobayashi M, Kobayashi K, Kuwaba K, et al. Collagen of chronically inflamed skin is over-modified and upregulates secretion of matrix metalloproteinase 2 and matrix-degrading enzymes by endothelial cells and fibroblasts. *J Invest Dermatol* (2003) **121**(6):1317–25. doi:10.1111/j.1523-1747.2003.12637.x

16. Chi N, Zheng S, Clutter E, Wang R. Silk-CNT mediated fibroblast stimulation toward chronic wound repair. *Recent Prog Mater* (2019) **1** (4): 16. doi:10.21926/rpm.1904007

17. Ansell DM, Holden KA, Hardman MJ. Animal models of wound repair: are they cutting it? *Exp Dermatol* (2012) **21**(8):581–5. doi:10.1111/j.1600-0625.2012.01540.x

18. Zomer HD, Trentin AG. Skin wound healing in humans and mice: challenges in translational research. *J Dermatol Sci* (2018) **90**(1):3–12. doi:10.1016/j.jdermsci.2017.12.009

19. Du Y, Wang J, Fan W, Huang R, Wang H, Liu G. Preclinical study of diabetic foot ulcers: from pathogenesis to vivo/vitro models and clinical therapeutic transformation. *Int Wound J* (2023) **20**:4394–409. doi:10.1111/iwj.14311

20. Lenzen S. The mechanisms of alloxan- and streptozotocin-induced diabetes. *Diabetologia* (2008) **51**:216–26. doi:10.1007/s00125-007-0886-7

21. Deeds MC, Anderson JM, Armstrong AS, Gastineau DA, Hiddinga HJ, Jahangir A, et al. Single dose streptozotocin-induced diabetes: considerations for study design in islet transplantation models. *Lab Anim* (2011) **45**:131–40. doi:10.1258/la.2010.010090

22. Matsumoto-Oda A, Utsumi D, Takahashi K, Hirata S, Nyachieo A, Chai D, et al. Inter-species differences in wound-healing rate: a comparative study involving primates and rodents. *Proceedings R Soc B: Biol Sci* (2025) **292** (2045): 20250233. doi:10.1098/rspb.2025.0233

23. Benavides F, Oberyszyn TM, VanBuskirk AM, Reeve VE, Kusewitt DF. The hairless mouse in skin research. *J Dermatol Sci* (2009) **53**:10–8. doi:10.1016/j.jdermsci.2008.08.012

24. Gurtner GC, Wong VW, Sorkin M, Glotzbach JP, Longaker MT. Surgical approaches to create murine models of human wound healing. *J Biomed Biotechnol* (2011) **2011**:969618. doi:10.1155/2011/969618

25. Lopez-Jornet P, Camacho-Alonso F, Gómez-Garcia F, Molina Miñano F, Cañas X, Serafín A, et al. Effects of potassium apigenin and verbena extract on the wound healing process of SKH-1 mouse skin. *Int Wound J* (2014) **11**(5):489–95. doi:10.1111/j.1742-481X.2012.01114.x

26. Bell RR, Dunstan RW, Khan NK. Skin wound healing in the SKH-1 female mouse following inducible nitric oxide synthase inhibition. *Br J Dermatol* (2007) **157**(4):656–61. doi:10.1111/j.1365-2133.2007.08096.x

27. Koivunotko E, Koivuniemi R, Monola J, Harjumäki R, Pridgeon CS, Madetoja M, et al. Cellulase-assisted platelet-rich plasma release from nanofibrillated cellulose hydrogel enhances wound healing. *J Controlled Release* (2024) **368**:397–412. doi:10.1016/j.jconrel.2024.02.041

28. Furman BL. Streptozotocin-induced diabetic models in mice and rats. *Curr Protoc* (2021) **1**(4):e78. doi:10.1002/cpz1.78

29. du Sert NP, Ahluwalia A, Alam S, Avey MT, Baker M, Browne WJ, et al. Reporting animal research: explanation and elaboration for the arrive guidelines 2.0. *PLoS Biol* (2020) **18** (7): e3000411. doi:10.1371/journal.pbio.3000411

30. Moreira C, Cassini-Vieira P, da Silva M, da BL. Skin wound healing model - excisional wounding and assessment of lesion area. *Bio Protoc* (2015) **5** (22): e1661. doi:10.21769/bioprotoc.1661

31. Koivuniemi R, Xu Q, Snirvi J, Lara-Sáez I, Merivaara A, Luukko K, et al. Comparison of the therapeutic effects of native and anionic nanofibrillar cellulose hydrogels for full-thickness skin wound healing. *Micro* (2021) **1**(2):194–214. doi:10.3390/micro1020015

32. Bankhead P, Loughrey MB, Fernández JA, Dombrowski Y, McArt DG, Dunne PD, et al. QuPath: open source software for digital pathology image analysis. *Sci Rep* (2017) **7**(1):16878. doi:10.1038/s41598-017-17204-5

33. Schaffer BS, Grayson MH, Wortham JM, Kubicek CB, McCleish AT, Prajapati SI, et al. Immune competency of a Hairless mouse strain for improved preclinical studies in genetically engineered mice. *Mol Cancer Ther* (2010) **9**(8):2354–64. doi:10.1158/1535-7163.MCT-10-0207

34. Silva-Santana G, Bax JC, Fernandes DCS, Bacellar DTL, Hooper C, Dias AASO, et al. Clinical hematological and biochemical parameters in Swiss, BALB/c, C57BL/6 and B6D2F1 *Mus musculus*. *Anim Model Exp Med* (2020) **3**(4):304–15. doi:10.1002/ame2.12139

35. Santos EW, Oliveira DCd, Hastreiter A, Silva GBd, Beltran JS, de O, et al. Hematological and biochemical reference values for C57BL/6, Swiss webster and BALB/c mice. *Braz J Vet Res Anim Sci* (2016) **53**(2):138. doi:10.11606/issn.1678-4456.v53i2p138-145

36. Kolb H. Mouse models of insulin dependent diabetes: low-dose streptozocin-induced diabetes and nonobese diabetic (NOD) mice. *Diabetes Metab Rev* (1987) **3**(3):751–78. doi:10.1002/dmr.5610030308

37. Klueh U, Liu Z, Cho B, Ouyang T, Feldman B, Henning TP, et al. Continuous glucose monitoring in normal mice and mice with prediabetes and diabetes. *Diabetes Technol Ther* (2006) **8**(3):402–12. doi:10.1089/dia.2006.8.402

38. Lennikov A, ElZaridi F, Yang M. Modified streptozotocin-induced diabetic model in rodents. *Anim Model Exp Med* (2024) **7**(5):777–80. doi:10.1002/ame2.12497

39. Chaudhry ZZ, Morris DL, Moss DR, Sims EK, Chiong Y, Kono T, et al. Streptozotocin is equally diabetogenic whether administered to fed or fasted mice. *Lab Anim* (2013) **47**(4):257–65. doi:10.1177/0023677213489548

40. Attrill EH, Scharapow O, Perera S, Mayne S, Sumargo N, Ross RM, et al. Controlled induction of type 2 diabetes in mice using high fat diet and osmotic-mini pump infused streptozotocin. *Sci Rep* (2025) **15**(1):8812. doi:10.1038/s41598-025-89162-2

41. Couturier A, Calissi C, Cracowski JL, Sigaudo-Roussel D, Khouri C, Roustit M. Mouse models of diabetes-related ulcers: a systematic review and network meta-analysis. *EBioMedicine* (2023) **98**:104856. doi:10.1016/j.ebiom.2023.104856

42. Anggraeni N, Syamsunarno MRAA, Widyastuti R, Puspitasari IM, Praptama S. Potential dual effect anti-inflammatory and anti-platelet of cogon grass ethanol extract on diabetic mice a preliminary study. *J Phys Conf Ser* (2019) **1246**: 012006. doi:10.1088/1742-6596/1246/1/012006

43. Wyles SP, Dashti P, Pirtskhalava T, Tekin B, Inman C, Gomez LS, et al. A chronic wound model to investigate skin cellular senescence. *Aging.* (2023) **15**(8): 2852–62. doi:10.18632/aging.204667

44. Ring EFJ, Ammer K. Infrared thermal imaging in medicine. *Physiol Meas* (2012) **33**:R33–R46. doi:10.1088/0967-3334/33/3/R33

45. Klama-Baryła A, Kitala D, Łabuś W, Kraut M, Szapski M, Smętek W. Infrared thermal imaging as a method of improving skin graft qualification procedure and skin graft survivability. *Transpl Proc* (2020) **52**(7):2223–30. doi:10.1016/j.transproceed.2020.01.108

46. Fridberg M, Bafor A, Iobst CA, Laugesen B, Jepsen JF, Rahbek O, et al. The role of thermography in assessment of wounds. A scoping review. *Injury* (2024) **55**(11): 111833. doi:10.1016/j.injury.2024.111833

47. dos Santos-Silva MA, Trajano ETL, Schanuel FS, Monte-Alto-Costa A. Heat delays skin wound healing in mice. *Exp Biol Med* (2017) **242** (3): 258–266. doi:10.1177/1535370216675066

48. Rattan SIS, Fernandes RA, Demirovic D, Dymek B, Lima CF. Heat stress and hormetin-induced hormesis in human cells: effects on aging, wound healing, angiogenesis, and differentiation. *Dose-Response* (2009) **7**(1):90–103. doi:10.2203/dose-response.08-014.Rattan

49. Li FXZ, Liu JJ, Lei LM, Li YH, Xu F, Lin X, et al. Mechanism of cold exposure delaying wound healing in mice. *J Nanobiotechnology* (2024) **22**(1):723. doi:10.1186/s12951-024-03009-y

50. Wright EH, Tyler M, Vojnovic B, Pleat J, Harris A, Furniss D. Human model of burn injury that quantifies the benefit of cooling as a first aid measure. *Br J Surg* (2019) **106**(11):1472–9. doi:10.1002/bjs.11263

51. Yang DR, Wang MY, Zhang CL, Wang Y. Endothelial dysfunction in vascular complications of diabetes: a comprehensive review of mechanisms and implications. *Front Endocrinol* (2024) **15**:1359255. doi:10.3389/fendo.2024.1359255

52. Shaterian A, Borboa A, Sawada R, Costantini T, Potenza B, Coimbra R, et al. Real-time analysis of the kinetics of angiogenesis and vascular permeability in an animal model of wound healing. *Burns* (2009) **35**(6):811–7. doi:10.1016/j.burns.2008.12.012

53. Aitcheson SM, Frentiu FD, Hurn SE, Edwards K, Murray RZ. Skin wound healing: normal macrophage function and macrophage dysfunction in diabetic wounds. *Molecules* (2021) **26**:4917. doi:10.3390/molecules26164917

54. Al SH. Macrophage phenotypes in normal and diabetic wound healing and therapeutic interventions. *Cells* (2022) **11** (15): 2430. doi:10.3390/cells11152430

55. Sasaki Y, Ohsawa K, Kanazawa H, Kohsaka S, Imai Y. Iba1 is an actin-cross-linking protein in macrophages/microglia. *Biochem Biophys Res Commun* (2001) **286**(2):292–7. doi:10.1006/bbrc.2001.5388

56. Keshav S, Chung P, Milon G, Gordon S. Lysozyme is an inducible marker of macrophage activation in murine tissues as demonstrated by *in situ* hybridization. *J Exp Med* (1991) **174**(5):1049–58. doi:10.1084/jem.174.5.1049

57. Zhao R, Liang H, Clarke E, Jackson C, Xue M. Inflammation in chronic wounds. *Int J Mol Sci* (2016) **17**: 2085. doi:10.3390/ijms17122085

58. Sharma S, Kishen A. Dysfunctional crosstalk between macrophages and fibroblasts under LPS-infected and hyperglycemic environment in diabetic wounds. *Sci Rep* (2025) **15**(1):17233. doi:10.1038/s41598-025-00673-4

EBM Experimental Biology and Medicine

TYPE Original Research
PUBLISHED 05 March 2026
DOI 10.3389/ebm.2026.10867

OPEN ACCESS

*CORRESPONDENCE
Mmei Cheryl Motshudi,
cheryl.motshudi@smu.ac.za

RECEIVED 19 October 2025
REVISED 10 January 2026
ACCEPTED 16 February 2026
PUBLISHED 05 March 2026

CITATION
Motshudi MC, Naidoo CM, Obi CL, Iweriebor BC, Prinsloo E, Zubair MS and Mkolo NM (2026) Metabolomics-guided identification of bioactive phytometabolites from South African plants targeting neuroblastoma. *Exp. Biol. Med.* 251:10867. doi: 10.3389/ebm.2026.10867

Metabolomics-guided identification of bioactive phytometabolites from South African plants targeting neuroblastoma

Mmei Cheryl Motshudi[1]*, Clarissa Marcelle Naidoo[1], Chikwelu Lawrence Obi[1], Benson Chucks Iweriebor[1], Earl Prinsloo[2], Muhammad Sulaiman Zubair[3] and Nqobile Monate Mkolo[1]

[1]Department of Biology, School of Science and Technology, Sefako Makgatho Health Science University, Pretoria, South Africa, [2]Department of Biotechnology, Rhodes University, Makhanda, South Africa, [3]Department of Pharmacy, University of Tadulako, Palu, Indonesia

Abstract

Neuroblastoma constitutes a solid tumor in pediatric populations, characterized by a dismal prognosis and a scarcity of effective therapeutic interventions. Medicinal flora from South Africa represents valuable sources of bioactive phytometabolites with potential relevance to neuroblastoma. This study employed an integrated workflow merging untargeted UPLC-MS/MS metabolomics, mitochondrial functional assays, and *in silico* absorption, distribution, metabolism, and excretion (ADME) prediction to systematically identify bioactive metabolites from *Acorus calamus* and *Lippia javanica* with activity against SH-SY5Y neuroblastoma cells. Cytotoxic effects were quantified utilizing the CCK-8 assay, while mitochondrial membrane potential ($\Delta\Psi m$) was conducted through JC-1 flow cytometry. Untargeted UPLC-MS/MS profiling yielded metabolomic fingerprints, through PCA, PLS-DA, and OPLS-DA. ADME and drug-likeness were predicted using SWISSADME. Both plant extracts exhibited dose-dependent inhibition of SH-SY5Y cell viability, with IC_{50} values determined at 0.2886 µg/µL for *A. calamus* and 0.3066 µg/µL for *L. javanica*. The $\Delta\Psi m$ assessment indicated enhanced mitochondrial polarization (68.2% and 65.4% compared to 58.8% in untreated controls), implying modulation of mitochondrial functional status. Metabolomic profiling unveiled distinct phytochemical signatures, including flavonoids, phenolics, jasmonates, and alkaloids, exhibiting significant species-level differentiation (F = 936.71, R^2 = 0.989, p = 0.005). Notable metabolites such as isopropyl β-glucoside, 6β-hydroxymethandienone, and 7-epi-12-hydroxyjasmonic acid demonstrated favorable ADME characteristics and permeability across the blood-brain barrier. This investigation elucidates that *A. calamus* and *L. javanica* possess

potential efficacy against neuroblastoma, underscoring the translational potential of African medicinal flora in pediatric oncology and necessitating further preclinical exploration.

KEYWORDS

Acorus calamus, ADME, *Lippia javanica*, metabolomics, mitochondrial membrane potential

Impact statement

This manuscript serves to investigate the medicinal flora for natural bioactive compounds as probable sources of therapeutic anticancer agents targeting SH-SY5Y neuroblastoma cells. Utilizing a multifaceted methodology that incorporates cytotoxicity assays, untargeted metabolomics, and in silico Absorption, Distribution, Metabolism, and Excretion modeling, we have identified phytometabolites exhibiting promising anticancer efficacy and have also predicted their permeability across the blood–brain barrier. The findings will offer different perspectives and insights into the metabolomic profiling and therapeutic potential of the medicinal plants, thereby enhancing the pharmacological comprehension of phytochemical agents in pediatric oncology.

This manuscript also highlights the current strategic plans for neuroblastoma treatment and approaches that could be applied in the future to improve the quality of life of patients with neuroblastoma, as well as to provide early diagnostic measures to reduce mortality rates of this fatal cancer. This information could be of great use for both clinical and scientific research.

Introduction

Neuroblastoma (NB) is a primary cancer detected in infants; it is a predominant solid tumor commonly found in the extracranial area in children [1]. Neuroblastoma accounts for approximately 10–15% of childhood malignancies, and the primary tumour generally stems from the sympathetic chain, usually in the abdomen or in the adrenal gland [2]. Patients with neuroblastoma tend to exhibit a wide range of biological, clinical, accompanied by prognostic heterogeneity, and a fundamental prognostic trait pertaining to neuroblastoma patients is the location of the primary tumour, which can originate in the adrenal gland, abdominal/retroperitoneal area, neck, thorax, pelvis, or, less frequently, in other sites [3, 4]. Due to the heterogeneous biological nature of neuroblastoma, its prognosis, along with clinical course, differs between spontaneous regression to high-risk cases, with several neuroblastoma tumours exhibit poorly responsive to intensive multimodal therapy [5, 6]. Presently treatment strategies involve aggressive amalgamation of radiotherapy, induction chemotherapy, elevated-dose chemotherapy with autologous stem-cell rescue, surgical removal of tumors, and applications of post-consolidation methods such as immunotherapy, as well as differentiation therapy [7]. The 5-year overall survival rate for high-risk neuroblastoma individuals continues to hover around 50–60% despite these integrated multimodal approaches, and late effects are usually imminent and frequently experienced by long-term survivors [8]. Regardless of advancement in multimodal therapy, outcomes for high-risk neuroblastoma persist to be suboptimal, highlighting the necessity for alternative and complementary therapeutic strategies.

The SH-SY5Y human neuroblastoma cell line comprises an N-type catecholaminergic subclone of neuroblastoma commonly used in research areas pertaining to neuroblastoma and neurobiology [9]. SH-SY5Y cell lines convey crucial elements of human catecholaminergic systems, which encompass components such as dopamine-β-hydroxylase and tyrosine hydroxylase [10]. Induced SHSY5Y cells can be differentiated into phenotypes that resemble neurons, therefore rendering them an adaptable *in vitro* model [11]. However, limitations such as inadequate maturation levels of neurons and restricted functionality of network systems, irrespective of the differentiation, emphasize the necessity of cautious interpretation of pharmacological responses [12]. Changes in mitochondrial membrane potential ($\Delta\Psi m$) and cellular redox balance can play context-dependent roles in cancer biology, acting as regulators of cell survival and cell death conditional on cellular state and therapeutic pressure [13]. Although moderate stabilization of mitochondrial function and redox homeostasis might permit tumour cell adaptation, excessive or dysregulated perturbation of these pathways can encourage cytotoxic or cytostatic outcomes via mitochondrial dysfunction [14, 15]. Accordingly, modulation of $\Delta\Psi m$ and redox-related processes has been explored as a functional vulnerability in cancer cells, also neuroblastoma, instead as a unidirectional pro-survival mechanism [16, 17].

Approximately 65% of the world's population, along with an estimated 80% of the population in Africa as well as Asia, depends on traditional herbal remedies to cure and furthermore prevent infectious ailments and chronic diseases [18, 19]. Ethnobotanical knowledge from southern Africa has showcased many species of aromatic origin known for their anticancer, anti-inflammatory, and anti-infective properties [20]. South African based medicinal plants are rich sources of structurally diverse phytometabolites with documented biological activities, and systematic investigation of these resources might permit the discovery of candidate anti-cancer

chemotypes or complementary approaches to present therapies [21–25]. *Lippia javanica* (Burm.f.) is a multi-branched woody shrub, that is commonly known as fever tea [9, 26]. *L. javanica* (Verbenaceae family) is an aromatic medicinal plant indigenous to eastern and southern Africa that has been broadly explored for its phytochemical composition and biological activities [26–30]. Previous studies have recognized phenolic, terpenoids, and flavonoids constituents, with apigenin- and luteolin-associated derivatives, which *in vitro* exhibit antioxidant and cytotoxic activities, supporting its importance for further assessment within a metabolomics-directed anticancer framework [31–36]. *Acorus calamus* Linn., (Aceraceae family), is classified as a perennial, semi-aquatic herb, that is commonly known as sweet flag {25]. *A. calamus* is an aromatic medicinal plant that has been extensively studied for its phytochemical diversity and biological activities, and it is frequently utilized in traditional Chinese and Indian medicine [37–41]. Notably, this plant comprises phenylpropanoid constituents for instance α- and β-asarone, for which extracts and isolated compounds have established anticancer activity in preclinical cancer models, also permitting its inclusion in metabolomics-directed anticancer investigations [42, 43]. Untargeted LC-MS metabolomics is commonly utilized to map systematic methods for enhancing quality control, distinguishing chemotypes, associating chemical properties with bioactivity of samples, and prioritizing key metabolites for further pharmacology analysis, alongside *in silico* ADME assessment through tools like SwissADME and the BOILED-Egg model [44–47].

Building on the above insight, while the phytochemistry and bioactivity of *L. javanica* and *A. calamus* have been previously reported in various biological contexts, their assessment within an integrated framework relating metabolomic composition to mitochondrial functional outcomes and pharmacokinetic possibility remains limited. In this study, we integrated untargeted UPLC-MS/MS metabolomics, mitochondrial membrane potential evaluation in SH-SY5Y neuroblastoma cells, and *in silico* ADME analysis to select metabolites with possible neuroblastoma importance.

Materials and methods

Plant collection and identification

Specimens of *L. javanica* and *A. calamus* were collected from Hartbeespoort in the North-West Province of South Africa (25.7236° S, 27.9653° E) in February 2023. Organ-matched sampling was applied to follow metabolomics reporting recommendations that highlight control of tissue-specific variability in comparative chemical analyses [48]. Species identification of both plants was authenticated by taxonomists at the National Herbarium, where voucher specimens were deposited under accession numbers NR 904 (*L. javanica*) and NR 905 (*A. calamus*). Plant material collection was completed in accordance with national regulatory requirements, under permit CF6-0234 released by the Department of Agriculture and Rural Development-Nature Conservation, South Africa (Permit Holder: Prof. Nqobile Monate Mkolo).

Anti-cancer assay analysis

Sample preparation

The *L. javanica* and *A. calamus* samples were pulverized into a powder using a mortar and pestle under liquid nitrogen. A precise weight of 0.5 g from each powdered sample was combined into a single 50 mL centrifuge tube. A total of 10 mL of buffer was added to the tube followed by extraction at a 4 °C. The extractant was filtered through a 0.45 μm filter, and the clearer supernatants were transferred into a new centrifuge tube. Crude extracts and intermediate preparations were stored at −20 °C in amber, light-protected containers to reduce degradation. Extracts were permitted to equilibrate to room temperature and were used within 1 week of preparation to allow stability and duplicability.

SH-SY5Y cell preparation

Human neuroblastoma SH-SY5Y cells (Cellonex ™, Johannesburg South Africa) were cultured in Dulbecco's Modified Eagle's Medium (DMEM) supplemented with 10% (v/v) heat-inactivated fetal bovine serum, 1% penicillin-streptomycin obtained from Gibco (New York, NY, United States), and maintained at 37 °C in a humidified incubator with 5% CO_2 [49]. Cells were washed by utilizing a 1 mL pipette to aspirate and discard the old medium. Gradually, 2 mL of Phosphate Buffered Saline (PBS) from Sigma-Aldrich (St. Louis, MO, United States), was poured along the edge of the T25 flask, and this flask was gently swirled to wash away any remaining medium. Cell digestion was conducted by gradually adding 1 mL of 0.25% trypsin digest solution (Sigma-Aldrich, St. Louis, MO, United States) into the T25 flask, ensuring it covered all the cells. The flask was then placed in a 37 °C CO_2 incubator for 2 min. Cells were examined, using an inverted microscope, for separation and formation of a spherical shape. To stop digestion, 4 mL of cell growth medium was added to the cells. Passage was done at a ratio of 1:4, where the cells were carefully pipetted for dispensation, and a single-cell suspension was confirmed under the microscope.

CCK-8 assay

The effect of chosen plant tissue (final concentration of 0.01–10 μg/mL) on SH-SY5Y cell viability was assessed using the CCK-8 assay according to the protocol [50]. SH-SY5Y cells were collected from an approximately 80% confluent T-25 flask using the standard trypsinization method. Afterward, 2×10^4

cells were seeded in a 96-well plate and incubated for 24 h at 37 °C. Then, the media was removed, rinsed with PBS, and the cells were treated with 100 μL of clear supernatants from the sample, while the cell medium served as the negative control. Following 24 h, 10 μL of CCK-8 was added to every well and allowed to incubate for 2 h. A microplate reader (Infinite M200, Tecan, Switzerland) scanned the 96-well plate at a wavelength of 450 nm. All CCK-8 experiments were performed utilizing three independent biological replicates, with each condition examined in technical triplicate. The subsequent formula was applied to determine the percentage of cell viability:

$$\text{Survival rate (\%)} = (\text{Asample} - \text{Ab}/\text{Ac} - \text{Ab}) \times 100$$

Wherein Asample, Ab, and Ac are the absorbance/Optical density of cells exposed to test reagents, absorbance/Optical density of blank, and negative control, respectively.

Mitochondrial membrane potential detection

The mitochondrial membrane potential (ΔΨm) of SHSY-5Y cells against *L. javanica* and *A. calamus* was determined by adopting a procedure of Sakamuru and co-workers [51]. SH-SY5Y cells were seeded in a 96-well plate (2×10^4 cells per well) according to experimental groups, which included the blank control group (non-treated SH-SYSY cell line), negative control of non-treated SH-SYSY cell line for gating, and the treated SH-SYSY cell line group (*L. javanica* and *A. calamus* at 1 μg/uL). After 24 h of treatment, the cells were collected using trypsin for adherent cells to avoid over-digestion and to prevent membrane potential damage. A JC-1 working solution was prepared using a diluted JC-1 stock solution with pre-warmed (37 °C) medium, which was added to the final concentration. The JC-1 working solution was then added to the cells and incubated at 37 °C in the dark for 15 min. JC-1 solution was removed, and cells were washed 3 times with pre-cooled PBS to remove unbound dye. The cells were collected using trypsin, then centrifuged and resuspended into PBS. The set flow cytometry channels were green fluorescence, which was the FL1 channel (Ex 488 nm, Em 530/30 nm), and red fluorescence, which was the FL2 channel (Ex 488 nm, Em 585/42 nm). The red fluorescence (normal mitochondria) and green fluorescence (decreased membrane potential) were then merged for analysis. Mitochondrial membrane potential (ΔΨm) assessments were conducted utilizing three independent biological replicates, with technical triplicates for each experimental condition.

Metabolomic characterization

Chemicals and instrumentation

Multiple chemicals and reagents, such as acetonitrile (Merck, Rahway, NJ, United States), methanol (Merck, Rahway, NJ, United States), DL-o-Chlorophenylalanine (Merck, Rahway, NJ, United States), and formic acid (Merck, Rahway, NJ, United States) were utilized. Additionally, instrumentation, namely ACQUITY UPLC HSS T3 (100 × 2.1 mm × 1.8 μm), Ultimate 3000LC combined with Q Exactive MS (Thermo, Waltham, MA, United States), and Temp functional Centrifugation (Eppendorf, Enfield, CT, United States) were utilized.

Sample preparation

The initial stages of the sample preparation comprised a freeze-drying process (lyophilization) of *A. calamus* and *L. javanica* leaf samples. The respective samples were subsequently dried and ground into powder; the resultant powder for each sample was transferred into a 5 mL homogenizing tube. A MM 400 mixer with four 5 mm diameter metal balls was utilized to mix the samples at 30 Hz. The subsequent product for each sample was added with 80% methanol at a volume of 800 μL. The resultant solution was vortexed for 30 s and sonicated thereafter for 30 min at 4 °C. Samples were stored at a temperature of −20 °C for an hour. Each sample was centrifuged thereafter at 12,000 rpm, 4 °C for 5 min. A total of 200 μL of each supernatant from the respective samples, along with 5 μL of DL-o-Chlorophenylalanine (140 μg/mL), were added to vials. The vials were then used for liquid chromatography–mass spectroscopy (LC-MS) analysis.

Untargeted plant metabolomics analysis using UPLC-MS/MS

Separation of compounds was carried out using the Ultimate 3000LC (Thermo, Waltham, MA, United States) combined with QExactive MS (Thermo) and additionally, screened with ESI-MS [27]. The first solvent of the mobile phase comprised 0.05% formic acid in water and the second solvent was acetonitrile with a subsequent gradient elution (0–1 min, 95% A; 1–12 min, 95%–5% A; 12–13.5 min, 5% A; 13.5–13.6 min, 5–95% A; 13.6–16 min, 95% A). The mobile phase had a flow rate of 0.3 mL·min^{-1}. The column temperature was kept at 40 °C, while the sample manager temperature was adjusted to 4 °C. The mass spectrometry settings for electrospray ionization ESI+ mode are detailed as follows: heater temperature 300 °C; sheath gas flow rate, 45 arb; auxiliary gas flow rate, 15 arb; sweep gas flow rate, 1 arb; spray voltage, 3.0 kV; capillary temperature, 350 °C; S-Lens RF level, 30%.

Quality control samples

Extracts of the respective plants were mixed as quality control samples (QC) to evaluate the methodology and stability of the LC-MS system. Raw data for the UPLC–MS/MS were obtained from Compound Discover (3.0, Thermo) based on the m/z value and the retention time of the ion signals. To ensure consistency and efficacy of the system, multiple QC samples were formulated through a combination of identical quantities of each isolated sample. The instrument's performance and repeatability were evaluated through pooled QC samples that were injected before the sample analysis until equilibrium was reached. The QC

samples were subsequently run in positive mode. The ion characteristics of the QC samples were utilized to determine the Relative Standard Deviation (RSD). Supplementary Figure S1 of the Supplementary Material displays the percentage of RSD distribution, with a significant portion of the RSD being below 30%. This indicates that the analytical method is reliable and appropriate for application to future sample analyses.

Identification of metabolites

Metabolite identification was performed at a putative level (MSI level 2) utilizing accurate mass measurements and MS/MS fragmentation data. Candidate metabolites were annotated by matching experimental spectra against the Human Metabolome Database[1], ChemSpider[2] and MassBank[3], all accessed 19 August 2024. Then manual evaluation of retention time consistency, isotope patterns, and MS/MS fragmentation spectra was done. Cross-validation across databases was achieved to enhance annotation confidence. Features detected in the ESI^+ mode were cross-checked for chromatographic and spectral consistency and combined where appropriate. Redundant ions and adducts were resolved utilizing mass accuracy criteria (<5 ppm), retention-time coherence, signal intensity, and % RSD across technical replicates to reduce duplication or erroneous assignments.

Pharmacokinetic and drug-likeness activity of differential metabolites

The properties of the ADME of significant metabolites were extrapolated through *in silico* methods, and their potential, along with their suitability as drug candidates, was evaluated. The SWISSADME platform[4] (accessed on 12 July 2025) was utilized for primary screening, which facilitated the high ranking of compounds that exhibited drug-like profiles and advantageous pharmacokinetic properties. Subsequently, further assessments were carried out with the assistance of recognized cheminformatics inclined tools for a more thorough evaluation of the pharmaceutical relevance of the metabolites. The parameters examined comprised physicochemical descriptors, which included molecular weight, number of heavy aromatic atoms, topological polar surface area (TPSA), molecular refractivity, number of hydrogen bonds, lipophilicity factors (logP), water solubility (logS), along other parameters were examined. Pharmacokinetic traits such as blood–brain barrier (BBB) permeation, gastrointestinal (GI) absorption, substrate specificity for P-glycoprotein (P-gp), inhibition potential essential key cytochrome P450 (CYP) isoenzymes (CYP1A2, CYP2C19, CYP2C9, CYP2D6, and CYP3A4), as well as skin permeation (logKp) were evaluated, and these aspects conjointly affect the metabolism of the potential and the likelihood of drug-to-drug interactions. Ultimately, the final analysis for drug-likeness was conducted using Lipinski, Ghose, Veber, Egan, Muegge, and bioavailability scores. These assessments provide a comprehensive view of the compounds' appropriateness for further progression.

Statistical analysis

In terms of anti-cancer analysis, GraphPad Prism version 8.2.0 (GraphPad Software, Inc., San Diego, CA, United States) was utilized to plot the dose-response curve and determine the IC_{50} of plant treatments.

While for metabolomics analysis, the raw data was collected and aligned utilizing Compound Discover (3.0, Thermo) according to the m/z values and the retention time of the ion signals. Ions from both ESI+ were combined and subsequently transferred into the SIMCA-P software (version 14.1) and Metaboanalyst version 6.0[5] (accessed on 12 August 2025) for multivariate analysis. Unsupervised principal component analysis (PCA) was achieved to evaluate intrinsic clusters and the structure of variance. Supervised partial least squares-discriminant analysis (PLS-DA) and orthogonal PLS-DA (OPLS-DA) were also achieved for maximizing class segregation and assessing statistically significant metabolites. Cross-validation of these models was completed, and the variance percentages clarified through orthogonal and predictive components were verified.

Statistically significant metabolites were verified and filtered by integrating the outcomes of the Variable Importance in Projection (VIP) score greater than 1.5, a p-value less than 0.05, FDR-adjusted $p < 0.05$ and a fold change (FC) greater than 2.0. The R^2 and Q^2 values can explain the quality of the fitted model. R^2 shows the variance accounted for in the model and reflects the goodness of the fit. Q^2 shows the variability in the data, reflecting the model's predictability.

Results

Anti-cancer activities

The anti-cancer activities of *A. calamus* and *L. javanica* extracts on SH-SY5Y neuroblastoma cells were assessed

1 www.hmdb.ca

2 www.chemspider.com

3 www.massbank.jp

4 http://www.swissadme.ch/index.php

5 https://www.metaboanalyst.ca

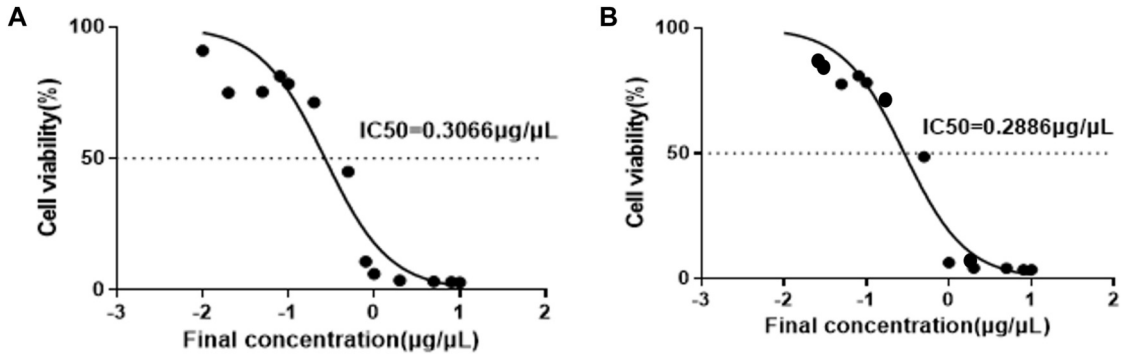

FIGURE 1
Dose-response curves for **(A)** *A. calamus* and **(B)** *L. javanica* extracts on SH-SY5Y neuroblastoma cells utilizing the CCK-8 assay.

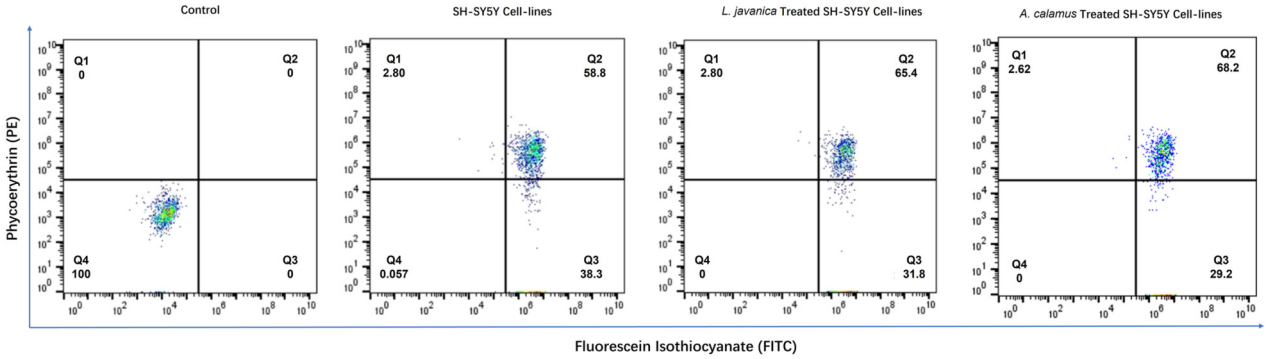

FIGURE 2
Mitochondrial membrane potential (ΔΨm) analysis of SH-SY5Y neuroblastoma cells using the JC-1 fluorescent probe and flow cytometry.

utilizing the CCK-8 assay. These plant extracts displayed a clear dose-dependent decrease in cell viability, as demonstrated by the sigmoidal dose-response curves (Figure 1). The estimated half maximal inhibitory concentration (IC_{50}) values were 0.2886 µg/µL for *A. calamus* and 0.3066 µg/µL for *L. javanica*, with 0.2976 µg/µL as an overall IC_{50} mean. However, *A. calamus* displayed slightly higher effectiveness in comparison to *L. javanica*.

Mitochondrial membrane potential analysis

Mitochondrial function in SH-SY5Y neuroblastoma cells was evaluated using flow cytometry and the JC-1 fluorescent probe to quantify variations in membrane potential (ΔΨm). As illustrated in Figure 2, in terms of untreated SH-SY5Y control cells, 58.8% of the population was within the Q2 gate, signifying cells with high ΔΨm (red fluorescence), although 38.3% of the population was situated in the Q3 gate, conforming to mitochondrial depolarization (green fluorescence). Following plant extract treatment, the proportion of the cells with high ΔΨm increased to 68.2% for *A. calamus* and 65.4% for *L. javanica*, implying increased mitochondrial polarization comparative to untreated controls.

UPLC-MS/MS base peak intensity chromatograms

The UPLC-MS/MS analysis of *A. calamus* and *L. javanica* completed in ESI+ mode produced (BPI) chromatograms, a wide profile of metabolites eluting over a specified retention time frame, as shown in Figure 3.

The chromatogram of *A. calamus* with the dominating of a particularly intense peak at ~400 s, with a highest intensity of ~1.2×10^{10}. Subsequent moderate peaks were detected at ~700, ~550, ~200, and ~50 s. Conversely, *L. javanica* offered an evenly

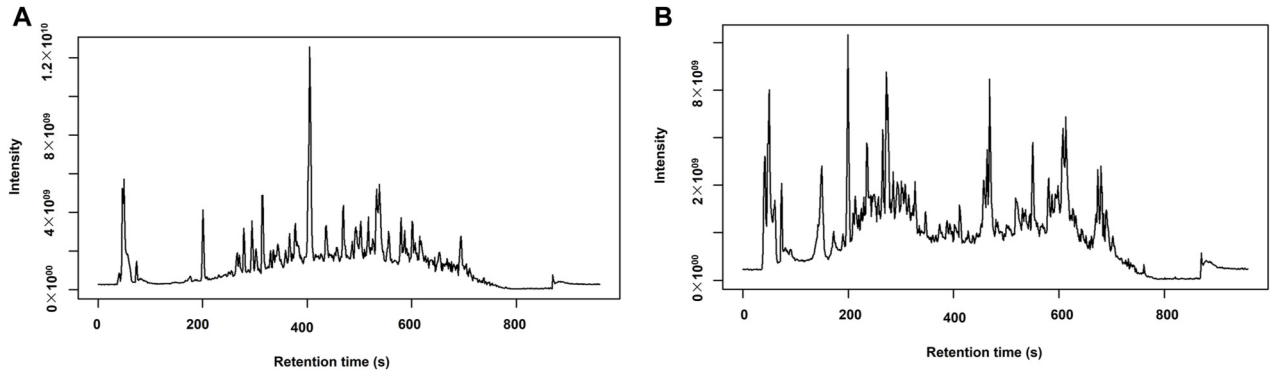

FIGURE 3
Base peak intensity (BPI) chromatograms from **(A)** *A. calamus* and **(B)** *L. javanica* in ESI+ mode.

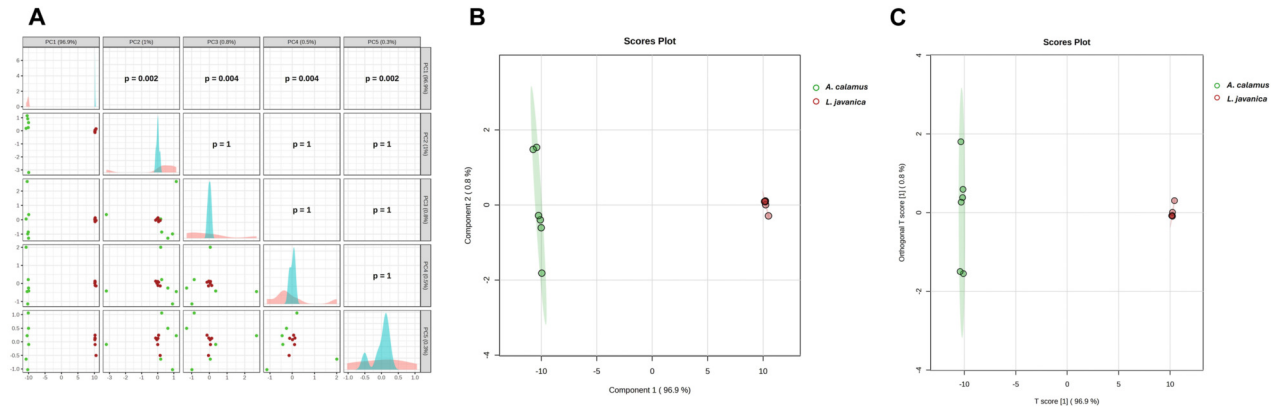

FIGURE 4
Multivariate analysis: **(A)** Principal Component Analysis (PCA) pairwise scatterplots, **(B)** Partial Least Squares Discriminant Analysis (PLS-DA) scores plot, and **(C)** Orthogonal Partial Least Squares Discriminant Analysis (OPLS-DA) scores plot of *A. calamus* (green) and *L. javanica* (red).

dispersed chromatographic profile with multiple peaks of medium to high intensity detected between 100s and 600s. The most intense peak occurred at ~220 s (~4.0 × 10^9). Additional prominent peaks were detected at ~720, ~600, ~400, and ~100 s.

Multivariate analysis of *A. calamus* and *L. javanica* data

Principal Component Analysis (PCA) score model of the associated features displays complete species segregation across PC1, with a variance of 96.9% (PC2 = 1.0%). The PCA pair-plot validates that cluster variances are concentrated on the first component and also noticeable, but smaller on higher components. The dispersals of scores vary significantly for PC2: p = 0.002, PC3: p = 0.004, PC4: p = 0.004, and PC5: p = 0.002 (Figure 4A). These results signify the possession of distinct global metabolomic fingerprints of the two species, dominated by variance expressed on PC1. The observed clustering patterns were statistically significantly validated using the PERMANOVA test, consisting of an F-value of 936.71, a p-value = 0.005, and R^2 = 0.98944.

Moreover, supervised Partial Least Squares-Discriminant Analysis (PLS-DA) generated the same qualitative pattern of PCA score model with distinct separated clusters driven by component 1 (96.9%), though component 2 represented insignificant variance of 0.8% (Figure 4B). Cross-validation metrics also validate with R^2 and Q^2 values that were close to 1.0 for all 5 tested components, which displayed consistently high performance. Moreover, the permutation test additionally validated the PLS-DA model, with a noticeable statistic positioned (p < 0.01, 0/100) that was distant outside the permutation distribution (Supplementary Figure S2).

TABLE 1 Differential metabolites distinguished from *A. calamus* and *L. javanica* in electrospray ionization ESI+ mode.

Compound name	RT (min)	Molecular Weight	*m/z*	HMDB_ID	Formula	Log^2(FC)	T-Test	FDR Log10 (p-adj)	VIP
ALKALOIDS									
5-Isothiocyanatoindane	3,015	115,17	157,1334	CSID642931	$C_6H_{13}NO$	-6,7198	4,54E-05	4,342703	1,830521
3-Indolehydracrylic acid	3,336	205,0736	206,0809	HMDB0059765	$C_{11}H_{11}NO_3$	5,338881	2,95E-05	4,52994	1,634694
Hydrocotarnine	4,956	221,1048	222,1121	HMDB0033701	$C_{12}H_{15}NO_3$	5,347002	4,08E-08	7,38938	1,6638
Mescaline	2,991	211,26	229,1543	HMDB0254474	$C_{11}H_{17}NO_3$	5,105346	4,88E-05	4,311856	1,602307
Perlolyrine	4,972	264,0895	265,0967	HMDB0030327	$C_{16}H_{12}N_2O_2$	-5,99531	0,001842	2,73468	1,680894
Prodolic acid	5,075	273,33	296,1276	HMDB0256794	$C_{16}H_{19}NO_3$	-6,27265	0,001789	2,747286	1,732869
CARBOHYDRATES									
Isopropyl β-glucoside	3,5	222,24	245,1016	HMDB0032705	$C_9H_{18}O_6$	10,83254	3,52E-05	4,453856	2,331036
Muramic acid	3,206	251,1014	252,1087	HMDB0003254	$C_9H_{17}NO_7$	8,105161	9,48E-05	4,023081	2,006866
1-O-Caffeoyl-beta-glucose	5,172	342,0944	343,1016	HMDB0302440	$C_{15}H_{18}O_9$	7,814332	1,86E-06	5,730844	1,977503
Cellulose, microcrystalline	2,156	370,35	393,136	HMDB0032197	$C_{14}H_{26}O_{11}$	6,787933	8,9E-06	5,050728	1,842234
O-Desmethyltramadol glucuronide	3,259	425,50	448,1957	HMDB0060856	$C_{21}H_{31}NO_8$	-6,19442	2,12E-05	4,673131	1,758105
Persicogenin 3'-glucoside	4,747	456,1638	479,1532	HMDB0041398	$C_{23}H_{26}O_{11}$	8,080171	1,16E-06	5,934704	2,012623
Hetastarch	4,045	736,70	759,2936	HMDB0253113	$C_{29}H_{52}O_{21}$	8,836521	2,09E-05	4,679721	2,134599
LIPIDS									
4-Methyl-2-pentenoic acid	4,046	114,14	156,1018	HMDB0031561	$C_6H_{10}O_2$	6,668955	6,85E-05	4,164162	1,833963
Undecylenic acid	4,113	184,27	226,1798	HMDB0033724	$C_{11}H_{20}O_2$	7,923542	8,84E-08	7,053706	2,029285
12-Hydroxydodecanoic acid	7,277	216,32	239,1638	HMDB0002059	$C_{12}H_{24}O_3$	-5,60027	1,14E-05	4,941239	1,679658
11-Dodecenoic acid	4,664	198,30	262,1797	HMDB0032248	$C_{12}H_{22}O_2$	6,21621	1,46E-06	5,834954	1,771416
9-Pentadecenoic acid	10,834	240,38	263,2002	HMDB0029765	$C_{15}H_{28}O_2$	-5,45158	0,000253	3,59735	1,674411
Stearidonic acid	9,676	276,40	299,1999	HMDB0006547	$C_{18}H_{28}O_2$	4,57766	1,96E-07	6,707939	1,521083
MG(18:3/0:0/0:0)	8,725	352,2605	353,2678	HMDB0011570	$C_{21}H_{36}O_4$	5,971525	2,8E-07	6,553359	1,761732
Prostaglandin A2	7,707	334,40	357,2028	HMDB0002752	$C_{20}H_{30}O_4$	7,579842	0,000121	3,916245	1,940373
Eicosanedioic acid	10,522	342,50	365,2678	HMDB0242141	$C_{20}H_{38}O_4$	6,161779	5,82E-06	5,23503	1,764398
Thromboxane B3	4,446	368,50	386,2529	HMDB0005099	$C_{20}H_{32}O_6$	-6,81951	0,000823	3,084822	1,814574
MG(5-iso PGF2VI/0:0/0:0)	6,209	400,50	423,2344	HMDB0260485	$C_{21}H_{36}O_7$	6,891431	1,09E-05	4,962081	1,86861
LysoPA(18:2/0:0)	4,868	434,50	457,2398	HMDB0007856	$C_{21}H_{39}O_7P$	6,062893	1,42E-06	5,847397	1,754746

(*Continued*)

10.3389/ebm.2026.10867

TABLE 1 Continued

Compound name	RT (min)	Molecular Weight	*m/z*	HMDB_ID	Formula	Log^2(FC)	T-Test	FDR Log10 (p-adj)	VIP
DG(20:4-2OH/0:0/2:0)	8,79	452,60	475,2682	HMDB0297002	$C_{25}H_{40}O_7$	-8,77228	1,31E-05	4,882486	2,094746
DG(2:0/PGD2/0:0)	7,165	468,60	491,2629	HMDB0296907	$C_{25}H_{40}O_8$	-5,07408	0,000151	3,820683	1,583894
DG(6 keto-PGF1alpha/2:0/0:0)	4,095	486,60	528,3155	HMDB0296912	$C_{25}H_{42}O_9$	5,338498	0,000864	3,063593	1,605199
LysoPE(22:2/0:0)	10,093	533,3475	534,3547	HMDB0011522	$C_{27}H_{52}NO_7P$	-6,18444	0,00202	2,694655	1,568301
NITROGEN COMPOUND									
1,3-Hexadien-3-amine	1,032	97,0895	98,09678	CSID67029750	$C_6H_{11}N$	6,805566	9,38E-06	5,027828	1,856891
2-Aminocyclohexanecarboxylic acid	1,229	143,0945	144,1017	CSID133327	$C_7H_{13}NO_2$	5,478209	4,02E-06	5,395528	1,656544
7-Aminomethyl-7-carbaguanine	1,725	179,0804	180,0877	HMDB0011690	$C_7H_9N_5O$	7,746392	4,59E-06	5,33773	2,019233
5-Fluoromethylornithine	4,624	164,18	187,0863	HMDB0245493	$C_6H_{13}FN_2O_2$	5,535211	8,43E-08	7,073976	1,674376
Succinyl proline	3,047	215,20	238,0682	CSID168469	$C_9H_{13}NO_5$	7,81002	9,47E-08	7,02377	1,978274
erythro-4-Hydroxyarginine	3,109	190,20	229,0704	HMDB0034326	$C_6H_{14}N_4O_3$	6,393116	3,43E-07	6,464989	1,81208
Pantothenic acid	9,416	219,23	237,1402	HMDB0000210	$C_9H_{17}NO_5$	-6,60822	0,000512	3,290701	1,785286
Phenylalanyl-Glycine	4,839	222,24	245,0917	HMDB0304788	$C_{11}H_{14}N_2O_3$	4,586087	6,19E-06	5,208442	1,522839
Glutaminylleucine	3,04	259,30	277,1906	HMDB0028801	$C_{11}H_{21}N_3O_4$	7,790423	1,82E-05	4,74028	1,971685
Glycyl-Tryptophan	3,196	261,279	279,1448	HMDB0028852	$C_{13}H_{15}N_3O_3$	-6,59597	0,001815	2,741203	1,589188
N-Acetyllactosamine	2,923	383,35	406,1337	HMDB0001542	$C_{14}H_{25}NO_{11}$	6,16663	0,000286	3,544322	1,745963
NUCLEOSIDE / NUCLEOTIDE									
2-Deoxy-ribono-1,4-lactone	5,407	132,0422	133,0495	HMDB0033958	$C_5H_8O_4$	4,608802	2,27E-05	4,644565	1,515139
2',3'-Didehydro-2',3'-dideoxycytidine	4,434	209,0811	210,0884	HMDB0245545	$C_9H_{11}N_3O_3$	-8,76604	1,28E-05	4,892618	2,092533
Keto-3-deoxy-manno-octulosonic acid	3,079	238,19	261,0601	HMDB0244292	$C_8H_{14}O_8$	6,750766	4,57E-06	5,340459	1,856524
5-(Hydroxymethyl)cytidine	2,821	273,0955	274,1027	CSID32720391	$C_{10}H_{15}N_3O_6$	4,788076	2,22E-06	5,653688	1,616127
2',3'-Dideoxyadenosine	6,718	235,24	277,1405	HMDB0245544	$C_{10}H_{13}N_5O_2$	-6,84114	4,18E-05	4,379233	1,84559
5-Methyldeoxycytidine	2,036	241,24	283,1396	HMDB0002224	$C_{10}H_{15}N_3O_4$	-8,43195	0,00119	2,924626	1,881698
3'-C-Ethynylcytidine	3,174	267,24	309,1174	HMDB0252093	$C_{11}H_{13}N_3O_5$	8,752045	3,19E-08	7,496043	2,107001
2'-Deoxy-5-formylcytidine	1,99	255,23	319,0993	CSID10291642	$C_{10}H_{13}N_3O_5$	5,632298	2,15E-06	5,666959	1,744307
Dimp	4,25	332,0524	333,0597	HMDB0006555	$C_{10}H_{13}N_4O_7P$	8,036495	2,38E-07	6,623169	2,006318
2-Methylguanosine	4,679	297,27	339,1407	HMDB0005862	$C_{11}H_{15}N_5O_5$	-5,73448	0,000162	3,789346	1,681938

(*Continued*)

10.3389/ebm.2026.10867

TABLE 1 Continued

Compound name	RT (min)	Molecular Weight	*m/z*	HMDB_ID	Formula	Log^2(FC)	T-Test	FDR Log10 (p-adj)	VIP
OTHER									
2,4-Pentadienal	10,135	82,04236	83,04964	HMDB0031597	C_5H_6O	7,510876	1,41E-06	5,850963	1,943115
5-Methylcytosine	6,097	125,0603	126,0676	HMDB0002894	$C_5H_7N_3O$	-8,4848	4,81E-06	5,317795	2,059602
xi-4-Hydroxy-4-methyl-2-cyclohexen-1-one	3,795	126,0681	127,0754	HMDB0033629	$C_7H_{10}O_2$	8,258472	6,02E-06	5,22045	2,034825
gamma-Butyrolactone	3,78	86,09	128,0706	HMDB0000549	$C_4H_6O_2$	7,403507	6,82E-06	5,166232	1,925084
Indol-2-one	3,251	131,0371	132,0444	HMDB0253466	C_8H_5NO	5,862663	3,16E-07	6,500593	1,718906
Methyl 2-thiofuroate	0,897	142,0115	143,0188	HMDB0037762	$C_6H_6O_2S$	4,48824	1,48E-05	4,829513	1,511626
Norcamphoric acid	3,195	158,15	200,0915	CSID207959	$C_7H_{10}O_4$	5,611922	7,34E-06	5,134455	1,720562
4-Guanidino-1-butanol	0,787	131,18	173,1396	CSID4476579	$C_5H_{13}N_3O$	-5,88882	0,001006	2,997208	1,515761
1-Oxo-1H-2-benzopyran-3-carboxaldehyde	4,626	174,0315	175,0388	HMDB0030577	$C_{10}H_6O_3$	6,426311	1,56E-05	4,807221	1,825317
3-Hydroxysuberic acid	2,866	190,19	232,1191	HMDB0000325	$C_8H_{14}O_5$	4,813224	4,4E-06	5,356159	1,568506
6-(2-Hydroxyethoxy)-6-oxohexanoic acid	3,717	190,19	213,0755	HMDB0061681	$C_8H_{14}O_5$	4,69247	4,65E-06	5,332964	1,552665
N-Lactoylphenylalanine	4,391	215,1177	238,1069	HMDB0062175	$C_{12}H_{15}NO_4$	5,606803	5,75E-07	6,240409	1,704328
2-(2-Furylmethyl)-1-indanol	3,905	214,26	237,0907	CSID40514807	$C_{14}H_{14}O_2$	-5,2121	0,000218	3,660803	1,591246
Piperdial	6,936	250,1565	251,1638	HMDB0035798	$C_{15}H_{22}O_3$	-5,12368	4,52E-06	5,345311	1,600008
1-(Ribofuranosyl)indoline	2,641	251,1153	252,1226	CSID67029342	$C_{13}H_{17}NO_4$	4,946661	1,05E-05	4,977423	1,570688
2-Hydroxyacorenone	9,271	236,35	259,1664	HMDB0030916	$C_{15}H_{24}O_2$	-7,68915	1,73E-06	5,761784	1,961428
Risbitin	5,609	222,32	264,1954	HMDB0302980	$C_{14}H_{22}O_2$	-5,92921	0,001049	2,979129	1,703258
Linamarin	1,312	247,24	270,0944	HMDB0033699	$C_{10}H_{17}NO_6$	-6,29487	0,000877	3,056864	1,759135
1-Hydroxyacorenone	7,673	250,33	273,1456	HMDB0030917	$C_{15}H_{22}O_3$	-7,10849	1,82E-06	5,739609	1,887368
4-Hydroxycyclohexylcarboxylic acid	4,619	144,17	289,1637	HMDB0001988	$C_7H_{12}O_3$	6,014314	5,86E-06	5,232144	1,73907
Pollenin A	4,254	302,042	303,0493	HMDB0303704	$C_{15}H_{10}O_7$	8,76912	2,16E-07	6,664657	2,126655
9,10-DiHODE	4,767	312,40	330,2632	HMDB0010221	$C_{18}H_{32}O_4$	-4,97006	0,000693	3,159427	1,553509
6β–Hydroxymethandienone	10,138	316,40	339,1922	HMDB0005832	$C_{20}H_{28}O_3$	10,73503	2,66E-06	5,575855	2,317918
Bisoprolol	5,313	325,40	348,2162	HMDB0014750	$C_{18}H_{31}NO_4$	5,110144	2,27E-05	4,643337	1,607036
6'-Hydroxyenterolactone	4,893	314,30	356,1482	HMDB0041697	$C_{18}H_{18}O_5$	6,599311	0,00027	3,568419	1,804397
Caryoptosidic acid	2,971	392,35	415,1204	HMDB0034249	$C_{16}H_{24}O_{11}$	6,037738	0,000224	3,649573	1,731817
Tyromycic acid	12,521	452,3278	453,3351	HMDB0035888	$C_{30}H_{44}O_3$	-5,71222	4,22E-05	4,374993	1,690313

(*Continued*)

10.3389/ebm.2026.10867

TABLE 1 Continued

Compound name	RT (min)	Molecular Weight	*m/z*	HMDB_ID	Formula	Log^2(FC)	T-Test	FDR Log10 (p-adj)	VIP
Fluocinolone	2,966	412,4	454,2062	HMDB0252347	$C_{21}H_{26}F_2O_6$	-5,03287	0,000493	3,307314	1,561579
Persiconin	4,285	478,1466	479,1539	HMDB0037482	$C_{23}H_{26}O_{11}$	8,487737	1,03E-06	5,987367	2,064423
Phaseolus epsilon	3,657	526,50	544,2378	HMDB0035039	$C_{25}H_{34}O_{12}$	7,87868	7,04E-05	4,152464	1,979816
19-Nor-5-androstenediol	9,685	276,40	553,4239	HMDB0004590	$C_{18}H_{28}O_2$	7,24471	8,58E-06	5,066603	1,926738
7-Dehydrologanin tetraacetate	3,488	556,1755	557,1828	CSID391585	$C_{25}H_{32}O_{14}$	-6,16628	0,003738	2,427367	1,709022
Procyanidin	3,823	578,1412	579,1484	HMDB0013690	$C_{30}H_{26}O_{12}$	-7,188	0,000208	3,681349	1,883821
Desglucocheirotoxol	13,088	552,70	591,2582	HMDB0033828	$C_{29}H_{44}O_{10}$	5,752651	2,39E-05	4,621974	1,696989
Neolicuroside	3,869	550,50	592,201	HMDB0040728	$C_{26}H_{30}O_{13}$	8,370981	5,7E-06	5,243925	2,048135
Marmesin rutinoside	2,724	554,50	596,2325	HMDB0041413	$C_{26}H_{34}O_{13}$	-6,94662	0,0022	2,657484	1,81168
Hesperidin methylchalcone	4,557	624,2032	625,2106	HMDB0253112	$C_{29}H_{36}O_{15}$	9,090381	1,04E-08	7,982463	2,139523
Glucoliquiritin apioside	3,01	712,60	730,2684	HMDB0041149	$C_{32}H_{40}O_{18}$	-6,08309	0,00112	2,950734	1,673043
Leonoside A	4,557	770,70	788,2936	HMDB0040342	$C_{35}H_{46}O_{19}$	9,611505	1,25E-05	4,904459	2,19735
PHENOLIC									
Coumarin	2,503	146,0365	147,0438	HMDB0001218	$C_9H_6O_2$	5,452435	0,000132	3,879057	1,64696
3 Hydroxycoumarin	4,771	162,0314	163,0387	HMDB0002149	$C_9H_6O_3$	4,910609	2,63E-07	6,580547	1,573768
4,8-Dimethyl-7-hydroxycoumarin	3,343	190,19	208,0965	CSID4512230	$C_{11}H_{10}O_3$	5,339346	1,67E-05	4,77794	1,635275
Vanillactic acid	1,727	212,0682	213,0755	HMDB0000913	$C_{10}H_{12}O_5$	7,713922	6,68E-07	6,175003	1,979313
Apigenin	5,177	270,0523	271,0596	HMDB0002124	$C_{15}H_{10}O_5$	5,845909	7,92E-05	4,101263	1,718134
Kaempferol	4,724	286,047	287,0542	HMDB0005801	$C_{15}H_{10}O_6$	7,038508	1,48E-06	5,830917	1,898751
3-Feruloyl-1,5-quinolactone	4,631	350,30	373,091	HMDB0029289	$C_{17}H_{18}O_8$	7,663669	2,15E-05	4,668116	1,956575
2-trans-O-Feruloylglucaric acid	3,606	386,0841	387,0913	HMDB0302546	$C_{16}H_{18}O_{11}$	9,917521	9,38E-06	5,027846	2,226979
Glucosyloxyanthraquinone	3,844	386,40	409,0911	CSID389045	$C_{20}H_{18}O_8$	-5,23257	0,000103	3,987626	1,611837
Eriodictin	4,559	434,1204	435,1277	HMDB0037480	$C_{21}H_{22}O_{10}$	8,417998	1,65E-10	9,781596	2,058779
Catechin 7-glucoside	3,177	452,131	453,1383	HMDB0037949	$C_{21}H_{24}O_{11}$	-5,3561	0,003285	2,483526	1,591291
Quercetin 3-O-glucuronide	4,241	478,0739	479,0812	HMDB0029212	$C_{21}H_{18}O_{13}$	9,420172	6,67E-08	7,175578	2,186479
Sesaminol glucoside	7,259	532,50	555,1482	HMDB0041209	$C_{26}H_{28}O_{12}$	4,976722	7,32E-05	4,135256	1,570614
Apigenin 7-O-diglucuronide	4,027	622,1149	623,1222	HMDB0301685	$C_{27}H_{26}O_{17}$	9,063099	3,86E-07	6,413527	2,131068
Tetramethylquercetin 3-rutinoside	4,052	666,60	708,2469	HMDB0039337	$C_{31}H_{38}O_{16}$	11,67918	1,57E-06	5,804899	2,418616

(*Continued*)

Published by Frontiers Society for Experimental Biology and Medicine

10.3389/ebm.2026.10867

TABLE 1 Continued

Compound name	RT (min)	Molecular Weight	*m/z*	HMDB_ID	Formula	Log^2(FC)	T-Test	FDR Log10 (p-adj)	VIP
POLYKETIDES									
1(2H)-Pentalenone	2,502	118,042	119,0493	CSID66739022	C_8H_6O	4,673748	0,000182	3,739442	1,516804
Phthalide	2,503	134,13	157,0282	HMDB0032469	$C_8H_6O_2$	8,291181	0,000232	3,634062	2,029866
Aflatoxin G2	6,708	330,0731	331,0804	HMDB0030475	$C_{17}H_{14}O_7$	7,294113	0,000298	3,526371	1,900981
TERPENOIDS									
Shinanolone	4,667	192,075	193,0823	HMDB0030580	$C_{11}H_{12}O_3$	-5,65953	0,005135	2,289432	1,589457
4,7-Megastigmadien-9-ol	8,59	194,1668	195,1741	HMDB0038731	$C_{13}H_{22}O$	-5,78981	3,46E-05	4,460445	1,700406
Vomifoliol	3,517	224,1409	225,1482	HMDB0303570	$C_{13}H_{20}O_3$	6,685312	3,63E-06	5,439498	1,850491
7-Epi-12-hydroxyjasmonic acid	3,942	226,12	227,1273	HMDB0303749	$C_{12}H_{18}O_4$	9,757035	2,83E-08	7,548945	2,218914
8-Hydroxygeraniol 8-O-glucoside	4,457	332.39	374,2165	HMDB0035025	$C_{16}H_{28}O_7$	5,392225	0,000565	3,248129	1,621572
3beta-Hydroxy-5-cholestenal	9,848	400,60	423,3249	HMDB0060131	$C_{27}H_{44}O_2$	-5,19836	1,33E-05	4,874901	1,62304
7a,12a-Dihydroxy-cholestene-3-one	10,46	416,60	439,3199	HMDB0002197	$C_{27}H_{44}O_3$	-7,53264	7,79E-06	5,108677	1,956674
Limonoate a-ring-lactone	6,644	488,2015	489,2088	HMDB0302537	$C_{26}H_{32}O_9$	-5,00973	0,001182	2,927482	1,561349
Cucumerin A	2,79	552,50	575,1571	HMDB0301967	$C_{29}H_{28}O_{11}$	6,765172	0,000685	3,164562	1,819729
Cholic acid glucuronide	12,017	584,70	623,2843	HMDB0002577	$C_{30}H_{48}O_{11}$	4,8136	9,02E-06	5,04476	1,549668
Linalool (8-hydroxydihydro-)	4,627	650,70	692,2884	HMDB0304700	$C_{32}H_{42}O_{14}$	6,441235	4,01E-05	4,396548	1,794936

Key: Highlighted top ten differential metabolites distinguished between *A. calamus* and *L. javanica*.

10.3389/ebm.2026.10867

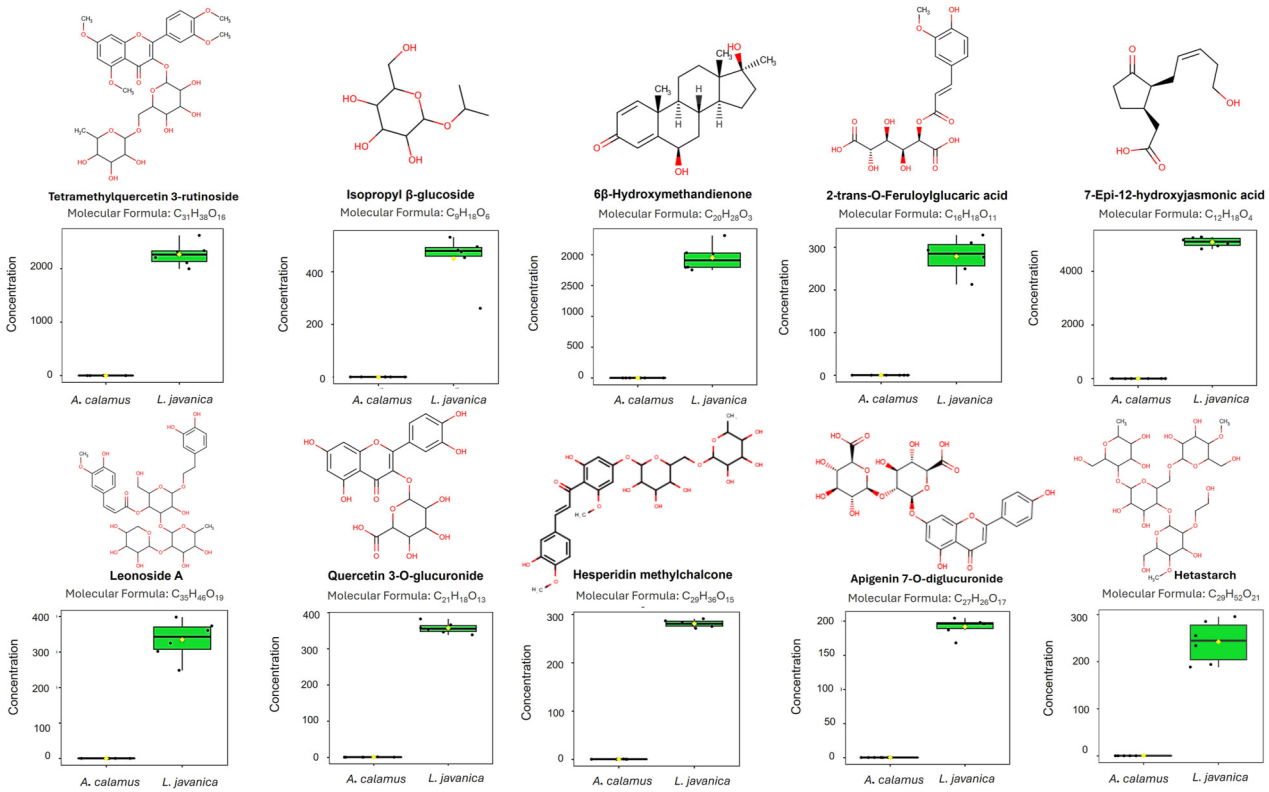

FIGURE 5
Differential metabolites distinguished between *A. calamus* and *L. javanica*. Molecular formulas, chemical structures, and boxplots of the top ten compounds (VIP >1.5, FC >2.0, $p < 0.05$, FDR-adjusted $p < 0.05$) are shown, with abundances in *A. calamus* and *L. javanica*.

Orthogonal PLS-DA (OPLS-DA) model additionally displays variation into a single predictive component (T score [1] = 96.9%) that segregates the plant species and an orthogonal component (Orthogonal T score [1] = 0.8%) representing within the class structure (Figure 4C). The model was further validated by cross-validation, where the model generated high explanatory and predictive performance, with $R^2Y = 1.0$, $R^2X = 0.969$, and $Q^2 = 0.999$. The related *p*-values for the predictive component (p1) were R^2X: 0.969; R^2Y: 1.0; Q^2: 0.999, whereas for the orthogonal component (o1) were R^2X: 0.00813, R^2Y: 0.00031, and Q^2: 7.04×10^{-5}, underscoring the model's explanatory and predictive capability. Further validation of the model was done using a permutation test, with Q^2 and R^2Y values of 0.969 and 0.979, respectively (Supplementary Figure S2).

Univariate analysis of *A. calamus* and *L. javanica* data

Univariate analysis recognized the top ten metabolites with VIP >2.0, FC >2.0, $p < 0.05$ and FDR-adjusted $p < 0.05$ that significantly differentiated the clusters of *A. calamus* and *L. javanica* (Table 1). Figure 5 depicts major significant metabolites comprising Tetramethylquercetin 3-rutinoside, Isopropyl β-glucoside, and 6β-Hydroxymethandienone, altogether presenting an extreme fold of enrichment. Further significant metabolites comprised of 2-trans-O-Feruloylglucaric acid, 7-Epi-12-hydroxyjasmonic acid, and Leonoside A. Flavonoid derivatives, for instance Quercetin 3-O-glucuronide, Hesperidin methylchalcone, and Apigenin 7-O-diglucuronide were also significantly differentiated. Additionally, Hetastarch also provided a contribution to the metabolic variance. Together, these compounds underscore jasmonates, flavonoid glycosides, and phenolic derivatives as crucial, statistically significant metabolites, supporting the distinct chemical divergence amongst the two plant species. These compounds show higher abundances constantly in *L. javanica* (Figure 5). A detailed chemical profiling of each compound is represented in the Supplementary Table S1.

Pharmacokinetic and drug-likeness activity of differential metabolites

The assessment of the ten most significant metabolites from *A. calamus* and *L. javanica* was conducted through the SWISSADME platform to acquire the ADME profiles of each

significant metabolite. This yields essential insights into their potential efficacy as neuroactive inhibitors targeting SH-SY5Y neuroblastoma cells (Table 2).

Physicochemical properties

There was a considerable amount of variability in molecular weight, polarity, and solubility of the ten-highest ranked metabolites, which was determined using the SWISSADME. Smaller molecules such as 7-epi-12-hydroxyjasmonic acid (MW 226.27 g/mol) and isopropyl β-glucoside (MW 222.24 g/mol) had a low topological polar surface area (TPSA <60 $Å^2$) and the absence of hydrogen bond donors, indicating a pronounced potential for passive permeability across biological membranes, and these molecules also met the physicochemical criteria for drug-like entities. In contrast, more complex glycosylated flavonoids, such as apigenin 7-O-diglucuronide (MW 622.49 g/mol) and Leonoside A (MW 770.73 g/mol), exhibited slightly elevated TPSA (>250 $Å^2$) and standout characteristics such as multiple hydrogen bond donors/acceptors, which are conventionally linked to restricted oral bioavailability.

The indices (consensus Log Po/w) for lipophilicity varied from −5.27 for hetastarch to 4.45 for 6β-hydroxymethandienone. This specifically emphasizes the solubility-permeability trade-offs across the metabolite library. Remarkably, 6β-hydroxymethandienone displayed favorable lipophilicity alongside an acceptable molecular weight, implying a significant potential for permeability; conversely, polar glucuronides (e.g., quercetin 3-O-glucuronide, consensus Log Po/w −0.47) are likely impeded in their capacity for cellular penetration.

Water solubility

Predictions regarding water solubility indicated that hetastarch is highly soluble (>2.0 × 10^4 mg/mL), while 6β-hydroxymethandienone displayed suboptimal solubility (4.32 × 10^{-3} mg/mL). Intermediate solubility profiles were noted for flavonoid derivatives, such as hesperidin methylchalcone and tetramethylquercetin 3-rutinoside. These findings suggest that formulation strategies may be necessary for highly lipophilic compounds exhibiting poor intrinsic solubility.

Pharmacokinetics

Predictions regarding gastrointestinal (GI) absorption depicted that 6β-hydroxymethandienone, isopropyl β-glucoside, and 7-epi-12-hydroxyjasmonic acid demonstrate high absorption potential, whereas the majority of glycosylated flavonoids exhibited low absorption due to their extensive polar surface areas. Blood-brain barrier (BBB) permeability was anticipated for the smaller hydrophobic compounds, particularly isopropyl β-glucoside, 6β-hydroxymethandienone, and 7-epi-12-hydroxyjasmonic acid, implying a potential for central nervous system (CNS) activity against SH-SY5Y neuroblastoma cells. Significantly, numerous compounds, including hesperidin methylchalcone and apigenin diglucuronide, were identified as substrates for P-glycoprotein (P-gp), suggesting a vulnerability to efflux and diminished intracellular accumulation.

Skin permeation (Log Kp) values were more favorable for lipophilic scaffolds (e.g., −4.33 cm/s for 6β-hydroxymethandienone) in comparison to highly polar compounds (−16.26 cm/s for hetastarch). The analysis of Cytochrome P450 (CYP) inhibition identified 6β-hydroxymethandienone as a multi-isoform inhibitor (CYP2C19, CYP2C9, CYP2D6, CYP3A4), indicating potential drug-drug interaction liabilities, whereas the majority of glycosides exhibited no alerts for CYP inhibition.

Drug-likeness

Filters for Drug-likeness indicated that only isopropyl β-glucoside, 6β-hydroxymethandienone, and 7-epi-12-hydroxyjasmonic acid fully conformed to Lipinski's rule of five, as well as Veber, Egan, and Muegge criteria, while the majority of glycosides surpassed thresholds for hydrogen bonding, molecular weight, and TPSA. Bioavailability scores corroborated these findings, revealing favorable values of 0.55 for the smaller drug-like molecules in contrast to ≤0.17 for the larger glycosides. These outcomes underscore isopropyl β-glucoside and 6β-hydroxymethandienone as promising candidates for oral bioavailability.

Medicinal chemistry filters

The identification of Brenk alerts, as well as PAINS (Pan-Assay Interference Compounds), has highlighted various flavonoid derivatives (such as hesperidin methylchalcone, Leonoside A, and quercetin 3-O-glucuronide) that exhibit Michael acceptor motifs or catechol, thereby indicating the likelihood of assay interferences. The synthetic accessibility scores exhibited a range from 2.31 (7-epi-12-hydroxyjasmonic acid, which is readily synthesizable) to 8.06 (hetastarch, which is characterized by high complexity), reflecting considerations of feasibility for prospective lead optimization endeavors. Lead-likeness was attained solely for 6β-hydroxymethandienone, while the remaining metabolites were hindered by excessive molecular dimensions or flexibility.

Therefore, the ADME profiling has prioritized three metabolites, namely isopropyl β-glucoside, 6β-hydroxymethandienone, and 7-epi-12-hydroxyjasmonic acid, which emerge as the most promising lead-like candidates for targeting of SH-SY5Y neuroblastoma cells. Larger polar flavonoid glycosides, despite their bioactivity, may necessitate structural simplification or the implementation of advanced delivery systems to mitigate challenges related to poor absorption and permeability. Their favourable oral bioavailability, blood-brain barrier permeability, and adherence to drug-likeness criteria substantiate their potential for subsequent preclinical validation.

TABLE 2 Physicochemical, pharmacokinetic, drug-likeness, and medicinal chemistry properties of the selected differential bioactive secondary metabolites.

Parameters	Isopropyl β-glucoside	Hetastarch	6β--hydroxymethandienone	Hesperidin methylchalcone	Leonoside A	2-trans-O-Feruloylglucaric acid	Quercetin 3-O-glucuronide	Apigenin 7-O-diglucuronide	Tetramethylquercetin 3-rutinoside	7-Epi-12-hydroxyjasmonic acid
Physicochemical Properties										
Formula	C9H18O6	C29H52O21	C20H28O3	C29H36O15	C35H46O19	C16H18O11	C21H18O13	C27H26O17	C31H38O16	C12H18O4
Molecular weight	222.24 g/mol	736.71 g/mol	316.43 g/mol	624.59 g/mol	770.73 g/mol	386.31 g/mol	478.36 g/mol	622.49 g/mol	666.62 g/mol	226.27 g/mol
No. heavy atoms	15	50	23	44	54	27	34	44	47	16
No. arom. heavy atoms	0	0	0	12	12	10	16	16	12	0
Fraction Csp3	1.00	1.00	0.60	0.48	0.57	0.44	0.24	0.37	0.48	0.50
No. of rotatable bonds	0	15	6	11	13	4	4	7	13	9
No. H-bond acceptors	6	21	3	15	19	11	13	17	16	4
No. H-bond donors	0	11	0	9	11	6	8	9	8	0
Molar Refractivity	49.89	156.69	93.83	148.42	179.64	87.17	110.77	139.71	158.16	61.42
TPSA	55.38 Å²	314.83 Å²	43.37 Å²	245.29 Å²	304.21 Å²	179.28 Å²	227.58 Å²	283.34 Å²	251.36 Å²	52.60 Å²
Lipophilicity										
Log Po/w (iLOGP)	3.13	2.21	4.00	2.15	2.28	0.90	1.13	0.28	3.47	3.17
Log Po/w (XLOGP3)	1.84	−7.70	5.49	−0.50	−1.60	−0.99	0.61	−0.24	0.07	2.22
Log Po/w (WLOGP)	2.05	−7.35	4.39	−1.12	−2.27	−1.61	−0.45	−1.94	−0.55	2.01
Log Po/w (MLOGP)	1.50	−7.42	3.48	−2.37	−3.75	−2.23	−2.60	−3.68	−1.99	1.94
Log Po/w (SILICOS-IT)	1.09	−6.09	4.87	−1.14	−2.61	−1.13	−1.04	−2.66	−0.61	2.53
Consensus Log Po/w	1.92	−5.27	4.45	−0.60	−1.59	−1.01	−0.47	−1.65	0.08	2.37
Water solubility										
Log S (ESOL)	−2.38	1.43	−4.86	−2.87	−2.92	−1.62	−3.27	−3.36	−3.35	−2.05
Solubility	9.33e-01 mg/mL; 4.20e-03 mol/L	2.00e+04 mg/mL; 2.71e+01 mol/L	4.32e-03 mg/mL; 1.37e-05 mol/L	8.36e-01 mg/mL; 1.34e-03 mol/L	9.33e-01 mg/mL; 1.21e-03 mol/L	9.24e+00 mg/mL; 2.39e-02 mol/L	2.54e-01 mg/mL; 5.32e-04 mol/L	2.75e-01 mg/mL; 4.41e-04 mol/L	2.99e-01 mg/mL; 4.49e-04 mol/L	2.03e+00 mg/mL; 8.96e-03 mol/L
Class	Soluble	Highly soluble	Moderately soluble	Soluble	Soluble	Very soluble	Soluble	Soluble	Soluble	Soluble

(*Continued*)

10.3389/ebm.2026.10867

TABLE 2 Continued

Parameters	Isopropyl β-glucoside	Hetastarch	6β--hydroxymethandienone	Hesperidin methylchalcone	Leonoside A	2-trans-O-Feruloylglucaric acid	Quercetin 3-O-glucuronide	Apigenin 7-O-diglucuronide	Tetramethylquercetin 3-rutinoside	7-Epi-12-hydroxyjasmonic acid
Log S (Ali)	−2.62	1.83	−6.16	−4.18	−4.28	−2.29	−4.96	−5.25	−4.90	−2.96
Solubility	5.29e-01 mg/mL; 2.38e-03 mol/L	4.95e+04 mg/mL; 6.72e+01 mol/L	2.19e-04 mg/mL; 6.94e-07 mol/L	4.09e-02 mg/mL; 6.55e-05 mol/L	4.05e-02 mg/mL; 5.26e-05 mol/L	1.99e+00 mg/mL; 5.14e-03 mol/L	5.20e-03 mg/mL; 1.09e-05 mol/L	3.48e-03 mg/mL; 5.59e-06 mol/L	8.35e-03 mg/mL; 1.25e-05 mol/L	2.48e-01 mg/mL; 1.10e-03 mol/L
Class	Soluble	Highly soluble	Poorly soluble	Moderately soluble	Moderately soluble	Soluble	Moderately soluble	Moderately soluble	Moderately soluble	Soluble
Log S (SILICOS-IT)	−1.45	5.00	−3.83	−0.22	1.04	−0.34	−1.04	0.05	−0.81	−2.55
Solubility	7.89e+00 mg/mL; 3.55e-02 mol/L	7.45e+07 mg/mL; 1.01e+05 mol/L	4.65e-02 mg/mL; 1.47e-04 mol/L	3.77e+02 mg/mL; 6.04e-01 mol/L	8.55e+03 mg/mL; 1.11e+01 mol/L	1.75e+02 mg/mL; 4.52e-01 mol/L	4.36e+01 mg/mL; 9.12e-02 mol/L	6.95e+02 mg/mL; 1.12e+00 mol/L	1.03e+02 mg/mL; 1.55e-01 mol/L	6.35e-01 mg/mL; 2.81e-03 mol/L
Class	Soluble	Soluble	Soluble	Soluble	Soluble	Soluble	Soluble	Soluble	Soluble	Soluble
Pharmacokinetics										
GI absorption	High	Low	High	Low	Low	Low	Low	Low	Low	High
BBB permeant	Yes	No	Yes	No	No	No	No	No	No	Yes
P-gp substrate	No	Yes	No	Yes	No	No	Yes	Yes	Yes	No
CYP1A2 inhibitor	No	No	No	No	No	No	No	No	No	No
CYP2C19 inhibitor	No	No	Yes	No	No	No	No	No	No	No
CYP2C9 inhibitor	Yes	No	Yes	No	No	No	No	No	No	No
CYP2D6 inhibitor	No	No	Yes	No	No	No	No	No	No	No
CYP3A4 inhibitor	No	No	Yes	No	No	No	No	No	No	No
Log Kp (skin permeation)	−6.35 cm/s	−16.26 cm/s	−4.33 cm/s	−10.46 cm/s	−12.14 cm/s	−9.36 cm/s	−8.78 cm/s	−10.27 cm/s	−10.32 cm/s	−6.10 cm/s
Drug likeness										
Lipinski	Yes; 0 violation	No; 3 violations: MW >500, NorO >10, NHorOH >5	Yes; 0 violation	No; 3 violations: MW >500, NorO >10, NHorOH >5	No; 3 violations: MW >500, NorO >10, NHorOH >5	No; 2 violations: NorO >10, NHorOH >5	No; 2 violations: NorO >10, NHorOH >5	No; 3 violations: MW >500, NorO >10, NHorOH >5	No; 3 violations: MW >500, NorO >10, NHorOH >5	Yes; 0 violation
Ghose	Yes	No; 4 violations: MW >480, WLOGP <−0.4, MR >130, #atoms >70	Yes	No; 4 violations: MW >480, WLOGP <−0.4, MR >130, #atoms >70	No; 4 violations: MW >480, WLOGP <−0.4, MR >130, #atoms >70	No; 1 violation: WLOGP <−0.4	No; 1 violation: WLOGP<−0.4	No; 3 violations: MW >480, WLOGP<−0.4, MR >130	No; 4 violations: MW >480, WLOGP <−0.4, MR >130, #atoms >70	Yes
Veber	Yes	No; 2 violations: Rotors >10, TPSA >140	Yes	No; 2 violations: Rotors >10, TPSA >140	No; 2 violations: Rotors >10, TPSA >140	No; 1 violation: TPSA >140	No; 1 violation: TPSA >140	No; 1 violation: TPSA >140	No; 2 violations: Rotors >10, TPSA >140	Yes

(*Continued*)

10.3389/ebm.2026.10867

10.3389/ebm.2026.10867

TABLE 2 Continued

Parameters	Isopropyl β-glucoside	Hetastarch	6β--hydroxymethandienone	Hesperidin methylchalcone	Leonoside A	2-trans-O-Feruloylglucaric acid	Quercetin 3-O-glucuronide	Apigenin 7-O-diglucuronide	Tetramethylquercetin 3-rutinoside	7-Epi-12-hydroxyjasmonic acid
Egan	Yes	No; 1 violation: TPSA >131.6	Yes	No; 1 violation: TPSA >131.6	No; 1 violation: TPSA >131.6	No; 1 violation: TPSA >131.6	No; 1 violation: TPSA >131.6	No; 1 violation: TPSA >131.6	No; 1 violation: TPSA >131.6	Yes
Muegge	Yes	No; 5 violations: MW >600, XLOGP3 <−2, TPSA >150, H-acc >10, H-don >5	No; 1 violation: XLOGP3 >5	No; 4 violations: MW >600, TPSA >150, H-acc >10, H-don >5	No; 4 violations: MW >600, TPSA >150, H-acc >10, H-don >5	No; 3 violations: TPSA >150, H-acc >10, H-don >5	No; 3 violations: TPSA >150, H-acc >10, H-don >5	No; 4 violations: MW >600, TPSA >150, H-acc >10, H-don >5	No; 4 violations: MW >600, TPSA >150, H-acc >10, H-don >5	Yes
Bioavailability score	0.55	0.17	0.55	0.17	0.17	0.17	0.11	0.11	0.17	0.55
Medicinal Chemistry										
PAINS	0 alert	0 alert	0 alert	1 alert: catechol_A	1 alert: catechol_A	0 alert	1 alert: catechol_A	0 alert	1 alert: catechol_A	0 alert
Brenk	1 alert: peroxide	0 alert	1 alert: isolated_alkene	2 alerts: catechol, michael_acceptor_1	2 alerts: catechol, michael_acceptor_1	1 alert: cumarine	1 alert: catechol	0 alert	3 alerts: catechol, michael_acceptor_1, more_than_2_esters	2 alerts: mchael_acceptor_1, more_than_2_esters
Leadlikeness	No; 1 violation: MW 250	No; 2 violations: MW >350, Rotors >7	No; 1 violation: XLOGP3 >3.5	No; 2 violations: MW >350, Rotors >7	No; 2 violations: MW >350, Rotors >7	No; 1 violation: MW >350	No; 1 violation: MW >350	No; 1 violation: MW >350	No; 2 violations: MW >350, Rotors >7	No; 2 violations: MW < 250, Rotors >7
Synthetic accessibility	4.34	8.06	4.72	6.37	7.45	5.05	5.26	6.26	6.57	2.31

Discussion

This study validates that extracts of *L. javanica* and *A. calamus* alter mitochondrial functional status and exert dose-dependent cytotoxic effects in SH-SY5Y neuroblastoma cells. The observed shifting toward increased mitochondrial membrane polarization, as evaluated by JC-1 staining, implies preservation or enrichment of mitochondrial reliability at levels of the tested exposure, rather than clear mitochondrial depolarization. Such effects are consistent with complex phytochemical concoctions in which mitochondrial responses might vary depending on exposure duration, concentration, and cellular context [14, 52].

Untargeted metabolomics analysis facilitated the chemical delineation of the phenotypic expressions of substances. With multivariate statistics verifying the distinct chemical differences between the two species, the metabolomic profiling identified a wide range of bioactive substances, including alkaloids, phenolics, flavonoid glycosides, and jasmonates. Separated and distinct groupings were exhibited by *L. javanica* and *A. calamus* in PCA, PLS-DA and OPLS-DA, with cross-validation by OPLS-DA and permutation analyses corroborating the non-random nature of the segregation of classes [53]. Given the propensity for supervised models to exhibit overfitting traits, the interpretation of data of the nearly perfect R^2/Q^2 values with circumspection, anchoring conclusions within the framework of unsupervised PCA delineation and independent univariate filters (VIP, fold-change, *p* values), which is indicative of optimal methodological procedures [54]. The principal discriminative compounds identified were isopropyl β-glucoside, 6β-hydroxymethandienone, 7-epi-12-hydroxyjasmonic acid, 2-trans-O-feruloylglucaric acid, and flavonoid glycosides (e.g., conjugates of quercetin and apigenin) [55]. The identification of a jasmonate (7-epi-12-hydroxyjasmonic acid) is of significant mechanistic relevance; most jasmonates and their derivatives possess the capability to induce cancer cell apoptosis through the disassociation of hexokinase II from the mitochondria, inadvertently, disrupting metabolic processes [56, 57], and multiple research investigations have documented ROS-mediated apoptotic responses across several tumor models [57, 58]. If jasmonate-like chemistry was enriched in *L. javanica*, the plant may contribute to cytotoxic effects at elevated concentrations, notwithstanding the net mixture's antioxidative behavior under the experimental conditions employed [35, 36].

The chemistry of *L. javanica* varies by chemotype (piperitenone-, carvone-, linalool, or myrcenone-rich), which can modulate biological effects [59]. The metabolomic analysis confirms the divergence of composition from *A. calamus* and focuses on phenylpropanoid, flavonoid, or jasmonate classes for fractionation [33]. The profile for *A. calamus* inherently invokes concerns pertaining to translation, although β-asarone and some crude extracts have the potential to exhibit antiproliferative activity both *in vitro* and *in vivo* [60–62]. β-asarone has been identified as a carcinogenic and genotoxic component in rodents as well as hepatotoxic in preclinical models; this necessitates the establishment of regulatory limits in phytomedicine as well as food products [62]. Consequently, any trajectory for the development of products must prioritize asarone-depleted fractions or alternatives devoid of asarone if the exploration of efficacy is to be conducted safely [42, 43, 62]. It is crucial to note that putative annotations of mescaline-and steroid-like compounds probable indicate structurally associated plant-derived analogues sharing common triterpenoid or phenethylamine biosynthetic scaffolds, instead of definitive identification of canonical reference molecules [48, 63].

Accordingly, SwissADME analysis was employed to provide functional prioritization of annotated metabolites. The SwissADME software was utilized alongside complementary cheminformatics principles (Lipinski, Veber, Ghose, Egan, Muegge), and in conjunction with gastrointestinal absorption/BBB predictions and alert panels (PAINS, Brenk, lead-likeness), this was done to examine the most discriminative metabolites [64–66]. Compounds such as isopropyl β-glucoside, 6β-hydroxymethandienone, and 7-epi-12-hydroxyjasmonic were identified through the internal ADME heatmap as advantageous lead-like candidates that are grounded in minimal rule infractions, bioavailability assessments, and feasible synthetic accessibility [44]. Although SwissADME's BOILED-Egg framework serves as an ideal tool for preliminary evaluation for BBB and gastrointestinal predictions, further orthogonal verification is usually required through experimental assays such as PAMPA, MDCK/P-gp transport, and microsomal stability as described in this study [47, 67]. Within this limitation-aware framework, *in silico* ADME predictions still serve as a critical early-stage filter for selecting candidate phytometabolites with translational possibility in neuroblastoma research [68]. Predicted BBB permeability is mostly applicable for neuroblastoma, given the connection of paraspinal, intracranial, or central nervous system-adjacent disease locations, where incomplete tissue penetration can restrict therapeutic efficacy [44]. Moreover, predicted P-glycoprotein (P-gp) substrate status alerts the probability of active efflux, which might decrease intracellular accumulation and influence multidrug resistance [69]. Lastly, cytochrome P450 (CYP) inhibition profiles present understanding into possible metabolic liabilities and drug-drug interaction risks, which are important considerations in pediatric oncology settings where integration therapies are common [70]. In general, these parameters reinforce rational prioritization of phytometabolites for downstream optimization, while emphasizing compounds that might need structural refinement or different delivery approaches.

Natural products remain significantly important as complementary or primary scaffolds for neuroblastoma-based therapies, particularly polyphenols, which are a class of

secondary metabolites known to influence apoptosis activity and autophagy, and may also specifically target neuroblastoma stem-like cell populations [71, 72]. A compilation of recent scholarly reviews has systematically outlined a variety of phytochemicals exhibiting preclinical activity against neuroblastoma and highlighted proposed combinations of probable strategies aimed at augmenting responses to standard therapeutic regimens [73]. Within this body of literature, our findings motivate a chemotype-specific follow-up: (i) to deprioritize asarone-rich fractions of *A. calamus* or to specifically eliminate β-asarone before experimental testing due to safety concerns [62], (ii) to assess and evaluate flavonoid conjugates for their potential to modulate redox status and kinase signaling pathways in neuroblastoma [74], and (iii) to extract jasmonate-like metabolites from *L. javanica* for the purpose of investigating the direct targeting of mitochondrial pathways [57].

Together, these results offer a rationale for structured future investigations that incorporate chemotype-informed isolation approaches, bioactivity-guided fractionation, and target-focused mechanistic assessment.

Future directions

Building on potential chemotypic signatures identified by incorporating univariate and multivariate metabolomic analyses, future work should prioritize targeted isolation of potential metabolites from dominant chemical classes. Bioactivity-guided fractionation methods can be critical to connect specific phytochemical fractions to functional effects studies in neuroblastoma cells and to isolate active constituents from complex extract mixtures. In silico structure-based molecular docking and molecular dynamics can be used to screen relevant molecular targets against neuroblastoma. To support rational prioritization of candidate chemotypes and guide hypothesis-driven mechanistic investigations.

Conclusion

This study employed an integrated workflow of untargeted metabolomics, mitochondrial functional assessment, and *in silico* ADME to explore phytometabolites from *L. javanica* and *A. calamus* in human SH-SY5Y neuroblastoma cells. Univariate and multivariate investigations uncovered distinct chemotypic signatures, with *L. javanica* characterized by flavonoid- and polyphenol-enriched profiles and *A. calamus* was dominated by jasmonate-, phenylpropanoid- and lipophilic terpenoid-associated metabolites. Extract exposure related to dose-dependent reductions in cell viability and modulation of mitochondrial membrane potential. In silico pharmacokinetic predictions supported early-stage prioritization of selected chemotypes such as isopropyl β-glucoside, 6β-hydroxymethandienone, and 7-epi-12-hydroxyjasmonic acid. These results are preliminary and hypothesis-generating, and further mechanistic confirmation and *in vivo* studies are recommended to establish biological mechanisms and translational importance.

Author contributions

Conceptualization, MM and NM; methodology, EP, NM, MZ, CO, BI, and MM; software, NM, MZ, BI, and EP; validation, CN, CO, NM, and MM; formal analysis, MM, NM, CN, MZ, and EP; investigation, MM, NM, and CN; resources, EP, MZ, CO, MM, BI, and NM; data curation, NM and MM; writing – original draft preparation, NM and MM; writing – review and editing, MM, CO, BI, EP, MZ, NM, and CN; visualization, MM, NM, BI, and CN; supervision, EP, MZ, CO, MM, BI, and NM; project administration, MM and NM; funding acquisition, MM, CO, and NM. All authors contributed to the article and approved the submitted version.

Data availability

The original contributions presented in the study are included in the article/Supplementary Material, further inquiries can be directed to the corresponding author.

Ethics statement

Ethical approval was not required for the studies on humans in accordance with the local legislation and institutional requirements because only commercially available established cell lines were used.

Funding

The author(s) declared that financial support was received for this work and/or its publication. This research was funded by South Africa's National Research Foundation grant number MND210524603403.

Acknowledgements

Research reported in this publication/article was supported by Sefako Makgatho Health Sciences University. We would also like to sincerely thank the South African Medical Research Council (SAMRC) through its Division of Research Capacity Development under the Research Capacity Development Initiative.

Conflict of interest

The author(s) declared no potential conflicts of interest with respect to the research, authorship, and/or publication of this article.

Generative AI statement

The author(s) declared that generative AI was not used in the creation of this manuscript.

Any alternative text (alt text) provided alongside figures in this article has been generated by Frontiers with the support of artificial intelligence and reasonable efforts have been made to ensure accuracy, including review by the authors wherever possible. If you identify any issues, please contact us.

Supplementary material

The Supplementary Material for this article can be found online at: https://www.ebm-journal.org/articles/10.3389/ebm.2026.10867/full#supplementary-material

References

1. National Cancer Institute. Childhood neuroblastoma treatment (PDQ®)–health professional version (2025). Available online at: https://www.cancer.gov/types/neuroblastoma/hp (Accessed September 12, 2025).

2. D'Ambrosio N, Lyo JK, Young RJ, Haque SS, Karimi S. Imaging of metastatic CNS neuroblastoma. *AJR Am J Roentgenol* (2010) **194**(5):1223–9. doi:10.2214/AJR.09.3203

3. Vo KT, Matthay KK, Neuhaus J, London WB, Hero B, Ambros PF, et al. Clinical, biologic, and prognostic differences on the basis of primary tumor site in neuroblastoma: a report from the international neuroblastoma risk group project. *J Clin Oncol* (2014) **32**(28):3169–76. doi:10.1200/JCO.2013.54.2315

4. Motshudi MC, Naidoo CM, Mkolo NM. The race against time for the enhancement of African national strategic plans in the neuroblastoma research heterogeneity. *Publications* (2024) **12**(4):45. doi:10.3390/publications12040045

5. Davidoff AM. Neuroblastoma. *Semin Pediatr Surg* (2012) **21**(1):2–14. doi:10.1053/j.sempedsurg.2011.10.009

6. Speleman F, Park JR. Henderson TO. Neuroblastoma: a tough nut to crack. *Am Soc Clin Oncol Educ Book* (2016) **35**:548–57. doi:10.1200/EDBK_159169

7. Cohn SL, Pearson ADJ, London WB, Monclair T, Ambros PF, Brodeur GM, et al. The international neuroblastoma risk group (INRG) classification system: an INRG task force report. *J Clin Oncol* (2009) **27**(2):289–97. doi:10.1200/JCO.2008.16.6785

8. Matthay KK, Maris JM, Schleiermacher G, Nakagawara A, Mackall CL, Diller L, et al. Neuroblastoma. *Nat Rev Dis Primers* (2016) **2**:16078. doi:10.1038/nrdp.2016.78

9. Kovalevich J, Langford D. *Considerations for the use of SH-SY5Y neuroblastoma cells in neurobiology*. New Jersey: Humana Press (2013). p. 9–21. doi:10.1007/978-1-62703-640-5_2.18

10. Xicoy H, Wieringa B, Martens GJ. The SH-SY5Y cell line in Parkinson's disease research: a systematic review. *Mol Neurodegener* (2017) **12**(1):10. doi:10.1186/s13024-017-0149-0

11. Shipley MM, Mangold CA, Szpara ML. Differentiation of the SH-SY5Y human neuroblastoma cell line. *J Vis Exp* (2016) **108**:53193. doi:10.3791/53193

12. Engel M, Do-Ha D, Muñoz SS, Ooi L. Common pitfalls of stem cell differentiation: a guide to improving protocols for neurodegenerative disease models and research. *Cell. Mol. Life Sci* (2016) **73**(19):3693–709. doi:10.1007/s00018-016-2265-3

13. Zorov DB, Juhaszova M, Sollott SJ. Mitochondrial reactive oxygen species (ROS) and ROS-induced ROS release. *Physiol Rev* (2014) **94**(3):909–50. doi:10.1152/physrev.00026.2013

14. Fulda S, Galluzzi L, Kroemer G. Targeting mitochondria for cancer therapy. *Nat Rev Drug Discov* (2010) **9**(6):447–64. doi:10.1038/nrd3137

15. Trachootham D, Alexandre J, Huang P. Targeting cancer cells by ROS-mediated mechanisms: a radical therapeutic approach? *Nat Rev Drug Discov* (2009) **8**(7):579–91. doi:10.1038/nrd2803

16. Schumacker PT. Reactive oxygen species in cancer cells: live by the sword, die by the sword. *Cancer Cell* (2006) **10**(3):175–6. doi:10.1016/j.ccr.2006.08.015

17. Selim NA, Wojtovich AP. Mitochondrial membrane potential and compartmentalized signaling: calcium, ROS, and beyond. *Redox Biol* (2025) **86**:103859. doi:10.1016/j.redox.2025.103859

18. Patil GV, Dass SK, Chandra R. *Artemisia afra* and modern diseases. *J Pharmacogenom Pharmacoprot* (2011) **2**(3):2153. doi:10.4172/2153-0645.1000105

19. Motshudi MC, Olaokun OO, Mkolo NM. Evaluation of GC×GC-TOF-MS untargeted metabolomics, cytotoxicity, and antimicrobial activity of leaf extracts of Artemisia afra (Jacq.) purchased from three local vendors. *J King Saud Univ Sci* (2021) **33**(4):101422. doi:10.1016/j.jksus.2021.101422

20. van Wyk BE. The potential of South African plants in the development of new medicinal products. *S Afr J Bot* (2011) **77**(4):812–29. doi:10.1016/j.sajb.2011.08.011

21. Mehrbod P, Abdalla MA, Njoya EM, Ahmed AS, Fotouhi F, Farahmand B, et al. South African medicinal plant extracts active against influenza A virus. *BMC Complement Altern Med* (2018) **18**(1):112. doi:10.1186/s12906-018-2184-y

22. Mkolo NM, Naidoo CM, Kadye R, Obi CL, Iweriebor BC, Olaokun OO, et al. Identification of South African plant-based bioactive compounds as potential inhibitors against the SARS-CoV-2 receptor. *Pharmaceuticals* (2024) **17**(7):821. doi:10.3390/ph17070821

23. Spies L, Koekemoer TC, Sowemimo AA, Goosen ED, Van de Venter M. Caspase-dependent apoptosis induced by *Artemisia afra* Jacq. ex willd in a mitochondria-dependent manner after G2/M arrest. *South Afr J Bot* (2013) **84**:104–9. doi:10.1016/j.sajb.2012.10.007

24. Miraj S, Alesaeidi S. A systematic review study of therapeutic effects of *Matricaria recuitta chamomile* (chamomile). *Electron Physician* (2016) **8**(9):3024–31. doi:10.19082/3024

25. van Loggenberg S, Willers C, van der Kooy F, Gouws C, Hamman JH, Steyn JD. Evaluating *in vitro* cytotoxic effects of *Artemisia afra* and *Artemisia annua* infusions against selected lung cancer cell lines. *South Afr J Bot* (2022) **150**:404–11. doi:10.1016/j.sajb.2022.07.028

26. Sobol Z, Homiski ML, Dickinson DA, Spellman RA, Li D, Scott A, et al. Development and validation of an *in vitro* micronucleus assay platform in TK6 cells. *Mutat Res* (2012) **746**(1):29–34. doi:10.1016/j.mrgentox.2012.02.005

27. Fabre N, Rustan I, de Hoffmann E, Quetin-Leclercq J. Determination of flavone, flavonol, and flavanone aglycones by negative ion liquid chromatography electrospray ion trap mass spectrometry. *J Am Soc Mass Spectrom* (2001) **12**(6):707–15. doi:10.1016/s1044-0305(01)00226-4

28. Liu TY, Tan ZJ, Jiang L, Gu JF, Wu XS, Cao Y, et al. Curcumin induces apoptosis in gallbladder carcinoma cell line GBC-SD cells. *Cancer Cell Int* (2013) **13**(1):64. doi:10.1186/1475-2867-13-64

29. Ru J, Li P, Wang J, Zhou W, Li B, Huang C, et al. TCMSP: a database of systems pharmacology for drug discovery from herbal medicines. *J Cheminform* (2014) **6**(1):13. doi:10.1186/1758-2946-6-13

30. Khan S, Madhi SA, Olwagen C. *In-silico* identification of potential inhibitors against FabI protein in Klebsiella pneumoniae. *J Biomol Struct Dyn* (2024) **42**(3):1506–17. doi:10.1080/07391102.2023.2200571

31. Mwangi JW, Addae-Mensah I, Munavu RM, Lwande W. Essential oils of Kenyan *Lippia* species. Part III. *Flavour Fragr J* (1991) **6**(3):221–4. doi:10.1002/ffj.2730060311

32. Manenzhe NJ, Potgieter N, Van Ree T. Composition and antimicrobial activities of volatile components of *Lippia javanica*. *Phytochemistry* (2004) **65**(16):2333–6. doi:10.1016/j.phytochem.2004.07.020

33. Viljoen AM, Subramoney S, van Vuuren SF, Başer KHC, Demirci B. The composition, geographical variation and antimicrobial activity of *Lippia javanica* (Verbenaceae) leaf essential oils. *J Ethnopharmacol* (2005) **96**(1–2):271–7. doi:10.1016/j.jep.2004.09.017

34. Lukwa N, Mølgaard P, Furu P, Bøgh C. *Lippia javanica* (Burm.f.) Spreng: its general constituents and bioactivity on mosquitoes. *Trop Biomed* (2009) 85–91.

35. Chagonda LS, Chalchat J-C. Essential oil composition of *Lippia javanica* (Burm.f.) Spreng chemotype from Western Zimbabwe. *J Essent Oil Bear Plants* (2015) **18**(2):482–5. doi:10.1080/0972060x.2014.1001140

36. Maroyi A. *Lippia javanica* (Burm.f.) spreng.: traditional and commercial uses and phytochemical and pharmacological significance in the African and Indian subcontinent. *Evid Based Complement Altern Med* (2017) **2017**(1):6746071. doi:10.1155/2017/6746071

37. Muranaka T, Saito K. Production of pharmaceuticals by plant tissue cultures. *Compreh Nat Prod Chem Biol* (2010) **3**:615–28. doi:10.1016/B978-008045382-8.00065-4

38. Sharma V, Sharma R, Gautam DS, Kuca K, Nepovimova E, Martins N. Role of vacha (*Acorus calamus* linn.) in neurological and metabolic disorders: evidence from ethnopharmacology, phytochemistry, pharmacology and clinical study. *J Clin Med* (2020) **9**(4):1176. doi:10.3390/jcm9041176

39. Liu NQ, Van der Kooy F, Verpoorte R. *Artemisia afra*: a potential flagship for African medicinal plants? *S Afr J Bot* (2009) **75**(2):185–95. doi:10.1016/j.sajb.2008.11.001

40. Lang SJ, Schmiech M, Hafner S, Paetz C, Steinborn C, Huber R, et al. Antitumor activity of an *Artemisia annua* herbal preparation and identification of active ingredients. *Phytomedicine* (2019) **62**:152962. doi:10.1016/j.phymed.2019.152962

41. Vogel D, Loots E, Oladimeji O, Gouws C, van der Kooy F. The anti-neoplastic activity of *Artemisia afra* in breast cancer cell lines. *S Afr J Bot* (2023) **157**:115–21. doi:10.1016/j.sajb.2023.03.049

42. Das BK, Swamy AHV, Koti BC, Gadad PC. Experimental evidence for use of *Acorus calamus* (Asarone) for cancer chemoprevention. *Heliyon* (2019) **5**(5):e01585. doi:10.1016/j.heliyon.2019.e01585

43. Yende SR, Harle U, Rajgure DT, Tuse T, Vyawahare NS. Pharmacological profile of *Acorus calamus:* an overview. *Pharmacogn Rev* (2008) **2**(4):23–6.

44. Daina A, Michielin O, Zoete V. SwissADME: a free web tool to evaluate pharmacokinetics, drug-likeness and medicinal chemistry friendliness of small molecules. *Sci Rep* (2017) **7**(1):42717. doi:10.1038/srep42717

45. Djoumbou Feunang Y, Eisner R, Knox C, Chepelev L, Hastings J, Owen G, et al. ClassyFire: automated chemical classification with a comprehensive, computable taxonomy. *J Cheminform* (2016) **8**(1):61. doi:10.1186/s13321-016-0174-y

46. Pires DEV, Blundell TL, Ascher DB. pkCSM: predicting small-molecule pharmacokinetic and toxicity properties using graph-based signatures. *J Med Chem* (2015) **58**(9):4066–72. doi:10.1021/acs.jmedchem.5b00104

47. Daina A, Zoete V. A BOILED-egg to predict gastrointestinal absorption and brain penetration of small molecules. *ChemMedChem* (2016) **11**(11):1117–21. doi:10.1002/cmdc.201600182

48. Sumner LW, Amberg A, Barrett D, Beale MH, Beger R, Daykin CA, et al. Proposed minimum reporting standards for chemical analysis chemical analysis working group (CAWG) metabolomics standards initiative (MSI). *Metabolomics* (2007) **3**:211–21. doi:10.1007/s11306-007-0082-2

49. Thermo Fisher Scientific. *Cell culture basics handbook*. Waltham, MA, USA: Thermo Fisher Scientific (2022). Available online at: https://www.thermofisher.com/cellculturebasics (Accessed September 12, 2025).

50. Dojindo molecular technologies, Inc. 2018. cell counting Kit-8 (CCK-8) protocol (2025). Available online at: https://www.dojindo.com/products/pdf/Protocol/Cell_Counting_Kit-8.pdf (Accessed 12 September, 2025).

51. Sakamuru S, Zhao J, Attene-Ramos MS, Xia M. *Mitochondrial membrane potential assay*. New York: Springer US (2022). p. 11–9. doi:10.1007/978-1-0716-2213-1_2

52. Kopustinskiene DM, Jakstas V, Savickas A, Bernatoniene J. Flavonoids as anticancer agents. *Nutrients* (2020) **12**(2):457. doi:10.3390/nu12020457

53. Newman DJ, Cragg GM. Natural products as sources of new drugs over the nearly four decades from 01/1981 to 09/2019. *J Nat Prod* (2020) **83**(3):770–803. doi:10.1021/acs.jnatprod.9b01285

54. Worley B, Powers R. Multivariate analysis in metabolomics. *Curr Metabolomics* (2013) **1**(1):92–107. doi:10.2174/2213235X11301010092

55. Triba MN, Le Moyec L, Amathieu R, Goossens C, Bouchemal N, Nahon P, et al. PLS/OPLS models in metabolomics: the impact of permutation of dataset rows on the K-fold cross-validation quality parameters. *Mol Biosyst* (2015) **11**(1):13–9. doi:10.1039/C4MB00414K

56. Wishart DS. Emerging applications of metabolomics in drug discovery and precision medicine. *Nat Rev Drug Discov* (2016) **15**(7):473–84. doi:10.1038/nrd2016.32

57. Rotem R, Heyfets A, Fingrut O, Blickstein D, Shaklai M, Flescher E. Jasmonates: novel anticancer agents acting directly and selectively on human cancer cell mitochondria. *Cancer Res* (2005) **65**(5):1984–93. doi:10.1158/0008-5472.CAN-04-3091

58. Flescher E. Jasmonates—A new family of anti-cancer agents. *Anticancer Drugs* (2005) **16**(9):911–6. doi:10.1097/01.cad.0000176501.63680.80

59. Fingrut O, Reischer D, Rotem R, Goldin N, Altboum I, Zan-Bar I, et al. Jasmonates induce nonapoptotic death in high-resistance mutant p53-Expressing B-Lymphoma cells. *Br J Pharmacol* (2005) **146**(6):800–8. doi:10.1038/sj.bjp.0706394

60. Mujovo SF, Hussein AA, Meyer JJ, Fourie B, Muthivhi T, Lall N. Bioactive compounds from *Lippia javanica* and *Hoslundia opposita*. *Nat Prod Res* (2008) **22**(12):1047–54. doi:10.1080/14786410802250037

61. Mukherjee PK, Kumar V, Mal M, Houghton P. *Acorus Calamus*: scientific validation of ayurvedic tradition from natural resources. *Pharm Biol* (2008) **45**(8):651–66. doi:10.1080/13880200701538724

62. Hasheminejad G, Caldwell J. Genotoxicity of the alkenylbenzenes α– and β-asarone, myristicin and elemicin as determined by the UDS assay in cultured rat hepatocytes. *Mutat Res* (1994) **321**(3):89–97. doi:10.1016/0278-6915(94)90194-5

63. Facchini FPJ. Alkaloid biosynthesis in plants: biochemistry, cell biology, molecular regulation, and metabolic engineering applications. *Annu Rev Plant Physiol Plant Mol Biol* (2001) **52**:29–66. doi:10.1146/annurev.arplant.52.1.29

64. Thimmappa R, Geisler K, Louveau T, O'Maille P, Osbourn A. Triterpene biosynthesis in plants. *Annu Rev Plant Biol* (2014) **65**:225–57. doi:10.1146/annurev-arplant-050312-120229

65. Lipinski CA, Lombardo F, Dominy BW, Feeney PJ. Experimental and computational approaches to estimate solubility and permeability in drug discovery and development settings. *Adv Drug Deliv Rev* (1997) **23**(1–3):3–25. doi:10.1016/S0169-409X(96)00423-1

66. Brenk R, Schipani A, James D, Krasowski A, Gilbert IH, Frearson J, et al. Lessons learnt from assembling screening libraries for drug discovery for neglected diseases. *ChemMedChem* (2008) **3**(3):435–44. doi:10.1002/cmdc.200700139

67. Avdeef AADrug Development. *Solubility, permeability, and charge state*. 2nd ed. New Jersey: John Wiley and Sons (2012). doi:10.1002/9781118286067#:~:text=10.1002/9781118286067

68. Pardridge WM. The blood-brain barrier: bottleneck in brain drug development. *NeuroRx* (2005) **2**(1):3–14. doi:10.1602/neurorx.2.1.3

69. Gottesman MM, Fojo T, Bates SE. Multidrug resistance in cancer: role of ATP-dependent transporters. *Nat Rev Cancer* (2002) **2**(1):48–58. doi:10.1038/nrc706

70. Zhou SF. Drugs behave as substrates, inhibitors and inducers of human cytochrome P450 3A4. *Curr Drug Metab* (2008) **9**(4):310–22. doi:10.2174/138920008784220664

71. Hill A, Gupta R, Zhao D, Vankina R, Amanam I, Salgia R. Targeted therapies in non-small-cell lung cancer. *Precision Medicine Cancer Therapy* (2019) **178**, 3–43. doi:10.1007/978-3-030-16391-4_1

72. Li Y, Liu T, Ivan C, Huang J, Shen D-Y, Kavanagh JJ, et al. Corrigendum: enhanced cytotoxic effects of combined valproic acid and the Aurora kinase inhibitor VE465 on gynecologic cancer cells. *Front Oncol* (2018) **8**:9. doi:10.3389/fonc.2018.00009

73. Cheung NKV, Dyer MA. Neuroblastoma: developmental biology, cancer genomics, and immunotherapy. *Nat Rev Cancer* (2013) **13**(6):515–34. doi:10.1038/nrc3526

74. Wang K, Zhang T, Dong Q, Nice EC, Huang C, Wei Y. Redox homeostasis: the linchpin in stem cell self-renewal and differentiation. *Cell Death Dis* (2013) **4**(3):e537. doi:10.1038/cddis.2013.50

EBM Experimental Biology and Medicine

TYPE Brief Communication
PUBLISHED 13 March 2026
DOI 10.3389/ebm.2026.10907

OPEN ACCESS

*CORRESPONDENCE
Damien P. Kuffler,
dkuffler@hotmail.com

RECEIVED 23 November 2025
REVISED 27 February 2026
ACCEPTED 04 March 2026
PUBLISHED 13 March 2026

CITATION
Kuffler DP, Reyes O, Sosa IJ and Foy CA (2026) A novel platelet-rich plasma clinically induces reliable, rapid, long-term chronic peripheral neuropathic pain elimination.
Exp. Biol. Med. 251:10907.
doi: 10.3389/ebm.2026.10907

A novel platelet-rich plasma clinically induces reliable, rapid, long-term chronic peripheral neuropathic pain elimination

Damien P. Kuffler[1]*, Onix Reyes[2], Ivan J. Sosa[3] and Christian A. Foy[4]

[1]Institute of Neurobiology, Medical School, University of Puerto Rico, San Juan, PR, United States, [2]Doctor's Center Hospital, Manati, PR, United States, [3]Section of Neurosurgery, Medical School, University of Puerto Rico, San Juan, PR, United States, [4]Section of Orthopedic Surgery, Medical Sciences Campus, University of Puerto Rico, San Juan, PR, United States

Abstract

Peripheral nerve trauma results in 50%–84% of patients developing chronic neuropathic pain, which is eliminated when axons reinnervate targets. Autografts reduce pain by promoting target reinnervation. We hypothesized that applying a novel platelet-rich plasma (PRP) formulation to proximal stumps would permanently eliminate the pain. This prospective case series compared analgesia levels after bridging nerve gaps with an autograft (autograft repair) vs. a PRP-filled collagen tube (PRP repair). Autograft repairs were performed on 16 nerves with a 5.75-cm mean gap length, 2.0-year repair delay, 42.3-year age, and 8.6 chronic neuropathic pain. PRP repairs were performed on 10 nerves with a 6.0-cm gap length, 1-year repair delay, 36.7-year age, with 88% having 9.1 chronic neuropathic pain. For autograft repairs, the pain began to decrease when axons reinnervated targets, reaching a mean of 0.3 in 18.2% of patients, and was eliminated in 81.8%. Following PRP repairs, the pain reduction began within 2 weeks and was eliminated by 2 months. Thus, autografts contribute to pain reduction/elimination by promoting target reinnervation. However, PRP directly and rapidly induced long-term pain elimination in all patients, while axons were regenerating, and without target reinnervation. These results prove that platelet-released factors reliably and rapidly eliminate chronic neuropathic pain.

KEYWORDS

autografts, chronic neuropathic pain, nerve regeneration, nerve trauma, PRP

Impact statement

Peripheral nerve trauma results in up to 85% of patients suffering chronic neuropathic pain, which can have a profound negative impact on patients' lives because no technique induces reliable or rapid long-term pain elimination. This study shows that applying PRP of a novel composition to nerves evoking chronic pain reliably and rapidly eliminated the

pain in each patient, regardless of age, repair delay, and lack of target reinnervation. The acceptance and broad application of this novel PRP to nerves evoking chronic neuropathic pain may eliminate chronic neuropathic pain in all patients.

Introduction

Peripheral nerve trauma not only eliminates sensory and motor function but also results in 50%–84% of individuals developing chronic neuropathic pain [1]. The first line of treatment for chronic neuropathic pain is pharmacological agents. While they may reduce/eliminate pain, their analgesic effects are limited, short-lived, and may cause severe side effects that preclude their use.

A secondary approach for restoring function and reducing chronic neuropathic pain is to use sensory nerve autografts, the clinical "gold standard" surgical technique, to bridge nerve gaps to restore function. Although autografts do not directly reduce or eliminate pain, they contribute to pain reduction/elimination by promoting axonal regeneration across the graft and into the distal part of the nerve, leading to target reinnervation, which, in turn, reduces/eliminates the pain [2]. The present case series was designed to determine whether, compared to autografts, bridging nerve gaps with a PRP-filled collagen tube results in greater long-term reduction or elimination of chronic neuropathic pain, while also restoring meaningful sensory and motor recovery. PRP has been shown to enhance axon regeneration and reduce pain [3]. The efficacy of PRP promoting recovery is discussed in a separate paper, while this paper focuses on PRP and its ability to eliminate chronic neuropathic pain.

Materials and methods

Research objectives

Determine the relative efficacy of bridging peripheral nerve gaps with an autograft vs. a PRP-filled collagen tube in reducing/eliminating chronic neuropathic pain and the duration of the pain suppression.

Hypothesis

Platelet-released factors induce long-term chronic neuropathic pain reduction/elimination.

Research subjects

Patients presenting to the Department of Orthopedic Surgery service who required a peripheral nerve gap repair.

Inclusion criteria

Subjects aged 18–75 years old with a nerve gap that required repair. Each exhibited one or more of the following three conditions that are known to reduce or prevent recovery: A gap larger than 5 cm, nerve repair delay more than 5 months post-injury, and age more than 25 years.

Experimental design

This formal prospective consecutive study treated the PRP repair individuals as experimental subjects, followed by the retrospective analysis of control autograft repair patients. The study compared the level of chronic neuropathic pain pre- and post-surgery following upper extremity nerve gap repairs using an autograft vs. a PRP-filled collagen tube.

Randomization

No.

Blinding

No blinding.

Sample size

Power analysis indicated that the study required a sample size of 8 patients to achieve a significance level of $p < 5\%$.

Surgery

Under full anesthesia, nerve injury sites were exposed, the damaged nerve tissue cut away with a scalpel, and the nerve stumps refreshed under a microscope, where clear nerve fascicles were seen in the proximal nerve stump, and no scarring was seen in the distal stump/s.

The resulting nerve gap/s were measured.

Collagen tubes

Before the availability of FDA-approved collagen tubes, collagen tubes were made using FDA-approved 2 × 8 cm collagen sheets (Veritas, Synovis Life Technologies, St. Paul, MN). The tubes were created by sewing a sheet around the handle of a surgical tool as a template. Tubes from 8 cm sheets

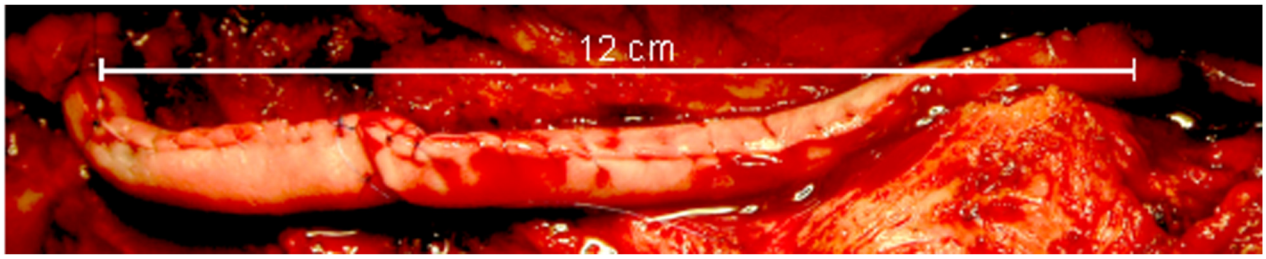

FIGURE 1
Repaired and PRP-filled 12-cm nerve gap. Two collagen sheets were sewn end-to-end, then into a tube, before being injected with PRP.

can be used to repair gaps ≤7.6 cm in length, allowing the autograft and nerve stump coaptation sites to be 1–2 mm inside the PRP-filled collagen tube. To bridge longer gaps, two collagen sheets were sewn together end-to-end and into a tube. Subsequently, commercially available NeuroMend Collagen tubes (Regenity Biosciences, Oakland, NY) were used.

Securing the nerve stumps within the collagen tube

Autografts were loosely secured with a single suture to the proximal and distal nerve stumps.

Preparation of platelet-rich fibrin

Under general anesthesia, but before any surgical intervention, 55 cc of whole blood were drawn from a peripheral vein into a 60-cc syringe containing 5 cc of citrate-based anticoagulant. The PRP was separated using Gravitation Platelet Separation III (GPS III) centrifuge tubes (Zimmer Biomet Corp., Warsaw, IN), yielding ca. 6 cc of PRP.

Filling the collagen tube with PRP

The PRP was drawn from the GPS centrifuge tube into a 10 mL syringe, while 0.6 cc of thrombin was drawn into a 1 cc syringe. The syringes were attached to a FibriJet Ratio Applicator Assembly SA-1001 with an attached flexible blending connector SA-3673 (Nordson Medical, Westlake, OH). The catheter was inserted into the collagen tube, and both syringe plungers were pressed simultaneously, mixing and injecting the syringe contents into and filling the collagen tube. The fibrin polymerized within 20 s, and the patient closed. Figure 1 shows the completed repair of a 12-cm-long nerve gap in a 58-year-old patient, which was repaired 3.25 years after nerve trauma.

Rules for stopping data collection

The original data collection was intended to stop when the last enrolled patient was 1.5 years post-surgery. However, the data of one patient, collected 10 months post-surgery, are included because he disappeared shortly after the electrophysiological and physical tests were performed.

Patient follow-up

To ensure consistency in the electrophysiological and physical studies and analyses, they were performed on all patients by the same clinicians within a few-month period.

Pain evaluation

Each patient self-evaluated their neuropathic pain level before and after surgery using the validated 11-point qualitative pain assessment linear pain scale, ranging from 0–10, where 0 = no pain and 10 = worst pain possible.

Statistical analysis

Statistical analysis involved using Excel to calculate means and standard deviations, and regression analysis was used to examine relationships among the variables.

Adverse events

No patient experienced any adverse events, such as infections or worsening or new neuropathic pain.

Ethical practice

This study was performed under a local IRB-approved protocol and in accordance with the World Medical Association Declaration of Helsinki (JBJS 79-A:1089-98,1997).

TABLE 1 Demographics and pain outcomes.

Descriptor	Autograft repairs	PRP repairs	% Difference
# Patients	11	8	
# Nerves	16	10	
Female/male	1/10	0/8	
Gap length	2–8 cm (mean 5.75 ± 2.05 SD)	2–12 cm (mean 6 ± 2.6 SD)	4.3% longer
Repair delay	0.25–6.3 years (mean 2.01 ± 0.59 SD)	2 weeks - 3.25 years (mean 1 ± 1.1 SD)	2-fold longer
Age	19–71 years (mean 42.3 ± 16.3SD	18–58 years (mean 36.7 ± 13.7 SD)	13.3% older
Patients with pre-surgery pain	100%	88%	12% fewer
Pre-surgery pain range	4–10	7–10	
% Patients with pain of 8–10	81.8%	86%	
Mean pre-surgery pain	8.6 ± 4.2 SD	9.1 ± 1.2 SD	
Post-surgery follow-up time range	1.1–3 years (mean 1 ± 0.7 SD)	10 months - 17.8 years (mean 13.3 ± 0.4 SD)	
Post-surgery pain range	0–2	0	
Mean post-surgery pain	0.3 ± 0.3 SD	0	
Patients with pain reduced	18.2%	--	
Patients with pain eliminated	81.8%	100%	

Informed consent

Each recruited patient signed an IRB-approved Written Consent Form.

Patient gender

Patients were enrolled as they presented, without consideration of gender.

Results

Demographics

The autograft repairs involved 16 upper extremity nerves in 11 patients, and the PRP repairs involved 10 upper extremity nerves in 8 patients. For the autograft and PRP repairs, the mean gap lengths were 5.75 and 6.0 cm, mean repair delays 2.0 and 1.0 years, respectively, and mean patient ages 42.3 and 36.7 years, respectively. Table 1 all the nerves were mixed sensory and motor, with 37.5% median and 56.3% ulnar. The gap locations were 12.5% elbow, 50% forearm, and 37.5% wrist.

Pain reduction/elimination

Before surgery, 100% of the autograft repair patients and 88% of the PRP repair patients suffered chronic neuropathic pain, respectively, with 81.8%and 86% having a mean pain of 8.6 vs. 9.1, respectively. Table 1 For autograft repairs, pain began to decrease around the time axons started to reinnervate targets, reaching a mean of 0.3 in 18.2% of patients, and was eliminated in 81.8% of patients. For the PRP repairs, each patient's pain began to decrease within 2 weeks of surgery and was eliminated within 2 months.

Discussion

Reducing chronic neuropathic pain: pharmacological agents and surgery

Peripheral nerve trauma leads to 50%–85% of patients suffering chronic neuropathic pain [1]. The level of pre-operative neuropathic pain is a good predictor of neuropathic pain persisting after the nerve repair [4]. Furthermore, increasing repair delays are associated with smaller reductions in post-repair chronic neuropathic pain [5].

Pharmaceutical agents, such as gabapentin, provide adequate pain control to only 30%–40% of patients, but they do not eliminate the pain. Further, they often induce debilitating and intolerable side effects that preclude their use.

More effective than pharmaceuticals in reducing neuropathic pain are autografts and allografts, the clinical "gold standard" techniques for repairing nerve gaps. They induce similar amounts of target reinnervation and meaningful recovery, which, in turn, leads to reliable chronic neuropathic pain reduction/elimination in <50% of patients [6].

It is hypothesized that neuropathic pain remains chronic as long as axons are regenerating and is only reduced/eliminated when axons reinnervate targets, stop regenerating [2], and pick up target-derived factor/s that stop the nociceptive axon hyperactivity that underlies the pain [7]. This hypothesis led to the development of targeted muscle reinnervation (TMR) and regenerative peripheral nerve interface (RPNI) techniques that reduce or eliminate chronic neuropathic pain.

In animal models [8] and clinically [9], TMR and RPNI reduce the development of pain-inducing neuromas, thereby reducing neuroma pain in 75%–100% of patients, and reducing both post-amputation and phantom limb pain (PLP) in 45%–80% [9]. However, TMR and RPNI have the limitations that their analgesic efficacy decreases when applied >3 months post-trauma [10]. Further, they cannot be used if one's goals are to reduce pain and restore meaningful sensory and motor function.

PRP efficacy in reducing pain

Animal model studies show that PRP reduces chronic pain behavior associated with *Mycobacterium leprae* (leprosy bacteria) induced lesions [11], and when applied to sites of skin burn-induced neuropathic pain [12], and rat spinal cord injury sites [13]. Clinically, chronic neuropathic pain is reduced by applying PRP to sciatic [14] and digital nerve crush sites [15], neurolysis surgery sites [16], when applied to nerves during carpal tunnel surgery [17], following PRP intraneural injection, when injected into the intervertebral disc epidural space [18], and into the perineurium of patients suffering from diabetic neuropathic pain [19]. A single PRP injection provides analgesia against lower back pain lasting up to 2 years [20]. However, despite multiple PRP injections, the analgesia was consistently incomplete and temporary, and about one-third of patients got no pain relief [20]. However, a recent case series showed that bridging nerve gaps with an autograft within a PRP-filled collagen tube resulted in reliable and rapid long-term reduction of chronic neuropathic pain in 11% of patients and complete pain elimination in 89% of the patients [3].

The present study compared the effect of bridging nerve gaps with an autograft vs. a PRP-filled collagen tube on chronic neuropathic pain levels. Before surgery, all the autograft repair patients suffered chronic neuropathic pain of 8.6, with 81.8% of 8–10. Each patient's pain began to decrease when axons started to reinnervate their targets, and was reduced to a mean of 0.3. Before the PRP repairs, 88% of the patients suffered a mean neuropathic pain of 9.1, with 86% of 8–10. Following surgery, each patient's pain began to decrease within 2 weeks, and was eliminated in all the patients within 2 months. Thus, the pain was eliminated while the axons were regenerating and before they had innervated any targets, which demonstrates that platelet-released factors alone can induce long-term chronic neuropathic pain reduction/elimination.

The greatly varied analgesic efficacy of PRP in different studies raises the question of why the PRP used in the present study was far more effective in inducing long-term pain elimination than other PRP. We propose that this was due to the manner in which the PRP was prepared and applied. First, commercial and non-commercial preparation systems yield PRP that varies significantly. These differences include major variations in blood components, glucose levels, pH, platelet concentration, percentage of activated vs. unactivated platelets, bioactive vs. non-bioactive factors, and the presence of other cell types, such as leukocytes and red blood cells. The PRP platelet concentration in this study was increased 9.3-fold, approximately 2-3-fold over PRP from other sources, such as following single-spin separation, which yields a 2.7-fold increase in platelet concentration, or double-spin, which yields PRP with a 2.5 - 5.7-fold increased platelet concentration, with PRP efficacy increasing with increasing platelet concentration [21].

Second, the PRP leukocyte concentration was increased 5-fold (Data on file at Biomet Biologics, LLC) compared to other PRP. While leukocytes can induce inflammation, they also exert anti-inflammatory and analgesic effects [22]. Third, most studies use a small PRP volume (<1 cc), whereas the present study used 4–6 cc. Fourth, while most studies merely apply PRP to the surface of nerves, the present study surrounded the PRP with a collagen tube, which, in rats, increases PRP efficacy [14].

In the present study, PRP eliminated the pain in each patient. In contrast, a larger study might find variability in the extent of pain reduction/elimination among the patients. These differences are best explained by variations in the patient's whole blood platelet concentration, which can vary up to 2-fold 23, and by physiological factors, such as diet, medications, and health issues [23].

Potential mechanisms of PRP action

Nerve injury induces nociceptive neurons to upregulate Nav1.8 sodium channel expression, leading to axon hyperexcitability, neuropathic pain, painful neuropathies, and inflammatory pain [24]. This makes the Nav1.8 channel a good target for reducing/eliminating chronic neuropathic pain. PRP may also reduce/eliminate pain by platelet-released transcription factor 4 (TCF4), down-regulating Nav1.8 channels [25], thus silencing chronically active nociceptive axons.

Among alternative mechanisms by which platelets may reduce pain is by their induction of monocytes to release the anti-inflammatory cytokine IL-10, which can reduce pain in several ways. First, by suppressing the production of pro-inflammatory cytokines and increasing the expression of anti-inflammatory cytokines [26]. It can also act directly on neurons [27] by down-regulating Nav1.6 and Nav1.8 [28], which contribute to chronic neuropathic pain. Second, platelets can reduce neuropathic pain by releasing TNF-α [29].

Conclusion

Before surgery, all autograft repair patients suffered a mean chronic neuropathic pain of 8.6. Which was reduced to a mean of 0.3, with 18.2% experiencing long-term pain reduction, and 81.2% long-term pain elimination. For the PRP repairs, before surgery, before surgery, 88% of the patients suffered chronic neuropathic pain of 9.1, which was eliminated in all the patients. For the autograft repairs, the pain began to decrease about the time the regenerating axons started reinnervating their targets. For the PRP repairs, their pain began to decrease within 2 weeks and was eliminated within 2 months. This elimination occurred while the axons were regenerating and long before any regenerating axons innervated targets. The extent of pain reduction/elimination was not influenced by higher pre-surgical pain levels or the increasing values of the independent variables of gap length, repair delay, and patient age. In conclusion, this study proves that platelet-released factors reliably induce long-term chronic neuropathic pain elimination within 2 months, while axons are regenerating, and without requiring target innervation.

Study limitations

The primary limitation of this study is its small sample size, although it was adequate for statistical analysis.

Author contributions

DK: Conceptualization, methodology, surgery, validation, formal analysis, investigation, resources, supervision, project administration, data curation, writing original and final draft of paper; OR and IS: methodology, surgery, data collection, formal analysis, review of final paper; CF: methodology, surgery, data collection, data analysis, review and editing final paper. All authors contributed to the article and approved the submitted version.

Data availability

The raw data supporting the conclusions of this article will be made available by the authors, without undue reservation.

Ethics statement

This study was performed under a clinical study protocol approved by the University of Puerto Rico Medical Sciences Campus Institutional Review Board, and in accordance with the World Medical Association Declaration of Helsinki (JBJS 79-A:1089-44 98,1997). Each patient provided written informed consent.

Funding

The author(s) declared that financial support was not received for this work and/or its publication.

Acknowledgements

We thank Jose Manuel Guzman Gutierrez and Jose G. Rodriguez Semidey for their assistance in tracking down and bringing in the patients, and Victor Rosado, Gerardo Olivella, and Norberto J. Torres Lugo for support in the electrophysiological and physical studies, and assistance in statistical analysis from the Biostatistics, Epidemiology, and Research Design Core of the Hispanic Alliance for Clinical and Translational (Alliance), supported by NIGMS/NIH Award #U54GM133807.

Conflict of interest

The author(s) declared no potential conflicts of interest with respect to the research, authorship, and/or publication of this article.

Generative AI statement

The author(s) declared that generative AI was not used in the creation of this manuscript.

Any alternative text (alt text) provided alongside figures in this article has been generated by Frontiers with the support of artificial intelligence and reasonable efforts have been made to ensure accuracy, including review by the authors wherever possible. If you identify any issues, please contact us.

References

1. Miclescu A, Straatmann A, Gkatziani P, Butler S, Karlsten R, Gordh T. Chronic neuropathic pain after traumatic peripheral nerve injuries in the upper extremity: prevalence, demographic and surgical determinants, impact on health and on pain medication. *Scand J Pain* (2019) **20**:95–108. doi:10.1515/sjpain-2019-0111

2. Lanier ST, Jordan SW, Ko JH, Dumanian GA. Targeted muscle reinnervation as a solution for nerve pain. *Plast Reconstr Surg* (2020) **146**:651e–63e. doi:10.1097/PRS.0000000000007235

3. Kuffler DP, Reyes O, Sosa IJ, Micheo WF, Santiago-Figueroa JM, Foy CA. Clinically reducing/eliminating chronic neuropathic pain by bridging peripheral

nerve gaps with an autograft within a PRP-filled collagen tube. *J Pain Res* (2025) **18**: 3207–16. doi:10.2147/JPR.S523451

4. Zuniga JR. Sensory outcomes after reconstruction of lingual and inferior alveolar nerve discontinuities using processed nerve allograft--a case series. *J Oral Maxillofac Surg* (2015) **73**:734–44. doi:10.1016/j.joms.2014.10.030

5. Felder JM, Ducic I. Chronic nerve injuries and delays in surgical treatment negatively impact patient-reported quality of life. *Plast Reconstr Surg Glob Open* (2021) **9**:e3570. doi:10.1097/GOX.0000000000003570

6. Ciaramitaro P, Padua L, Devigili G, Rota E, Tamburin S, Eleopra R, et al. Neuropathic pain special interest group of the Italian Neurological S. Prevalence of neuropathic pain in patients with Traumatic brachial plexus injury: a multicenter prospective hospital-based study. *Pain Med* (2017) **18**:2428–32. doi:10.1093/pm/pnw360

7. Valerio I, Schulz SA, West J, Westenberg RF, Eberlin KR. Targeted muscle reinnervation combined with a vascularized pedicled regenerative peripheral nerve interface. *Plast Reconstr Surg Glob Open* (2020) **8**:e2689. doi:10.1097/GOX.0000000000002689

8. Kloehn AJ, Errante EL, Costello MC, Burks SS. Commentary: a direct comparison of targeted muscle reinnervation and regenerative peripheral nerve interfaces to prevent neuroma pain. *Neurosurgery* (2023) **93**:e125–e126. doi:10.1227/neu.0000000000002567

9. Mauch JT, Kao DS, Friedly JL, Liu Y. Targeted muscle reinnervation and regenerative peripheral nerve interfaces for pain prophylaxis and treatment: a systematic review. *PM R* (2023) **15**:1457–65. doi:10.1002/pmrj.12972

10. Roth E, Linehan A, Weihrauch D, Stucky C, Hogan Q, Hoben G. Targeted muscle reinnervation prevents and reverses rat pain behaviors after nerve transection. *Pain* (2023) **164**:316–24. doi:10.1097/j.pain.0000000000002702

11. Anjayani S, Wirohadidjojo YW, Adam AM, Suwandi D, Seweng A, Amiruddin MD. Sensory improvement of leprosy peripheral neuropathy in patients treated with perineural injection of platelet-rich plasma. *Int J Dermatol* (2014) **53**:109–13. doi:10.1111/ijd.12162

12. Huang SH, Wu SH, Lee SS, Lin YN, Chai CY, Lai CS, et al. Platelet-rich plasma injection in burn scar areas alleviates neuropathic scar pain. *Int J Med Sci* (2018) **15**: 238–47. doi:10.7150/ijms.22563

13. Behroozi Z, Ramezani F, Janzadeh A, Rahimi B, Nasirinezhad F. Platelet-rich plasma in umbilical cord blood reduces neuropathic pain in spinal cord injury by altering the expression of ATP receptors. *Physiol Behav* (2021) **228**:113186. doi:10.1016/j.physbeh.2020.113186

14. Vares P, Dehghan MM, Bastami F, Biazar E, Shamloo N, Heidari Keshel S, et al. Effects of platelet-rich Fibrin/Collagen membrane on sciatic nerve regeneration. *J Craniofac Surg* (2021) **32**:794–8. doi:10.1097/SCS.0000000000007003

15. Ikumi A, Hara Y, Okano E, Kohyama S, Arai N, Taniguchi Y, et al. Intraoperative local administration of platelet-rich plasma (PRP) during neurolysis surgery for the treatment of digital nerve crush injury. *Case Rep Orthop* (2018) **2018**:1275713. doi:10.1155/2018/1275713

16. Hibner M, Castellanos ME, Drachman D, Balducci J. Repeat operation for treatment of persistent pudendal nerve entrapment after pudendal neurolysis. *J Minim Invasive Gynecol* (2012) **19**:325–30. doi:10.1016/j.jmig.2011.12.022

17. Dong C, Sun Y, Qi Y, Zhu Y, Wei H, Wu D, et al. Effect of platelet-rich plasma injection on mild or moderate carpal tunnel syndrome: an updated systematic review and meta-analysis of randomized controlled trials. *Biomed Res Int* (2020) **2020**:5089378. doi:10.1155/2020/5089378

18. Barbieri M, Colombini A, Stogicza A, de Girolamo L. Effectiveness of plasma rich in growth factors in the management of chronic spinal pain: a case series of 32 patients. *Regen Med* (2022) **17**:175–84. doi:10.2217/rme-2021-0128

19. Hassanien M, Elawamy A, Kamel EZ, Khalifa WA, Abolfadl GM, Roushdy ASI, et al. Perineural platelet-rich plasma for diabetic neuropathic pain, could it make a difference? *Pain Med* (2020) **21**:757–65. doi:10.1093/pm/pnz140

20. Centeno C, Markle J, Dodson E, Stemper I, Hyzy M, Williams C, et al. The use of lumbar epidural injection of platelet lysate for treatment of radicular pain. *J Exp Orthop* (2017) **4**:38. doi:10.1186/s40634-017-0113-5

21. Aufiero D, Vincent H, Sampson S, Bodor M. Regenerative injection treatment in the spine: review and case series with platelet rich plasma. *J Stem Cells Res Rev & Rep* (2015) **2**:1019.

22. Xiong Y, Gong C, Peng X, Liu X, Su X, Tao X, et al. Efficacy and safety of platelet-rich plasma injections for the treatment of osteoarthritis: a systematic review and meta-analysis of randomized controlled trials. *Front Med (Lausanne)* (2023) **10**:1204144. doi:10.3389/fmed.2023.1204144

23. Kuffler DP. Platelet-rich plasma promotes axon regeneration, wound healing, and pain reduction: fact or fiction. *Mol Neurobiol* (2015) **52**:990–1014. doi:10.1007/s12035-015-9251-x

24. Xiao Y, Barbosa C, Pei Z, Xie W, Strong JA, Zhang JM, et al. Increased resurgent sodium currents in Nav1.8 contribute to nociceptive sensory neuron hyperexcitability associated with peripheral neuropathies. *J Neurosci* (2019) **39**: 1539–50. doi:10.1523/JNEUROSCI.0468-18.2018

25. Li N, Liu B, Wu W, Hong Y, Zhang J, Liu Y, et al. Upregulation of transcription factor 4 downregulates Na(V)1.8 expression in DRG neurons and prevents the development of rat inflammatory and neuropathic hypersensitivity. *Exp Neurol* (2020) **327**:113240. doi:10.1016/j.expneurol.2020.113240

26. Yu ML, Wei RD, Zhang T, Wang JM, Cheng Y, Qin FF, et al. Electroacupuncture relieves pain and attenuates inflammation progression through inducing IL-10 production in CFA-induced mice. *Inflammation* (2020) **43**:1233–45. doi:10.1007/s10753-020-01203-2

27. Krukowski K, Eijkelkamp N, Laumet G, Hack CE, Li Y, Dougherty PM, et al. CD8+ T cells and endogenous IL-10 are required for resolution of chemotherapy-induced neuropathic pain. *J Neurosci* (2016) **36**:11074–83. doi:10.1523/JNEUROSCI.3708-15.2016

28. Liu XG. Normalization of neuroinflammation: a new strategy for treatment of persistent pain and memory/emotional deficits in chronic pain. *J Inflamm Res* (2022) **15**:5201–33. doi:10.2147/JIR.S379093

29. Sorkin LS, Doom CM. Epineurial application of TNF elicits an acute mechanical hyperalgesia in the awake rat. *J Peripher Nerv Syst* (2000) **5**:96–100. doi:10.1046/j.1529-8027.2000.00012.x

EBM Experimental Biology and Medicine

EBM is the official journal of the Society for Experimental Biology and Medicine

Experimental Biology and Medicine (EBM) is a global, peer-reviewed journal dedicated to the publication of multidisciplinary and interdisciplinary research in the biomedical sciences.

Discover more of our Special Issues

See more →

Contact

development@ebm-journal.org

See more

ebm-journal.org

publishingpartnerships.frontiersin.org/our-partners